AD_______________

Award Number: DAMD17-98-1-8141

TITLE: Quantitative Three-dimensional Ultrasonic Mammography

PRINCIPAL INVESTIGATOR: T. Douglas Mast, Ph.D.

CONTRACTING ORGANIZATION: The Pennsylvania State University
Applied Research Laboratory
State College, Pennsylvania 16804-0030

REPORT DATE: October 2001

TYPE OF REPORT: Final

PREPARED FOR: U.S. Army Medical Research and Materiel Command
Fort Detrick, Maryland 21702-5012

DISTRIBUTION STATEMENT: Approved for Public Release;
Distribution Unlimited

The views, opinions and/or findings contained in this report are those of the author(s) and should not be construed as an official Department of the Army position, policy or decision unless so designated by other documentation.

20020910 081

REPORT DOCUMENTATION PAGE	*Form Approved OMB No. 074-0188*

Public reporting burden for this collection of information is estimated to average 1 hour per response, including the time for reviewing instructions, searching existing data sources, gathering and maintaining the data needed, and completing and reviewing this collection of information. Send comments regarding this burden estimate or any other aspect of this collection of information, including suggestions for reducing this burden to Washington Headquarters Services, Directorate for Information Operations and Reports, 1215 Jefferson Davis Highway, Suite 1204, Arlington, VA 22202-4302, and to the Office of Management and Budget, Paperwork Reduction Project (0704-0188), Washington, DC 20503

1. AGENCY USE ONLY (Leave blank)	**2. REPORT DATE** October 2001	**3. REPORT TYPE AND DATES COVERED** Final (01 Jul 98 - 30 Sep 01)

4. TITLE AND SUBTITLE
Quantitative Three-dimensional Ultrasonic Mammography

5. FUNDING NUMBERS
DAMD17-98-1-8141

6. AUTHOR(S)
T. Douglas Mast, Ph.D.

7. PERFORMING ORGANIZATION NAME(S) AND ADDRESS(ES)
The Pennsylvania State University Applied Research Laboratory
State College, Pennsylvania 16804-0030

E-Mail: mast@sabine.acs.psu.edu

8. PERFORMING ORGANIZATION REPORT NUMBER

9. SPONSORING / MONITORING AGENCY NAME(S) AND ADDRESS(ES)

U.S. Army Medical Research and Materiel Command
Fort Detrick, Maryland 21702-5012

10. SPONSORING / MONITORING AGENCY REPORT NUMBER

11. SUPPLEMENTARY NOTES

12a. DISTRIBUTION / AVAILABILITY STATEMENT
Approved for Public Release; Distribution Unlimited

12b. DISTRIBUTION CODE

13. ABSTRACT ***(Maximum 200 Words)***

An investigation of three-dimensional ultrasonic mammography has been completed. Three-dimensional quantitative ultrasonic imaging of breast tissue is now possible using novel inverse scattering methods invented by the Principal Investigator and coworkers. Use of full time-domain scattering information provides images with high point resolution, contrast resolution, and quantitative accuracy without significant artifacts. Nonlinear forms of these methods provide a robust approach to adaptive imaging that is based on compensation for scattering from actual tissue structure. Realistic tissue models for simulation of ultrasound-breast interaction have been developed using specimen cross sections as well as available high-resolution volume photographic data. Calculated scattering from these tissue models provides accurate characterization of ultrasonic propagation within breast tissue and realistic data for quantitative imaging algorithms. Quantitative two- and three-dimensional images, reconstructed from simulated and measured scattering data, show the usefulness of these methods for practical ultrasonic mammography. The results of this research program will make possible new mammographic applications of ultrasound that will provide clinicians with previously unavailable information and detail. These applications are expected to comprise a lower-cost, more effective, and safer modality for diagnosis, detection, and monitoring of breast cancer.

14. SUBJECT TERMS Breast cancer, ultrasound, three-dimensional, imaging, diagnosis	**15. NUMBER OF PAGES** 186
	16. PRICE CODE

17. SECURITY CLASSIFICATION OF REPORT Unclassified	**18. SECURITY CLASSIFICATION OF THIS PAGE** Unclassified	**19. SECURITY CLASSIFICATION OF ABSTRACT** Unclassified	**20. LIMITATION OF ABSTRACT** Unlimited

NSN 7540-01-280-5500

Standard Form 298 (Rev. 2-89)
Prescribed by ANSI Std. Z39-18

Table of Contents

Title Page i
Report Documentation Page (SF 298) ii
Table of Contents 1
I. Introduction 2
II. Body of Report 3
  A. Quantitative Imaging Algorithm Development 3
  B. Tissue Modeling 4
  C. Quantitative Imaging Algorithm Implementation 7
  D. Evaluation and Comparison of Results 8
III. Key Research Accomplishments 11
IV. Reportable Outcomes 13
V. Conclusions 15
VI. References 17
VII. Appendices 19
  A. Wideband quantitative ultrasonic imaging by time-domain diffraction tomography
  B. Time-domain ultrasound diffraction tomography
  C. Abberation correction for time-domain ultrasound diffraction tomography
  D. Simulation of ultrasonic pulse propagation, distortion, and attenuation in the human chest wall
  E. A k-space method for large-scale models of wave propagation in tissue
  F. Validation of FFT-based algorithms for large-scale modeling of wave propagation in tissue
  G. A new k-space method for coupled first-order acoustic propagation equations
  H. Empirical relationships between acoustic parameters in human soft tissues
  I. Two- and three-dimensional simulations of ultrasonic propagation through human breast tissue
  J. Deconvolution of scattered acoustic fields for ultrasonic imaging
  K. Abstracts
  L. Curriculum Vitae (T. Douglas Mast, Principal Investigator)

I. Introduction

An investigation of three-dimensional ultrasonic mammography has been completed. The ultimate goal of the research has been to lay the foundations for improved diagnosis of breast cancer by quantitative, high-resolution three-dimensional ultrasonic imaging. This goal has been reached by a thorough program that synthesizes recent advances in tissue modeling, adaptive imaging, instrumentation, and signal processing. The final results of the research are believed to comprise a major advance in quantitative three-dimensional ultrasonic mammography.

Improved resolution, accurate quantitative information on tissue properties, and precise determination of three-dimensional breast structure can provide crucial new information for detection, diagnosis, and monitoring of breast cancer. Three-dimensional quantitative ultrasonic imaging of breast tissue is now possible using novel inverse scattering methods invented by the Principal Investigator and coworkers. Use of full time-domain scattering information provides images with high point resolution, contrast resolution, and quantitative accuracy without significant artifacts. Nonlinear forms of these methods provide a robust approach to adaptive imaging that is based on compensation for three-dimensional scattering from actual tissue structure. Unlike previous adaptive imaging methods based on assumptions of phase-screen aberrators and point scatterers, these methods provide aberration correction ideally suited to distributed inhomogeneous tissue like the breast.

A unique and innovative aspect of the research has been the use of realistic tissue models for ultrasonic propagation through breast tissue. Such models have been shown to realistically model wavefront distortion in the human abdominal wall, but have not to date been applied to the human breast. Tissue modeling techniques employ tissue maps obtained from specimen cross sections as well as from newly available high-resolution volume photographic data. Calculated scattering from these tissue models provides accurate characterization of ultrasonic propagation within breast tissue and realistic data for quantitative imaging algorithms. The above studies have applied breakthroughs from tissue modeling, inverse scattering, and signal processing to the critical application of ultrasonic mammography. Quantitative two- and three-dimensional images reconstructed from simulated and measured scattering data show the practical applicability of the new methods to clinical breast cancer imaging. The results of this research program will make possible new mammographic applications of ultrasound that will provide clinicians with previously unavailable information and detail. The end result will be a lower-cost, more effective, and safer modality for diagnosis, detection, and monitoring of breast cancer.

II. Body of Report

Below, the accomplishments of the three-year research program are summarized under the four categories of the approved Statement of Work. Details are given for how these accomplishments fit into the overall research plan. Greater detail is provided by the publications included in the Appendices section.

A. Quantitative Imaging Algorithm Development

In this USAMRMC-funded Breast Cancer Research Program project, great progress has been made on development of new quantitative imaging algorithms for three-dimensional ultrasonic mammography. The primary achievement in this area was development, implementation, and testing of a novel time-domain quantitative imaging method incorporating aberration correction [1]–[4]. Refs. [1], [3], and [4] are included as Appendices A, B, and C of this report.

The imaging portion of the present research began with a nonlinear (aberration-corrected) implementation of a method for quantitative imaging using eigenfunctions of the scattering operator [5]–[6]. Preliminary work on iterative nonlinear inverse scattering, with application to quantitative imaging of strongly scattering media such as the human breast, showed promise for the potential of aberration correction to improve quantitative ultrasonic mammography. Since the nonlinear eigenfunction method provides a simple approach to aberration correction (improved reconstructions are obtained using numerical retransmission of eigenfunctions into the estimated medium), this procedure is much more efficient than previously available nonlinear inverse scattering methods. This form of nonlinear aberration correction, in conjunction with the new time-domain imaging method described above, provide all the capabilities required for the proposed method of three-dimensional quantitative ultrasonic mammography. Such aberration correction was later incorporated into the more efficient time-domain imaging method described below.

A time-domain diffraction tomography method, specifically tailored to ultrasonic mammography, has been the primary focus of the quantitative imaging portion of this research. This method allows quantitative, high-resolution images to be obtained using direct synthetic-aperture processing of time-domain scattered fields. An archival manuscript regarding the method was completed, revised, and published during the second year of this project and is included as Appendix A of this report [1].

The new time-domain diffraction tomography method [1]–[4], which is specifically designed for ultrasonic mammography, allows quantitative, high-resolution images to be obtained using direct synthetic-aperture processing of time-domain scattered fields. This method provides tomographic images of inhomogeneous media using scattering measurements made on a surface surrounding the medium of interest, *e.g.*, on a circle for two-dimensional problems or on a sphere for three-dimensional problems. Images of compressibility variations are then reconstructed using coherent combination of the far-field scattered waveforms, delayed and summed in a manner that numerically focuses on the unknown medium. This approach is closely related to synthetic aperture imaging; however, unlike conventional synthetic-aperture methods, the present method provides quantitative reconstructions of compressibility variations, analogous to frequency-compounded filtered backpropagation images weighted by the spectrum of the incident wave. A complete description of the method, with example two-dimensional and three-dimensional reconstruction results, is given in Ref. [1], included as Appendix A of this report. A brief abstract describing the work [2], presented at Forum Acusticum 99, is included in the Appendix K.

Additional results, including the reconstructions from experimentally measured ultrasonic scattering data, were presented at the 1999 IEEE Ultrasonics Symposium in November 1999; a published manuscript from the Symposium Proceedings [3] is included here as Appendix B. These experimental reconstructions show considerable promise for breast cancer detection. Particularly encouraging is the fact that sub-resolvable structures appear as smoothed variations rather than as speckle.

Work continued on the new time-domain imaging method with implementation of methods for nonlinear aberration correction. Such correction provides improved synthetic focusing capability based on medium models determined from quantitative image data. In one approach, improved images are reconstructed using numerical propagation of wavefields into estimates of the unknown medium [5, 8]. In another, much more efficient approach, the quantitative sound-speed reconstruction obtained by the time-domain imaging method is employed to determine time shifts that, when applied to the measured scattering data, compensate for focus aberration caused by inhomogeneous breast tissue [4]. An efficient implementation, in which the necessary line integrals are performed using a DDA (digital differential analyzer) method, allows each iteration to be performed as rapidly as the initial linear reconstruction. Results obtained using this method were presented at the DoD Era of Hope meeting [9] (abstracts provided in Appendix K) and are described in detail in Ref. [4] (Appendix C).

The capabilities of the new time-domain imaging method are exciting for several reasons. First, the images are both higher in quality and more efficiently computed than conventional single-frequency quantitative images. The high point and contrast resolution, as well as absence of artifacts usually associated with diffraction tomography, suggests that this method will be very useful for detection and characterization of breast lesions. Second, because of the close analogy between the new method and delay-and-sum imaging, the new method could be implemented in hardware using beamforming technology already present on digital ultrasound scanners. Third, the quantitative reconstructions provided by the new method allow aberration correction to be implemented much more robustly than possible in conventional pulse-echo imaging. The new time-domain method also has the capability to incorporate other imaging techniques (*e.g.*, time-gain compensation and harmonic imaging) currently used in clinical and experimental B-scan systems.

B. Tissue Modeling

Greatly improved modeling for ultrasound-breast tissue interaction have been achieved in the research reported here through advances both in numerical techniques and in tissue modeling. These advances are described below.

A finite-difference time-domain simulation of ultrasonic propagation through cross-sectional models of chest wall tissue [10, 11] generated several important results directly relevant to the simulation of propagation through breast tissue. First, this work expanded upon previous models [12, 13] by including tissue-dependent absorption effects. The absorption model developed was an important part of the later two-dimensional and three-dimensional simulations of ultrasonic scattering from breast tissue. Second, the chest study contained an analysis of the frequency dependence of ultrasonic wavefront distortion. A comparison of distortion effects for varying pulse center frequencies showed that, for soft tissue paths through the chest wall, energy level and waveform distortion increase markedly with rising ultrasonic frequency and that arrival-time fluctuations increase to a lesser degree. Since breast tissue has been observed to be more strongly scattering than other soft tissues [14], these results are of particular importance for ultrasonic mammography. A full description of this study, with numerical results including statistical summaries, is given in Ref. [11], included here as Appendix D. An abstract describing the work, presented at the 136th Meeting of the Acoustical Society of America, is included in the Appendix K.

In accordance with the Statement of Work, scattering was computed for canonically-shaped inhomogeneities including spheres, cylinders, and rectangular slabs. Time-domain scattered fields were computed using exact solutions [15] for spheres and cylinders with sound speed and density different from the surrounding medium. Time-domain scattered fields were also computed, using a weak scattering approximation, for rectangular slabs with a sound speed different from the surrounding medium. The purpose of these computations was to provide definitive test data for quantitative imaging algorithms. Example reconstructions based on these computations are provided in Ref. [1], provided as Appendix A.

A new k-space method was implemented for simulating wave propagation in soft tissue [16]. Numerical results, including quantitative comparisons of accuracy, showed that the k-space method can achieve very accurate results for large-scale ultrasonic propagation through soft tissue. The computational efficiency obtained with the new k-space method is much greater than that of existing finite difference or pseudospectral methods. The computational method is also fully parallelizable, since most of the computational load can be associated with execution of multithreaded fast Fourier transforms. The method is described and quantitatively analyzed in Ref. [16], included here as Appendix E.

Work continued with optimization of speed and accuracy of the k-space method for scattering computations. A collaborative effort with Weidlinger Associates and the University of Rochester provided detailed quantitative comparisons between a new k-space method and a state-of-the-art pseudospectral solver. This study showed that the k-space method has strong advantages for large-scale simulations of propagation through soft tissue. In particular, the k-space code allows accurate results to be obtained with much larger time steps and fewer independent variables, so that the k-space code is superior both in computational speed and in storage requirements. Both of these considerations are critical for three-dimensional computations of scattering from breast tissue. The comparison was presented at the 1999 IEEE Ultrasonics Symposium and has been published in the proceedings of that symposium; a copy of that publication is included here as Appendix F [17].

Knowledge gained from the abovementioned comparison project led to a number of improvements in the k-space method, including improved computational efficiency, more accurate interpolation of simulated pressure signals, and more effective methods to compute scattering from media including discontinuities. These improvements were reported in a presentation to the Acoustical Society of America [8], (abstract provided in Appendix K). These comparisons, as well as new analysis that explains the remarkable stability and accuracy of the k-space method, greatly improved the extensively revised version of the archival paper [16] that is provided here as Appendix E.

A modified k-space method that solves coupled first-order acoustic propagation equations was also developed during the project. Like k-space methods based on second-order wave equations, this method is exact for homogeneous media, unconditionally stable for "slow" ($c(\mathbf{x}) \leq c_0$) me-

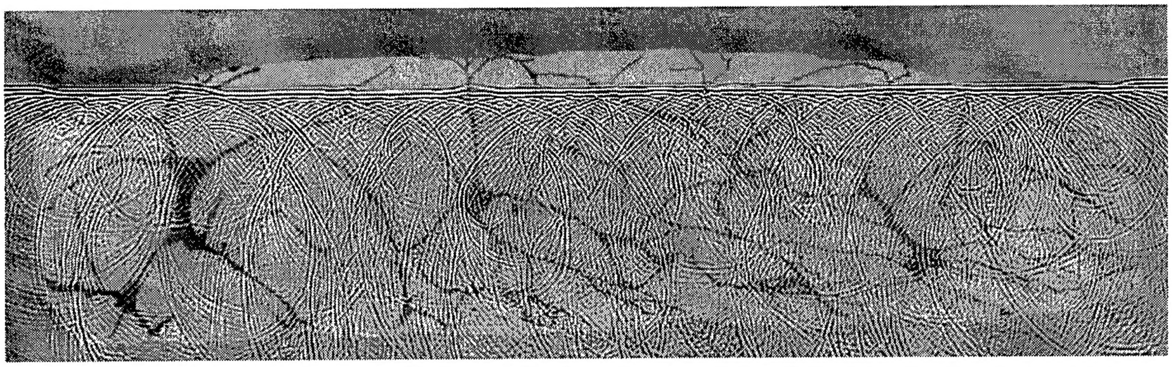

Figure 1: Ultrasonic propagation of a 2.5 MHz pulse through a two-dimensional breast cross-sectional model obtained from a segmented, stained breast tissue cross section. An area of 167 × 50 mm^2 is shown.

dia, and highly accurate for general weakly scattering media. In addition, unlike previous k-space methods, the form of the method allowed straightforward inclusion of relaxation absorption and perfectly matched layer (PML) nonreflecting boundary conditions. A technique for reduction of Gibbs phenomenon artifacts, in which compressibility and exponentially-scaled density functions are smoothed by half-band filtering, was also introduced. When employed together with this smoothing technique, this k-space method provides high accuracy for media including discontinuities, high-contrast inhomogeneities, and scattering structures smaller than the spatial grid resolution. The results are described in detail in Ref. [18], included here as Appendix G.

Once a robust, efficient three-dimensional method for computation of ultrasonic propagation was established, work on mapping of breast tissue became a high priority. In collaboration with colleagues at the University of Rochester, cross-sectional breast tissue specimens have been sectioned and stained for high-resolution segmentation by tissue type. One such tissue cross section is shown, together with a computed ultrasonic pulse propagating within the tissue, in Fig. 1. Simulations of point-source propagation, focusing, and transmit and receive focus correction have been performed employing these cross-sectional breast tissue models. Focus degradation for breast tissue was shown, consistent with previous experimental results [14], to be greater than that for abdominal wall tissue. These results will be formally reported in a forthcoming paper [19].

Also related to the breast modeling effort was a study of empirical relationships between acoustic parameters of human soft tissues, completed and published during 2000 ([20], included as Appendix H). This study showed that sound speed, density, and compressibility variations are all closely (and nearly linearly) related for human soft tissues, so that measurements or estimates of one of these parameters can be used to obtain useful values for the others. In addition, the nonlinearity parameter and attenuation coefficient of soft tissues were found to correlate with sound speed, density, and compressibility, although correlations were lower, particularly for attenuation coefficients. This work is crucial to current efforts in obtaining realistic 3D breast tissue models from the Visible Woman data set [21].

Because of the remarkable accuracy and efficiency of the new k-space method, a three-dimensional version of this method, incorporating the absorption model of Ref. [11] (Appendix D),

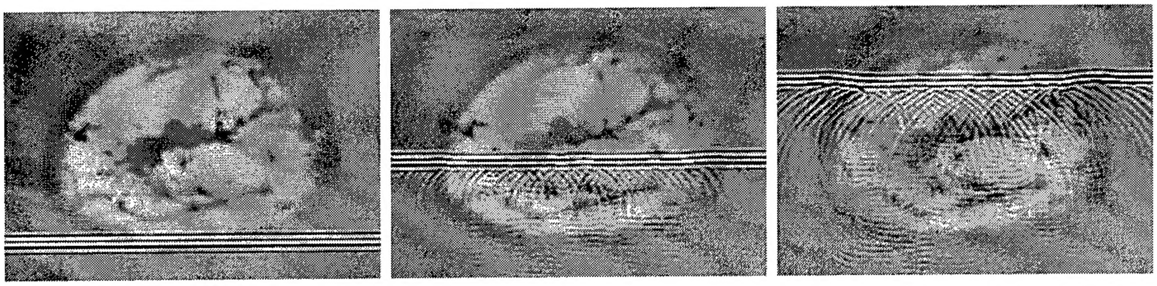

Figure 2: Three frames showing ultrasonic propagation of a 1 MHz pulse through a two-dimensional breast cross-sectional model obtained from the Visible Woman data set. Each panel shows an area of 97 × 69 mm^2.

was employed for three-dimensional computations of propagation through breast tissue. To obtain realistic three-dimensional tissue models, photographic image data from the Visible Woman data set [21] was analyzed to obtain quantitative maps of breast tissue for simulation studies and testing of imaging algorithms. A method in which hue, saturation, and value are mapped to tissue type was applied; this method also incorporates nonlinear processing to enforce uniformity among multiple layers in three-dimensional breast models. An example two-dimensional simulation, using the k-space method and a Visible Woman breast model, is shown in Fig. 2.

The three-dimensional k-space method and new tissue mapping methods were used to perform 3D simuations of ultrasonic propagation through breast tissue. Full details are given in Ref. [22], included here as Appendix I. Breast tissue models were created by processing of volumetric photographic data from the Visible Woman project. Tissue types were empirically mapped to hue, saturation, and value parameters of the photographic data; acoustic parameters of tissue were then mapped using empirical linear relationships between mass density, sound speed, and ultrasonic absorption. Computations of ultrasonic propagation were performed in two and three dimensions using a k-space method incorporating tissue-dependent absorption and reduced-reflection boundary conditions. The results showed wavefront distortion effects similar to measurements on breast tissue. Wavefront distortion was significantly more severe for the three-dimensional simulations than for the two-dimensional simulations, indicating that three-dimensional propagation effects are important to practical problems of ultrasonic mammography.

C. Quantitative Imaging Algorithm Implementation

Implementation of quantitative imaging algorithms, including the time-domain diffraction tomography method and the nonlinear eigenfunction method described above, has been primarily performed using simulated data. Initial quantitative reconstructions performed using the time-domain diffraction tomography method are shown in Ref. [1] (Appendix A) for simulated two-dimensional and three-dimensional scattering data. These results are promising for ultrasonic mammography. As discussed below in section D (Evaluation and Comparison of Results), time-domain quantitative images show parametric accuracy, high resolution, and few artifacts. Effects of limited scattering data, shown in Fig. 3 of Appendix A for the 2D case, indicate that accurate images can be obtained without the necessity of apertures that entirely enclose the breast.

Experimental testing of the new time-domain quantitative imaging method, in collaboration with colleagues at the University of Rochester, was also performed. Tissue-mimicking phantoms composed of agar gel with glass spheres were constructed. High-quality reconstructions obtained using time-domain scattering data, measured with the 2048-element University of Rochester ring transducer [23], were used as input for testing of the new time-domain quantitative imaging method. Example reconstructions from experimental data are shown in Ref. [3], included in this report as Appendix B. As discussed below in Section D., these reconstructions show that phantoms containing tissue-like random scattering structure can be imaged effectively with the new method. These reconstructions show great promise for practical implementation of the new time-domain diffraction tomography method for breast imaging *in vivo*.

Nonlinear aberration correction for the new time-domain inverse scattering method was also implemented and tested using simulated data (from the breast tissue models described above in section B, Tissue Modeling). Full details are given in Ref.[4] (Appendix C). The form of the time-domain diffraction tomography solution ([1], Appendix A) suggested that the full nonlinear inverse scattering problem can be approximated by applying appropriate angle- and space-dependent time shifts to the time-domain scattering data; this analogy led to a general approach to aberration correction. Two related methods for aberration correction were implemented: one in which delays are computed from estimates of the medium using an efficient straight-ray approximation, and one in which delays are applied directly to a time-dependent linearized reconstruction. The latter of these methods is related to a time-domain imaging method implemented by colleagues of the Principal Investigator [24]; their implementation was based on an eigenfunction method previously developed in collaborative work with the Principal Investigator [5]–[8]. Numerical results indicated that these correction methods achieve substantial quality improvments for imaging of large scatterers. The parametric range of applicability for the time-domain diffraction tomography method was increased by about a factor of two in the case of aberration correction.

A further advance in quantitative imaging algorithm implementation came from James F. Kelly, a participant in the ARL Penn State Mathematics Honors Program whom the Principal Investigator advised. Mr. Kelly investigated the utility of several deconvolution methods that can improve the quality of limited-aperture tomographic reconstructions. His results show that substantial improvement of limited-aperture quantitative images can be gained from appropriate use of inverse filtering as well as cepstral deconvolution methods. The results are described in detail in his Honors paper, included here as Appendix J. Such improvements could allow the quantitative imaging methods described above to be applied to ultrasonic mammography in pulse-echo mode using conventional clinical scanners. Quantitative tissue maps obtained in this way could be employed not only as diagnostic images, but as accurate tissue models for aberration-corrected pulse-echo imaging. Thus, this approach should be of great interest for future work in practical implementation of the imaging methods developed here.

D. Evaluation and Comparison of Results

Analysis of the initial time-domain imaging results for simulated data is given in Ref. [1] (Appendix A). These results indicate that high quantitative accuracy can be achieved. Computations of point-spread functions (Fig. 2 in Appendix A) show that the time-domain method yields higher point and contrast resolution than single-frequency diffraction tomography. For the 3D case, the level of the first sidelobe is reduced by 13 dB, while the second sidelobe is reduced by 18 dB. Because of the broadband scattering information employed, the width of the main lobe indicates point resolution of features smaller than one-half wavelength at the center frequency. Evaluation of quantitative accuracy (Fig. 4) shows that the time-domain diffraction tomography method provides parametric accuracy similar to established single-frequency methods while showing much more immunity from artifacts.

The new nonlinear aberration correction methods described above provide high quantitative accuracy even for imaging of large inhomogeneities for which the Born approximation does not hold. Quantitative analysis was also performed for images obtained using these aberration-corrected inverse scattering methods ([4], Appendix C). This analysis indicates the relative advantages and disadvantages of the two aberration-correcton approaches investigated. In the case of reconstruction of strongly-scattering cylinders (Fig. 1 of Appendix C) the initial (Born) reconstruction shows mainly the edges of the cylinder; further iterations using adaptive focus correction improve the accuracy within the cylinder interior. This process somewhat resembles the inverse scattering method of layer stripping, in which an unknown medium is iteratively reconstructed with each iteration probing further into the medium interior. In the case of adaptive delays applied to the time-domain scattering potential, the initial reconstruction captures the cylinder interior very well. Further iterations slightly increase the reconstructed contrast near the edges, but also introduce artifacts not present in the initial reconstruction. For the reconstructions shown in this figure, images of size 128 × 128 pixels were computed from time-domain scattering data for 96 incident-wave directions and 384 measurement directions. The computation time required on a 650 Mhz Athlon processor was about 6 CPU minutes per iteration for the $t = 0$ image criterion (about 38 minutes total for the six iterations performed) and about 45 CPU minutes per iteration for the $t = t_{\text{peak}}$ criterion.

Previous qualitative studies of the validity of the Born approximation [1] have established a threshold for valid Born reconstructions at $ka \cdot \gamma \sim 2$, which corresponds to a normalized RMS error of about 0.5 (Fig. 2 in Appendix C). Given this somewhat arbitrary threshold for the maximum allowable error, both aberration correction methods employed here have a similar range of validity, up to about $ka{\cdot}\gamma \sim 4$. Thus, either approach extends the parametric range of validity for time-domain diffraction tomography by about a factor of two. Each image criterion also introduces characteristic artifacts. The $t = 0$ criterion with adaptive focusing acts in part as a low-pass filter to reconstructions, consistent with the well-known low-pass filtering effect of conventional diffraction tomography. The $t = t_{\text{peak}}$ criterion introduces edge artifacts that have the qualitative effect of erroneously sharpening images. Still, notable is that adaptive demodulation from the waveform $v(t)$, as employed in Ref. [24], may provide more robust reconstruction quality, particularly for scattering data corrupted by noise.

Quantitative evaluation of the k-space method for simulation of ultrasonic propagation has been performed and is reported in Refs. [16] (Appendix E) and [17] (Appendix F). These results show that the k-space method provides much higher accuracy than finite-difference or pseudospectral methods. A particularly striking result is that simulated ultrasonic waves can propagate many thousands of wavelengths without distortion [8]. Since this accuracy allows relatively large spatial and time steps to be employed, this method is ideal for large-scale 3D computations like the breast simulations reported in Ref. [22] (Appendix I).

The new adaptation of the k-space method to coupled first-order propagation equations, which incorporates perfectly matched layer absorbing boundary conditions and relaxation-process absorption, was also quantitatively evaluated. ([18], Appendix G). The implementation of relaxation-process absorption was found to agree well with theoretical predictions. The new k-space method was shown to exhibit temporal accuracy almost identical to the k-space method of Ref. [16]. In addition, the use of coupled first-order equations in the new k-space method can provide greater accuracy for strongly-scattering media. These advantages are illustrated in Ref. [18] (Appendix G) using a benchmark computation for a 2 mm "bone" cylinder, introduced in Ref. [16]. Both before and after smoothing of the model medium, the present k-space method achieves much higher accuracy than the previous method (L^2 error, relative to an exact series solution, was 0.2292 vs. 0.3060 before smoothing; 0.0263 vs. 0.2687 after smoothing). Greatly improved accuracy was also obtained for modeled scattering from a bone-mimicking cylinder of sub-grid resolution size (radius 0.02 mm). In each of these cases, artifacts are greatly reduced in the computations employing the present k-space method.

Models constructed for simulation of propagation through breast tissue ([22], Appendix I) were found to accurately mimic experimentally-measured scattering effects [14]. In Ref. [14], mean distortion statistics found for 9 breast specimens included a mean rms arrival time fluctuation of 66.8 ns, a mean rms energy level fluctuation of 5.03 dB, and a mean waveform similarity factor of 0.910, while the 3D simulations resulted in a mean rms arrival time fluctuation of 65.2 ns, a mean rms energy level fluctuation of 2.56 dB, and a waveform similarity factor of 0.895. The corresponding values for the 2D simulations were 48.5 ns, 1.82 dB, and 0.949, indicating that 3D effects are critical to accurate modeling of ultrasonic propagation in strongly scattering tissue media such as the human breast.

Regarding the task of dissemination of results, the project has resulted to date in seven published or accepted manuscripts, two manuscripts submitted for publication, and one academic technical report. Dissemination of the research at many scientific meetings is represented by the seven published abstracts included below in Appendix K.

III. Key Research Accomplishments

The key research accomplishments achieved during this project can be summarized as follows:

- Development of a new time-domain quantitative imaging method designed specifically for ultrasonic mammography.
- Numerical implementation and testing of the new time-domain imaging method, showing that this method provides high accuracy with greater efficiency than previous inverse scattering methods.
- Testing of the time-domain imaging method using scattering data measured by a 2048-element ring transducer.
- Implementation and testing of two abberation correction methods for the time-domain quantitative imaging method, one based on adaptive focus correction and one based on temporal correction of time-domain reconstructions.
- Implementation of several deconvolution approaches for improved image quality in time-domain quantitative imaging for limited-aperture scattering data.
- Implementation of a tissue-dependent absorption model for simulations of scattering and propagation.
- Characterization of the frequency dependence of ultrasonic scattering from human soft tissues.
- Exact computation of time-domain scattering from simple objects for testing of quantitative imaging methods.
- Implementation and testing of a new k-space method for computation of scattering, indicating that the method is accurate and extremely efficient, and therefore ideal for 3D computations of scattering from breast tissue.
- Extension of the new k-space method to include tissue-dependent absorption, absorbing boundary layers, and three-dimensional scattering.
- Establishment of empirical relations between acoustic properties of human tissue, including sound speed, density, absorption, and nonlinearity parameter, for more realistic modeling of ultrasound-tissue interaction.
- Development of realistic breast tissue models using stained tissue cross sections and photographic data from the Visible Woman data set.
- Use of the k-space method to compute time-domain scattering data from realistic 2D and 3D breast tissue models, for analysis of wavefront distortion and testing of quantitative imaging algorithms.

- Quantitative analysis of inverse scattering results, indicating that time-domain reconstructions provide much higher point resolution, contrast resolution, and freedom from artifacts than single-frequency reconstructions.
- Quantitative analysis of aberration correction performance, indicating that the present aberration correction methods significantly improve the applicability of time-domain diffraction tomography methods to ultrasonic imaging of whole breasts for cancer detection and characterization.

IV. Reportable Outcomes

Personnel participating in this project have included the Principal Investigator, T. Douglas Mast, ARL Mathematics Honors Student James F. Kelly (not directly funded by the USAMRMC), and ARL support personnel including Connie M. Emberton and April L. Brumbaugh.

Reportable outcomes for this project have included four papers published in archival journals [1, 11, 16, 20], one additional accepted paper [18], two papers submitted to archival journals for publication [4, 22], two papers published in the 1999 IEEE Ultrasonics Symposium Proceedings [3, 17], and five published abstracts presented at scientific meetings [2, 8, 9, 10, 25]. All of these publications are included below in the Appendices. Also included in the Appendices are one internal report (a paper prepared for the ARL Penn State Mathematics Honors Program by a student working with the Principal Investigator) and a current Curriculum Vitae for the Principal Investigator.

Accomplishments performed under the USAMRMC-funded project have facilitated applications for other funding support. The proposal "High-Resolution Breast Tissue Mapping using Pulse-Echo Ultrasonography" (T. Douglas Mast, Principal Investigator) was submitted to the Concept Award program of the USAMRMC. This study was not funded. An additional proposal, "Optimized Intracavitary Ultrasound Array for Uniform Hyperthermia Treatment of Prostate Cancer" (Nadine B. Smith, Principal Investigator; T. Douglas Mast, Co-Principal Investigator) was submitted to the DoD Prostate Cancer Research Program. Although this proposal was not initially funded, a revised version, "Optimized Hyperthermia Treatment of Prostate Cancer using a Novel Intracavitary Ultrasound Array," was submitted in 2001 and recommended for funding. Although not a direct extension of the present ultrasonic mammography project, this project will leverage the advanced tissue modeling techniques developed for the project reported here. An additional proposal, "High-resolution breast tissue mapping by adaptive pulse-echo ultrasound" was also submitted during 2001 to the USAMRMC Breast Cancer Research Program under the IDEA mechanism. This project, a collaboration with Penn State colleagues including Richard Tutwiler, proposes extensions of the quantitative imaging methods reported here to pulse-echo imaging using apparatus similar to present clinical scanners.

During the span of this project, the Principal Investigator of was appointed to the position of Assistant Professor in the Pennsylvania State University Graduate Program in Acoustics. During the Spring of 2000, he taught a well-received upper-level graduate course on acoustic scattering. This course included a comprehensive treatment of ultrasonic scattering by human tissues, and was greatly enriched by the Principal Investigator's research performed for the USAMRMC-funded project.

A student, James F. Kelly, was added to the project team in 2000. Mr. Kelly was not directly funded by the USAMRMC, but by the Mathematics Honors program of the Penn State Applied Research Laboratory. He explored aspects of the time-domain inverse scattering problem, including deconvolution of scattered wavefields, that extend the present Statement of Work (some of this includes research into ideas discussed in the abovementioned Concept Award proposal and recent IDEA proposal). These exploratory studies should allow the imaging methods developed under the USAMRMC-funded research to achieve practical application even more rapidly. A summary of Mr. Kelly's work is given in Appendix J.

After the scheduled end of this project, the Principal Investigator accepted employment with Ethicon Endo-Surgery, a Johnson and Johnson company specializing in innovative, minimally-invasive surgical devices. A no-cost extension granted by the USAMRMC has facilitated the time and administrative support necessary for timely completion of this final report. The Principal Investigator has continued, and will continue, to work on a part-time basis to complete the planned dissemination of the project's results. On the prostate cancer project described above, he will be replaced as Co-Principal-Investigator by the eminently qualified Robert Keolian, a senior and highly creative researcher with relevant previous experience in biomechanics, medical imaging, and thermodynamics. If the abovementioned BCRP IDEA proposal is funded, he will work with his colleagues at Penn State as possible to facilitate their achievement of the research goals.

V. Conclusions

This USAMRMC-funded project has yielded considerable progress toward the goal of improved diagnosis of breast cancer by three-dimensional ultrasonic imaging. Several breakthroughs have been made which will provide a solid foundation for future practical applications of tissue modeling and quantitative imaging in ultrasonic mammography.

Breakthroughs in the area of quantitative imaging have included invention of a new time-domain diffaction tomography method ideal for ultrasonic mammography [1], successful imaging of tissue-mimicking phantoms using measured scattering data [3], and implementation of a new aberration correction approach for quantitative ultrasonic mammography [4]. The present method is potentially of very great importance for breast cancer diagnosis for several reasons: (1) images have higher quality than that achievable by conventional inverse scattering methods or by current ultrasound scanners, (2) tissue parameters are computed and quantitatively imaged with high accuracy, and (3) the close analogy between the new method and conventional synthetic-aperture imaging will allow rapid implementation of the new method on hardware similar to currently used beamformers. The additional improvement of aberration correction increases the value of this method even more, because the strong scattering inherent to breast tissue [14] is an important limiting factor to existing ultrasonic imaging methods.

In the area of breast tissue modeling, simulation methods have been developed that allow efficient computation of scattering from fully three-dimensional models of breast tissue. A model for tissue absorption, important for realistic simulation of scattering in breast tissue, has been implemented [11]. The frequency dependence of ultrasonic scattering from soft tissue has been shown to be a critical consideration for aberrating media such as the breast. A new k-space method has been implemented, rigorously tested [16, 17], and extended to include absorbing boundary conditions as well as tissue-dependent ultrasonic absorption [18]. The method has been shown to provide the accuracy and efficiency needed for large-scale computations of ultrasonic propagation within the human breast.

A three-dimensional version of the k-space method has been implemented for large-scale 3D simulations of ultrasonic propagation through breast tissue [22]. Breast tissue models for use with this simulation method have been developed using both stained cross sections of human breast tissue and photographic image data from the Visible Woman project of the National Library of Medicine [21]. Crucial to the development of three-dimensional models was a set of new empirical relationships between acoustic properties of human soft tissues [20]. These simulation results show the importance of realistic 3D tissue modeling for future testing of improved ultrasonic mammography methods.

Definitive aberration-corrected reconstructions have been performed for simulated scattering data obtained using detailed breast models. These results show the potential of the present aberration-corrected ultrasonic mammography method for practical breast cancer detection and characterization. Rapid implementation of these methods on present clinical instruments is also possible, as shown by the encouraging results of a study on applying deconvolution methods to improvement of limited-aperture images.

The final outcome of the successfully completed project is a novel method for early detection, characterization, and treatment monitoring of breast cancer lesions. Results obtained over the past three years indicate that this method can provide image quality and diagnostic information greatly superior to current 2D and 3D ultrasonic mammography methods. The final method should result in a new clinical approach to ultrasonic mammography. expected to be competitive with magnetic resonance imaging and x-ray computed tomography as a tool for breast cancer diagnosis, while maintaining inherent advantages of ultrasound such as lower cost, ability to characterize cystic and solid lesions, and safe nonionizing radiation.

VI. References

[1] Mast, T. D., "Wideband quantitative ultrasonic imaging by time-domain diffraction tomography," *J. Acoust. Soc. Am.* **106**, 3061–3071 (1999).

[2] Mast, T. D., "Time-domain ultrasound diffraction tomography," J. Acoust. Soc. Am. **105**, 1014 (1999).

[3] Mast, T. D., Lin, F., and Waag, R. C., "Time-domain ultrasound diffraction tomography," *1999 IEEE Ultrasonics Symposium Proceedings*, Vol. 2, pp. 1617-1620.

[4] Mast, T. D., "Aberration correction for time-domain ultrasound diffraction tomography," *J. Acoust. Soc. Am.* , submitted (2001).

[5] Mast, T. D., Nachman, A. I., and Waag, R. C., "Focusing and imaging using eigenfunctions of the scattering operator," *J. Acoust. Soc. Am.* **102**, 715–725 (1997).

[6] Mast, T. D., Nachman, A. I., Liu, D.-L., and Waag, R. C., "Quantitative imaging with eigenfunctions of the scattering operator," *1997 IEEE Ultrasonics Symposium Proceedings*, Vol. 2, pp. 1507–1510.

[7] Waag, R. C., Mast, T. D., Nachman, A. I., and Liu, D.-L., "Quantitative imaging with eigenfunctions of the scattering operator," *J. Ultrasound Med.* **17**, S104 (1998).

[8] T. D. Mast, D.-L. D. Liu, L. P. Souriau, A. I. Nachman, and R. C. Waag, "A new k-space method for simulation of ultrasonic propagation in tissue," *J. Acoust. Soc. Am.* **106**, 2135 (1999).

[9] Mast, T. D., "Time-domain inverse scattering for quantitative ultrasonic mammography," in *Era of Hope: Proceedings of the Department of Defense Breast Cancer Research Program Meeting*, Vol. 1, p. 224 (2000).

[10] Mast, T. D., Hinkelman, L. M., and Waag, R. C., "Simulation of ultrasonic propagation, scattering, and attenuation in the human chest wall," *J. Acoust. Soc. Am.* **104,** 1844 (1998).

[11] Mast, T. D., Hinkelman, L. M., Metlay, L. A., Orr, M. J., and Waag, R. C., "Simulation of ultrasonic pulse propagation, distortion, and attenuation in the human chest wall," *J. Acoust. Soc. Am.* **106**, 3665–3677 (1999).

[12] Mast, T. D., Hinkelman, L. M., Orr, M. J., Sparrow, V. W., and Waag, R. C., "Simulation of ultrasonic pulse propagation through abdominal wall," *J. Acoust. Soc. Am.* **102**, 1177–1190 (1997).

[13] Mast, T. D., Hinkelman, L. M., Orr, M. J., and Waag, R. C., "The effect of abdominal wall morphology on ultrasonic pulse distortion. Part II: Simulations," *J. Acoust. Soc. Am.* **104**, 3650–3664 (1998).

[14] Hinkelman, L. M., Liu, D.-L., Waag, R. C., Zhu, Q., and Steinberg, B. D., "Measurement and correction of ultrasonic pulse distortion produced by the human breast," *J. Acoust. Soc. Am.* **97**, 1958–1969 (1995).

[15] Morse, P. M. and Ingard, K. U., *Theoretical Acoustics* (McGraw-Hill, New York, 1968), ch. 8.

[16] Mast, T. D., Souriau, L. P., Liu, D.-L., Tabei, M., Nachman, A. I., and Waag, R. C., "A *k*-space method for large-scale models of wave propagation in tissue," *IEEE Trans. Ultrason., Ferroelect., Freq. Contr.* **48**, 341–354 (2001).

[17] Mould, J. C. Wojcik, G. L., Carcione, L. M., Tabei, M., Mast, T. D., and Waag, R. C., "Validation of FFT-based algorithms for large-scale modeling of wave propagation in tissue," *1999 IEEE Ultrasonics Symposium Proceedings*, Vol. 2, pp. 1551-1556.

[18] Tabei, M., Mast, T. D., and Waag, R. C., "A new *k*-space method for coupled first-order acoustic propagation equations," *J. Acoust. Soc. Am.* , accepted (2001).

[19] Mast, T. D., Tabei, M., and Waag, R. C., "Simulation of ultrasonic focus aberration and correction through human tissue," *J. Acoust. Soc. Am.* , in preparation (2001).

[20] Mast, T. D., "Empirical relationships between acoustic parameters in human soft tissues," *Acoustics Research Letters Online* **1**, 37–42 (2000).

[21] National Library of Medicine (US) Board of Regents, "Electronic Imaging: Report of the Board of Regents," NIH Publication 90-2197 (1990).

[22] Mast, T. D., "Two- and three-dimensional simulations of ultrasonic propagation through human breast tissue," *Acoustics Research Letters Online*, submitted (2001).

[23] Jansson, T. T., Mast T. D., and Waag, R. C., "Measurements of differential scattering cross-section using a ring transducer," *J. Acoust. Soc. Am.* **103**, 3169–3179 (1998).

[24] F. Lin, A. I. Nachman, and R. C. Waag, "Quantitative imaging using a time-domain eigenfunction method," *J. Acoust. Soc. Am.* **108**, 899–912 (2000).

[25] Mast, T. D., "Aberration-corrected time-domain ultrasound diffraction tomography," *J. Acoust. Soc. Am.* **109**, 2397 (2001).

VII. Appendices

The following appendices include all of the published, accepted, and submitted manuscripts, as well as all the presented abstracts, resulting from this research project to date.

A. Mast, T. D., "Wideband quantitative ultrasonic imaging by time-domain diffraction tomography," *J. Acoust. Soc. Am.* **106**, 3061–3171 (1999).

B. Mast, T. D., Lin, F., and Waag, R. C., "Time-domain ultrasound diffraction tomography," *Proc. 1999 IEEE Ultrason. Symp.*, vol. 2, pp. 1617–1620 (1999).

C. Mast, T. D., "Aberration correction for time-domain ultrasound diffraction tomography," *J. Acoust. Soc. Am.*, submitted (2001).

D. Mast, T. D., Hinkelman, L. M., Metlay, L. A., Orr, M. J., and Waag, R. C., "Simulation of ultrasonic pulse propagation, distortion, and attenuation in the human chest wall," *J. Acoust. Soc. Am.* **106**, 3665–3677 (1999).

E. Mast, T. D., Souriau, L. P., Liu, D.-L., Tabei, M., Nachman, A. I., and Waag, R. C., "A *k*-space method for large-scale models of wave propagation in tissue," *IEEE Trans. Ultrason., Ferroelect., Freq. Contr.* **48**, 341–354 (2001).

F. Mould, J. C. Wojcik, G. L., Carcione, L. M., Tabei, M., Mast, T. D., and Waag, R. C., "Validation of FFT-based algorithms for large-scale modeling of wave propagation in tissue," *1999 IEEE Ultrasonics Symposium Proceedings*, Vol. 2, pp. 1551-1556.

G. Tabei, M., Mast, T. D., and Waag, R. C., "A new *k*-space method for coupled first-order acoustic propagation equations," *J. Acoust. Soc. Am.*, accepted (2001).

H. Mast, T. D., "Empirical relationships between acoustic parameters in human soft tissues," *Acoustics Research Letters Online* **1**, 37–42 (2000).

I. Mast, T. D., "Two- and three-dimensional simulations of ultrasonic propagation through human breast tissue," *Acoustics Research Letters Online*, submitted (2001).

J. Kelly, J. F., "Deconvolution of scattered acoustic fields for ultrasonic imaging," Mathematics Honors Program, Applied Research Laboratory, The Pennsylvania State University (2001).

K. Abstracts

1. "Simulation of ultrasonic pulse propagation, distortion, and attenuation in the human chest wall," *J. Acoust. Soc. Am.* **104**, 1844 (1998), presented at the 136th Meeting of the Acoustical Society of America.
2. Mast, T. D., "Time-domain ultrasound diffraction tomography," *J. Acoust. Soc. Am.* **105**, 1014 (1999), presented at Forum Acusticum 99 [Joint Meeting: 137th Meeting of the Acous-

tical Society of America, 2nd Convention of the European Acoustics Association, and 25th German Acoustics DAGA Conference].

3. "A new k-space method for simulation of ultrasonic propagation in tissue," *J. Acoust. Soc. Am.* **106**, 2135 (1999), presented at the 138th Meeting of the Acoustical Society of America.
4. "Time-domain inverse scattering for quantitative ultrasonic mammography" (Technical and Lay/Public Abstracts), in *Era of Hope: Proceedings of the Department of Defense Breast Cancer Research Program Meeting*, Vol. 1, p. 224 (2000).
5. Mast, T. D., "Aberration-corrected time-domain ultrasound diffraction tomography," *J. Acoust. Soc. Am.* **109**, 2397 (2001), Presented at the 141st Meeting of the Acoustical Society of America.

L. Curriculum Vitae, T. Douglas Mast, Principal Investigator.

Wideband quantitative ultrasonic imaging by time-domain diffraction tomography

T. Douglas Mast
Applied Research Laboratory, The Pennsylvania State University, University Park, Pennsylvania 16802

(Received 3 April 1999; revised 27 August 1999; accepted 30 August 1999)

A quantitative ultrasonic imaging method employing time-domain scattering data is presented. This method provides tomographic images of medium properties such as the sound speed contrast; these images are equivalent to multiple-frequency filtered-backpropagation reconstructions using all frequencies within the bandwidth of the incident pulse employed. However, image synthesis is performed directly in the time domain using coherent combination of far-field scattered pressure waveforms, delayed and summed to numerically focus on the unknown medium. The time-domain method is more efficient than multiple-frequency diffraction tomography methods, and can, in some cases, be more efficient than single-frequency diffraction tomography. Example reconstructions, obtained using synthetic data for two- and three-dimensional scattering of wideband pulses, show that the time-domain reconstruction method provides image quality superior to single-frequency reconstructions for objects of size and contrast relevant to medical imaging problems such as ultrasonic mammography. The present method is closely related to existing synthetic-aperture imaging methods such as those employed in clinical ultrasound scanners. Thus, the new method can be extended to incorporate available image-enhancement techniques such as time-gain compensation to correct for medium absorption and aberration correction methods to reduce error associated with weak scattering approximations. © *1999 Acoustical Society of America.*
[S0001-4966(99)04612-3]

PACS numbers: 43.20.Fn, 43.60.Rw, 43.80.Vj, 43.20.Px [ANN]

INTRODUCTION

Quantitative imaging of tissue properties is a potentially useful technique for diagnosis of cancer and other pathological conditions. Inverse scattering methods such as diffraction tomography can provide quantitative reconstruction of tissue properties including sound speed, density, and absorption. However, although previous inverse scattering methods have achieved high resolution and quantitative accuracy, such methods have not yet been incorporated into commercially successful medical ultrasound imaging systems.

Current inverse scattering methods are lacking in several respects with respect to conventional B-scan and synthetic aperture imaging techniques. Previous methods of diffraction tomography, including methods based on the Born and Rytov approximations,[1,2] and higher-order nonlinear approaches,[3,4] have usually been based on single-frequency scattering, while current diagnostic ultrasound scanners employ wideband time-domain signals. The use of wideband information in image reconstruction is known to provide increased point and contrast resolution,[5,6] both of which are important for medical diagnosis.[5,7,8]

Several approaches have been used to incorporate wideband scattering information into quantitative ultrasonic imaging. One group of methods employs time-domain tomography based on Radon-transform relationships that hold (under the assumption of weak scattering) between scattered acoustic fields and the reflectivity or scattering strength of the medium. Pioneering work in this area[9,10] employed measurements of reflectivity in pulse-echo mode, while later studies have incorporated aberration correction[11,12] and multiple-angle scattering measurements.[13,14] A limitation of these methods, however, is that the Radon transform relationship strictly holds only when the medium is insonified by an impulsive (infinite bandwidth) wave. When pulses of finite bandwidth are employed, image quality can degrade significantly.[15]

A number of linear and nonlinear diffraction tomography methods have been implemented using scattering data for a number of discrete frequencies (e.g., Refs. 16–19). Although use of multiple-frequency data provides improvements in image quality, computational requirements for multiple-frequency imaging are typically large because the computational cost is proportional to the number of frequencies employed. To achieve image quality competitive with present diagnostic scanners, together with quantitative imaging of tissue properties, present frequency-domain methods may require solution of the inverse scattering problem for many frequencies within the bandwidth of the transducer employed. This approach thus demands a high computational cost, so that high-quality real-time imaging may not be presently feasible using current frequency-domain inverse scattering methods.

Very few previous workers have investigated direct use of time-domain waveform data for inverse scattering methods analogous to frequency-domain diffraction tomography. Several methods[20,21] have used frequency decomposition of scattered pulses to construct a wideband estimate of the spatial Fourier transform of an unknown medium; after appropriate averaging and interpolation, this transform can be inverted to obtain a wideband Born reconstruction of the medium. A study reported in Ref. 22 has showed that broadband synthetic aperture imaging using linear arrays is closely related to inverse scattering using filtered backpropagation. A related method, suggested in Ref. 23, provides a time-domain reconstruction algorithm that employs filtered backpropagation of scattered waveforms measured on a circular boundary. However, the time domain reconstruction formula of Ref. 23 yields reconstructions that are less general than multiple-frequency reconstructions obtained using the same signal bandwidth.

Another approach, related both to multiple-frequency methods and direct time-domain methods, has recently been presented.[24] This work extends the eigenfunction method of Ref. 19 to use the full bandwidth of the incident pulse waveform. In the extended method, eigenfunctions and eigenvalues of a scattering operator are computed to obtain a frequency-dependent representation of the scattering medium. Fourier synthesis is then applied to obtain a time-dependent estimate of the medium. A cross-correlation operation removes the time dependence of the estimate as well as its dependence on the waveform employed.

The present paper offers a new approach to wideband quantitative imaging: a time-domain inverse scattering method that overcomes some of the limitations of previous frequency-domain and time-domain quantitative imaging methods. The new method provides tomographic reconstructions of unknown scattering media using the entire available bandwidth of the signals employed. Reconstructions are performed using scattering data measured on a surface surrounding the region of interest, so that the method is well suited to ultrasonic mammography. The reconstruction algorithm is derived as a simple delay-and-sum formula similar to synthetic-aperture algorithms employed in conventional clinical scanners. However, unlike current clinical scanners, the present method can provide quantitative images of tissue properties such as the spatially dependent sound speed. Reconstructions obtained in this manner are equivalent to reconstructions obtained by combining conventional frequency-domain diffraction tomography reconstructions for all frequencies within the signal bandwidth of interest. The current method, however, can be even more efficient than single-frequency diffraction tomography. The method is applicable both to two-dimensional and three-dimensional image reconstruction. The direct time-domain nature of the reconstruction algorithm allows straightforward incorporation of depth- and frequency-dependent amplitude correction to compensate for medium absorption as well as aberration correction methods to overcome limitations of the Born approximation.

I. THEORY

A. The time-domain reconstruction algorithm

An inverse scattering algorithm, applicable to quantitative imaging of tissue and other inhomogeneous media, is derived below. For simplicity of derivation, the medium is modeled as a fluid medium defined by the sound speed contrast function

$$\gamma(\mathbf{r})=\frac{c_0^2}{c(\mathbf{r})^2}-1, \tag{1}$$

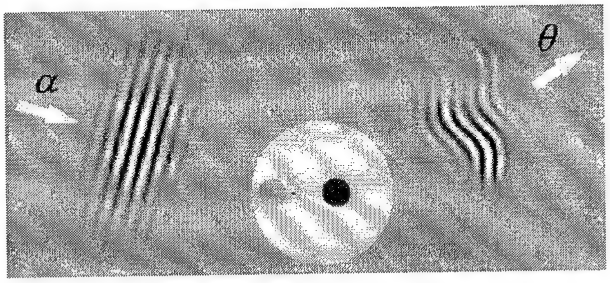

FIG. 1. Scattering configuration. An incident pressure pulse $f(t-\boldsymbol{\alpha}\cdot r/c)$ is scattered by an inhomogeneous medium and the time-domain scattered pressure $p_s(\boldsymbol{\theta},\boldsymbol{\alpha},t)$ is measured at a radius R in the far field.

where c_0 is a background sound speed and $c(\mathbf{r})$ is the spatially dependent sound speed defined at all points $\mathbf{r}$. For the scope of the initial derivation, the medium is assumed to have constant density, no absorption, and weak scattering characteristics; extensions to the reconstruction algorithm that overcome these limiting assumptions are discussed in the following section.

For the model of the scattering medium represented by Eq. (1), the time-domain scattered acoustic pressure $p_s(\mathbf{r},t)$ obeys the wave equation[25]

$$\nabla^2 p_s(\mathbf{r},t)-\frac{1}{c_0^2}\frac{\partial^2 p_s(\mathbf{r},t)}{\partial t^2}=\frac{\gamma(\mathbf{r})}{c_0^2}\frac{\partial^2 p(\mathbf{r},t)}{\partial t^2}, \tag{2}$$

where $p(\mathbf{r},t)$ is the total acoustic pressure in the medium.

The scattering configuration considered here is sketched in Fig. 1. The medium is subjected to a pulsatile plane wave propagating in the direction of the unit vector $\boldsymbol{\alpha}$,

$$p_{\mathrm{inc}}(\mathbf{r},\boldsymbol{\alpha},t)=f(t-\mathbf{r}\cdot\boldsymbol{\alpha}/c_0), \tag{3}$$

where f is the time-domain waveform and c_0 is the background sound speed. The scattered wavefield $p_s(\boldsymbol{\theta},\boldsymbol{\alpha},t)$ is measured at a fixed radius R in the far field, where $\boldsymbol{\theta}$ corresponds to the direction unit vector of a receiving transducer element. (Alternatively, if scattering measurements are made in the near field, the far-field acoustic pressure can be computed using exact transforms that represent propagation through a homogeneous medium.[16])

A general time-domain solution for the wave equation (2), valid for two-dimensional (2D) or three-dimensional (3D) scattering, is then

$$p_s(\boldsymbol{\theta},\boldsymbol{\alpha},t)=\int_{-\infty}^{\infty}\hat{p}_s(\boldsymbol{\theta},\boldsymbol{\alpha},\omega)e^{-i\omega t}d\omega, \tag{4}$$

where $\hat{p}_s(\boldsymbol{\theta},\boldsymbol{\alpha},\omega)$ is a single frequency component of the scattered wavefield,

$$\hat{p}_s(\boldsymbol{\theta},\boldsymbol{\alpha},\omega)\equiv\frac{1}{2\pi}\int_{-\infty}^{\infty}p_s(\boldsymbol{\theta},\boldsymbol{\alpha},t)e^{i\omega t}dt, \tag{5}$$

given exactly by[25]

$$\hat{p}_s(\boldsymbol{\theta},\boldsymbol{\alpha},\omega)=k^2\hat{f}(\omega)\int \mathrm{G}_0(R\boldsymbol{\theta}-\mathbf{r}_0,\omega) \times\gamma(\mathbf{r}_0)\hat{p}(\mathbf{r},\boldsymbol{\alpha},\omega)dV_0. \tag{6}$$

In Eq. (6), k is the wave number ω/c_0 and $\hat{p}(\mathbf{r}_0,\boldsymbol{\alpha},\omega)$ is the total acoustic pressure associated with the unit-amplitude incident plane wave $e^{ik\boldsymbol{\alpha}\cdot\mathbf{r}_0}$. The integral in Eq. (6) is taken over the entire support of γ in $\mathbb{R}^2$ for 2D scattering or in $\mathbb{R}^3$

for 3D scattering. The free-space Green's function, represented by G_0 in Eq. (6), is[26]

$$\begin{aligned} G_0(\mathbf{r},\omega) &= \frac{i}{4}H_0^{(1)}(kr) \quad \text{for 2D scattering} \\ &\text{and} \\ G_0(\mathbf{r},\omega) &= \frac{e^{ikr}}{4\pi r} \quad \text{for 3D scattering,} \end{aligned} \tag{7}$$

where $H_0^{(1)}$ is the zeroth-order Hankel function of the first kind and r is the magnitude of the vector $\mathbf{r}$.

The far-field scattered pressure, when specified for all incident-wave directions $\boldsymbol{\alpha}$, measurement directions $\boldsymbol{\theta}$, and times t, comprises the data set to be used for reconstruction of the unknown medium. The inverse scattering problem, specified by Eq. (6) for a single frequency component, is to reconstruct the unknown medium contrast $\gamma(\mathbf{r})$ using the measured data $\hat{p}_s(\boldsymbol{\theta},\boldsymbol{\alpha},\omega)$.

The starting point for the present time-domain inverse scattering method is conventional single-frequency diffraction tomography. Under the assumption of weak scattering, one can make the Born approximation, in which the total pressure $\hat{p}(\boldsymbol{\alpha},\omega)$ in Eq. (6) is replaced by the plane wave $e^{ik\mathbf{r}\cdot\boldsymbol{\alpha}}$. For scattering measurements made at a radius R in the far field, the linearized inverse problem of Eq. (6) can be then solved for any frequency component using filtered backpropagation,[2,16,27] i.e.,

$$\begin{aligned} \gamma_B(\mathbf{r},\omega) = \frac{\hat{\mu}(\omega)e^{-ikR}}{\hat{f}(\omega)} \int\int \Phi(\boldsymbol{\theta},\boldsymbol{\alpha}) \\ \times \hat{p}_s(\boldsymbol{\theta},\boldsymbol{\alpha},\omega)e^{ik(\boldsymbol{\theta}-\boldsymbol{\alpha})\cdot\mathbf{r}}dS_\alpha dS_\theta, \end{aligned} \tag{8}$$

where

$$\begin{aligned} &\hat{\mu}(\omega) = -\sqrt{\frac{kR}{8i\pi^3}}, \\ &\Phi(\boldsymbol{\theta},\boldsymbol{\alpha}) = |\sin(\theta-\alpha)| \quad \text{in 2D,} \\ &\text{and} \\ &\hat{\mu}(\omega) = \frac{kR}{4\pi^3}, \quad \Phi(\boldsymbol{\theta},\boldsymbol{\alpha}) = |\boldsymbol{\theta}-\boldsymbol{\alpha}| \quad \text{in 3D.} \end{aligned} \tag{9}$$

Each surface integral in Eq. (8) is performed over the entire measurement circle for the 2D case and over the entire measurement sphere for the 3D case. Equation (8) provides an exact solution to the linearized inverse scattering problem for a single frequency component of the scattered wavefield $p_s(\boldsymbol{\theta},\boldsymbol{\alpha},t)$. The resulting reconstruction, $\gamma_B(\mathbf{r},\omega)$, has spatial frequency content limited by the "Ewald sphere" of radius $2k$ in wavespace.[1]

To improve upon the single-frequency formulas specified by Eq. (8), one can extend the spatial-frequency content of reconstructions by exploiting wideband scattering information. The method outlined here synthesizes a "multiple-frequency" reconstruction $\gamma_M(\mathbf{r})$ by formally integrating single-frequency reconstructions $\gamma_B(\mathbf{r},\omega)$ over a range of frequencies ω. A generalized formula for this approach can be written

$$\gamma_M(\mathbf{r}) = \frac{\int_0^\infty \hat{g}(\omega)\gamma_B(\mathbf{r},\omega)d\omega}{\int_0^\infty \hat{g}(\omega)d\omega}, \tag{10}$$

where $\hat{g}(\omega)$ is an appropriate frequency-dependent weighting function. In practice, the weighting function $\hat{g}(\omega)$ is chosen to be bandlimited because (for a given set of physical scattering measurements) the frequency-dependent contrast $\gamma_B(\mathbf{r},\omega)$ can only be reliably reconstructed for a finite range of frequencies ω associated with the spectra of the incident waves employed. Thus, the integrands in Eq. (10) are nonzero only over the support of $\hat{g}(\omega)$ and the corresponding integrals are finite.

Using Eq. (8), and making the definition

$$N \equiv 2\int_0^\infty \hat{g}(\omega)d\omega, \tag{11}$$

Eq. (10) can be written in the form

$$\begin{aligned} \gamma_M(\mathbf{r}) = \frac{2}{N}\int_0^\infty \hat{g}(\omega)\frac{\hat{\mu}(\omega)e^{-ikR}}{\hat{f}(\omega)} \int\int \Phi(\boldsymbol{\theta},\boldsymbol{\alpha}) \\ \times \hat{p}_s(\boldsymbol{\theta},\boldsymbol{\alpha},\omega)e^{ik(\boldsymbol{\theta}-\boldsymbol{\alpha})\cdot\mathbf{r}}dS_\alpha dS_\theta d\omega. \end{aligned} \tag{12}$$

If the frequency weight $\hat{g}(\omega)$ is now specified to incorporate the incident-pulse spectrum $\hat{f}(\omega)$ and to compensate for the frequency- and dimension-dependent coefficient $\hat{\mu}(\omega)$,

$$\hat{g}(\omega) = \frac{\hat{f}(\omega)}{\hat{\mu}(\omega)}, \tag{13}$$

Eq. (12) reduces to the form

$$\begin{aligned} \gamma_M(\mathbf{r}) = \frac{2}{N}\int\int \Phi(\boldsymbol{\theta},\boldsymbol{\alpha}) \int_0^\infty \hat{p}_s(\boldsymbol{\theta},\boldsymbol{\alpha},\omega) \\ \times e^{-ik[R+(\boldsymbol{\alpha}-\boldsymbol{\theta})\cdot\mathbf{r}]}d\omega dS_\alpha dS_\theta. \end{aligned} \tag{14}$$

The choice of frequency weight from Eq. (13) allows the multiple-frequency reconstruction formula of Eq. (12) to be greatly simplified. Specifically, the inner integral of Eq. (14) resembles a weighted inverse Fourier transform of the frequency-domain scattered field $\hat{p}(\boldsymbol{\theta},\alpha,\omega)$. To obtain an explicit time-domain expression for $\gamma_M(\mathbf{r})$, Eq. (14) can be rewritten using the definition of $\hat{p}_s(\boldsymbol{\theta},\boldsymbol{\alpha},\omega)$ from Eq. (5) to yield

$$\begin{aligned} \gamma_M(\mathbf{r}) = \frac{1}{N}\int\int \Phi(\boldsymbol{\theta},\boldsymbol{\alpha}) \\ \times \mathbf{L}\left[p_s\left(\boldsymbol{\theta},\boldsymbol{\alpha},R/c_0 + \frac{(\boldsymbol{\alpha}-\boldsymbol{\theta})\cdot\mathbf{r}}{c_0}\right)\right]dS_\alpha dS_\theta, \end{aligned} \tag{15}$$

where $\mathbf{L}$ denotes the linear operator

$$\mathbf{L}[\psi(t)] = 2\int_0^\infty \hat{\psi}(\omega)e^{-i\omega t}d\omega \tag{16}$$

and $\hat{\psi}(\omega)$ is the Fourier transform of $\psi(t)$ using the definition from Eq. (5).

Using the conjugate symmetry of $\hat{\psi}(\omega)$ [i.e., $\hat{\psi}(\boldsymbol{\theta},\boldsymbol{\alpha},\omega) = \hat{\psi}^*(\boldsymbol{\theta},\boldsymbol{\alpha},-\omega)$ for any real $\psi(t)$], the real part of

$\mathbf{L}[\psi(t)]$ is shown to be simply $\psi(t)$. Similarly, using the convolution theorem as well as the conjugate symmetry of $\psi(t)$, the imaginary part of $\mathbf{L}[\psi(t)]$ is seen to be an inverse Hilbert transform[28] of $\psi(t)$,

$$\mathrm{Im}[\mathbf{L}[\psi(t)]] = -\frac{1}{\pi}\int_{-\infty}^{\infty}\frac{\psi(\tau)}{t-\tau}\,d\tau = \mathbf{H}^{-1}[\psi(t)]. \qquad (17)$$

This transform, also known as a quadrature filter, applies a phase shift of $\pi/2$ to each frequency component of the input signal.

Thus, the time-domain reconstruction formula can finally be written

$$\gamma_M(\mathbf{r}) = \frac{1}{N}\int\int \Phi(\boldsymbol{\theta},\boldsymbol{\alpha})\Big(p_s(\boldsymbol{\theta},\alpha,\tau) + i\mathbf{H}^{-1}[p_s(\boldsymbol{\theta},\alpha,\tau)]\Big)\,dS_\alpha\,dS_\theta, \qquad (18)$$

where

$$\tau = R/c_0 + \frac{(\boldsymbol{\alpha}-\boldsymbol{\theta})\cdot\mathbf{r}}{c_0}. \qquad (19)$$

The direction-dependent weight $\Phi(\boldsymbol{\theta},\boldsymbol{\alpha})$, which is the same as the "filter" employed in single-frequency filtered backpropagation, is given for the 2D and 3D cases by Eq. (9).

Equation (18) is notable in several respects. First, it provides a linearized reconstruction that employs scattering information from the entire signal bandwidth without any frequency decomposition of the scattered wavefield. Second, the delay term τ corresponds exactly to the delay required to construct a focus at the point $\mathbf{r}$ by delaying and summing the scattered wavefield $p_s(\boldsymbol{\theta},\boldsymbol{\alpha},t)$ for all measurement directions $\boldsymbol{\theta}$ and incident-wave directions $\boldsymbol{\alpha}$. Thus, the time-domain reconstruction formula given by Eq. (18) can be regarded as a quantitative generalization of confocal time-domain synthetic aperture imaging, in which signals are synthetically delayed and summed for each transmit/receive pair to focus at the image point of interest.[22,29,30]

A reconstruction formula similar to, although less general than, Eq. (18) was independently derived in Ref. 23 for the two-dimensional inverse scattering problem. In view of the present derivation, the method of "probing by plane pulses" in Ref. 23 can be regarded to yield a multiple-frequency reconstruction of $\mathrm{Re}[\gamma_M(\mathbf{r})]$, while the present method yields the complex function $\gamma_M(\mathbf{r})$. In Ref. 23, this method was proposed as a more convenient way to implement narrow-band diffraction tomography. However, the numerical results given below show that the reconstruction formula of Eq. (18), when directly implemented using wideband signals, provides considerable improvement in image quality over narrow-band reconstructions.

Reconstructions using Eq. (18) can be performed using any pulse waveform. However, the frequency compounding defined by Eq. (10) is most straightforwardly interpreted if the frequency weight $\hat{g}(\omega)$ has a phase that is independent of frequency. This criterion can be met, for instance, if the incident pulse waveform $f(t)$ is even in time,

$$f(t) = f(-t), \qquad (20)$$

so that $\hat{f}(\omega)$ is purely real. [Similarly, if the incident pulse waveform is odd in time, $\hat{f}(\omega)$ is purely imaginary and Eq. (18) can still be employed.]

However, supposition of a frequency-independent phase for $\hat{f}(\omega)$ does not result in any loss of generality. For any linear-phase signal, such that the Fourier transform has the form

$$\hat{f}(\omega) = |\hat{f}(\omega)|e^{i\omega\zeta}, \quad \omega>0, \qquad (21)$$

an additional delay term of magnitude ζ can be applied to all scattered signals to obtain the signals associated with the purely-real spectrum $|\hat{f}(\omega)|$. In general, the scattered field associated with a desired waveform $f(t)$ can be determined for an arbitrary waveform $u(t)$ from the deconvolution operation

$$[p_s(\boldsymbol{\theta},\boldsymbol{\alpha},t)]_{f(t)} = \mathbf{F}^{-1}\left[\frac{\hat{f}(\omega)}{\hat{u}(\omega)}[p_s(\boldsymbol{\theta},\boldsymbol{\alpha},t)]_{u(t)}\right]. \qquad (22)$$

For stable deconvolution using Eq. (22), the desired $\hat{f}(\omega)$ should not have significant frequency components outside the bandwidth of $\hat{u}(\omega)$.

B. Extensions to the reconstruction algorithm

For large tissue structures at high ultrasonic frequencies, weak scattering approximations such as the Born approximation are of limited validity. Thus, for problems of interest to medical ultrasonic imaging, reconstructed image quality can be improved by aberration correction methods that incorporate higher-order scattering and propagation effects. The present time-domain reconstruction formula (18) provides a natural framework for quantitative imaging with aberration correction. In general, if the background medium is known or can be estimated, the received scattered signals can be processed to provide an estimate of the scattered field that would be measured for the same scatterer within a homogeneous background medium. This approach essentially removes higher-order scattering effects from the measured far field scattering, so that a Born inversion can be performed on the modified data; similar processes occur implicitly in many nonlinear inverse scattering methods.[31]

For example, a simple implementation of aberration correction can be derived if one makes the assumption that background inhomogeneities result only in cumulative delays (or advances) of the incident and scattered wavefronts. This crude model does not include many propagation and scattering effects important to ultrasonic aberration, but has been shown to provide a reasonable first approximation of local delays in wavefronts propagating through large-scale tissue models.[32,33] Given this approximation, the total delay for an angle ϕ and a point position $\mathbf{r}$ is given by

$$\delta\tau(\boldsymbol{\phi},\mathbf{r}) = \int_{\xi} c(\boldsymbol{\xi})^{-1}d\xi - \frac{R}{c_0}, \qquad (23)$$

where the integral is performed along the line that joins the spatial points $\mathbf{r}$ and $R\boldsymbol{\phi}$, Aberration-corrected reconstructions can then be performed using Eq. (18) with τ replaced by the corrected delay term

$$\tau \to R/c_0 + \frac{(\boldsymbol{\alpha}-\boldsymbol{\theta})\cdot\mathbf{r}}{c_0} + \delta\tau(\boldsymbol{\alpha},\mathbf{r}) + \delta\tau(\boldsymbol{\theta},\mathbf{r}). \tag{24}$$

Improved approximations could be obtained by application of the delay function $\delta\tau(\boldsymbol{\phi},\mathbf{r})$ after numerical backpropagation of the far-field scattered wavefronts through a homogeneous medium[34,35] or by compensation for both delay and amplitude variations.[36,37] More general, although much more computationally expensive, aberration correction could also be performed by synthetic focusing using full-wave numerical computation of acoustic fields within an estimated realization of the unknown medium. A method of this kind has been implemented, within the context of a frequency-domain diffraction tomography method, in Ref. 19.

The present imaging method has been derived using simplifying assumptions including zero absorption and constant density for the scattering medium. However, these assumptions do not substantially restrict the validity of the method. For example, the effect of absorption can be reduced using time-gain compensation, with or without frequency-dependent corrections,[38] of received scattered signals for each transmit/receive pair. Such time-gain compensation could be performed either using an estimated bulk attenuation for the medium (as with current clinical ultrasound scanners), or by implementation of an adaptive attenuation model in a manner similar to the time-shift compensation scheme discussed above.

Inclusion of density variations as well as sound speed variations adds additional complication to the time-domain diffraction tomography algorithm derived here. For single-frequency diffraction tomography in the presence of sound speed and density variations, the quantity $\gamma_B(\mathbf{r},\omega)$ reconstructed by Eq. (8) can be shown[39] to provide an estimate of a physical quantity that depends both on sound speed variations and density variations. In the notation used here, this quantity can be written

$$\gamma'(\mathbf{r}) = \gamma(\mathbf{r}) - \gamma(\mathbf{r})\gamma_\rho(\mathbf{r}) + \frac{1}{2k^2}\nabla^2\gamma_\rho(\mathbf{r}), \tag{25}$$

where the density variation is defined $\gamma_\rho = 1-\rho_0/\rho(\mathbf{r})$. Thus, for time-domain reconstructions of media with density variations, the reconstruction formula of Eq. (18) will provide the estimate

$$\gamma_M(\mathbf{r}) \approx \gamma(\mathbf{r}) - \gamma(\mathbf{r})\gamma_\rho(\mathbf{r}) + \frac{1}{2k_0^2}\nabla^2\gamma_\rho(\mathbf{r}), \tag{26}$$

where k_0 is the wave number corresponding to the center frequency of the pulse employed. For media such as human tissue, where density variations are fairly small and abrupt density transitions are rare, the last two terms of Eq. (26) are small compared to $\gamma(\mathbf{r})$, so that the reconstruction algorithm derived above can still be regarded to provide an image of the sound-speed variation function $\gamma(\mathbf{r})$. However, if desired, a reconstruction employing pulses with two distinct center frequencies could allow separation of sound speed and density variations by techniques similar to those described in Ref. 16 or 39.

II. COMPUTATIONAL METHODS

The time-domain inverse scattering method described above has been tested with 2D and 3D synthetic data prepared using three numerical methods: a Born approximation method for point scatterers and 3D slabs, an exact series solution for cylindrical inhomogeneities, and a k-space method for arbitrary 2D inhomogeneous media.

The time-domain waveform employed for all the computations reported here was

$$f(t) = \cos(\omega_0 t)e^{-t^2/(2\sigma^2)}, \tag{27}$$

where $\omega_0 = 2\pi f_0$ for a center frequency of f_0 and σ is the temporal Gaussian parameter. This waveform has the real, even Fourier transform

$$\hat{f}(\omega) = \sqrt{\frac{\sigma^2}{8\pi}}\left(e^{-\sigma^2(\omega-\omega_0)^2/2} + e^{-\sigma^2(\omega+\omega_0)^2/2}\right). \tag{28}$$

Values used for the computations reported here were $f_0 = 2.5$ MHz and $\sigma = 0.25$ μs, so that the -6 dB bandwidth of the signal was 1.5 MHz. These parameters correspond closely to those of an existing 2048-element ring transducer.[40]

For the case of point scatterers, the contrast function γ was assumed to take the form

$$\gamma(\mathbf{r}) = \sum_1^M \mu_j \delta(\mathbf{r}-\mathbf{r_j}). \tag{29}$$

Using the far-field form of the 2D Green's function and neglecting multiple scattering, Eq. (6) for the scattered far field can be rewritten as

$$\hat{p}_s(\boldsymbol{\theta},\boldsymbol{\alpha},\omega) = -k^2\sqrt{\frac{i}{8\pi kR}}\hat{f}(\omega)\sum_j \mu_j e^{ik(\boldsymbol{\alpha}-\boldsymbol{\theta})\cdot\mathbf{r}_j} \tag{30}$$

for each frequency component of interest. Time-domain waveforms were synthesized by using Eq. (30) for each frequency with $\hat{f}(\omega) > 10^{-3}$ and inverting the frequency-domain scattered wavefield by a fast Fourier transform (FFT) implementation of Eq. (4). The temporal sampling rate employed was 10 MHz. An analogous formula, with a different multiplicative constant, was also employed for the 3D case.

The Born approximation was also used to compute three-dimensional scattering for slab-shaped objects defined by the equation

$$\gamma(\mathbf{r}) = \gamma_0 H(a_x-|x|)H(a_y-|y|)H(a_z-|z|). \tag{31}$$

For this object, the linearized forward problem can be solved analytically. Under the Born approximation, the frequency-domain scattered far field has the form

$$\begin{aligned}\hat{p}_s(\boldsymbol{\theta},\boldsymbol{\alpha},\omega) &= 2\hat{f}(\omega)\gamma_0 a_x a_y a_z e^{ikR}/(\pi R)\\ &\times\frac{\sin[kL_x(\boldsymbol{\alpha}-\boldsymbol{\theta})\cdot\mathbf{e}_x]}{kL_x(\boldsymbol{\alpha}-\boldsymbol{\theta})\cdot\mathbf{e}_x}\,\frac{\sin[kL_y(\boldsymbol{\alpha}-\boldsymbol{\theta})\cdot\mathbf{e}_y]}{kL_y(\boldsymbol{\alpha}-\boldsymbol{\theta})\cdot\mathbf{e}_y}\\ &\times\frac{\sin[kL_z(\boldsymbol{\alpha}-\boldsymbol{\theta})\cdot\mathbf{e}_z]}{kL_z(\boldsymbol{\alpha}-\boldsymbol{\theta})\cdot\mathbf{e}_z},\end{aligned} \tag{32}$$

where $\mathbf{e}_x$, $\mathbf{e}_y$, and $\mathbf{e}_z$ represent unit vectors in the x, y, and z directions. The time domain scattered pressure $p_s(\boldsymbol{\theta},\boldsymbol{\alpha},t)$ is

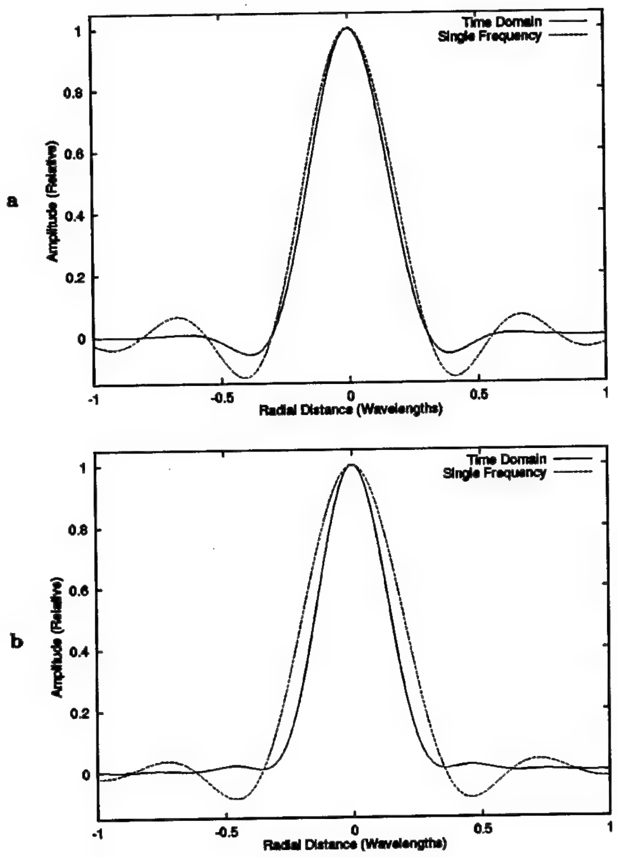

FIG. 2. Point-spread functions for time-domain and single-frequency diffraction tomography methods. In each panel, the vertical scale corresponds to the relative amplitude of the reconstructed contrast $\gamma(\mathbf{r})$, while the horizontal scale corresponds to number of wavelengths at the center frequency. (a) Two-dimensional case. (b) Three-dimensional case.

obtained, as for the point scatterer case described above, by inverse transformation of the frequency-domain wavefield for all frequencies within the bandwidth of interest.

For 2D cylindrical inhomogeneities, an analogous procedure was followed, except that the frequency-domain scattered wavefield $\hat{p}_s(\boldsymbol{\theta},\boldsymbol{\alpha},\omega)$ was computed using an exact series solution[25] for each frequency component of interest. In implementation of the series solution, summations were truncated when the magnitude of a single coefficient dropped below 10^{-12} times the sum of all coefficients.

Solutions were also obtained for arbitrary 2D inhomogeneous media using a time-domain k-space method.[41] Grid sizes of 256×256 points, a spatial step of 0.0833 mm, and a time step of 0.02734 μs were employed. Scattered acoustic pressure signals on a circle of virtual receivers were recorded at a sampling rate of 9.144 MHz. The receiver circle, which had a radius of 3.0 mm in these computations, completely contained the inhomogeneities used. Far-field waveforms were computed by Fourier transforming the time-domain waveforms on the near-field measurement circle, transforming these to far-field waveforms for each frequency using a numerically exact transformation method,[16] and performing inverse Fourier transformation to yield time-domain far-field waveforms. All forward and inverse temporal Fourier transforms, as well as angular transforms occurring in the near-field-far-field transformation,[16] were performed by FFT.

The time-domain imaging method was directly implemented using Eq. (18), evaluated using straightforward numerical integration over all incident-wave and measurement directions employed. The reconstruction formula employed can be explicitly written as

$$\gamma_M(\mathbf{r})=\frac{1}{N_{2D}}\int_0^{2\pi}\int_0^{2\pi}|\sin(\alpha-\theta)|\Big(p_s(\boldsymbol{\theta},\boldsymbol{\alpha},\tau)\\ +i\mathbf{H}^{-1}[p_s(\boldsymbol{\theta},\boldsymbol{\alpha},\tau)]\Big)\,d\alpha\, d\theta,$$

$$\tau=R/c_0+\frac{(\cos\alpha-\cos\theta)\cdot x+(\sin\alpha-\sin\theta)\cdot y}{c_0} \tag{33}$$

for the 2D case, where α and θ are the angles corresponding to the direction vectors $\boldsymbol{\alpha}$ and $\boldsymbol{\theta}$, and as

$$\gamma_M(\mathbf{r})=\frac{1}{N_{3D}}\int_0^{2\pi}\int_0^{\pi}\int_0^{2\pi}\int_0^{\pi}|\boldsymbol{\alpha}-\boldsymbol{\theta}|\Big(p_s(\boldsymbol{\theta},\boldsymbol{\alpha},\tau)\\ +i\mathbf{H}^{-1}[p_s(\boldsymbol{\theta},\boldsymbol{\alpha},\tau)]\Big)\sin(\Phi_\alpha)\sin(\Phi_\theta)\,d\Phi_\alpha\\ \times d\Theta_\alpha d\Phi_\theta d\Theta_\theta,$$

$$\tau=R/c_0+\frac{(\boldsymbol{\alpha}-\boldsymbol{\theta})\cdot\mathbf{r}}{c_0}, \tag{34}$$

$$\boldsymbol{\alpha}-\boldsymbol{\theta}=(\cos\Theta_\alpha\sin\Phi_\alpha-\cos\Theta_\theta\sin\Phi_\theta)\cdot\mathbf{e}_x\\ +(\sin\Theta_\alpha\sin\Phi_\alpha-\sin\Theta_\theta\sin\Phi_\theta)\cdot\mathbf{e}_y\\ +(\cos\Phi_\alpha-\cos\Phi_\theta)\cdot\mathbf{e}_z$$

for the 3D case, where Θ_α and Φ_α are direction angles for the incident-wave direction $\boldsymbol{\alpha}$ and Θ_θ and Φ_θ are direction angles for the measurement direction $\boldsymbol{\theta}$. For each case, the normalization factor N was determined from Eq. (11) with $\hat{g}(\omega)=\hat{f}(\omega)/\hat{\mu}(\omega)$ and $\mu(\omega)$ given by Eq. (9). Before evaluation of the argument τ for each signal, the time-domain waveforms were resampled at a sampling rate of 16 times the original rate. This resampling was performed using FFT-based Fourier interpolation. The inverse Hilbert transform was performed for each signal using an FFT implementation of Eq. (16). Values of the pressure signals at the time τ were then determined using linear interpolation between samples of the resampled waveforms. The integrals of Eqs. (33) and (34) were implemented using discrete summation over all transmission and measurement directions employed.

Computations were also performed using the time-domain diffraction tomography algorithm for limited-aperture data. For these reconstructions, the integrals of Eq. (33) were evaluated only for angles corresponding to transmitters and receivers within a specified aperture of angular width ϕ_{ap}, i.e.,

$$|\alpha|\leqslant\phi_{\mathrm{ap}}/2,\quad |\theta-\pi|\leqslant\phi_{\mathrm{ap}}/2. \tag{35}$$

Use of a small value for ϕ_{ap} corresponds to use of a small aperture in pulse-echo mode.

III. NUMERICAL RESULTS

Two-dimensional and three-dimensional point-spread functions (PSF) for the present time-domain diffraction tomography method are illustrated in Fig. 2. The time-domain reconstructions shown here, like the other time-domain reconstructions shown in this paper, were obtained using a incident pulse of center frequency 2.5 MHz and a Gaussian envelope corresponding to a -6 dB bandwidth of 1.5 MHz. Point-spread functions were determined by reconstructing a point scatterer located at the origin. For the 2D case, in which the point scatterer can be regarded as a thin wire, synthetic scattering data was obtained using the Born approximation method outlined above for 16 incident-wave directions and 64 measurement directions. The 3D time-domain reconstruction was obtained using Born data for 72 incident-wave directions and 288 measurement directions, each evenly spaced on a rectangular grid defined by the angles Θ and Φ. For comparison, analogous point-spread functions are also shown for standard frequency-domain diffraction tomography reconstructions using single-frequency (2.5 MHz) data.

For the 2D case illustrated in Fig. 2, the time-domain PSF has a slightly narrower peak, indicating that point resolution has been slightly improved by the increased bandwidth employed in the time domain method. More significantly, sidelobes of the time-domain PSF are significantly smaller than those for the single-frequency PSF (the first sidelobe is reduced by 7 dB, while the second is reduced by 19 dB), so that contrast resolution for time-domain diffraction tomography is seen to be much higher than for single-frequency diffraction tomography. For the 3D case, the time-domain reconstruction shows a much more dramatic improvement over the single-frequency reconstruction. In this case, the time-domain solution shows significant increases in both the point resolution (PSF width at half-maximum reduced by 27%) and contrast resolution (first sidelobe reduced by 13 dB and second sidelobe reduced by 18 dB). Furthermore, a comparison of the PSFs for 2D and 3D time-domain reconstruction indicates that much higher image quality is achievable for 3D time-domain imaging than for the 2D case. This increase in image quality suggests that the time-domain diffraction tomography method proposed here may benefit from the overdetermined nature of the general wideband 3D inverse scattering problem.[42,43]

The effect of transmit and receive aperture characteristics on image quality is illustrated in Fig. 3. Panels (a) and (b) of Fig. 3 show the point-spread function for a number of aperture configurations, each employing 64 measurement directions. Figure 3(a) shows the point-spread function for reconstructions obtained using 1, 4, 8, and 16 incident-wave directions. The point scatterer is clearly imaged even for the reconstruction using one incident-wave direction. Optimal image quality (indistinguishable from reconstructions with 64 incident-wave directions) is obtained for 16 incident-wave directions, so that scattering data obtained using one incident-wave direction for each group of four measurement directions appears to be sufficient for the present reconstruction method.

The effect of limited view range on the point spread function is also illustrated in Fig. 3. Panel (b) shows the point-spread function for four differently limited apertures, while panel (c) shows reconstructions of a homogeneous cylinder ($a=1.0$ mm, $\gamma=0.02$) for the same apertures. In each case, limitation of the transmit and receive apertures to angles near the backscatter direction (aperture size $\pi/2$) results in images that resemble a conventional B-scans. Use of apertures corresponding to pulse-echo mode in the large-aperture limit (aperture size π) yield higher resolution in all directions. Using three-fourths of a circular aperture (size $3\pi/2$) yields image quality close to that for the full aperture (2π) case. The characteristics of all these images result from the set of spatial-frequency vectors interrogated by each group of scattering measurements.[1] Apertures with only a limited range of transmit and receive directions [e.g., the ''b-scan'' apertures shown in the first column of panels (b) and (c)] provide only information corresponding to large spatial frequency vectors oriented nearly on-axis, so that such images mainly show those edges that are nearly perpendicular to the axis of the aperture.

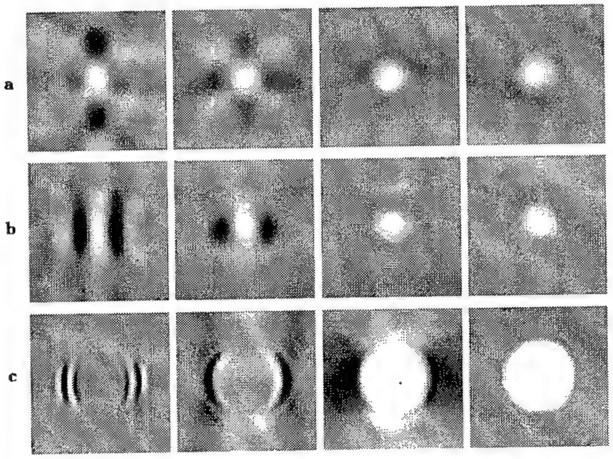

FIG. 3. Effect of aperture characteristics on image quality. Each panel shows the real part of a time-domain reconstruction, Re$[\gamma_M]$, on a linear grayscale with white representing the maximum amplitude of $|\gamma_M(\mathbf{r})|$ and black represents -1 times the maximum amplitude. (a) Point-spread functions for the same waveform parameters as Fig. 2. Each panel shows an area of 0.6×0.6 mm^2, corresponding to one square wavelength at the center frequency. Left to right: 1, 4, 8, and 16 incident-wave directions. (b) Point-spread functions for aperture sizes of $\pi/2$, π, $3\pi/2$, and 2π radians, format as in previous panel. (c) Real parts of reconstructions for a homogeneous cylinder ($a=1.0$ mm, $\gamma=0.02$). The area shown in each panel is 2.0×2.0 mm^2. Left to right: aperture sizes of $\pi/2$, π, $3\pi/2$, and 2π radians.

Reconstructions performed using exact solutions for scattering from cylindrical inhomogeneities provide a straightforward means to assess the accuracy of the time-domain scattering method for a range of object sizes and contrasts. A number of example reconstructions are shown in Figs. 4 and 5. The number of measurement directions for all cylinder reconstructions was chosen based on an empirical test of the number required for a satisfactory image of a homogeneous cylinder; for a cylinder of radius 1 mm, the required number of measurement directions was determined to be approximately 96. Based on spatial-frequency sampling considerations, the number of measurement directions was increased in proportion to the size of the inhomogeneous

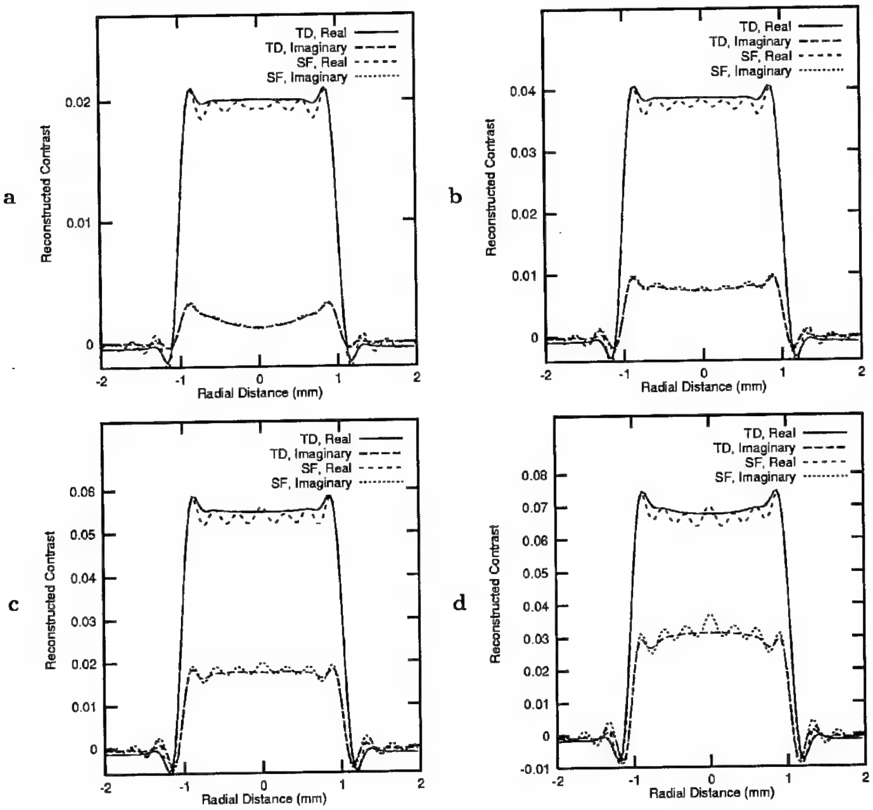

FIG. 4. Cross sections of reconstructed contrast functions $\gamma(\mathbf{r})$ for a cylinder of radius 1 mm, using time-domain (TD) and single-frequency (SF) diffraction tomography. Waveform parameters are as in Fig. 1. (a) $\gamma=0.02$. (b) $\gamma=0.04$. (c) $\gamma=0.06$. (d) $\gamma=0.08$.

region to be reconstructed. Since the results shown in Fig. 3 indicate that considerably fewer incident-wave directions than measurement directions are needed, the number of incident directions was chosen to be one-quarter the number of measurement directions in each case.

Cross sections of time-domain and single-frequency reconstructions, plotted in Fig. 4, show the relative accuracy of each reconstruction method for a cylinder of 1-mm radius and purely real contrast ranging from $\gamma=0.02$ to $\gamma=0.08$. For the synthetic scattering data in each case, 96 measurement directions and 24 incident-wave directions were employed. The time-domain reconstructions show improvement over the single-frequency reconstructions both in improved contrast resolution (smaller sidelobes outside the support of the cylinder) and in decreased ringing (Gibbs phenomenon) artifacts within the support of the cylinder. However, for increasing contrast values, both methods show similar increases in phase error, as indicated by increased imaginary parts of the reconstructed contrast. This error results from the Born approximation, which is based on the assumption that the incident wave propagates through the inhomogeneous medium without distortion. Perturbations in the local arrival time of the incident wavefront, which are more severe for higher contrasts and larger inhomogeneities, can result in a scattered field that is phase shifted relative to the ideal case assumed in the Born approximation; linear inversion of this phase-distorted data naturally results in a phase-distorted reconstruction of the scattering medium. (A complementary explanation of this phase error, based on the unitarity of the scattering operator, is given in Ref. 19.)

A test of image fidelity for the time-domain reconstruction method is shown in Fig. 5. The real parts of time-domain reconstructions are shown as grayscale images for homogeneous cylinders with radii between 1 and 4 mm and contrasts between $\gamma=0.02$ and $\gamma=0.08$. The number of measurement directions employed for the synthetic scattering data was 96 for the 1-mm radius cylinders, 192 for the 2-mm cylinders, 288 for the 3-mm cylinders, and 384 for the 4-mm cylinders. In each case, four incident-wave directions per measurement direction were used. The first row of this figure corresponds to the time-domain reconstructions shown in Fig. 4.

The images shown in Fig. 5 provide a basis for evaluating the ability of the present time-domain diffraction tomography method to image homogeneous objects of various sizes and contrasts. In this figure, images of $\mathrm{Re}[\gamma_M]$ show uniform quality for small cylinder sizes and contrasts, but poorer image quality for larger sizes and contrasts. For the largest size and contrast employed ($a=4.0$ mm, $\gamma=0.08$), the reconstruction primarily shows the edges of the cylinder and fails to image the interior. Particularly notable is that the ''matrix'' of images in Fig. 5 is nearly diagonal; that is, a linear increase in object contrast causes image degradation comparable to a corresponding linear increase in object size. Thus, a nondimensional parameter directly relevant to image quality for homogeneous objects is $ka\,\gamma$, where k is a domi-

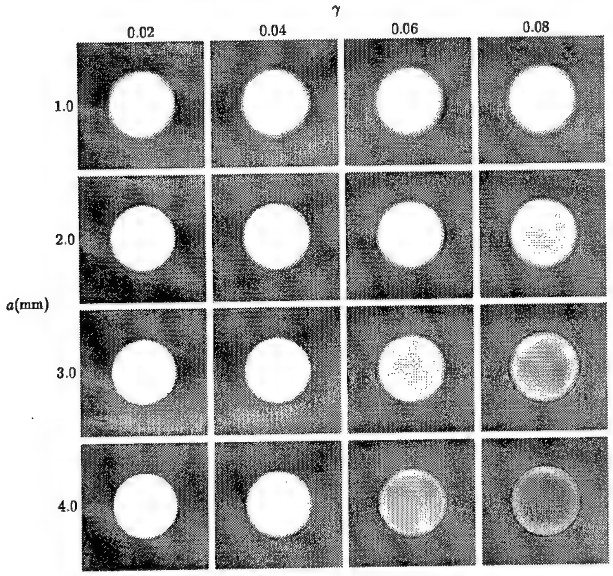

FIG. 5. Images of time-domain reconstructions for cylinders of varying radius a and contrast γ. Each panel shows the real part of the reconstructed contrast, $\mathrm{Re}[\gamma_M(\mathbf{r})]$, for a pulse of center frequency 2.5 MHz and -6 dB bandwidth 1.5 MHz. The area shown in each panel is $2a\times 2a$. All images are shown on a linear, bipolar gray scale where white represents the maximum amplitude of $|\gamma_M(\mathbf{r})|$ and black represents -1 times the maximum amplitude.

nant wave number, a is the object radius, and γ is the object contrast. Using the wave number $k_0=10.472$ rad/mm corresponding to the center frequency of 2.5 MHz and a sound speed of 1.5 mm/μs, the reconstructions shown in Fig. 5 indicate that the interior of the cylinder is imaged satisfactorily for the approximate range $ka\ \gamma<2.5$. This result is consistent with a previous study of single-frequency diffraction tomography, in which adequate Born reconstructions of cylinders were obtained for the parameter range $ka\ \gamma\leqslant 2.2$.[44]

Reconstructions for several scattering objects without special symmetry are shown in Fig. 6. All of these reconstructions were performed using synthetic data produced by the k-space method described in Ref. 41. Synthetic scattering data were computed for 64 incident-wave directions and 256 measurement directions in each case. The first panel shows a reconstruction of a cylinder of radius 2.5 mm and contrast $\gamma=-0.0295$ with an internal cylinder of radius 0.2 mm and contrast $\gamma=0.0632$. These contrast values correspond, based on tissue parameters given in Ref. 32, to the sound-speed contrasts of human skeletal muscle for the outer cylinder and of human fat for the inner cylinder. The second panel shows a reconstruction of a 2.5-mm-radius cylinder with random internal structure. The third reconstruction shown employed a portion of a chest wall tissue map from Ref. 45. In this case, the synthetic data was obtained using a tissue model[45] that incorporates both sound speed and density variations, so that the reconstructed quantity is given by Eq. (26). In Fig. 6(c), black denotes connective tissue ($\gamma=-0.1073$, $\gamma_\rho=0.1134$), dark gray denotes muscle ($\gamma=-0.0295$, $\gamma_\rho=0.0543$), and light gray denotes fat ($\gamma=0.0632$, $\gamma_\rho=-0.0453$).

The real part of each reconstruction in Fig. 6 shows good image quality, with high resolution and very little evidence of artifacts. Particularly notable is the accurately detailed imaging of internal structure for the random cylinder and the chest wall cross section. As expected, the density variations present in the chest wall cross section have not greatly affected the image appearance; there is, however, a slight edge enhancement, associated with the Laplacian term in Eq. (26), at boundaries between tissue regions. Also notable is the nearly complete absence of any artifacts outside the scatterer in each case; this result indicates that high contrast resolution has been achieved. However, in each case, the imaginary part of the reconstruction is nonzero, indicating that the Born approximation is not fully applicable. The imaginary parts of each reconstruction are, however, small compared to the real parts. Thus, simple aberration correction methods [of which one example is given by Eq. (24)] could substantially reduce this phase error, as for multiple-frequency diffraction tomography in Ref. 19.

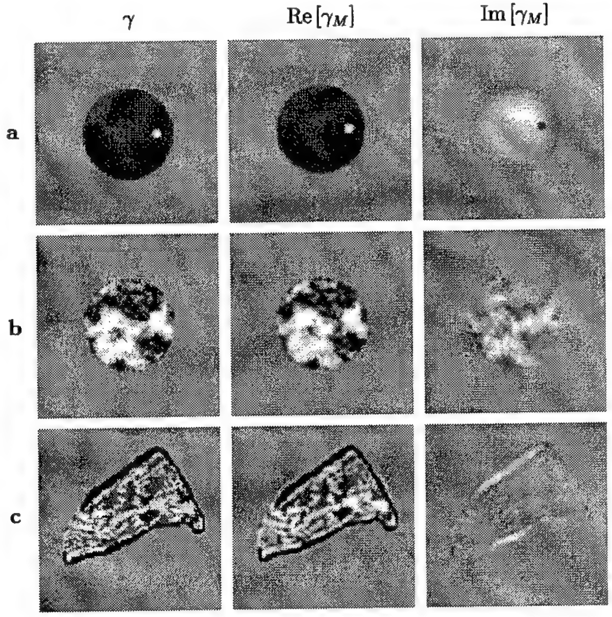

FIG. 6. Time-domain reconstructions from full-wave synthetic data for three arbitrary scattering objects. Each row shows the actual (purely real) contrast function γ together with the real and imaginary parts of the reconstructed contrast function γ_M, using the same linear bipolar gray scale for each panel. Each panel shows a reconstruction area of 5×5 mm^2. (a) Cylinder, radius 2.5 mm, with an internal cylinder of radius 0.2 mm. (b) Cylinder, radius 2.5 mm, with random internal structure. (c) Tissue structure, with variable sound speed and density, from chest wall cross section 5L in Ref. 45.

Three-dimensional reconstructions of a homogeneous slab are shown in Fig. 7. The scatterer is characterized by Eq. (31) with $\gamma_0=0.01$, $a_x=0.5$ mm, $a_y=1.0$ mm, and $a_z=1.5$ mm. Synthetic data was computed using Eq. (34) for 288 incident-wave directions and 1152 measurement directions, each evenly spaced in the angles Φ and Θ. Signal parameters were as for the examples above, except that the initial sampling rate for the time-domain signals was 9.0 MHz. Isosurface renderings of the real part of γ_M are shown for the surfaces $\gamma_M=0.0025$. Since the scattering data were obtained using a Born approximation for the 3D case, the

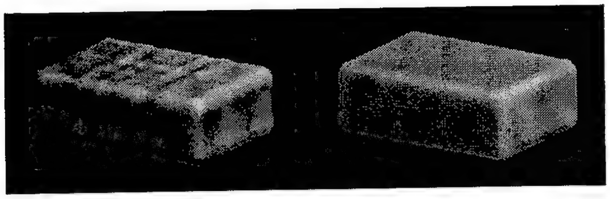

FIG. 7. Three-dimensional reconstructions of a uniform slab with contrast $\gamma=0.01$. Each reconstruction shows an isosurface rendering of the surface $\gamma_M=0.0025$. Left: single-frequency reconstruction. Right: time-domain reconstruction.

imaginary part of each reconstruction is identically zero for both reconstructions. Consistent with the point-spread functions shown in Fig. 2, the time-domain reconstruction is much more accurate than the single-frequency reconstruction. While the single-frequency reconstruction shows an erroneously rippled surface, the time-domain reconstruction is smooth. The time-domain reconstruction is nearly identical to the original object except for some rounding of the sharp edges due to the limited high-frequency content of the signal employed. The length scale of the rounded edges is on the order of one-half the wavelength of the highest frequency in the pulse, i.e., about 0.2 mm for the -6-dB cutoff of 3.25 MHz.

Since three-dimensional inverse scattering is a computationally demanding problem, comparison of computational efficiency for single-frequency and time-domain methods is of interest. For both reconstructions shown in Fig. 7, identical discretizations of the reconstructed medium were employed. Both computations included solution of the applicable linearized forward problem as well as the inverse problem. Nonetheless, the time-domain method was more efficient than the single-frequency method; the total CPU time required on a 200-MHz AMD K6 processor was 133.3 CPU min for the time-domain method and 287.4 CPU min for the single-frequency method. This gain in efficiency was possible because the greatest computational expense occurred in the "backpropagation" of the signals for each reconstruction point. For the single-frequency method, this step required evaluation of complex exponentials for each incident-wave direction, measurement direction, and spatial point. For the time-domain method, however, the computationally intensive steps (including the forward problem solution and Fourier interpolation of the scattered signals) needed only to be performed once for each transmit/receive pair. For the backpropagation step, performed at each point in the 3D spatial grid, the time-domain reconstruction method required only linear interpolation of the oversampled farfield pressure waveforms.

IV. CONCLUSIONS

A new method for time-domain ultrasound diffraction tomography has been presented. The method provides quantitative images of sound speed variations in unknown media; when two pulse center frequencies are employed, the method is also capable of imaging density variations. Reconstructions performed using this method are equivalent to multiple-frequency reconstructions using filtered backpropagation, but can be obtained with much greater efficiency.

The time-domain reconstruction algorithm has been derived as a simple filtered delay-and-sum operation applied to far-field scattered signals. This algorithm is closely related to time-domain confocal synthetic aperture imaging, so that it can be considered a generalization of imaging algorithms employed in current clinical instruments. The simplicity of the imaging algorithm allows straightforward addition of features such as time-gain compensation and aberration correction.

Numerical results obtained using synthetic data for 2D and 3D scattering objects show that the time-domain method can yield significantly higher image quality (and, in some cases, also greater efficiency) than single-frequency diffraction tomography. Quantitative reconstructions, obtained using signal parameters comparable to those for present-day clinical instruments, show accurate imaging of objects with simple deterministic structure, random internal structure, and structure based on a cross-sectional tissue model. The method is hoped to be useful for diagnostic imaging problems such as the detection and characterization of lesions in ultrasonic mammography.

ACKNOWLEDGMENTS

This research was funded by the Breast Cancer Research Program of the U.S. Army Medical Research and Material Command, under Grant No. DAMD17-98-1-8141. The author is grateful for helpful discussions with Adrian I. Nachman, Feng Lin, and Robert C. Waag.

[1] E. Wolf, "Three-dimensional structure determination of semi-transparent objects from holographic data," Opt. Commun. **1**, 153–156 (1969).

[2] A. J. Devaney, "A filtered backpropagation algorithm for diffraction tomography," Ultrason. Imaging **4**, 336–350 (1982).

[3] D. T. Borup, S. A. Johnson, W. W. Kim, and M. J. Berggren, "Nonperturbative diffraction tomography via Gauss-Newton iteration applied to the scattering integral equation," Ultrason. Imaging **14**, 69–85 (1992).

[4] S. Gutman and M. Klibanov, "Two versions of quasi-Newton method for multidimensional inverse scattering problem," J. Comput. Acoust. **1**, 197–228 (1993).

[5] F. W. Kremkau, *Diagnostic Ultrasound: Physical Principles and Exercises* (Grune and Stratton, New York, 1980).

[6] J. L. Schwartz and B. D. Steinberg, "Ultrasparse, ultrawideband arrays," IEEE Trans. Ultrason. Ferroelectr. Freq. Control **45**, 376–393 (1998).

[7] S. H. Maslak, "Computed sonography," in *Ultrasound Annual 1985* (Raven, New York, 1985), pp. 1–16.

[8] E. L. Madsen, B. S. Garra, J. A. Parks, A. C. Skelly, and J. A. Zagzebski, *AIUM Quality Control Manual for Gray-Scale Ultrasound Scanners* (American Institute of Ultrasound in Medicine, Laurel, MD, 1995).

[9] S. J. Norton, "Reconstruction of a two-dimensional reflecting medium over a circular domain: exact solution," J. Acoust. Soc. Am. **67**, 1266–1273 (1980).

[10] S. J. Norton and M. Linzer, "Ultrasonic reflectivity imaging in three dimensions: exact inverse scattering solutions for plane, cylindrical, and circular apertures," IEEE Trans. Biomed. Eng. **28**, 202–220 (1980).

[11] J. H. Kim, S. B. Park, and S. A. Johnson, "Tomographic imaging of ultrasonic reflectivity with correction for acoustic speed variations," Ultrason. Imaging **6**, 304–312 (1984).

[12] C. Q. Lan and W. Xiong, "An iterative method of ultrasonic reflection mode tomography," IEEE Trans. Med. Imaging **13**, 419–425 (1994).

[13] D. Miller, M. Oristaglio, and G. Beylkin, "A new slant on seismic imaging: migration and internal geometry," Geophysics **52**, 943–964 (1987).

[14] T. Melamed, Y. Ehrlich, and E. Heymann, "Short-pulse inversion of inhomogeneous media: a time-domain diffraction tomography," Inverse Probl. **12**, 977–993 (1996).

[15] S. Pourjavid and O. Tretiak, "Ultrasound imaging through time-domain diffraction tomography," IEEE Trans. Ultrason. Ferroelectr. Freq. Control **38**, 74–85 (1991).

[16] A. Witten, J. Tuggle, and R. C. Waag, "A practical approach to ultrasonic imaging using diffraction tomography," J. Acoust. Soc. Am. **83**, 1645–1652 (1988).

[17] T. J. Cavicchi and W. D. O'Brien, "Numerical study of higher-order diffraction tomography via the sinc basis moment method," Ultrason. Imaging **11**, 42–74 (1989).

[18] H. Gan, R. Ludwig, and P. L. Levin, "Nonlinear diffractive inverse scattering for multiple scattering in inhomogeneous acoustic background media," J. Acoust. Soc. Am. **97**, 764–776 (1995).

[19] T. D. Mast, A. I. Nachman, and R. C. Waag, "Focusing and imaging using eigenfunctions of the scattering operator," J. Acoust. Soc. Am. **102**, 715–725 (1997).

[20] J. M. Blackledge, R. E. Burge, K. I. Hopcraft, and R. J. Wombell, "Quantitative diffraction tomography: I. Pulsed acoustic fields," J. Phys. D **20**, 1–10 (1987).

[21] S. Mensah and J.-P. Lefebvre, "Enhanced compressibility tomography," IEEE Trans. Ultrason. Ferroelectr. Freq. Control **44**, 1245–1252 (1997).

[22] G. Prokoph and H. Ermert, "A comparison of broadband holographic and tomographic imaging concepts," Acoust. Imaging **18**, 381–390 (1991).

[23] V. A. Burov and O. D. Rumyantseva, "Linearized inverse problem of scattering in monochromatic and pulse modes," Acoust. Phys. **40**, 34–42 (1996).

[24] F. Lin, A. I. Nachman, and R. C. Waag, "Quantitative imaging using a time-domain eigenfunction method," submitted to J. Acoust. Soc. Am. (1999).

[25] P. M. Morse and K. U. Ingard, *Theoretical Acoustics* (New York, McGraw-Hill, 1968), Chap. 8.

[26] P. M. Morse and H. Feshbach, *Methods of Theoretical Physics* (McGraw–Hill, New York, 1953), Vol. I.

[27] G. Beylkin, "The fundamental identity for iterated spherical means and the inversion formula for diffraction tomography and inverse scattering," J. Math. Phys. **24**, 1399–1400 (1982).

[28] A. Papoulis, *The Fourier Integral and Its Applications* (McGraw–Hill, New York, 1962), Chap. 10.

[29] J. Ylitalo, E. Alasaarela, and J. Koivukangas, "Ultrasound holographic B-scan imaging," IEEE Trans. Ultrason. Ferroelectr. Freq. Control **36**, 376–383 (1989).

[30] K. E. Thomenius, "Evolution of ultrasound beamformers," Proc. IEEE Ultrason. Symp. **2**, 1615–1622 (1996).

[31] R. Snieder, "A perturbative analysis of non-linear inversion," Geophys. J. Int. **101**, 545–556 (1990).

[32] T. D. Mast, L. M. Hinkelman, M. J. Orr, V. W. Sparrow, and R. C. Waag, "Simulation of ultrasonic pulse propagation through the abdominal wall," J. Acoust. Soc. Am. **102**, 1177–1190 (1997) [Erratum: **104**, 1124–1125 (1998)].

[33] T. D. Mast, L. M. Hinkelman, M. J. Orr, and R. C. Waag, "The effect of abdominal wall morphology on ultrasonic pulse distortion. Part II. Simulations," J. Acoust. Soc. Am. **104**, 3651–3664 (1998).

[34] D.-L. Liu and R. C. Waag, "Correction of ultrasonic wavefront distortion using backpropagation and a reference waveform method for time-shift compensation," J. Acoust. Soc. Am. **96**, 649–660 (1994).

[35] C. Dorme and M. Fink, "Ultrasonic beam steering through inhomogeneous layers with a time reversal mirror," IEEE Trans. Ultrason. Ferroelectr. Freq. Control **43**(1), 167–175 (1996).

[36] S. Kirshnan, P.-C. Li, and M. O'Donnell, "Adaptive compensation for phase and magnitude aberrations," IEEE Trans. Ultrason. Ferroelectr. Freq. Control **43**(1), 44–55 (1996).

[37] Q. Zhu and B. D. Steinberg, "Deabberation of incoherent wavefront distortion: an approach toward inverse filtering," IEEE Trans. Ultrason. Ferroelectr. Freq. Control **44**, 575–589 (1997).

[38] I. Claesson and G. Salomonsson, "Frequency- and depth-dependent compensation of ultrasonic signals," IEEE Trans. Ultrason. Ferroelectr. Freq. Control **35**, 582–592 (1988).

[39] A. J. Devaney, "Variable density acoustics tomography," J. Acoust. Soc. Am. **78**, 120–130 (1985).

[40] T. T. Jansson, T. D. Mast, and R. C. Waag, "Measurements of differential scattering cross section using a ring transducer," J. Acoust. Soc. Am. **103**, 3169–3179 (1998).

[41] L. P. Souriau, T. D. Mast, D.-L. D. Liu, M.. Tabei, A. I. Nachman, and R. C. Waag, "A *k*-space method for large-scale models of wave propagation in tissue," submitted to IEEE Trans. Ultrason. Ferrolectr. Freq. Control. (1999).

[42] A. Nachman, "Reconstructions from boundary measurements," Ann. Math. **128**, 531–576 (1988).

[43] D. Colton and R. Kress, *Inverse Acoustic and Electromagnetic Scattering Theory*, 2nd ed. (Springer-Verlag, Berlin, 1998), Chap. 10.

[44] M. Slaney, A. C. Kak, and L. E. Larsen, "Limitations of imaging with first-order diffraction tomography," IEEE Trans. Microwave Theory Tech. **32**, 860–874 (1984).

[45] T. D. Mast, L. M. Hinkelman, M. J. Orr, and R. C. Waag, "Simulation of ultrasonic pulse propagation, distortion, and attenuation in the human chest wall," submitted to J. Acoust. Soc. Am. **106**, 3665–3677 (1999).

APPENDIX B

Time-Domain Ultrasound Diffraction Tomography

T. Douglas Mast,[1] Feng Lin,[2] and Robert C. Waag[2,3]

[1]Applied Research Laboratory, The Pennsylvania State University, University Park, PA 16802
[2]Dept. of Electrical Engineering, University of Rochester, Rochester, NY 14627
[3]Dept. of Radiology, University of Rochester, Rochester, NY 14642

Abstract— **A quantitative ultrasonic imaging method employing time-domain scattering data is presented. This method provides tomographic images of medium properties such as the sound speed contrast; these images are equivalent to multiple-frequency filtered-backpropagation reconstructions using all frequencies within the bandwidth of the incident pulse employed. However, image synthesis is performed directly in the time domain using coherent combination of farfield scattered pressure waveforms, delayed and summed to numerically focus on the unknown medium. The time-domain method is more efficient than multiple-frequency diffraction tomography methods, and can, in some cases, be more efficient than single-frequency diffraction tomography. Example reconstructions, obtained using synthetic data for two-dimensional and three-dimensional scattering of wideband pulses as well as measured scattering data from a 2048-element ring transducer, show that the time-domain reconstruction method provides image quality superior to single-frequency reconstructions for objects of size and contrast relevant to medical imaging problems such as ultrasonic mammography. The present method is closely related to existing synthetic-aperture imaging methods such as those employed in clinical ultrasound scanners. Thus, the new method can be extended to incorporate available image-enhancement techniques such as time-gain compensation to correct for medium absorption and aberration correction methods to reduce error associated with weak scattering approximations.**

I. INTRODUCTION

Quantitative imaging of tissue properties is a potentially useful technique for diagnosis of cancer and other disease. Inverse scattering methods such as diffraction tomography can provide quantitative reconstruction of tissue properties including sound speed, density, and absorption. However, although previous inverse scattering methods have achieved high resolution and quantitative accuracy, such methods have not yet been incorporated into commercially successful medical ultrasound imaging systems. Previous methods of diffraction tomography have usually been based on single-frequency scattering, while current diagnostic ultrasound scanners employ wideband time-domain signals. The use of wideband information in image reconstruction is known to provide increased point and contrast resolution, both of which are important for medical diagnosis.

Relatively few previous workers have investigated direct use of wideband scattering data for inverse scattering methods analogous to single-frequency diffraction tomography. A review of several approaches is given in Ref. [1], including linear and nonlinear diffraction tomography methods using scattering data for a number of discrete frequencies [2]–[4], a direct (but not completely general) time-domain reconstruction algorithm [5], and an extension of the eigenfunction method from Ref. [4] to use the full bandwidth of the incident pulse waveform [6].

Recently, a new approach to wideband quantitative imaging has been offered: a time-domain inverse scattering method that overcomes some of the limitations of previous frequency-domain and time-domain quantitative imaging methods [1]. In this paper, the new time-domain diffraction tomography algorithm is briefly reviewed. The capabilities of the method are demonstrated using simulated reconstructions of two-dimensional and three-dimensional scatterers. The practical capability of the method for ultrasonic mammography is then illustrated by reconstructions of tissue-mimicking phantoms from scattering data measured by a 2.5 MHz, 2048-element ring transducer.

II. THEORY

A new time-domain inverse scattering algorithm, applicable to quantitative imaging of tissue and other inhomogeneous media, is derived in Ref. [1] and summarized briefly below. The medium is modeled as a fluid medium defined by the sound speed contrast function $\gamma(\mathbf{r}) = c_0^2/c(\mathbf{r})^2 - 1$, where c_0 is a background sound speed and $c(\mathbf{r})$ is the spatially-dependent sound speed defined at all points $\mathbf{r}$. For the scope of the present paper, the medium is assumed to have constant density, no absorption, and weak scattering characteristics; extensions to the reconstruction algorithm that overcome these limiting assumptions are discussed in Ref. [1].

The medium is subjected to a pulsatile plane wave of the form $p_{\text{inc}}(\mathbf{r},\boldsymbol{\alpha},t) = f(t - \mathbf{r}\cdot\boldsymbol{\alpha}/c_0)$, where $\boldsymbol{\alpha}$ is a unit vector in the direction of propagation, f is the time-domain waveform, and c_0 is the background sound speed. The scattered wavefield $p_s(\boldsymbol{\theta},\boldsymbol{\alpha},t)$ is measured at a fixed radius R in the farfield, where $\boldsymbol{\theta}$ corresponds to the direction unit vector of a receiving transducer element. (Alternatively, if scattering measurements are made in the nearfield, the farfield acoustic pressure can be computed using exact transforms that represent propagation through a homogeneous medium [2].) The farfield scattered pressure, when specified for all incident-wave directions $\boldsymbol{\alpha}$, measurement directions $\boldsymbol{\theta}$, and times t, comprises the data set to be used for reconstruction of the unknown medium. The inverse scattering problem is to reconstruct the unknown medium contrast $\gamma(\mathbf{r})$ using the scattered field $\hat{p}_s(\boldsymbol{\theta},\boldsymbol{\alpha},\omega)$ measured at a fixed radius R.

The starting point for the present time-domain inverse scattering method is single-frequency filtered backpropagation [2], [7], [8]. Under the assumption of weak scattering, such that the Born approximation holds, the solution to the single-frequency inverse scattering problem is given by the formula

$$\gamma_B(\mathbf{r},\omega) = \frac{\hat{\mu}(\omega)\, e^{-ikR}}{\hat{f}(\omega)} \iint \Phi(\boldsymbol{\theta},\boldsymbol{\alpha})\, \hat{p}_s(\boldsymbol{\theta},\boldsymbol{\alpha},\omega) \times e^{ik(\boldsymbol{\theta}-\boldsymbol{\alpha})\cdot\mathbf{r}}\, dS_\alpha\, dS_\theta, \text{ where} \quad (1)$$

1999 IEEE Ultrasonics Symposium
(c) 1999 IEEE
0-7803-5725-6/99/$10.00

$$\hat{\mu}(\omega) = \sqrt{\frac{kR}{8i\pi^3}},\ \Phi(\boldsymbol{\theta},\boldsymbol{\alpha}) = |\sin(\theta-\alpha)| \text{ in 2D, and}$$
$$\hat{\mu}(\omega) = \frac{kR}{4\pi^3},\ \Phi(\boldsymbol{\theta},\boldsymbol{\alpha}) = |\boldsymbol{\theta}-\boldsymbol{\alpha}| \text{ in 3D.} \qquad (2)$$

Each surface integral in Eq. (1) is performed over the entire measurement circle for the 2D case and over the entire measurement sphere for the 3D case. Equation (1) provides an exact solution to the linearized inverse scattering problem for a single frequency component of the scattered wavefield $p_s(\boldsymbol{\theta},\boldsymbol{\alpha},t)$. The resulting reconstruction, $\gamma_B(\mathbf{r},\omega)$, has spatial frequency content limited by the "Ewald sphere" of radius $2k$ in wavespace [9].

To improve upon the single-frequency formulas specified by Eq. (1), one can extend the spatial-frequency content of reconstructions by exploiting wideband scattering information. The method outlined here synthesizes a "multiple-frequency" reconstruction $\gamma_M(\mathbf{r})$ by formally integrating single-frequency reconstructions $\gamma_B(\mathbf{r},\omega)$ over a range of frequencies ω. A general formula for this approach is

$$\gamma_M(\mathbf{r}) = \frac{\int_0^\infty \hat{g}(\omega)\,\gamma_B(\mathbf{r},\omega)\,d\omega}{\int_0^\infty \hat{g}(\omega)\,d\omega}, \qquad (3)$$

where $\hat{g}(\omega)$ is an appropriate frequency-dependent weighting function. In practice, the weighting function $\hat{g}(\omega)$ is chosen to be bandlimited because (for a given set of physical scattering measurements) the frequency-dependent contrast $\gamma_B(\mathbf{r},\omega)$ can only be reliably reconstructed for a finite range of frequencies ω associated with the spectra of the incident waves employed. Thus, the integrands in Eq. (3) are nonzero only over the support of $\hat{g}(\omega)$ and the corresponding integrals are finite.

If the frequency weighting function is now specified to incorporate the incident-pulse spectrum as well as the frequency- and dimension-dependent coefficient $\hat{\mu}(\omega)$, such that $g(\omega) = \hat{f}(\omega)/\hat{\mu}(\omega)$, Eq. (3) reduces to the form [1]

$$\gamma_M(\mathbf{r}) = \frac{1}{N}\iint \Phi(\boldsymbol{\theta},\boldsymbol{\alpha})\,\big(p_s(\boldsymbol{\theta},\alpha,\tau) + i\,\mathbf{H}^{-1}[p_s(\boldsymbol{\theta},\alpha,\tau)]\big)\,dS_\alpha\,dS_\theta, \text{ where} \qquad (4)$$
$$\tau = R/c_0 + \frac{(\boldsymbol{\alpha}-\boldsymbol{\theta})\cdot\mathbf{r}}{c_0},\quad N = 2\int_0^\infty \hat{g}(\omega)\,d\omega,$$

and $\mathbf{H}^{-1}$ is the inverse Hilbert transform, also known as a quadrature filter.

Equation (4) is notable in several respects. First, it provides a linearized reconstruction that employs scattering information from the entire signal bandwidth without any frequency decomposition of the scattered wavefield. Second, the delay term τ corresponds exactly to the delay required to construct a focus at the point $\mathbf{r}$ by delaying and summing the scattered wavefield $p_s(\boldsymbol{\theta},\boldsymbol{\alpha},t)$ for all measurement directions $\boldsymbol{\theta}$ and incident-wave directions $\boldsymbol{\alpha}$. Thus, the time-domain reconstruction formula given by Eq. (4) can be regarded as a quantitative generalization of confocal time-domain synthetic aperture imaging (*e.g.*, the "gold standard" beamformer of Ref. [10]), in which signals are synthetically delayed and summed for each transmit/receive pair to focus at the image point of interest.

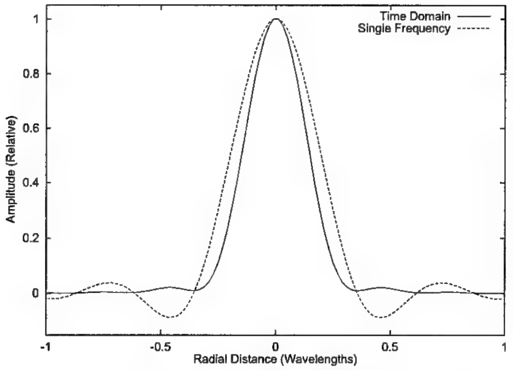

Fig. 1. Point-spread function for three-dimensional time-domain and single-frequency diffraction tomography methods. The vertical scale corresponds to the relative amplitude of the reconstructed contrast $\gamma(\mathbf{r})$, while the horizontal scale corresponds to number of wavelengths at the center frequency.

III. SIMULATIONS

Below, the time-domain diffraction tomography method of Ref. [1] is illustrated using results of simulation tests with 2D and 3D synthetic data. The synthetic scattering data employed were obtained using a Born approximation method for point scatterers and 3D slabs, and a k-space method [11] for arbitrary 2D inhomogeneous media. Additional results, presented in Ref. [1], show reconstructions performed using using exact time-domain solutions for scattering from compressible cylinders as well as reconstructions from limited-aperture data. The time-domain waveform employed for all the simulations reported here was $f(t) = \cos(2\pi f_0 t)\,e^{-t^2/(2\sigma^2)}$, with $f_0 = 2.5$ MHz and $\sigma = 0.25$ μs, so that the -6 dB bandwidth of the signal was 1.5 MHz. These parameters correspond closely to those of the ring transducer used in the measurements reported in the next section.

The time-domain imaging method was directly implemented using Eq. (4), evaluated using straightforward numerical integration over all incident-wave and measurement directions employed. The synthetic data employed was sampled at rates slightly larger than the Nyquist frequency. Before evaluation of the argument τ for each signal, the time-domain waveforms were Fourier interpolated at a sampling rate of 16 times the original rate. This resampling, as well as the inverse Hilbert transform from Eq. (4), were performed by FFT. Values of the pressure signals at the time τ were then determined using linear interpolation between samples of the resampled waveforms.

A three-dimensional point-spread function (PSF) for the present time-domain diffraction tomography method is illustrated in Fig. 1. The PSF was determined by reconstructing an ideal point scatterer located at the origin. The time-domain reconstruction shows a dramatic improvement over the single-frequency reconstruction, with significant increases in both the point resolution (PSF width at half-maximum reduced by 27%) and contrast resolution (first sidelobe reduced by 13 dB and second sidelobe reduced by 18 dB).

Reconstructions for several arbitrary scattering objects are shown in Fig. 2. All of these reconstructions were performed using synthetic data produced by the k-space method described in Ref. [11]. Synthetic scattering data were computed for 64 incident-wave directions and 256 measure-

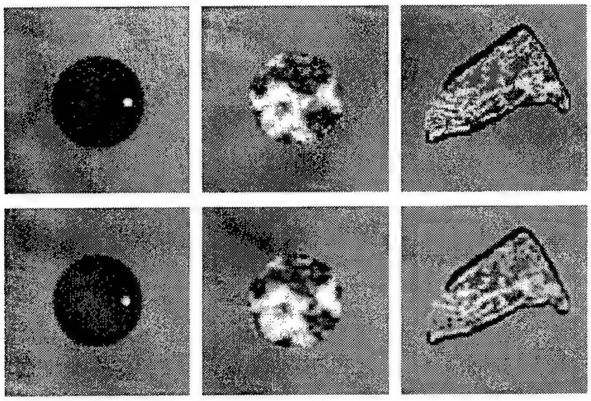

Fig. 2. Time-domain reconstructions from full-wave synthetic data for three arbitrary scattering objects. The upper row shows the contrast function γ for each object, while the lower row shows the real part of the reconstructed contrast γ_M. Each panel shows a reconstruction area of 5 mm × 5 mm using a linear bipolar gray scale. Left to right: (a) Cylinder, radius 2.5 mm, with an internal cylinder of radius 0.2 mm. (b) Cylinder, radius 2.5 mm, with random internal structure. (c) Tissue structure, with variable sound speed and density, from a chest wall cross section.

ment directions in each case. The first panel shows a reconstruction of a cylinder of radius 2.5 mm and contrast $\gamma = -0.0295$ with an internal cylinder of radius 0.2 mm and contrast $\gamma = 0.0632$. These contrast values correspond, based on tissue parameters given in Ref. [12], to the sound-speed contrasts of human skeletal muscle for the outer cylinder and of human fat for the inner cylinder. The second panel shows a reconstruction of a 2.5 mm-radius cylinder with random internal structure. The third reconstruction shown employed a portion of a chest wall tissue map from Ref. [13]. In this case, the synthetic data was obtained using a tissue model that incorporates both sound speed and density variations, so that the actual reconstructed quantity is slightly different from γ_M [1]. In Fig. 2(c), black denotes connective tissue, dark gray denotes muscle, and light gray denotes fat.

The real part of each reconstruction in Fig. 2 shows good image quality, with high resolution and very little evidence of artifacts. Particularly notable is the accurately detailed imaging of internal structure for the random cylinder and the chest wall cross section. As discussed in Ref. [1], the density variations present in the chest wall cross section have not greatly affected the image appearance; there is, however, a slight edge enhancement at boundaries between tissue regions. Also notable is the nearly-complete absence of any artifacts outside the scatterer in each case; this result indicates that high contrast resolution has been achieved.

Three-dimensional reconstructions of a homogeneous slab with sound speed contrast $\gamma = 0.01$ and dimensions 1 mm × 2 mm × 3 mm, are shown in Fig. 3. Synthetic data was computed using a weak scattering approximation for 288 incident-wave directions and 1152 measurement directions, each evenly spaced in the angles Φ and Θ. Isosurface renderings of the real part of the reconstructed γ_M are shown for the surfaces $\gamma_M = 0.0025$. Consistent with the point-spread function shown in Fig. 1, the time-domain reconstruction is much more accurate than the single-frequency reconstruction. While the single-frequency reconstruction shows an erroneously rippled surface, the time-domain reconstruction is smooth. The time-domain reconstruction is nearly identical to the original object except for some rounding of the sharp edges due to the limited high-frequency content of the signal employed. The length scale of the rounded edges is on the order of one-half the wavelength of the highest frequency in the pulse, *i.e.*, about 0.2 mm for the −6 dB cutoff of 3.25 MHz. Notable is that the time-domain method was more efficient than the single-frequency method in this case; the total CPU time required on a 233 MHz Pentium II processor was 100.0 CPU min for the time-domain method and 233.4 CPU min for the single-frequency method (both computations included solution of the applicable linearized forward problem as well as the inverse problem). This gain in efficiency was possible because the greatest computational expense occurred in the "backpropagation" of the signals, which required evaluation of complex exponentials for the single-frequency method, but only linear interpolation of the oversampled farfield pressure waveforms for the time-domain method.

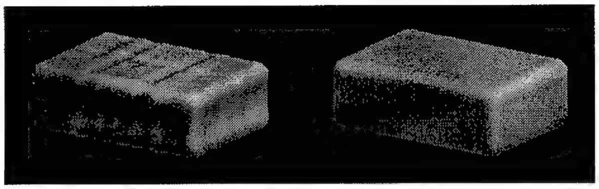

Fig. 3. Three-dimensional reconstructions of a uniform slab with contrast $\gamma = 0.01$. Each reconstruction shows an isosurface rendering of the surface $\gamma_M = 0.0025$. Left: single-frequency reconstruction. Right: time-domain reconstruction.

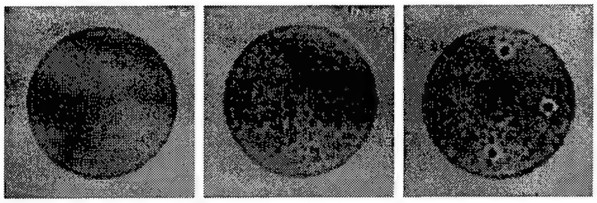

Fig. 4. Reconstructions of three phantoms from measured scattering data. Each panel shows an area of 9 mm × 9 mm using a bipolar logarithmic scale with a 30 dB dynamic range. Left to right: (a) Homogeneous agar cylinder. (b) Agar with glass spheres. (c) Agar with glass spheres and three nylon filaments.

IV. MEASUREMENTS

The practical capability of the time-domain diffraction tomography method to image tissue-like media has been tested using measured scattering data for three tissue-mimicking phantoms, each of diameter 6 mm. Details of the phantom construction and measurement procedure are given in Ref. [6] and briefly summarized here. The phantoms are primarily composed of agar (nominal sound speed 1510 m/s); one is homogeneous, another contains tiny (subresolution), randomly distributed glass beads, and a third contains three nylon filaments as well as glass beads. Measurements were made using a ring transducer system [14] that consists of 2048 elements, each of which can be used independently as a transmitter or receiver. This fixed transducer configuration avoids signal degradation from phase jitter and excessive scanning time associated with moving transducers. The control electronics associated with the ring transducer provide the capability to program arbitrary transmit waveforms. The element pitch is 0.23 mm, less than one half of the wavelength at the nominal center frequency of 2.5 MHz.

Spatially-limited plane wave pulses were transmitted from 128 positions equally spaced around the ring. To construct the spatially-limited plane waves, a 4 mm-width cosine rolloff was added to each side of a 10 mm-width uniform central region to provide a smooth transition in amplitude and reduce wavefront spreading. A backpropagation method [15] was then used to obtain the transmit waveforms that produced the desired incident wave.

The incident field (without the scattering object) and the total field (with the scattering object) were measured around the ring for each incident view. To compensate for sound speed changes due to water temperature variations, the background sound speed was tracked using a probe beam during the measurement of both the incident and total fields. The sound speed in the background was estimated from knowledge of the arrival time and the travel distance of the probe beam, which was a spatially limited plane wave directed to the side of the phantom. The resulting speed estimate was used to equalize the time scale of all waveforms. A temperature-compensated incident field $p_i(\boldsymbol{\theta}, \boldsymbol{\alpha}, t)$ was subtracted from the total field $p(\boldsymbol{\theta}, \boldsymbol{\alpha}, t)$ to obtain the scattered field $p_s(\boldsymbol{\alpha}, \boldsymbol{\theta}, t)$. Finally, wavefields were extrapolated to 128 measurement positions at a radius of 7500 mm by an exact spatio-temporal transformation [2], [6].

Far-field scattered waveforms for each incident-wave direction were further processed by a deconvolution operation [1] that compensated for transducer-dependent variations in the incident pulse. The result for each incident-wave direction was an estimate of the scattered farfield pressure associated with an ideal incident pulse of the form $f(t) = \cos(2\pi f_0 t)\, e^{-t^2/(2\sigma^2)}$, with $f_0 = 2.25$ MHz and $\sigma = 0.25$ μs. The preprocessed data $p_s(\boldsymbol{\theta}, \boldsymbol{\alpha}, t)$ were then inverted using numerical integration of Eq. (4). The inversion procedure was the same as for the simulations described above, except that the initial sampling rate was 20 MHz and that signals were oversampled to 80 MHz by Fourier interpolation.

Reconstructions for the three phantoms are shown in Fig. 4. Each panel shows good reconstruction quality with a uniform background and high point and contrast resolution as well as quantitative accuracy (similar reconstructions, obtained using an eigenfunction-based inverse scattering method, are presented in Ref. [6]). The subresolution glass spheres do not cause speckle as in pulse-echo B-scan imaging, but instead appear as slight local variations in contrast consistent with weak point scatterers. Both nylon filaments and glass spheres appear dark because higher sound speed corresponds to negative contrast γ as defined above. In panel (c), reconstructions of the nylon wires show slight sidelobe artifacts; these artifacts could be removed by careful choice of an optimal pulse $f(t)$ in the preprocessing of the scattered field [6].

V. CONCLUSIONS

A new method for time-domain ultrasound diffraction tomography has been presented and validated using synthetic and measured scattering data. The method provides quantitative images of sound speed variations in unknown media. These reconstructions are equivalent to multiple-frequency reconstructions using filtered backpropagation, but can be obtained with much greater efficiency. The time-domain reconstruction algorithm has been derived as a simple filtered delay-and-sum operation, closely related to time-domain confocal synthetic aperture imaging, so that it can be considered a generalization of imaging algorithms employed in current clinical instruments. The simplicity of the imaging algorithm allows straightforward addition of features such as time-gain compensation and aberration correction.

Numerical results obtained using synthetic and measured data show that the time-domain method can yield significantly higher image quality (and, in some cases, also greater efficiency) than single-frequency diffraction tomography. Quantitative reconstructions, obtained using signal parameters comparable to those for present-day clinical instruments, show accurate imaging of objects with simple deterministic structure, random internal structure, and structure based on a cross-sectional tissue model. Reconstructions of tissue-mimicking phantoms suggest that the method will be useful for diagnostic imaging problems such as the detection and characterization of lesions in ultrasonic mammography.

ACKNOWLEDGMENTS

This research was funded by the Breast Cancer Research Program of the U.S. Army Medical Research and Materiel Command, under Grant No. DAMD17-98-1-8141 (TDM), and by NIH Grants DK 45533, HL 50855, and CA 74050, DARPA Grant N00014-96-0749, and the University of Rochester Diagnostic Ultrasound Research Laboratory Industrial Associates (FL and RCW).

REFERENCES

[1] T. D. Mast, "Wideband quantitative ultrasonic imaging by time-domain diffraction tomography," to appear in J. Acoust. Soc. Am. (1999).

[2] A. Witten, J. Tuggle, and R. C. Waag, "A practical approach to ultrasonic imaging using diffraction tomography," J. Acoust. Soc. Am. **83**, 1645–1652 (1988).

[3] T. J. Cavicchi and W. D. O'Brien, "Numerical study of higher-order diffraction tomography via the sinc basis moment method," Ultrasonic Imaging **11**, 42–74 (1989).

[4] T. D. Mast, A. I. Nachman, and R. C. Waag, "Focusing and imaging using eigenfunctions of the scattering operator," *J. Acoust. Soc. Am.* **102**, 715–725 (1997).

[5] V. A. Burov and O. D. Rumyantseva, "Linearized inverse problem of scattering in monochromatic and pulse modes," Acoustical Physics **40**, 34–42 (1996).

[6] F. Lin, A. I. Nachman, and R. C. Waag, "Quantitative imaging using a time-domain eigenfunction method," submitted to J. Acoust. Soc. Am. (1999).

[7] A. J. Devaney, "A filtered backpropagation algorithm for diffraction tomography," Ultrason. Imag. **4**, 336–350 (1982).

[8] G. Beylkin, "The fundamental identity for iterated spherical means and the inversion formula for diffraction tomography and inverse scattering," J. Math. Phys. **24**, 1399–1400 (1982).

[9] E. Wolf, "Three-dimensional structure determination of semi-transparent objects from holographic data," Optics Comm. **1**, 153–156 (1969).

[10] K. E. Thomenius, "Evolution of ultrasound beamformers," Proc. IEEE Ultrason. Symp. **2**, 1615–1622 (1996).

[11] L. P. Souriau, T. D. Mast, D.-L. Liu, M. Tabei, A. I. Nachman, and R. C. Waag, "A k-space method for large-scale models of wave propagation in tissue," submitted to IEEE Trans. Ultrason. Ferrolectr. Freq. Contr. (1999).

[12] T. D. Mast, L. M. Hinkelman, M. J. Orr, V. W. Sparrow, and R. C. Waag, "Simulation of ultrasonic pulse propagation through the abdominal wall," J. Acoust. Soc. Am. **102**, 1177–1190 (1997).

[13] T. D. Mast, L. M. Hinkelman, M. J. Orr, and R. C. Waag, "Simulation of ultrasonic pulse propagation, distortion, and attenuation in the human chest wall," submitted to J. Acoust. Soc. Am. (1999).

[14] T. T. Jansson, T. D. Mast, and R. C. Waag, "Measurements of differential scattering cross section using a ring transducer," J. Acoust. Soc. Am. **103**, 3169–3179 (1998).

[15] D.-L. Liu and R. C. Waag, "Propagation and backpropagation for ultrasonic wavefront design," IEEE Trans. Ultrason., Ferroelect., Freq. Contr. **44**, 1–13 (1997).

(c) 1999 IEEE

Aberration correction for time-domain ultrasound diffraction tomography

T. Douglas Mast

Applied Research Laboratory, The Pennsylvania State University, University Park, Pennsylvania 16802

Abbreviated title: Abberation correction for diffraction tomography

Abstract

Extensions of a time-domain diffraction tomography method, which reconstructs spatially-dependent sound speed variations from far-field time-domain acoustic scattering measurements, are presented and analyzed. The resulting reconstructions are quantitative images with applications including ultrasonic mammography, and can also be considered candidate solutions to the time-domain inverse scattering problem. Here, the linearized time-domain inverse scattering problem is shown to have no general solution for finite signal bandwidth. However, an approximate solution to the linearized problem is constructed using a simple delay-and-sum method analogous to "gold standard" ultrasonic beamforming. The form of this solution suggests that the full nonlinear inverse scattering problem can be approximated by applying appropriate angle- and space-dependent time shifts to the time-domain scattering data; this analogy leads to a general approach to aberration correction. Two related methods for aberration correction are presented: one in which delays are computed from estimates of the medium using an efficient straight-ray approximation, and one in which delays are applied directly to a time-dependent linearized reconstruction. Numerical results indicate that these correction methods achieve substantial quality improvments for imaging of large scatterers. The parametric range of applicability for the time-domain diffraction tomography method is increased by about a factor of two by aberration correction.

PACS: 43.20.F, 43.80.Q, 43.60.P

Typeset using REVTEX

I. INTRODUCTION

This paper concerns time-domain diffraction tomography methods for solution of the time-domain inverse scattering problem, in which an unknown inhomogeneous medium is determined from its far-field acoustic scattering. This problem is of interest for medical ultrasonic imaging, since inverse scattering methods such as diffraction tomography can provide quantitative reconstruction of tissue properties including sound speed, density, and absorption.

Most practical inverse scattering methods to date have been based on linearization of the inverse problem using the Born or Rytov approximation.[1,2] These are weak scattering approximations, in which the variation of medium properties is assumed to be a small perturbation from a uniform background. Nonlinear inverse scattering methods,[3,4] which consider contributions of strong and multiple scattering, are much more complex and computationally intensive. However, since large-scale tissue structures cannot be considered weak scatterers at diagnostic ultrasound imaging frequencies,[5,6] linearized inverse scattering methods are of limited use for medical ultrasonic imaging.

A similar problem arises in conventional B-scan and synthetic-aperture imaging,[8,9] which form the basis for current diagnostic ultrasound scanners. Current scanners form synthetic images based on the assumption of a uniform background sound speed, which is essentially the Born approximation. The invalidity of this assumption is associated with image artifacts and focus aberration.[5,7] Considerable effort has been devoted to methods for aberration-corrected imaging, which is analogous to nonlinear inverse scattering. Approaches to aberration correction for pulse-echo imaging have been designed to correct distortion associated with several simplified propagation models, including refraction by homogeneous layers,[10,11] phase aberration close to the transducer aperture,[12–14] and aberration caused by a hypothetical phase screen away from the aperture.[15–17] All of these aberration correction methods require indirect estimation of the medium-induced distortion based on the received scattering data.

A time-domain diffraction tomography method has been introduced recently.[18,19] This method provides tomographic reconstructions of unknown scattering media from scattering data measured on a surface surrounding the region of interest, using the entire available bandwidth of the signals employed. The reconstruction algorithm is derived as a simple delay-and-sum formula similar to synthetic-aperture algorithms employed in conventional clinical scanners.[8,9] However, unlike current clinical scanners, the present method provides quantitative images of the spatially-dependent tissue sound speed. These quantitative sound speed maps offer considerable potential for aberration correction, since the medium-induced distortion can be estimated directly from the image data.

The image reconstruction algorithm of Ref. 18 was derived from the frequency-domain exact solution to the linearized inverse scattering problem, *i.e.*, diffraction tomography employing the Born approximation. Inverse scattering approaches based on the Born approximation form adequate images only for relatively small, weakly scattering objects,[18,20] so that this approximation has limited utility for large-scale imaging problems such as ultrasonic mammography. In the present paper, an aberration correction approach, which significantly extends the range of validity of the time-domain diffraction tomography method, is introduced. The reconstruction method of Ref. 18 is shown to result in an approximate solution to the time-domain linearized inverse scattering problem; application of aberration correction results in reconstructions that better approximate the solution to the full nonlinear time-domain inverse problem.

Two related methods for aberration correction are presented here. The first, suggested by the synthetic-aperture nature of the reconstruction algorithm, employs a focus correction approach in which delays are computed from estimates of the medium using an efficient straight-ray approximation. The second approach is suggested by examination of the reconstruction itself in the time domain, as in Ref. 21. In this approach, delays are applied directly to a time-dependent linearized reconstruction. Numerical results show that both methods increase the parameter range for which valid images can be obtained and illustrate differences in performance between the two.

II. THEORY

The imaging problem considered here concerns reconstruction of an unknown medium from far-field, time-domain scattering measurements. Solutions of this inverse problem are quantitative images of scattering media such as biological tissue. Below, the linearized inverse scattering problem (*e.g.*, quantitative ultrasonic imaging without aberration correction) is considered and shown to have no general solution. However, approximate solutions to the nonlinear inverse problem result in useful aberration correction methods for quantitative imaging.

A. The linearized time-domain inverse scattering problem

The time-domain inverse scattering problem analyzed below is defined as follows. A quiescent, inhomogeneous, fluid medium is subjected to an incident plane wave pulse propagating in the direction $\boldsymbol{\alpha}$,

$$p_{\mathrm{i}}(\mathbf{r},t) = u(t - \mathbf{r}\cdot\boldsymbol{\alpha}/c_0), \tag{1}$$

where c_0 is a reference or "background" sound speed. The medium is assumed to have spatially-varying sound speed, constant density, and no absorption, and to be completely characterized by a contrast function $\gamma(\mathbf{r})$, defined as

$$\gamma(\mathbf{r}) = \frac{c_0^2}{c(\mathbf{r})^2} - 1, \tag{2}$$

where $c(\mathbf{r})$ is the local sound speed at position $\mathbf{r}$. The inverse scattering problem is the determination of the medium contrast $\gamma(\mathbf{r})$ from time-domain measurements of the scattered field $p_{\mathrm{s}}(\boldsymbol{\theta},\boldsymbol{\alpha},t)$ for all measurement directions $\boldsymbol{\theta}$, incident-wave directions $\boldsymbol{\alpha}$, and times t. The implicit neglect of density variations is not severely limiting, since the contrast given by Eq. (2) dominates reconstructed images even in the presence of density variations.[18]

A general time-domain solution for the scattered acoustic pressure at a far-field measurement radius R, valid for two-dimensional (2D) or three-dimensional (3D) scattering, is then

$$p_s(\boldsymbol{\theta}, \boldsymbol{\alpha}, t) = \mathbf{F}^{-1}[\hat{p}_s(\boldsymbol{\theta}, \boldsymbol{\alpha}, f)] \equiv \int_{-\infty}^{\infty} \hat{p}_s(\boldsymbol{\theta}, \boldsymbol{\alpha}, f)\, e^{-i2\pi f t}\, df, \tag{3}$$

where $\hat{p}_s(\boldsymbol{\theta}, \boldsymbol{\alpha}, f)$ is a single frequency component of the scattered wavefield, given in the far field by

$$\begin{aligned} \hat{p}_s(\boldsymbol{\theta}, \boldsymbol{\alpha}, f) = \mathbf{F}[p_s(\boldsymbol{\theta}, \boldsymbol{\alpha}, t)] &\equiv \int_{-\infty}^{\infty} p_s(\boldsymbol{\theta}, \boldsymbol{\alpha}, t)\, e^{i2\pi f t}\, dt \\ &= k^2\, \Gamma(R, f) \int e^{-ik\boldsymbol{\theta}\cdot\mathbf{r}}\, \gamma(\mathbf{r}_0)\, \hat{p}_u(\mathbf{r}, \alpha, \omega)\, dV_0. \end{aligned} \tag{4}$$

In Eq. (4), k is the wavenumber ω/c_0 and $\hat{p}_u(\mathbf{r}_0, \boldsymbol{\alpha}, \omega)$ is the total frequency-domain acoustic pressure associated with an incident plane wave $\hat{u}(f)\, e^{ik\boldsymbol{\alpha}\cdot\mathbf{r}_0}$ [*i.e.*, one frequency component of the plane wave pulse $u(t - \boldsymbol{\alpha}\cdot\mathbf{r}/c_0)$]. The integral in Eq. (4) is taken over the entire support of γ in $\Re^2$ for 2D scattering or in $\Re^3$ for 3D scattering. The terms $\Gamma(R, f)$, which are associated with the far-field forms of the free-space Green's functions for the Helmholtz equation,[22] are

$$\begin{aligned} \Gamma(R, f) &= -\sqrt{\frac{i}{8\pi k R}} \quad \text{for 2D scattering and} \\ \Gamma(R, f) &= \frac{1}{4\pi r} \quad \text{for 3D scattering.} \end{aligned} \tag{5}$$

The time-domain inverse scattering problem is given by the Fourier inverse of Eq. (4):

$$p_s(\boldsymbol{\theta}, \boldsymbol{\alpha}, t) = \int_V \mathbf{L}\left[p_u\left(\mathbf{r}, \boldsymbol{\alpha}, t - \frac{R}{c_0} + \frac{\boldsymbol{\theta}\cdot\mathbf{r}}{c_0}\right)\right] \gamma(\mathbf{r})\, dV, \tag{6}$$

where $p_u(\mathbf{r}, \boldsymbol{\alpha}, t)$ is the total time-domain acoustic pressure associated with the incident plane wave $u(t - \mathbf{r}\cdot\boldsymbol{\alpha}/c_0)$ and the linear operator $\mathbf{L}$ is defined as

$$\begin{aligned} \mathbf{L}[p(\mathbf{r}, t)] &= \frac{1}{c_0^2}\mathbf{F}^{-1}\left[\sqrt{\frac{i}{8\pi k R}}\, \mathbf{F}\left[\ddot{p}(\mathbf{r}, t)\right]\right] \quad \text{for 2D scattering and} \\ \mathbf{L}[p(\mathbf{r}, t)] &= -\frac{1}{4\pi c_0^2 R}\, \ddot{p}(\mathbf{r}, \boldsymbol{\alpha}, t) \quad \text{for 3D scattering.} \end{aligned} \tag{7}$$

Eq. (6) defines a nonlinear inverse problem for the contrast $\gamma(\mathbf{r})$; the nonlinearity is associated with the dependence of $p(\mathbf{r}, \boldsymbol{\alpha}, t)$ on $\gamma(\mathbf{r})$.

The nonlinear time-domain inverse scattering problem defined by Eq. (6) can be linearized by invoking the Born approximation, in which the total acoustic pressure is approximated by the incident wave. The resulting linearized equation is

$$p_s(\boldsymbol{\theta}, \boldsymbol{\alpha}, t) = \int_V \mathbf{L}\Big[u\big(t - \tau(\boldsymbol{\theta}, \boldsymbol{\alpha}, \mathbf{r})\big)\Big]\, \gamma_L(\mathbf{r})\, dV, \tag{8}$$

where the true potential $\gamma(\mathbf{r})$ has been replaced by $\gamma_L(\mathbf{r})$, a hypothetical solution to the linearized inverse problem, and the propagation delay term $\tau(\boldsymbol{\theta}, \boldsymbol{\alpha}, \mathbf{r})$ is defined

$$\tau(\boldsymbol{\theta}, \boldsymbol{\alpha}, \mathbf{r}) \equiv \frac{R}{c_0} - \frac{(\boldsymbol{\theta} - \boldsymbol{\alpha}) \cdot \mathbf{r}}{c_0}. \tag{9}$$

The delay specified by Eq. (9) is precisely that required to refocus scattered waves through a homogeneous ($c = c_0$) medium onto each image point.

In the asymptotic weak scattering limit, the linearized inverse scattering problem (8) is equivalent to the original nonlinear problem (6), so that an exact solution for any waveform $u(t)$ is given by $\gamma_L(\mathbf{r}) \to \gamma(\mathbf{r})$ as $\gamma(\mathbf{r}) \to 0$. However, unlike the frequency-domain linearized inverse scattering problem, the inverse problem of Eq. (8) has no general solution for nonzero $\gamma(\mathbf{r})$. To prove this, one may examine the Fourier transform of Eq. (8), which is simply the linearization of Eq. (4):

$$\hat{p}_s(\boldsymbol{\theta}, \boldsymbol{\alpha}, f) = \Gamma(R, f)\, \hat{u}(f) \int e^{-ik(\boldsymbol{\theta}-\boldsymbol{\alpha})\cdot\mathbf{r}}\, \gamma_L(\mathbf{r})\, dV, \tag{10}$$

where k is the wavenumber $2\pi f / c_0$. Thus, any general time-independent solution of Eq. (8) must also be a frequency-independent solution to the linearized frequency-domain inverse scattering problem (10).

For $\boldsymbol{\theta} = \boldsymbol{\alpha}$ (the forward scattering case), Eq. (10) leads to the condition

$$\frac{\hat{p}_s(\boldsymbol{\theta}, \boldsymbol{\theta}, f)\, e^{-ikR}}{k^2\, \hat{u}(f)} = \frac{1}{4\pi R} \int \gamma_L(\mathbf{r})\, dV = \text{constant } (\forall f) \tag{11}$$

for existence of a general solution to Eq. (8). This requirement is easily seen by counterexample to be impossible. For example, Eq. (11) requires that, for all frequencies f, the magnitude of the forward scattered pressure should (for a unit-amplitude incident wave) be proportional to f^2. A counterexample is given by any high-contrast scatterer (*e.g.*, $\gamma \sim 1$), for which this f^2 dependence occurs only at very low frequencies, such that the scatterer's dimensions are much smaller than the wavelength c_0/f.[23] Thus, although the nonlinear time-domain inverse scattering problem has an exact solution (equal to the true contrast $\gamma(\mathbf{r})$), the corresponding linearized problem has no general solution for nonzero signal bandwidth except in the limiting case $\gamma \to 0$.

B. Approximate linearized solutions by Fourier synthesis

Although no solution $\gamma_L(\mathbf{r})$ to the quantitative imaging problem of Eq. (8) exists in general, one can still obtain approximate solutions by applying Fourier synthesis to the well-known exact solution of the frequency-domain linearized inverse scattering problem. For any frequency component of $p_s(\boldsymbol{\theta}, \boldsymbol{\alpha}, t)$, the frequency-domain linearized inverse problem (10) has an exact, frequency-dependent solution given by the frequency-domain filtered backpropagation formula[2,24]

$$\gamma_B(\mathbf{r}, f) = \frac{\hat{\mu}(f)\, e^{-ikR}}{\hat{u}(f)} \iint \Phi(\boldsymbol{\theta}, \boldsymbol{\alpha})\, \hat{p}_s(\boldsymbol{\theta}, \alpha, f)\, e^{ik(\boldsymbol{\theta}-\boldsymbol{\alpha})\cdot\mathbf{r}}\, dS_\alpha\, dS_\theta, \tag{12}$$

where

$$\begin{aligned} \hat{\mu}(f) &= \sqrt{\frac{kR}{8i\pi^3}}, \;\; \Phi(\boldsymbol{\theta}, \boldsymbol{\alpha}) = |\sin(\theta - \alpha)| \;\text{ in 2D, and} \\ \hat{\mu}(f) &= \frac{kR}{4\pi^3}, \;\; \Phi(\boldsymbol{\theta}, \boldsymbol{\alpha}) = |\boldsymbol{\theta} - \boldsymbol{\alpha}| \;\text{ in 3D.} \end{aligned} \tag{13}$$

Each surface integral in Eq. (12) is performed over the entire measurement circle for the 2D case and over the entire measurement sphere for the 3D case.

Fourier inversion of Eq. (10) into the time domain can be performed using the convolution theorem.[25] The result, with the hypothetical linearized solution $\gamma_L(\mathbf{r})$ replaced by the Born reconstruction $\hat{\gamma}_B(\mathbf{r}, f)$, is

$$p_s(\boldsymbol{\theta}, \boldsymbol{\alpha}, t) = -\frac{1}{4\pi c_0^2 R} \int \ddot{u}\Big(t - \tau(\boldsymbol{\theta}, \boldsymbol{\alpha}, \mathbf{r})\Big) \otimes \gamma_B(\mathbf{r}, t)\, dV, \tag{14}$$

where $\gamma_B(\mathbf{r}, t)$ is the inverse Fourier transform of the frequency-domain solution $\hat{\gamma}_B(\mathbf{r}, f)$. The time-domain reconstruction $\gamma_B(\mathbf{r}, t)$ is an exact solution of the integral equation (14), which is similar but not equivalent to the linearized time-domain inverse scattering problem of Eq. (8). Because $\hat{\gamma}_B(\mathbf{r}, f)$ is conjugate symmetric, the time-domain potential $\gamma_B(\mathbf{r}, t)$ is purely real.[21]

Comparison of Eqs. (8) and (14) shows that, in the weak scattering limit,

$$\gamma_B(\mathbf{r},t) \to \gamma(\mathbf{r})\,\delta(t) + \psi(\mathbf{r},t), \tag{15}$$

where $\psi(\mathbf{r},t)$ is a "nonradiating source"[26] that satisfies the constraint

$$\int_V \ddot{u}\Big(t - \tau(\boldsymbol{\theta},\boldsymbol{\alpha},\mathbf{r})\Big) \otimes \psi(\mathbf{r},t)\,dV = 0. \tag{16}$$

The presence of the nonradiating source term $\psi(\mathbf{r},t)$ is consistent with the nonuniqueness of solutions to Eq. (14).[27] For example, additional solutions to Eq. (14) include the class of functions $\gamma_B(\mathbf{r},t) + \phi(\mathbf{r})$, where $\phi(\mathbf{r})$ is the inverse Fourier transform of any function $\Phi(\mathbf{k})$ that is zero inside the Ewald sphere,[1] defined for the upper frequency limit of the incident pulse as $\mathbf{k} \leq 4\pi f_h/c_0$, where f_h is the upper limit of the pulse frequency content.

A straightforward approach to estimate $\gamma_B(\mathbf{r},t)$ (and thus $\gamma(\mathbf{r})$) is to perform inverse Fourier transformation on the frequency-domain Born inversion $\hat{\gamma}_B(\mathbf{r},f)$. A natural estimate of the medium contrast is a reconstruction employing information from multiple frequencies contained in the incident pulse, *e.g.*,

$$\gamma_v(\mathbf{r},t) = \int \hat{\gamma}_B(\mathbf{r},f)\,\hat{v}(f)\,e^{-2\pi i f t}\,df \Big/ \int \hat{v}(f)\,df \tag{17}$$

$$= \gamma_B(\mathbf{r},t) \otimes v(t) \big/ v(0) \tag{18}$$

$$\approx \gamma(\mathbf{r})\,v(t) \big/ v(0), \tag{19}$$

where the final expression results from Eq. (15). The frequency weight $\hat{v}(f)$ must be integrable and have no support outside the support of $\hat{u}(f)$, but is otherwise arbitrary. The time dependence of the reconstructed contrast can be removed from Eq. (19) by setting $t = 0$ (called the "imaging condition" in Ref. 28).

If the incident waveform is sinusoidal, so that, for instance, $\hat{u}(f) = \delta(f - f_0) + \delta(f + f_0)$, the reconstructed potential $\gamma_v(\mathbf{r},0)$ is equal to the real part of the frequency-domain solution $\hat{\gamma}_B(\mathbf{r},f_0)$. Thus, $\gamma_v(\mathbf{r},0)$ is an exact solution of the linearized inverse problem in the single-frequency limit. However, as proven above, no time-independent reconstruction can solve the general linearized time-domain inverse scattering problem, so that $\gamma_v(\mathbf{r},0)$ is only an *approximate* solution for any nonzero-bandwidth incident waveform $u(t)$.

The Fourier inversion of Eq. (17) can be performed either numerically or analytically. Numerical inversion, using frequency-domain reconstructions at a number of discrete frequencies within the bandwidth of the incident pulse, was the approach employed by Lin, Nachman, and Waag.[21] (However, the frequency-domain inversions of Ref. 21 were performed using eigenfunctions of the far-field scattering operator[29] instead of filtered backpropagation.) Alternatively, particular choices of the weight $\hat{v}(f)$ allow analytic inversion of the frequency-domain reconstruction $\gamma_B(\mathbf{r}, f)$ into the time domain, resulting in a simple delay-and-sum formula. For the weight $\hat{v}(f) = \hat{u}(f)/\hat{\mu}(f)$, the resulting formula is

$$\gamma_v(\mathbf{r}, t) = \mathrm{Re}\left[\frac{1}{N} \iint \Phi(\boldsymbol{\theta}, \boldsymbol{\alpha}) \, \left(p_s(\boldsymbol{\theta}, \alpha, \tau) + i\mathbf{H}^{-1}\left[p_s(\boldsymbol{\theta}, \alpha, t + \tau)\right]\right) \, dS_\alpha \, dS_\theta\right], \tag{20}$$

where

$$N = 2 \int_0^\infty \frac{\hat{u}(f)}{\hat{\mu}(f)} \, df, \tag{21}$$

τ is given by Eq. (9), and $\mathbf{H}^{-1}$ is the inverse Hilbert transform operator (quadrature filter).

The reconstruction formula of Eq. (20) is identical to that derived in Ref. 18 and similar to that derived in Ref. 30. In view of the present derivation, these previous methods are understood to provide approximate solutions to the linearized time-domain inverse scattering problem (8).

C. Aberration-corrected solutions

The form of the approximate linearized solution derived above suggests possible approaches to improvement of images beyond the limits of the Born approximation.

First, one may observe that the reconstruction formula of Eq. (20) synthetically focuses the time-domain scattered field back onto each point in the medium.[18] This observation leads to the idea of aberration correction by iterative refinement of the focus quality. Since the reconstruction provides an estimate of the medium itself, this refinement is fairly straightforward. One simple implementation employs an assumption that background inhomogeneities result only in cumulative delays (or advances) of the incident and scattered wavefronts, so that the total delay for an angle ϕ and a point position $\mathbf{r}$ is given by

$$\delta\tau(\boldsymbol{\phi}, \mathbf{r}) = \int_{\xi} c(\boldsymbol{\xi})^{-1}\, d\xi - \frac{R}{c_0} \tag{22}$$

where the integral is performed along the line that joins the spatial points $\mathbf{r}$ and $R\boldsymbol{\phi}$, Aberration-corrected reconstructions can then be performed using Eq. (20) with τ replaced by the corrected delay term

$$\tau \to R/c_0 + \frac{(\boldsymbol{\alpha} - \boldsymbol{\theta}) \cdot \mathbf{r}}{c_0} + \delta\tau(\boldsymbol{\alpha}, \mathbf{r}) + \delta\tau(\boldsymbol{\theta}, \mathbf{r}) \tag{23}$$

and by then computing $\gamma_v(\mathbf{r}, 0)$ using Eq. (20).

An alternative approach to aberration correction is motivated by the observation, made in Ref. 21, that temporal delays from wave propagation in the inhomogeneous medium result in corresponding delays to the time-domain reconstruction of Eq. (17). That is, the reconstructed waveforms $\gamma_v(\mathbf{r}, t)$ may be delayed or advanced relative to the waveform $v(t)$. In Ref. 21, correction for this temporal aberration was implemented by adaptive demodulation of $\gamma_v(\mathbf{r}, t)$ from the weighting waveform $v(t)$. Here, envelope detection is applied to $\gamma_v(\mathbf{r}, t)$ and the time of maximum envelope amplitude $t_{\max}$ is found for each point $\mathbf{r}$, resulting in the aberration-corrected reconstruction

$$\gamma(\mathbf{r}) \approx \gamma_v\Big(\mathbf{r}, t_{\max}(\mathbf{r})\Big). \tag{24}$$

Envelope detection can also be applied to iterative reconstructions obtained using the focus correction given by Eq. (22).

III. COMPUTATIONAL METHODS

The present aberration correction methods have been tested using simulated scattering data for a number of two-dimensional test objects. The computational configuration was chosen to mimic the characteristics of an available 2048-element ring transducer.[31] The time-domain waveform employed for all the computations reported here was

$$u(t) = \cos(\omega_0 t)\, e^{-t^2/(2\sigma^2)}, \tag{25}$$

where $\omega_0 = 2\pi f_0$ for a center frequency of f_0, taken here to be 2.5 MHz, and σ is the temporal Gaussian parameter. The value of σ chosen here was 0.25, which corresponds to a −6 dB bandwidth of 1.5 MHz.

For 2D cylindrical inhomogeneities, the frequency-domain scattered field $\hat{p}_s(\boldsymbol{\theta}, \boldsymbol{\alpha}, \omega)$ was computed using an exact series solution[32] for each frequency component of interest. In implementation of the series solution, summations were truncated when the magnitude of a single coefficient dropped below 10^{-12} times the sum of all coefficients. These single-frequency solutions, which correspond to Fourier coefficients of the time-domain scattered field, were weighted and inverted by discrete Fourier transform to obtain the exact time-domain scattered field associated with the incident pulse of Eq. (25). Scattering from cylinders of radius 4.0 mm and contrasts ranging from $\gamma = 0.001$ to $\gamma = 0.14$ was computed on a measurement circle of radius 176 mm for 384 incident-wave directions and 96 measurement directions. The sampling rate employed was 9.14 MHz.

Solutions were also obtained for a large-scale breast model using a time-domain k-space method.[33] The breast model was obtained by image processing a coronal cross section of three-dimensional photographic data from the Visible Human Female data set with a pixel size of 0.333 mm. Hue, saturation, and value were mapped to sound speed and density using empirically determined relations; sound speed and density were assumed to be linearly proportional.[34] Sound speed and density maps were smoothed using a Gaussian filter to reduce artifacts associated with the slicing process. The tissue map employed is shown in

Fig. 3. This tissue model was scaled down by a factor of 0.6 from the original data set and mapped onto a grid of 512 × 512 points with a spatial step of 0.111 mm. A time step of 0.0546 μs, corresponding to a Courant-Friedrichs-Lewy number of 0.75, was employed. Based on the scaling of the tissue model, the scattered field obtained is equivalent to that of the full-scale breast model (largest dimension 75 mm) for a center frequency of 0.5 MHz.

Scattered acoustic pressure signals were recorded at a sampling rate of 9.15 MHz for 128 incident-wave directions. A circle of 512 simulated point receivers, which had a radius of 9.0 mm in these computations, completely contained the scaled-down breast model. Farfield waveforms were computed by Fourier transforming the time-domain waveforms on the nearfield measurement circle, transforming these to farfield waveforms for each frequency using a numerically exact transformation method,[21,35] and performing inverse Fourier transformation to yield time-domain farfield waveforms at a measurement circle of radius 234 cm. All forward and inverse temporal Fourier transforms, as well as angular transforms occurring in the nearfield-farfield transformation, were performed by fast Fourier transforms (FFT).[36]

The time-domain imaging method was directly implemented using Eq. (20), evaluated using straightforward numerical integration over all incident-wave and measurement directions employed. In one implementation, similar to that from Ref. 18, images were evaluated only for the time $t = 0$. In this case, before evaluation of the argument τ for each signal, the time-domain waveforms were resampled at a sampling rate of 16 times the original rate. This resampling was performed using FFT-based Fourier interpolation. The inverse Hilbert transform was implicitly performed using the same FFT operation. Values of the pressure signals at the time τ were then determined using linear interpolation between samples of the resampled waveforms. The integrals of Eq. (20) were implemented using discrete summation over all transmission and measurement directions employed.

In the implementation of reconstructions for multiple times, storage and computation time requirements necessitated modification of the algorithm implementation. For multiple-time reconstructions, a reconstruction of $\gamma_v(\mathbf{r}, t)$ at the sampling rate of the scattering data was first obtained by direct integration. Delays of the time-domain scattered waveforms were implemented using cubic spline interpolation.[37] Reconstructions were performed for an interval of length 2.4 μs, multiplied by a window with cosine tapers of length 0.6 μs at each end, and upsampled by a factor of eight using Fourier interpolation. Inverse Hilbert transformation of $\gamma_v(\mathbf{r}, t)$ was performed by the same FFT operation used to implement the Fourier interpolation. Finally, the temporal position of the envelope peak was found from the zero crossing of the envelope derivative,

$$\frac{\partial \left|\gamma_v(\mathbf{r}, t_{\text{peak}}) + i\,\mathrm{H}^{-1}[\gamma_v(\mathbf{r}, t_{\text{peak}})]\right|}{\partial t} = 0. \tag{26}$$

The derivative in Eq. 26 was evaluated using a second-order-accurate center-difference scheme.

Focus correction was implemented using a straight-ray approximation, which is based on the assumption that background inhomogeneities result only in cumulative delays (or advances) of the incident and scattered wavefronts. In this approximation, the total delay for an image position $\mathbf{r}$ and a direction $\boldsymbol{\phi}$ is given by Eq. (22) and aberration-corrected reconstructions are performed using Eq. (20) with τ replaced by the corrected delay term of Eq. (23). The path integrals of Eq. (23) were performed using an algorithm based on the digital differential analyzer (DDA) image processing method.[38] This method very efficiently finds the nearest neighbors to a line of specified starting position and slope; thus, the integrals can be evaluated by simple summation without any need for interpolation. Since the reconstruction process acts in part as a low-pass filter, the integral performed using nearest neighbors to the line of interest is sufficiently accurate.

Iterative focus correction was performed by first constructed an uncorrected image, either for $t = 0$ or $t = t_{\text{peak}}$. The reconstructed sound speed was then employed to evaluate the delay corrections of Eq. (23) using the DDA implementation of the integrals from Eq. (22). To avoid spurious modification of image points outside the support of the scatterer, the delay term of Eq. (23) was multiplied by the factor

$$A = \begin{cases} 1, & |\gamma_v(\mathbf{r})| \geq \gamma_{\max}/2 \\ (1 - \cos[2\pi\,|\gamma_v(\mathbf{r})|\,/\gamma_{\max}])/2, & |\gamma_v(\mathbf{r})| < \gamma_{\max}/2, \end{cases} \tag{27}$$

where γ_{max} is the maximum value of $|\gamma_v(\mathbf{r})|$ for the previous reconstruction and the temporal criterion ($t = 0$ or $t = t_{\text{peak}}$) employed.

Iteration proceeded as follows. A new reconstruction was compared to the previous reconstruction; if the relative RMS error between the two was greater than 5%, further iterations were carried out up to a prescribed maximum number of iterations, taken here to be 20. Due to the efficiency of the delay computation, each iteration required about the same computation time as the original reconstruction.

IV. NUMERICAL RESULTS

The performance of aberration-corrected time-domain diffraction tomography imaging, using the two approaches introduced above, is illustrated by the numerical examples presented in this section.

Figure 1 shows reconstructions of a homogeneous cylinder with a radius of 4 mm and a contrast $\gamma = 0.08$. For the center frequency of 2.5 MHz, this corresponds to a nondimensional radius $ka = 41.2$. Panel (a) shows cross sections of reconstructions obtained using the $t = 0$ criterion. The "0" curve refers to an uncorrected (Born approximation) reconstruction, while curves labeled "1" and higher correspond to subsequent iterations of focus correction performed using the delay correction of Eq. (23) as described in the Computational Methods section. Panel (b) shows corresponding cross sections obtained using the $t = t_{\text{peak}}$ criterion. One may observe that iterative focus correction greatly improves reconstructions for the $t = 0$ criterion. The initial (Born) reconstruction shows mainly the edges of the cylinder; further iterations improve the accuracy within the cylinder interior. This process somewhat resembles the inverse scattering method of layer stripping,[39,40] in which an unknown medium is iteratively reconstructed with each iteration probing further into the medium interior.

In contrast, iterative focus correction provides little, if any, improvement to the reconstructions obtained using the $t = t_{\text{peak}}$ criterion [Fig. 1(b)]. In this case, the initial reconstruction captures the cylinder interior very well. Further iterations slightly increase the reconstructed contrast near the edges, but also introduce artifacts not present in the initial reconstruction. After convergence, the reconstructed value is more accurate than the $t = 0$ image for the cylinder edges but less accurate for the interior.

For the reconstructions shown in Fig. 1, images of size 128 × 128 pixels were computed from time-domain scattering data for 96 incident-wave directions and 384 measurement directions. The computation time required on a 650 Mhz Athlon processor was about 6 CPU minutes per iteration for the $t = 0$ image criterion (about 38 minutes total for the six iterations performed) and about 45 CPU minutes per iteration for the $t = t_{\text{peak}}$

criterion.

The relative performance of iterative focus correction using the two image criteria is illustrated in Fig. VI. Here, reconstructions were based on exact scattering data for a 4 mm cylinder with contrast $0.01 \leq \gamma \leq 0.12$. Since previous studies have shown that the accuracy of diffraction tomography reconstructions is roughly a function of the nondimensional parameter $ka \cdot \gamma$,[18,20] the relative error is plotted as a function of this nondimensional parameter. The Born approximation is considered to provide useful images for cylinders up to $ka \cdot \gamma \sim 2$;[18,20] by this standard, the iterative focus correction implemented here increases the upper limit of validity for $t = 0$ images to $ka \cdot \gamma \sim 4$. As in Fig. 1, iterative focus correction is seen to provide little improvement in accuracy for images obtained using the $t = t_{\text{peak}}$ criterion. The quantitative accuracy of reconstructions is slightly increased by iteration for large values of the parameter $ka \cdot \gamma$, but can be slightly diminished for smaller values. Also notable is that iteration using the $t = 0$ criterion fails completely above $ka \cdot \gamma \sim 4$, while the $t = t_{\text{peak}}$ criterion reaches a comparable error level around $ka \cdot \gamma \sim 4$ and then increases gradually in error with increasing scatterer contrast.

Quantitative images of a large-scale 2D breast model, used to generate simulated scattering data in the manner described in the Numerical Methods section, are shown in Figs. 3 and 4. Panel (a) of Fig. 3 shows the 2D model used to generate the synthetic data. Panel (b) of Fig. 3 shows the image reconstructed using the $t = t_{\text{peak}}$ criterion without any focus correction. In this case, the reconstructed image appears to be artifactually sharpened compared to the original model. Although there is a close correspondence between most features of the model and the reconstruction, some differences exist. For example, the reconstructed skin thickness is significantly smaller than that of the actual model in several locations.

Reconstructions of the 2D breast model, obtained using the $t = 0$ criterion and iterative focus correction, are shown in Fig. 4. In this case, the initial (Born) reconstruction renders the skin layer fairly well, but the interior of the breast model is reconstructed poorly. Subsequent iterations improve the rendering of the connective and glandular tissue structure within the breast. Both focus quality and quantitative accuracy of the reconstructions improve with iteration. The converged reconstruction (iteration 5) resembles a low-pass filtered version of the original model [Fig. 3(a)] except for a small area of spuriously high reconstructed contrast within the interior glandular tissue.

For the large-scale 2D breast model, computation times required for 256 × 256 pixel images, 128 incident-wave directions, and 512 measurement directions were about 1.3 CPU hours per iteration for the $t = 0$ image criterion (8.0 hours for the six iterations up to convergence) and about 4.6 CPU hours for the initial reconstruction using the $t = t_{\mathrm{peak}}$ criterion.

V. DISCUSSION

The two abberation correction methods considered here may be compared as follows. Both methods have the effect of improving the alignment of the time-domain reconstruction $\gamma_v(\mathbf{r}, t)$. In the case of $t = 0$ images with adaptive focus correction, the time-domain reconstruction is implicitly aligned by compensation for propagation delay within the inhomogeneous medium. The $t = t_{\text{peak}}$ criterion can be thought of as an explicit alignment of the time-domain reconstruction.

Previous qualitative studies of the validity of the Born approximation[18,20] have established a threshold for valid Born reconstructions at $ka \cdot \gamma \sim 2$, which corresponds to a normalized RMS error of about 0.5 [Fig. VI]. Given this somewhat arbitrary threshold for the maximum allowable error, both aberration correction methods employed here have a similar range of validity, up to about $ka \cdot \gamma \sim 4$. Thus, either approach extends the parametric range of validity for time-domain diffraction tomography by about a factor of two.

Each image criterion also introduces characteristic artifacts. The $t = 0$ criterion with adaptive focusing acts in part as a low-pass filter to reconstructions, consistent with the well-known low-pass filtering effect of conventional diffraction tomography.[1] The $t = t_{\text{peak}}$ criterion introduces edge artifacts that have the qualitative effect of erroneously sharpening images. Still, notable is that adaptive demodulation from the waveform $v(t)$, as employed in Ref. 21, may provide more robust reconstruction quality, particularly for scattering data corrupted by noise.

The $t = 0$ image criterion can provide faster reconstructions, since the reconstructed contrast $\gamma_v(\mathbf{r}, t)$ needs only to be evaluated for one time. However, for large or high-contrast scatterers, iterative aberration correction is necessary to obtain high-quality reconstructions. The $t = t_{\text{peak}}$ criterion requires longer computation time for each reconstruction; however, because this criterion implicitly incorporates a form of aberration correction, subsequent iterations provide little additional benefit. As a result, computation times required for a given level of accuracy can be comparable for either image criterion.

Notable is that reconstruction quality, as characterized by criteria such as the point-spread function of a quantitative image, can be improved by optimization of the weight $\hat{v}(f)$.[21] Although the delay-and-sum reconstruction formula (20) depends on a frequency weight determined by the incident waveform $u(t)$, any desired weight $\hat{v}(f)$ can still be applied by preprocessing of the scattering data. That is, the inverse problem associated with an arbitrary incident waveform $w(t)$ (such as the impulse response of a particular electroacoustic transducer) can be transformed into the inverse problem associated with a desired waveform $u(t)$ by applying the deconvolution operation

$$[p_s(\boldsymbol{\theta}, \boldsymbol{\alpha}, t)]_{u(t)} = \mathbf{F}^{-1}\left[\frac{\hat{u}(f)}{\hat{w}(f)}\,\mathbf{F}\,[p_s(\boldsymbol{\theta}, \boldsymbol{\alpha}, t)]_{w(t)}\right], \tag{28}$$

where $\mathbf{F}$ denotes temporal Fourier transformation, to the measured scattering data. This operation transforms the measured data into the corresponding data that would be measured using an optimal incident pulse $u(t)$. For reasons of stability, the effective bandwidth of $\hat{u}(f)$ should be comparable to that of $\hat{w}(f)$ (as determined, for instance, by the noise floor of a given measurement).

The adaptive focusing implemented here employed a simple straight-ray approximation for wavefront aberration incurred in tissue. However, the principle of aberration correction by adaptive focusing should allow greater improvements to be gained using more complete distortion models. For example, the distortion caused by a strongly-scattering medium can be accurately modeled using a full-wave computational method such as that of Ref. 33. In principle, appropriate deconvolution could be employed to remove the effects of the intervening medium for each incident-wave direction, measurement direction, and image location, so that an aberration-corrected reconstruction could then be performed by applying Eq. (20) the corrected scattering data. In some cases, *a priori* information on the scattering medium may be exploited to improve the convergence of such adaptive focusing algorithms. This basic approach, in which a linearized reconstruction is performed on scattering data that has been transformed to remove higher-order scattering effects, is common to a number of existing nonlinear inverse scattering methods.[41]

The methods of aberration correction proposed here differ from most adaptive imaging methods for pulse-echo ultrasound (*e.g.*, Refs. 12 and 16) because adaptive focusing is performed using a direct reconstruction of the medium rather than a simpler distortion estimate. Thus, aberration correction using quantitative imaging methods could be of great interest for pulse-echo systems such as current clinical scanners. However, the limited spatial-frequency information provided in pulse-echo mode[1,18] reduces the quality of quantitative images of this kind. One possible approach to increasing the spatial-frequency content of pulse-echo quantitative images could be to apply deconvolution to the scattered signals.[42–44] If such deconvolution methods could increase the spatial-frequency coverage sufficiently to obtain accurate (although possibly low-resolution) quantitative sound-speed maps, such maps could be employed directly for adaptive focusing in pulse-echo images.

VI. CONCLUSIONS

Two related approaches to aberration correction for quantitative ultrasonic imaging have been presented. These methods are based on approximate solutions to the linearized time-domain inverse scattering problem, implemented using adaptations of two previous time-domain diffraction tomography methods.[18,21] One approach, based on a delay-and-sum reconstruction formula, applies adaptive focusing based on estimates of the scattering medium. The other approach implements aberration correction by applying appropriate delays to a time-dependent reconstruction.

Numerical results show that each of the considered aberration correction approaches increases the parametric range of validity for time-domain diffraction tomography by about a factor of two. The extended range of validity is sufficient to allow effective quantitative imaging of large-scale scattering media, such as the 75 mm breast model imaged here at 0.5 MHz. Adaptive focusing correction based on more complete scattering models could further increase this range of validity. Given sufficient *a priori* information on the unknown medium, the principle of focus correction may allow accurate quantitative images to be obtained for strongly-scattering media at larger scales and higher frequencies.

The approaches presented here may also be useful for aberration correction in pulse-echo imaging. If sufficiently broadband information can be extracted from pulse-echo scattering data, the time-domain diffraction tomography methods considered here may allow quantitative tissue characterization using clinically convenient measurement configurations. Quantitative maps obtained in this manner would also be useful as medium models for aberration correction in conventional b-scan and synthetic-aperture imaging.

ACKNOWLEDGMENTS

This work was supported by the Breast Cancer Research Program of the U.S. Army Medical Research and Materiel Command under Grant DAMD17-98-1-8141. Any opinions, findings, conclusions, or recommendations expressed in this publication are those of the author and do not necessarily reflect the views of the U.S. Army. The author is grateful for helpful discussions with James F. Kelly, Adrian I. Nachman, Feng Lin, and Robert C. Waag.

REFERENCES

[1] E. Wolf, "Three-dimensional structure determination of semi-transparent objects from holographic data," Optics Comm. **1**, 153–156 (1969).

[2] A. J. Devaney, "Inversion formula for inverse scattering within the Born approximation," Opt. Lett. **1**, 111–112 (1982).

[3] D. T. Borup, S. A. Johnson, W. W. Kim, and M. J. Berggren, "Nonperturbative diffraction tomography via Gauss-Newton iteration applied to the scattering integral equation," Ultrason. Imag. **14**, 69–85 (1992).

[4] S. Gutman and M. Klibanov, "Two versions of quasi-Newton method for multidimensional inverse scattering problem," J. Comp. Acoust. **1**, 197–228 (1993).

[5] L. M. Hinkelman, D.-L. Liu, R. C. Waag, Q. Zhu, and B. D. Steinberg, "Measurement and correction of ultrasonic pulse distortion produced by the human breast," J. Acoust. Soc. Am. **97**(3), 1958–1969 (1995).

[6] T. D. Mast, L. M. Hinkelman, M. J. Orr, V. W. Sparrow, and R. C. Waag, "Simulation of ultrasonic pulse propagation through the abdominal wall," J. Acoust. Soc. Am. **102**, 1177–1190 (1997). [Erratum: J. Acoust. Soc. Am. **104**, 1124–1125 (1998).]

[7] L. M. Hinkelman, T. D. Mast, L. A. Metlay, and R. C. Waag, "The effect of abdominal wall morphology on ultrasonic pulse distortion. Part I: Measurements," J. Acoust. Soc. Am. **104**, 3635–3649 (1998).

[8] J. Ylitalo, E. Alasaarela, and J. Koivukangas, "Ultrasound holographic B-scan imaging," IEEE Trans. Ultrason. Ferrolectr. Freq. Contr. **36**, 376–383 (1989).

[9] K. E. Thomenius, "Evolution of ultrasound beamformers," Proc. IEEE Ultrason. Symp. **2**, 1615–1622 (1996).

[10] S. W. Smith, G. E. Trahey, and O. T. von Ramm, "Phased array ultrasound imaging through planar tissue layers," Ultrasound in Med. and Biol. **12**(3) 229–243 (1986).

[11] G. Kossoff, D. A. Carpenter, D. E. Robinson, D. Ostry, and P. L. Ho, "A sonographic technique to reduce beam distortion by curved interfaces," Ultrasound in Med. and Biol. **15**(4), 375–382 (1989).

[12] M. O'Donnell and S. W. Flax, "Phase-aberration correction using signals from point reflectors and diffuse scatterers: Measurements," IEEE Trans. Ultrason. Ferroelect. Freq. Control **35**(6), 768–774 (1988).

[13] L. Nock, G. E. Trahey, and S. W. Smith, "Phase aberration correction in medical ultrasound using speckle brightness as a quality factor," J. Acoust. Soc. Am. **85**(5), 1819–1833 (1989).

[14] D. Rachlin, "Direct estimation of aberrating delays in pulse-echo imaging systems," J. Acoust. Soc. Am. **88**(1), 191–198 (1990).

[15] M. Hirama, O. Ikeda, and T. Sato, "Adaptive ultrasonic array imaging through an inhomogeneous layer," J. Acoust. Soc. Am. **71**(1), 100–109 (1982).

[16] D.-L. Liu and R. C. Waag, "Correction of ultrasonic wavefront distortion using backpropagation and a reference waveform method for time-shift compensation," J. Acoust. Soc. Am. **96**(2), 649–660 (1994).

[17] C. Dorme and M. Fink, "Ultrasonic beam steering through inhomogeneous layers with a time reversal mirror," IEEE Trans. Ultrason. Ferroelect. Freq. Control **43**(1), 167–175 (1996).

[18] T. D. Mast, "Wideband quantitative ultrasonic imaging by time-domain diffraction tomography," J. Acoust. Soc. Am. **106**, 3061–3071 (1999).

[19] T. D. Mast, F. Lin, and R. C. Waag, "Time-domain ultrasound diffraction tomography," *1999 IEEE Ultrasonics Symposium Proceedings*, Vol. 2, pp. 1617–1620.

[20] M. Slaney, A. C. Kak, and L. E. Larsen, "Limitations of imaging with first-order diffraction tomography," IEEE Trans. Microwave Theory Tech. **32**, 860–874 (1984).

[21] F. Lin, A. I. Nachman, and R. C. Waag, "Quantitative imaging using a time-domain eigenfunction method," J. Acoust. Soc. Am. **108**, 899–912 (2000).

[22] P. M. Morse and H. Feshbach, *Methods of Theoretical Physics* (New York: McGraw-Hill, 1953), v. I, ch. 7.

[23] Allan D. Pierce, *Acoustics: an Introduction to its Physical Principles and Applications*, 2nd Edition (Woodbury, New York: Acoustical Society of America, 1989), ch. 9.

[24] G. Beylkin, "The fundamental identity for iterated spherical means and the inversion formula for diffraction tomography and inverse scattering," J. Math. Phys. **24**, 1399–1400 (1983).

[25] C. Gasquet and P. Witomski, *Fourier Analysis and Applications: Filtering, Numerical Computation, Wavelets* (New York, Springer-Verlag, 1999).

[26] K. Kim and E. Wolf, "Non-radiating monochromatic sources and their fields," Opt. Comm. **59**, 1–6 (1986).

[27] N. Bleistein and J. K. Cohen, "Nonuniqueness in the inverse source problem in acoustics and electromagnetics," J. Math Phys. **18**, 194–201 (1977).

[28] T. Melamed, Y. Ehrlich and E. Heymann, "Short-pulse inversion of inhomogeneous media: a time-domain diffraction tomography," Inverse Problems **12**, 977–993 (1996).

[29] T. D. Mast, A. I. Nachman, and R. C. Waag, "Focusing and imaging using eigenfunctions of the scattering operator," J. Acoust. Soc. Am. **102**, 715–725 (1997).

[30] V. A. Burov and O. D. Rumyantseva, "Linearized inverse problem of scattering in monochromatic and pulse modes," Acoustical Physics **40**, 34–42 (1996).

[31] T. T. Jansson, T. D. Mast, and R. C. Waag, "Measurements of differential scattering cross section using a ring transducer," J. Acoust. Soc. Am. **103**, 3169–3179 (1998).

[32] P. M. Morse and K. U. Ingard, *Theoretical Acoustics* (New York, McGraw-Hill, 1968), ch. 8.

[33] T. D. Mast, L. P. Souriau, D.-L. Liu, M. Tabei, A. I. Nachman, and R. C. Waag, "A k-space method for large-scale models of wave propagation in tissue," IEEE Trans. Ultrason., Ferroelect., Freq. Contr. **48**, 341–354 (2001).

[34] T. D. Mast, "Empirical relationships between acoustic parameters in human soft tissues," Acoustics Research Letters Online **1**, 37–42 (2000).

[35] S. Wang, "Finite-difference time-domain approach to underwater acoustic scattering problems," J. Acoust. Soc. Am. **99**, 1924–1931 (1996).

[36] M. Frigo and S. G. Johnson, "FFTW: An adaptive software architecture for the FFT," *Proceedings of the ICASSP*, vol. 3, pp. 1381–1384, 1998.

[37] W. H. Press, S. A. Teukolsky, W. T. Vetterling, and B. P. Flannery, *Numerical Recipes in Fortran* (New York, Cambridge University Press, 1986), ch. 3.3.

[38] D. F. Rogers, *Procedural Elements for Computer Graphics* (Boston, McGraw-Hill, 1998), ch. 2.

[39] A. E. Yagle and B. C. Levy, "Layer-stripping solutions of multidimensional inverse scattering problems," J. Math. Phys. **27**, 1701–1710 (1986).

[40] Y. Chen, "Inverse scattering via skin effect," Inverse Problems **13**, 647–667 (1997).

[41] R. Snieder, "A perturbative analysis of non-linear inversion," Geophys. J. Int. **101**, 545–556 (1990).

[42] J. A. Jensen and S. Leeman, "Nonparametric estimation of ultrasound pulses," IEEE Trans. Biomed. Eng. **41**, 929–936 (1994).

[43] P. Lasaygues and J.-P. Lefebvre, "Improvement of resolution in ultrasonic reflection tomography," The e-Journal of Nondestructive Testing, **3**(8) (1998) [http://www.ndt.net/].

[44] O. Husby, T. Lie, T. Lango, J. Hokland, and H. Rue, "Bayesian 2-D deconvolution: a model for diffuse ultrasound scattering," IEEE Trans. Ultrason., Ferroelect., Freq. Control **48** 121–130 (2001).

FIGURES

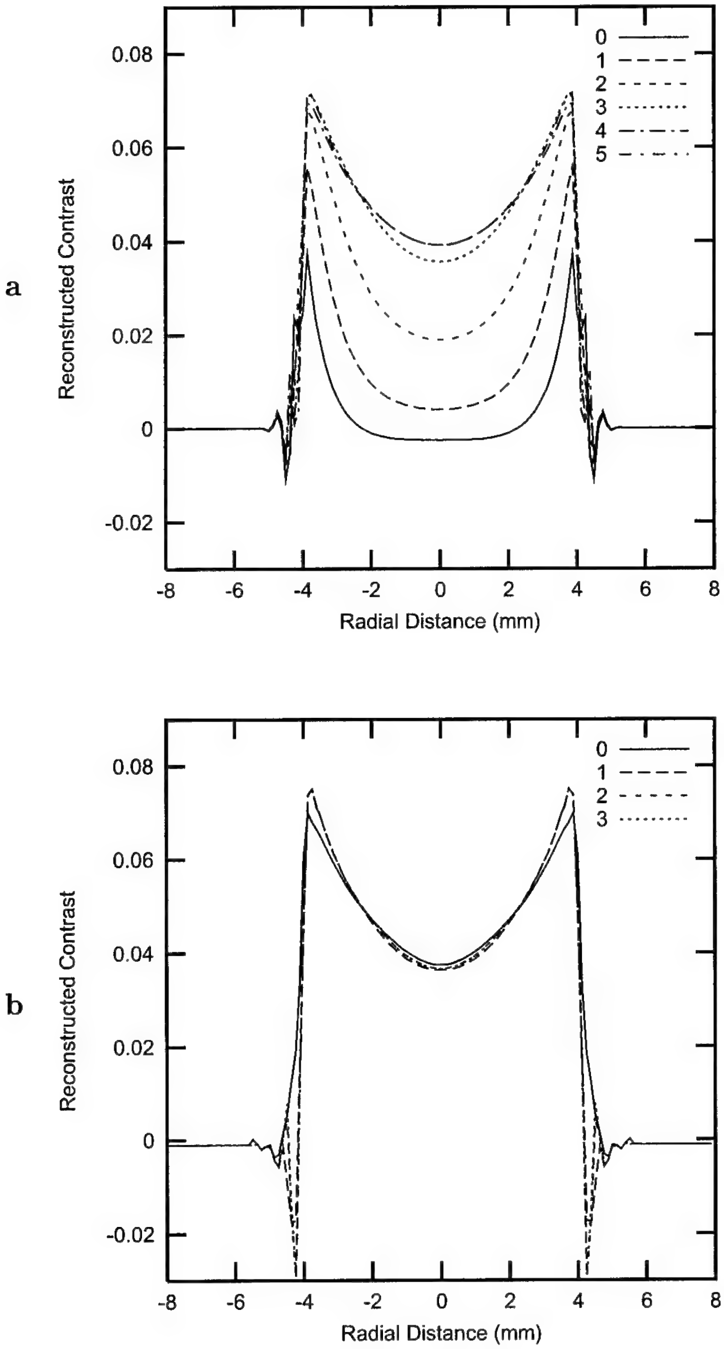

FIG. 1. Cross sections of time-domain reconstructions with adaptive focus correction for both imaging criteria. Reconstructions are of a homogeneous cylinder with a radius of 4 mm ($ka = 41.2$) and a contrast $\gamma = 0.08$. In each case, the "0" curve refers to an uncorrected reconstruction, while curves labeled "1" and higher correspond to subsequent iterations of focus correction. (a) $t = 0$. (b) $t = t_{\text{peak}}$.

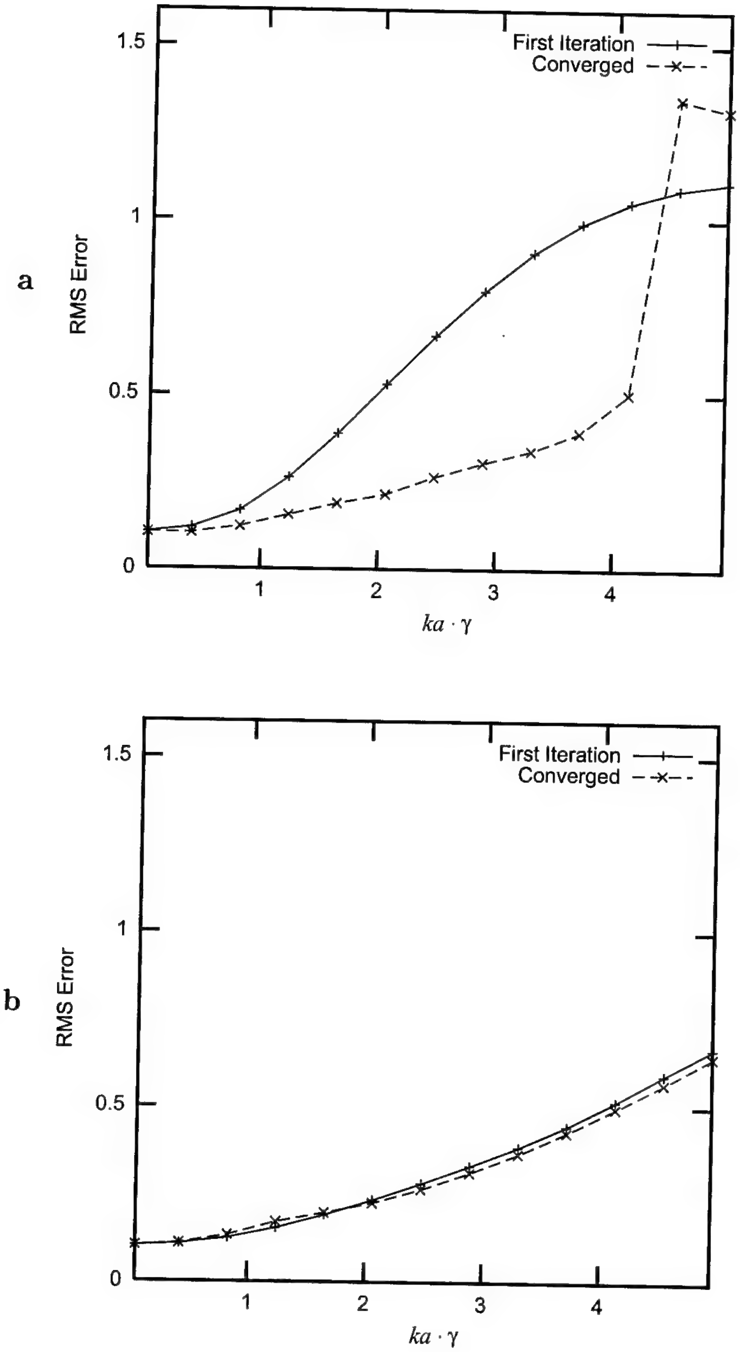

FIG. 2. RMS error for reconstructions of a 4.0 mm radius cylinder with both imaging criteria, with adaptive focus correction (solid lines) and without (dashed lines) (a) $t = 0$. (b) $t = t_{\text{peak}}$.

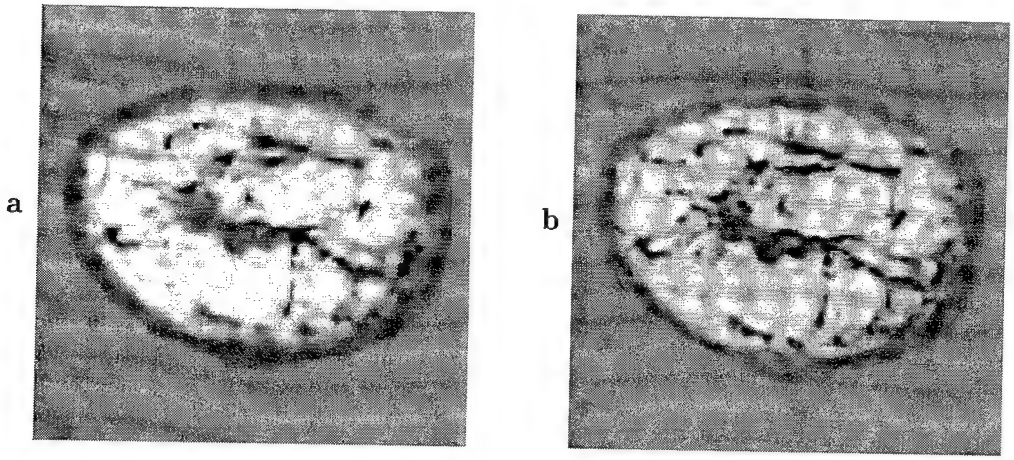

FIG. 3. Reconstruction of a large-scale two-dimensional breast model from simulated scattering data. (a) Model. (b) Initial time-domain reconstruction using $t = t_{\text{peak}}$ criterion.

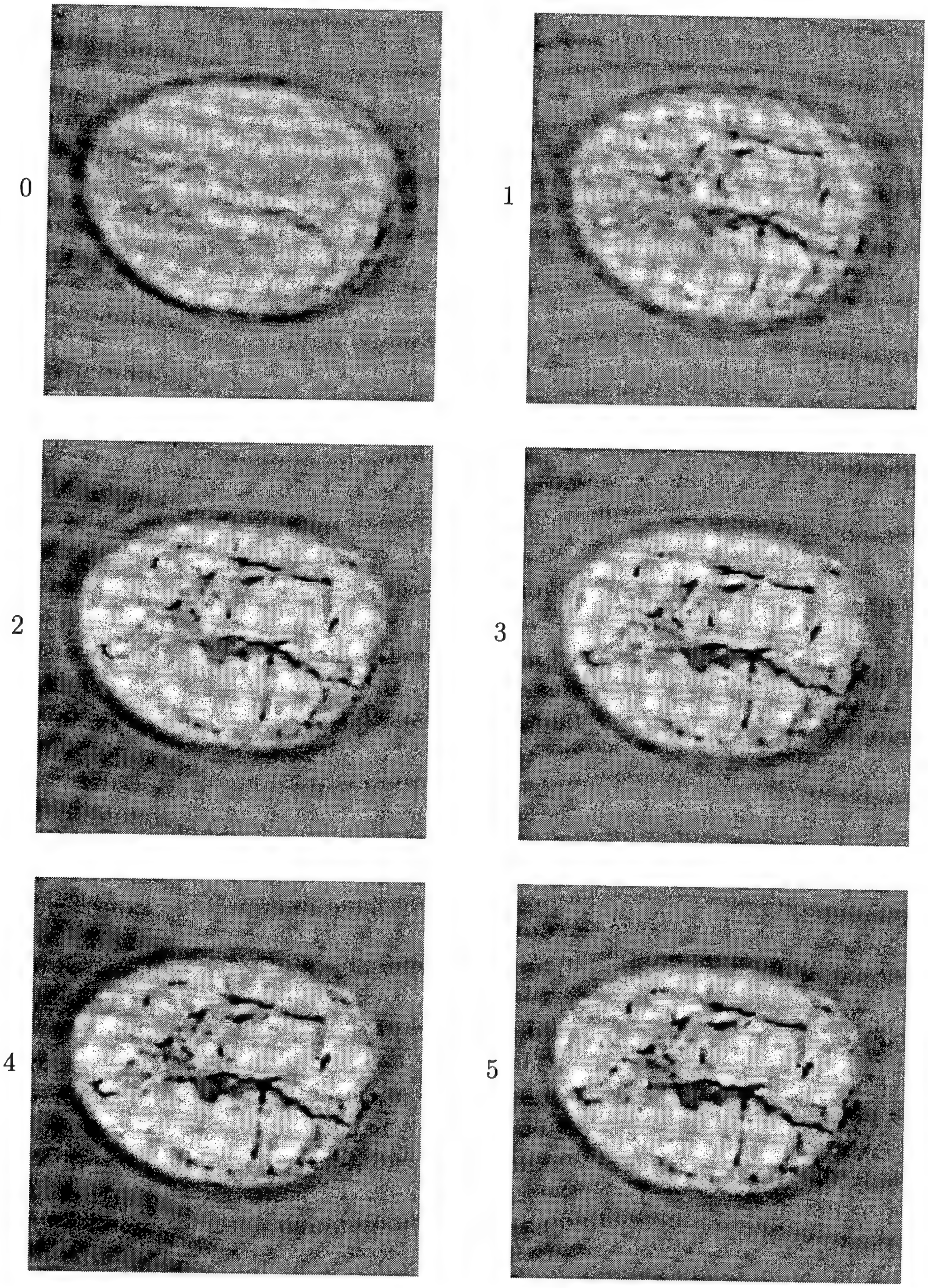

FIG. 4. Images of the large-scale breast model obtained using the $t = 0$ criterion with adaptive focusing. Panel 0 shows the initial (linear) reconstruction and panels 1–5 show the subsequent iterations up to convergence.

Simulation of ultrasonic pulse propagation, distortion, and attenuation in the human chest wall

T. Douglas Mast
Applied Research Laboratory, The Pennsylvania State University, University Park, Pennsylvania 16802

Laura M. Hinkelman[a]
Department of Electrical and Computer Engineering, University of Rochester, Rochester, New York 14627

Leon A. Metlay
Department of Pathology and Laboratory Medicine, University of Rochester Medical School, Rochester, New York 14642

Michael J. Orr
Department of Electrical and Computer Engineering, University of Rochester, Rochester, New York 14627

Robert C. Waag
Departments of Electrical and Computer Engineering and Radiology, University of Rochester, Rochester, New York 14627

(Received 5 April 1999; accepted for publication 23 August 1999)

A finite-difference time-domain model for ultrasonic pulse propagation through soft tissue has been extended to incorporate absorption effects as well as longitudinal-wave propagation in cartilage and bone. This extended model has been used to simulate ultrasonic propagation through anatomically detailed representations of chest wall structure. The inhomogeneous chest wall tissue is represented by two-dimensional maps determined by staining chest wall cross sections to distinguish between tissue types, digitally scanning the stained cross sections, and mapping each pixel of the scanned images to fat, muscle, connective tissue, cartilage, or bone. Each pixel of the tissue map is then assigned a sound speed, density, and absorption value determined from published measurements and assumed to be representative of the local tissue type. Computational results for energy level fluctuations and arrival time fluctuations show qualitative agreement with measurements performed on the same specimens, but show significantly less waveform distortion than measurements. Visualization of simulated tissue–ultrasound interactions in the chest wall shows possible mechanisms for image aberration in echocardiography, including effects associated with reflection and diffraction caused by rib structures. A comparison of distortion effects for varying pulse center frequencies shows that, for soft tissue paths through the chest wall, energy level and waveform distortion increase markedly with rising ultrasonic frequency and that arrival-time fluctuations increase to a lesser degree. © *1999 Acoustical Society of America.* [S0001-4966(99)03212-9]

PACS numbers: 43.80.Qf, 43.80.Cs, 43.58.Ta, 43.20.Fn [FD]

INTRODUCTION

Echocardiography is widely employed for diagnosis of cardiac diseases including valvular defects, pericardial effusion, and wall motion abnormalities.[1–3] Commonly, echocardiography is performed noninvasively through the chest (transthoracic) using an external probe placed on the chest wall. The chest wall, however, can considerably degrade image quality because acoustic paths between the skin and heart may contain ribs and cartilage as well as inhomogeneous muscle and fatty tissue. The result is that as many as 10–30% of patients cannot be successfully imaged with present transthoracic techniques.[4] This limitation of transthoracic echocardiography has led to the development of transesophageal echocardiography, in which the heart is imaged by a transducer inserted into the esophagus.[1–4] Although transesophageal echocardiography provides superior image quality, resulting in high diagnostic sensitivity and specificity, the invasiveness of the procedure is accompanied by increased risk.[3–6] For this reason, improvements in the noninvasive transthoracic approach are desirable, for example, by the development of methods to compensate for image degradation caused by the chest wall.

An understanding of ultrasonic aberration produced by the chest wall is important to the development of appropriate compensation methods for transthoracic ultrasonic imaging. Direct measurements of ultrasonic distortion produced by chest wall specimens[7,8] have been helpful. Results reported in Ref. 7 show that propagation through the chest wall causes substantial beam distortion. However, that study did not distinguish the effect of soft tissue from effects caused by rib structures. In Ref. 8, a detailed study of distortion caused by soft tissue paths indicates that soft tissue distortion in the chest wall is substantially less than the corresponding distortion in the human abdominal wall. However, distortion caused by ribs was only treated qualitatively in the latter study because the physical mechanisms of rib-induced distortion could not be adequately described by the method reported there. Although a model of ultrasound propagation in the chest wall has previously been described,[9] that model is based on coarse depictions of chest wall morphology including homogeneous tissue layers and evenly-spaced, uniformly-shaped ribs. These previous experiments and simulations, therefore, have left gaps in the current knowledge about the physical causes of ultrasonic wavefront distortion caused by the chest wall.

---

[a] Present address: Department of Meteorology, The Pennsylvania State University, University Park, PA 16802.

Recent work on the simulation of ultrasonic pulse propagation[10–12] has provided insight about the wavefront distortion caused by the human abdominal wall. Although these studies have provided specific information about the relationships between soft tissue morphology and ultrasonic wavefront distortion, the work is not fully applicable to distortion caused by the human chest wall. The morphology of chest wall soft tissue is different from that of the abdominal wall in ways that can affect ultrasonic wavefront distortion.[8] Furthermore, imaging through the chest wall is complicated by ribs that limit the usable acoustic window size and cause scattering and reflection.

The study reported here applies quantitative simulation methods, similar to those presented in Refs. 10 and 12, to anatomically detailed chest wall models that include the ribs. Accurate depiction of rib–ultrasound interactions requires not only representation of the strong reflections associated with sound speed and density contrast between ribs and soft tissue (already accurately modeled by the finite difference method of Ref. 10), but also modeling of the strong losses associated with propagation through bone and cartilage. For this reason, the finite-difference method described in Ref. 10 has been extended to include tissue-dependent absorption. Quantitative descriptions of the distortion caused by soft tissues are obtained by statistical analysis of simulated distortion. Visualizations of wavefronts propagating through maps of chest cross sections provide evidence about physical relationships between wavefront distortion and the morphology of ribs and soft tissue structures in the chest wall. Further insight about wavefront distortion mechanisms is provided by a comparison of distortion results for incident pulses of different center frequencies.

I. THEORY

Ultrasonic pulse propagation through the human chest wall is modeled here using the equations of motion for a fluid of variable sound speed, density, and absorption. The tissue is assumed motionless except for small acoustic perturbations. Absorption is included using an adaptation of the Maxwell solid model,[13] in which all absorption effects are represented by a single relaxation time. This assumption results in frequency-independent absorption characteristics. Equivalent treatments of tissue-dependent absorption have been employed by a number of previous models for ultrasonic propagation in biological tissues.[14–16] For such a fluid, the linearized equations of mass conservation, momentum conservation, and state can be combined to obtain the first-order, two-dimensional, coupled propagation equations,

$$\frac{\partial p(x,y,t)}{\partial t} + \rho(x,y)\, c(x,y)^2\, \nabla \cdot \mathbf{v}(x,y,t) = -\,\alpha(x,y)\, p(x,y,t), \qquad (1)$$

$$\rho(x,y)\, \frac{\partial \mathbf{v}(x,y,t)}{\partial t} + \nabla p(x,y,t) = 0. \qquad (2)$$

Here, $p(x,y,t)$ is the acoustic perturbation in fluid pressure, $\mathbf{v}(x,y,t)$ is the vector acoustic particle velocity, $\rho(x,y)$ is the ambient density, $c(x,y)$ is the ambient sound speed, and $\alpha(x,y)$ is an absorption coefficient that is equivalent to the inverse of a spatially-dependent relaxation time $\tau(x,y)$.

The absorption coefficient α, defined as a real quantity, is related to the energy lost per unit length as follows. The propagation equations (1) and (2) lead, for plane-wave propagation of the form $p = e^{i(kx-\omega t)}$, to the dispersion relation

$$k = \frac{\omega}{c} \sqrt{1 + \frac{i\alpha}{\omega}}, \qquad (3)$$

where k is the complex wavenumber, ω is the (real) radial frequency $2\pi f$, and c is the (real) sound speed. The imaginary part of the wavenumber k is the absorption in nepers per unit length. Thus, the absorption parameter α can be obtained by a numerical solution of the equation

$$\mathrm{Im}[k] = \frac{\text{loss (dB/length)}}{20 \log_{10}(e)} = \mathrm{Im}\left[\frac{\omega}{c} \sqrt{1 + \frac{i\alpha}{\omega}} \right]. \qquad (4)$$

Solution of Eq. (4) results in wavenumbers having a real part that differs from ω/c. Since this discrepancy is less than 1% over the range of tissue properties employed in the present study, use of absorption coefficients computed from Eq. (4) does not significantly affect propagation characteristics except by adding the specified absorption.

Equations (1) and (2) were solved numerically using the finite-difference time-domain (FDTD) method described in Refs. 10 and 17. This method is a two-step MacCormack predictor–corrector algorithm that is fourth-order accurate in space and second-order accurate in time. The computations employed a spatial step size of 15 points per wavelength at the pulse center frequency of 2.3 MHz. Time step sizes were computed using a Courant–Friedrichs–Lewy number of 0.25. Further details on this class of finite difference algorithms can be found in Refs. 18–20.

The initial condition was chosen to model the experimental configuration in Ref. 8, in which a spatially broad, nearly planar wavefront was emitted from a wideband, pulsed, unfocused source far from the tissue layer. The initial wavefront was represented in the present simulation as a plane wave pulse propagating in the $+y$ direction:

$$p(x,y,0) = -\sin[k_0(y-y_0)]\, e^{-(y-y_0)^2/(2\sigma^2)},$$

$$u(x,y,0) = 0,$$

and $\qquad (5)$

$$v(x,y,0) = \frac{p(x,y,0)}{\rho c},$$

where the wavenumber k_0 is equal to $2\pi f_0/c$ for a center frequency of f_0, σ is the Gaussian parameter of the pulse temporal envelope, and u and v are the x and y components of the vector acoustic particle velocity $\mathbf{v}$. The spatial Gaussian parameter σ was chosen to simulate the bandwidth of the pulse used in the experiments, as discussed below in the Method section.

The computational configuration is analogous to that described in Ref. 10. The domain of computation is two-dimensional, with the y direction taken to be parallel to the direction of propagation and the x direction parallel to the initial wavefront. As in Ref. 10, periodic boundary conditions were applied on the domain edges that were parallel to the direction of propagation, while radiation boundary conditions were applied on the edges perpendicular to the direction of propagation.

II. METHOD

This study employed six chest wall specimens obtained during the autopsies of four different donors between 79 and 85 years of age at death. One specimen (4L) was from a white female, while the others were from white males. After the specimens were obtained, they were stored unfixed at −20 °C and thawed when needed for study. Wavefront distortion measurements were made on these and other specimens as part of a study described in Ref. 8. In those measurements, 2.3 MHz ultrasonic pulses generated by a 0.5-in. piston transducer propagated through individual chest wall specimens immersed in a 37 °C water bath and the transmitted pulses were measured by a 96-element broadband cardiac array scanned to synthesize a two-dimensional aperture. Statistics describing wavefront distortion, including arrival time fluctuations, energy level fluctuations, and wave shape distortion, were computed for the measured pulses.

For the present study, six of the previously measured specimens were cut into ~7-mm thick cross sections using the technique described in Ref. 10. The slices were then fixed and stained with a modified Gomori's trichrome stain according to the procedure detailed in Ref. 21, so that tissue types could be distinguished. This stain colored muscle tissue red and connective tissue blue while leaving the fat its natural color. Calcified tissue, including bone and cartilage in the current specimens, was not differentially stained by this technique, but the natural contrast between bone, cartilage, and marrow was sufficient to allow tissue mapping. Full-color 300 d.p.i. images of the cross sections were created by placing each stained tissue cross section directly onto the surface of a flatbed digital scanner. Image editing packages (Adobe Photoshop, Version 3.0, and the Gnu Image Manipulation Program, Version 1.0) were used to manually segment the cross sectional images, i.e., to map the images into regions that corresponded to one of six media. The media were water (representing water external to specimens or blood inside blood vessels), fat (including subcutaneous fat, fat interlaced within muscle layers, and marrow), muscle, connective tissue (including skin, septa, and fasciae), cartilage, and bone (including cortical bone and trabeculae within cancellous bone).

The nomenclature employed here for the cross sections corresponds to that of Ref. 8 for the whole specimens from which the cross sections were taken; each cross section is identified by a donor number together with "L" or "R" to indicate whether the corresponding specimen was taken from the left or right side of the breastplate. Additional numbers were used in Ref. 8 to indicate the intercostal space used in each measurement; here, lower-case letters are used to indicate independent acoustic paths. Wavefront distortion measurement results from four of the specimens employed here (4L, 5L, 7L, and 7R) were reported in Ref. 8. Distortion statistics for specimens 8L and 8R were not presented in Ref. 8 because of limited acoustic windows. No new measurements were made for the present study; statistics describing measured distortion are taken directly from Ref. 8.

The six segmented tissue maps are shown in Fig. 1. All of the cross sections contain a layer of septated subcutaneous fat below the skin. Most of the cross sections also include a layer composed primarily of the major pectoral muscles and their connective fasciae above the ribs. Between the ribs are regions of muscle (internal intercostal and external intercostal groups) interlaced with fat. In some cases, additional thin layers of fat between muscle layers are apparent. Cross sections 4L and 7R are cut along the intercostal spaces parallel to the ribs, so that in each a wide cross section of soft tissue appears. Cross sections 5L, 7L, and 8L are cut perpendicular to the ribs, so that each contains soft-tissue acoustic paths with width equal to the width of the corresponding intercostal spaces. Cross section 8R is cut perpendicular to the sternum at a location of large curvature in the ribs, so that the ribs are diagonally sectioned. Several blood vessels appear in cross sections 4L, 7L, 7R, and 8R; the largest of these is the internal mammary artery.

The basic structure of the cross sections is consistent with standard descriptions of chest wall anatomy.[22,23] Ribs appear in each cross section; each rib is composed of a "costal cartilage" near the sternum (shown in most of the cross sections considered here) attached to a "true rib" (composed primarily of cancellous bone) at the edge farther from the sternum. In the cross sections considered here, the costal cartilages are primarily composed of calcified cartilage, surrounded by a thin layer of cortical bone (solid, dense bone with microscopic porous structure), which in turn is surrounded by the periosteum, a thin membrane of connective tissue. Cross sections 7L and 7R also appear to contain a small amount of cortical bone in the central portion of the ribs. This phenomenon may be associated with advanced calcification known to occur in aging humans.[24] Cancellous bone, composed of thin trabeculae that form macroscopic cells filled with marrow, is seen in all the ribs of cross section 5L, which was taken at a distance farther from the sternum so that the true ribs, rather than the costal cartilages, were included in this cross section. Some cancellous bone is also apparent within portions of the ribs of cross sections 4L and 8R. In each case, the cancellous bone is surrounded by a thin layer of cortical bone and by the periosteum. A portion of the sternum, composed of cancellous bone surrounded by cortical bone, is visible at the left side of cross section 4L.

The density and sound speed grids needed for the finite-

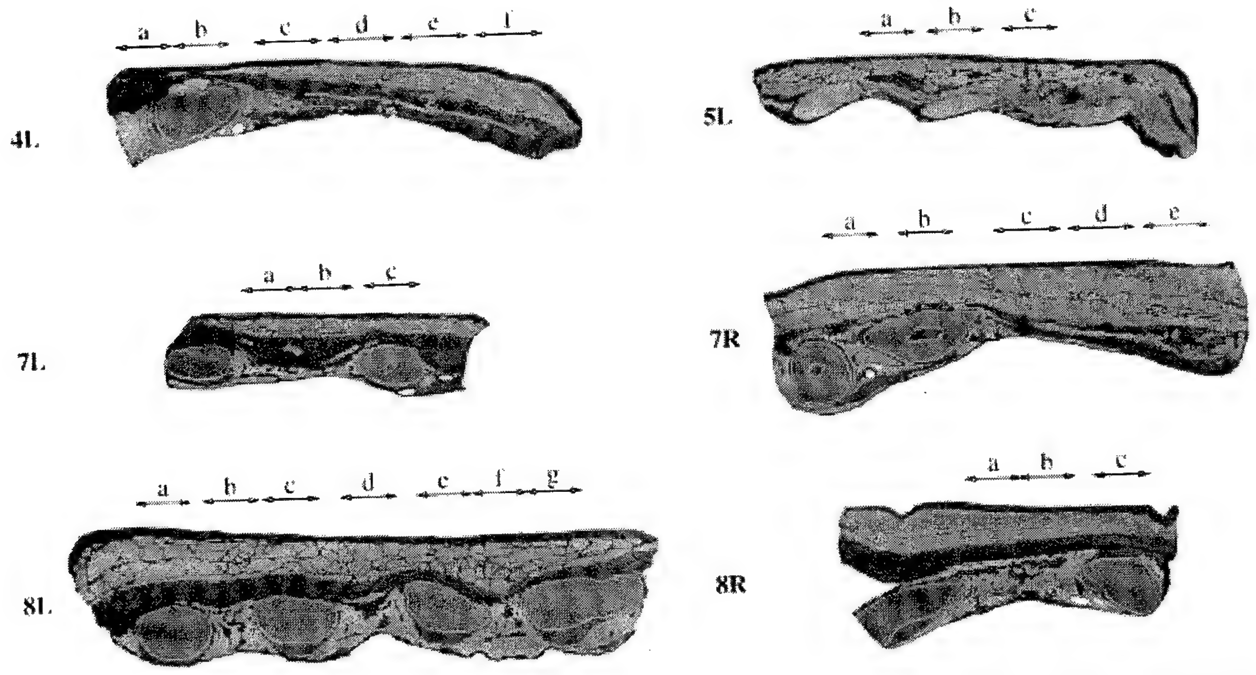

FIG. 1. Chest tissue maps used in simulations. In each map, blue denotes skin and connective tissue, cyan denotes fat, purple denotes muscle, orange denotes bone, and green denotes cartilage. Blood vessels appear as small water-filled (white) regions. Simulated apertures are indicated using lower-case letters for each cross section; the letters correspond to the acoustic path labels used throughout, while the length of the arrow beneath each letter corresponds to the extent of the simulated aperture. Smaller arrows indicate 55-element (11.60-mm) apertures while large arrows indicate 68-element (14.28-mm) apertures.

difference computation were created by mapping regions of the segmented tissue images to reference density and sound speed values for the five tissue types and water. The water sound speed and density employed are those of pure water at body temperature (37.0 °C).[25,26] Sound speeds for muscle and fat were obtained by averaging values for human tissues given in Refs. 27 and 28. A representative sound speed for connective tissue was determined using an empirical formula relating collagen content to ultrasonic sound speed[29] together with a measured value for the collagen content of human skin.[30] The sound speed employed for bone was obtained from an average of values reported in Ref. 31 for longitudinal-wave propagation in human cortical bone. The sound speed used here for cartilage is that given in Ref. 32 as quoted in Ref. 27. Density values for soft tissues were determined from Ref. 33 by averaging values reported for adipose tissue, skeletal muscle, and skin, respectively. Density values employed for bone and cartilage are average values from Ref. 31.

Absorption values were determined from attenuation measurements summarized in Ref. 27 for human fat at 37 °C, human bicep muscle at 37 °C, human skin at 40 °C, human and bovine cartilage at 23 °C, and human skull (temperature not reported). Attenuation values reported at other ultrasonic frequencies were interpolated (or, for the skull data, extrapolated) to obtain values for 2.3 MHz (corresponding to the pulse center frequency employed here and in Ref. 8) assuming a linear dependence of attenuation on frequency. This assumed linear dependence is a simplifying approximation; tissue measurements show that attenuation varies approximately as $\alpha \propto f^{\beta}$, where β is typically between 0.9 and 1.5 for various human soft tissues.[34] The absorption for water was estimated by extrapolating frequency- and temperature-dependent absorption values summarized in Ref. 35 to 2.3 MHz and 37.0 °C. The values of tissue parameters employed in the present study are given in Table I.

The finite-difference program was employed to compute propagation of a plane wave pulse through each scanned cross section from the skin to the peritoneal membrane, mimicking the propagation path employed in the distortion measurements of Ref. 8. The spatial step size of the finite-difference grid was chosen to be 0.0442 mm, or 1/15 wavelength in water at the center frequency of 2.3 MHz. The temporal step size was chosen to be 0.00725 μs, for an optimal Courant–Friedrichs–Lewy number $c\Delta t/\Delta x$ of 0.25.[20] The Gaussian parameter σ of the source pulse was chosen to be 0.4766 mm in accordance with the experimentally measured pulse bandwidth (for pulses transmitted through a water path) of 1.2 MHz. A visual comparison confirmed that the

TABLE I. Assumed physical properties for each tissue type employed in the simulations.

Tissue type	Sound speed (mm/μs)	Density (g/cc)	Absorption (dB/mm)
Water	1.524	0.993	0.0007
Fat	1.478	0.950	0.12
Muscle	1.547	1.050	0.21
Connective	1.613	1.120	0.37
Cartilage	1.665	1.098	0.97
Bone	3.540	1.990	4.37

simulated pulse closely matched the measured pulses in shape and length.

Each simulation was performed on a workstation with 128 MB of random-access memory. Finite-difference grids on the order of 1500×1000 points were employed. At each time step, the wave field was updated on a grid subset chosen to include the entire support of the acoustic wave but to exclude quiescent regions. The entire pressure field was saved as a raster image at intervals of 0.725 μs for later visualization. The computation time for each simulation was on the order of five hours.[36]

Signals were recorded for 8.62 μs at a sampling frequency of 138 MHz by simulated apertures with dimensions close to those in the experimental study of Ref. 8. Positions of all simulated apertures employed are sketched in Fig. 1. The simulation of receiving elements was performed by integrating the locally-computed pressure over the element pitch of 0.21 mm. For cross sections cut parallel to the ribs, the simulated apertures contained 68 elements for an aperture width of 14.28 mm. For cross sections cut perpendicular to the ribs, 55 simulated elements were used to form 11.55 mm apertures. Element directivity effects were implicitly incorporated by the integration of acoustic fields over the width of each element; the resulting directivity functions correspond to those for an idealized line element of width 0.21 mm.

A one-dimensional version of the reference waveform method[10,37] was used to calculate the arrival time of the pulse at each receiving position in the simulation data. In this method, the relative arrival time of each received waveform is computed by cross-correlation with a reference waveform. The arrival time fluctuations across the receiving aperture are then calculated by subtracting a linear fit from these calculated arrival times, and the root-mean-square value of these fluctuations is computed. Energy level fluctuations in the data were calculated by summing the squared amplitudes of each waveform over a 2.4-μs window that isolated the main pulse, converting to decibel units, and subtracting the best linear fit from the resulting values. As for polynomial fits previously employed in wavefront distortion measurements,[8] the purpose of the linear fit removal in each case was to compensate for gross changes in tissue thickness across the array. Variations in pulse shape across the aperture were evaluated using the waveform similarity factor;[37] this quantity, which can be considered a generalized cross-correlation coefficient, has a maximum of unity when all received waveforms are identically shaped.

To test the frequency dependence of chest wall wavefront distortion, propagation through eight portions of specimens, each containing only soft tissue, was also computed for wavefronts having center frequencies of 1.6 and 3.0 MHz. In each case, the initial wavefront was chosen to have the same temporal envelope as above. The absorption coefficient at these frequencies for each tissue type was extrapolated from the value employed at 2.3 MHz using the assumption that absorption depended linearly on the center frequency. The spatial and temporal sampling rates were also varied in inverse proportion to the pulse center frequency. All runs were otherwise identical in configuration and processing to those described above.

TABLE II. Statistics of simulated wavefront distortion caused by thirteen soft tissue paths within chest wall cross sections. The "Path" column shows the cross section label and aperture letter for each path; these labels correspond to those shown in Fig. 1. The statistics shown include the average specimen thickness for the tissue path considered, rms values and correlation lengths (CL) of the arrival time fluctuations (ATF) and the energy level fluctuations (ELF), the waveform similarity factor (WSF), and the total attenuation.

		ATF		ELF			
Path	Thickness (mm)	rms (ns)	CL (mm)	rms (dB)	CL (mm)	WSF	Attenuation (dB)
4L-c	15.4	32.0	0.60	1.98	1.68	0.981	5.62
4L-d	12.7	10.0	2.58	0.46	1.23	0.999	4.08
4L-e	16.0	10.0	1.37	1.61	1.74	0.998	5.26
4L-f	17.0	17.3	2.48	0.92	1.61	0.999	5.33
5L-a	11.0	11.6	0.95	1.51	1.13	0.991	4.29
5L-c	15.0	14.8	1.03	1.15	1.19	0.996	5.01
7L-a	16.2	16.8	2.64	0.95	1.29	0.999	5.46
7L-b	14.9	22.5	2.66	1.19	1.61	0.998	4.91
7R-c	17.7	17.4	1.77	2.52	2.07	0.997	5.83
7R-d	21.0	8.3	1.10	0.85	1.79	0.999	7.07
7R-e	24.7	13.7	1.37	1.06	1.62	0.997	8.69
8R-a	23.8	26.6	1.78	2.58	1.40	0.992	7.76
8R-b	22.2	29.9	1.44	1.95	1.11	0.989	6.09
Mean	17.5	17.8	1.67	1.44	1.50	0.995	5.80
St. Dev.	4.2	7.8	0.71	0.66	0.30	0.005	1.33

III. RESULTS

Simulated wavefront distortion results for 13 soft tissue paths (i.e., paths in which wavefront distortion was not significantly influenced by the ribs) are shown in Table II. These results indicate that soft tissue paths cause a wide range of wavefront distortion effects depending on the specific morphology of each path. For instance, path 7R-c causes arrival time and energy level fluctuations that are more than twice the magnitude of those caused by the adjacent path 7R-d. This difference is thought to arise from morphological features, including muscle tissue with interlaced fat and a large amount of connective tissue, of the tissue within path 7R-c. Also notable is that the specimen thickness does not closely correspond to variations in distortion. The largest rms arrival time fluctuation and lowest waveform similarity factor, for example, are caused by path 4L-c, which has an average thickness less than the mean for all the tissue paths.

Wavefront distortion statistics for the 13 soft tissue paths are graphically summarized in Fig. 2 together with corresponding statistics for all of the soft tissue measurements reported in Ref. 8. This comparison indicates that wavefront distortion caused by soft tissues in the chest wall simulations is comparable to measured distortion. Arrival time fluctuations and energy level fluctuations for simulated distortion are slightly less than measured values, but mean values of both fluctuations for the simulations fall well within one standard deviation of the corresponding mean fluctuation for the measurements. The waveform similarity factor, however, is substantially higher for simulations than measurements, indicating that simulated waveforms were distorted considerably less than measured waveforms. Correlation lengths for the simulated distortions are somewhat less

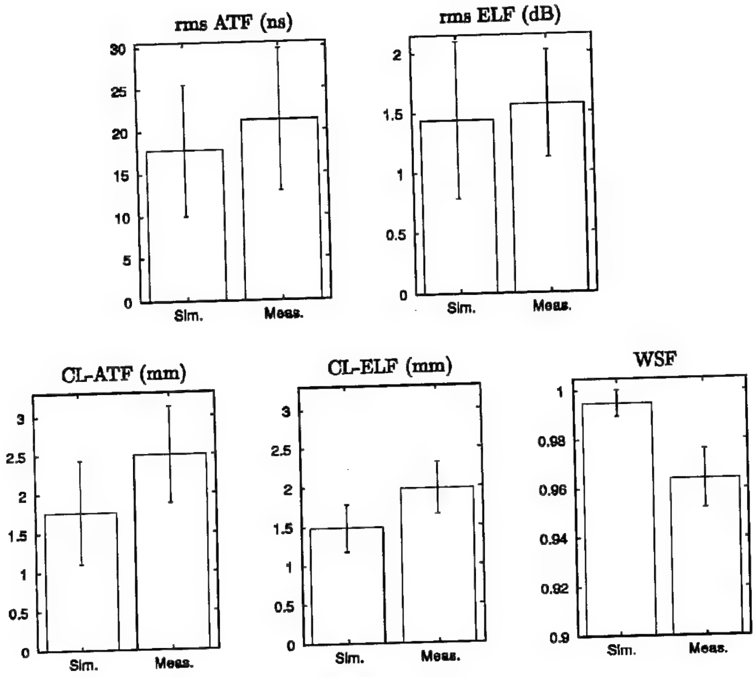

FIG. 2. Summary of distortion statistics for soft tissue paths. The bar chart shows mean values of the rms arrival time fluctuations (ATF), rms energy level fluctuations (ELF), correlation lengths (CL) of these fluctuations, and waveform similarity factors (WSF) for the simulations performed in the present paper and the experiments reported in Ref. 8. Error bars indicate a range of plus or minus one standard deviation from the mean.

than measured values. However, consistent with measurements, the mean correlation length of the simulated arrival time fluctuations is greater than that for the simulated energy level fluctuations.

As in Ref. 8, rib structures were found to cause much more distortion than soft tissue alone. The varied nature of distortion caused by rib effects is illustrated in Fig. 3, which shows three representative sets of measured signals for specimen 8L. These measurements were made during the study reported in Ref. 8. The first panel shows 96 adjacent measured signals, along the array direction (approximately parallel to the ribs) for propagation through a tissue path within an intercostal space. The signals are not severely distorted; secondary arrivals are discernible, but are of lower amplitude than the main arrival. The second panel shows 96 measured signals for an elevation over a rib. Here, all signals are severely distorted. Multiple arrivals, as well as high-amplitude spatially-random fluctuations, are seen. The third panel shows 50 measured signals along the elevation direction (perpendicular to the ribs), centered over the soft tissue between the ribs. Here, the main wavefront is curved rather than straight, an additional arrival behind the main wavefront is seen, and portions of the signals from over the ribs (at both edges of the panel) are advanced relative to the signals from the central soft tissue region.

The present simulations allow more detailed qualitative and quantitative investigation of rib effects than were possible from the previous measurements. Propagation through two rib-influenced paths is illustrated in Figs. 4 and 5, in which computed ultrasonic pulses are superimposed on portions of the tissue maps from Fig. 1. (Similar visualizations of propagation through soft human body wall tissue were shown in Ref. 10.)

Figure 4 shows propagation through a thin rib, composed chiefly of cancellous bone, in cross section 5L (corresponding approximately to path 5L-b). A strong reflection

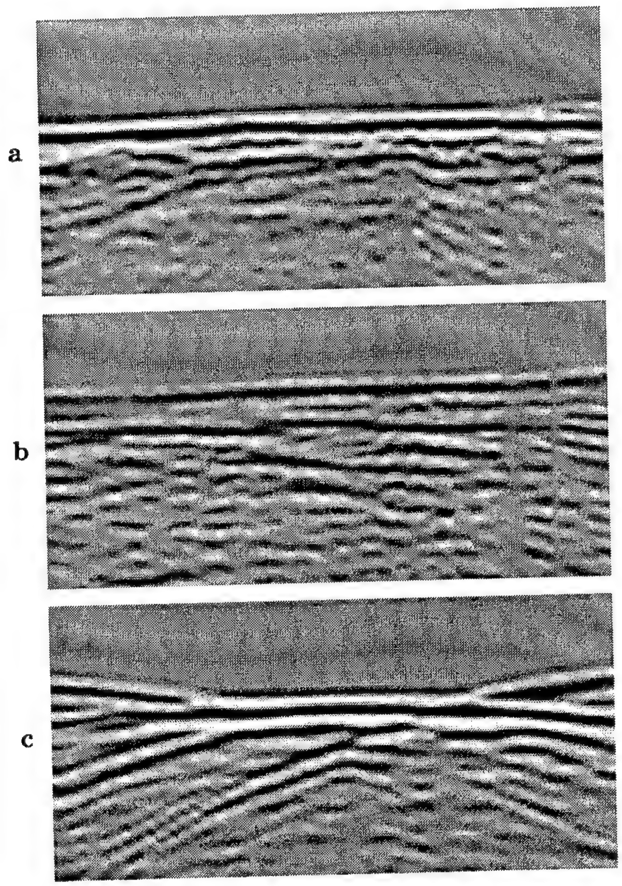

FIG. 3. Measured waveforms for three propagation paths in specimen 8L. Each panel shows received waveforms on a bipolar logarithmic gray scale with a dynamic range of 40 dB. The horizontal range shown in each panel is 20 mm and the vertical range shown is 6.4 μs. (a) Tissue path between two ribs, in azimuth direction (parallel to ribs). (b) Path including a rib, azimuth direction. (c) Tissue path including intercostal space between two ribs, elevation direction (perpendicular to ribs).

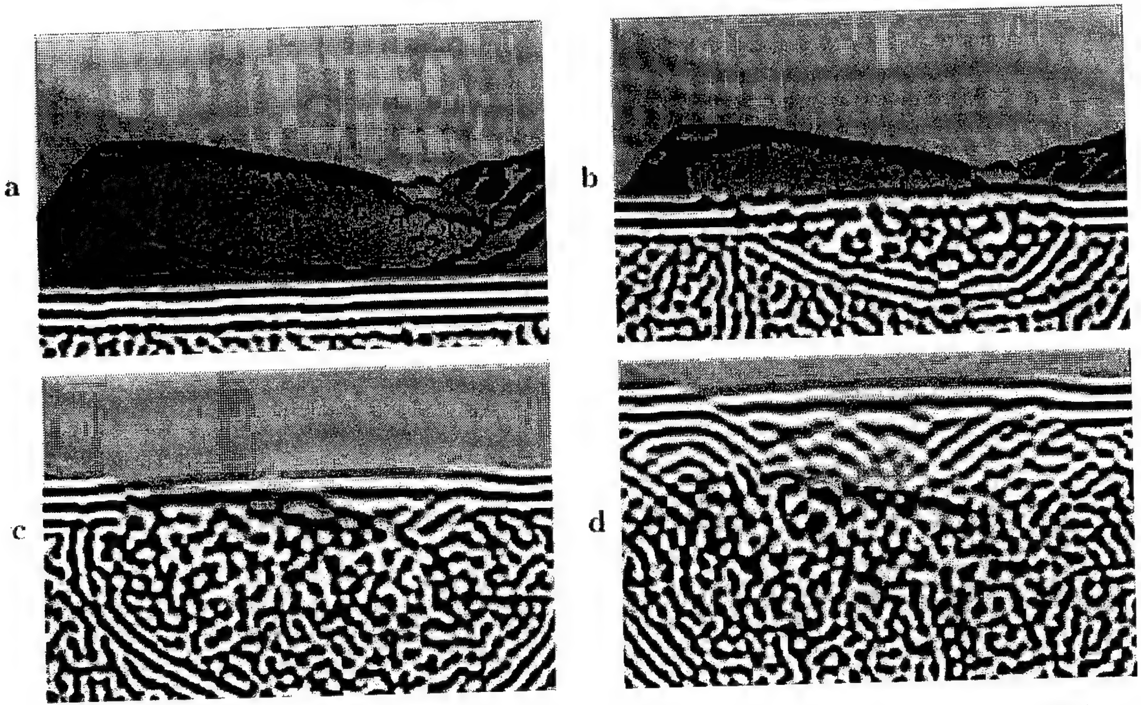

FIG. 4. Simulated propagation through the central rib in cross section 5L (path 5L-b). Panels (a)–(d) show instantaneous acoustic pressure fields at successive intervals of 2.17 μs. Each panel shows an area that spans 20.32 mm horizontally and 14.58 mm vertically. Logarithmically compressed wavefronts are shown on a bipolar scale with black representing minimum pressure, white representing maximum pressure, and a dynamic range of 57 dB.

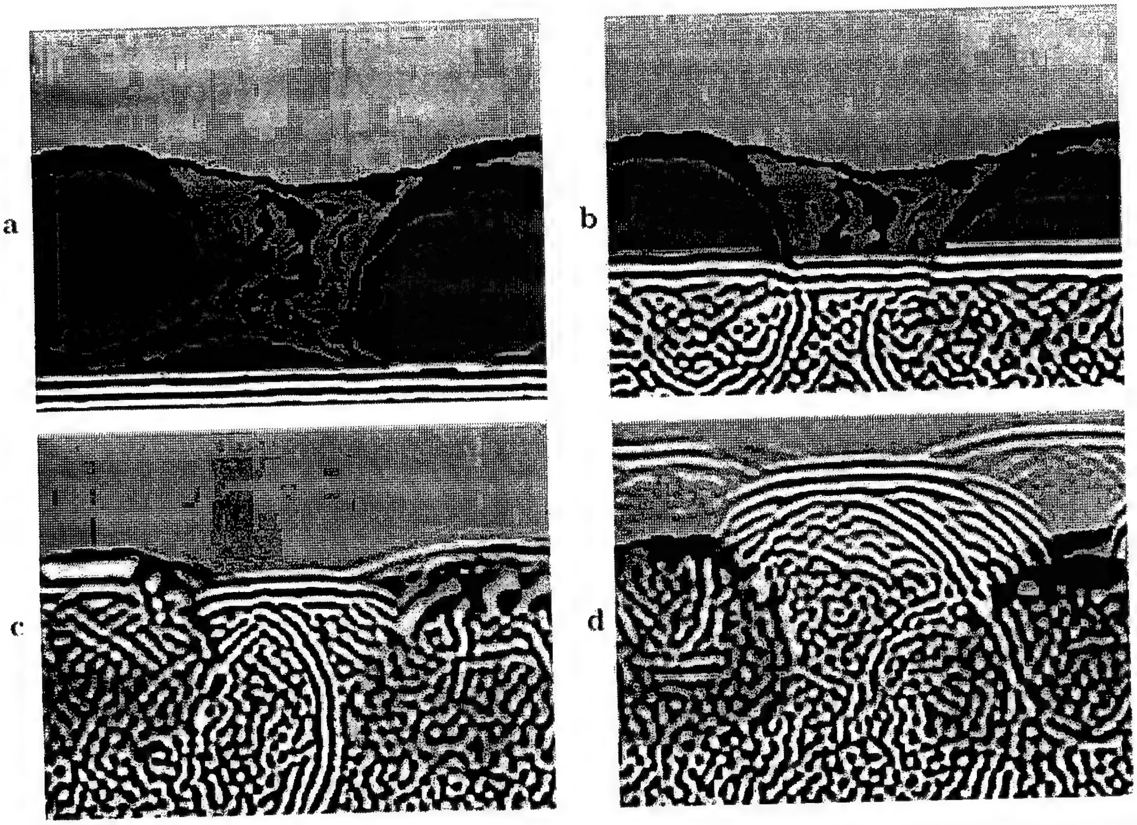

FIG. 5. Simulated propagation through an intercostal space in cross section 8L (path 8L-b). Panels (a)–(d) show instantaneous wavefields at successive intervals of 3.62 μs. Each panel shows an area that spans 28.27 mm horizontally and 21.20 mm vertically. Wavefronts are shown using the same format as in Fig. 4.

occurs at the first interface between bone and soft tissue, removing a substantial amount of energy from the main wavefront. The small, high-contrast trabeculae within the rib cause considerable scattering, as can be observed in panel (b) of Fig. 4. The scattering causes random fluctuations behind the main wavefront; these fluctuations somewhat resemble those seen in the measured data of Fig. 3(b). After passing through the rib, as seen in panels (c) and (d) of Fig. 4, the central portion of the wavefront shows substantial attenuation and distortion. However, the average arrival time of the wavefront is not greatly changed by propagation through the rib, but is advanced by only about one-half period. This phenomenon apparently occurs because the influence of the "slow" marrow (modeled here as fat) counteracts the influence of the "fast" trabeculae. Noteworthy is that the predominant ultrasonic wavelength has increased after propagation through the rib, so that the effective center frequency of the wavefront has been lowered. Since the absorption model used in the present study includes only frequency-independent absorption, the loss of short-wavelength components in this simulation results only from frequency-dependent scattering caused by the trabeculae.

Propagation within path 8L-b, which includes two larger ribs and the corresponding intercostal space, is illustrated in Fig. 5. At the position of the cross section, these ribs are composed primarily of cartilage and surrounded by a thin layer of cortical bone. Since the cartilage and bone of these ribs are modeled as homogeneous structures, small-scale scattering within these tissues did not occur in this simulation. Instead, the wavefront is reflected from interfaces between cartilage, bone, and soft tissue.

The visualization shown in Fig. 5 provides physical reasons for all the rib-related distortion phenomena seen in the measured data of Fig. 3(c). The wavefronts propagating through the ribs show greater attenuation than that in Fig. 4, both because of the high absorption of the ribs and because of the reflections noted above. These wavefronts are also advanced relative to the wavefront propagating through the intercostal space, because of the higher sound speed of both bone and cartilage. The wavefront propagating through the intercostal space is distorted somewhat by the inhomogeneous soft tissue path, as can be observed in panels (b) and (c). However, much greater distortion results from interaction between the wavefront and the ribs. A rightward-propagating reflection, seen in panels (b) and (c), combines with the main wavefront in panel (d) to result in severe distortion at the right side of the central wavefront. A leftward-propagating reflection from the other rib is also apparent. Furthermore, diffraction from the edges of the ribs results in large curvature of the soft tissue wavefront.

TABLE III. Statistics of simulated wavefront distortion caused by fourteen tissue paths including rib structures. The footnotes associated with the label for each path indicate morphological features and physical phenomena that affected the wavefront distortion computed for that path. The format is analogous to that in Table II.

		ATF		ELF			
Path	Thickness (mm)	rms (ns)	CL (mm)	rms (dB)	CL (mm)	WSF	Attenuation (dB)
4L-a[a,b,c,d]	21.0	260.3	3.00	2.58	2.72	0.968	15.33
4L-b[b,c]	17.6	161.9	1.90	4.16	1.49	0.641	43.35
5L-b[b]	14.2	92.5	0.69	3.06	1.92	0.775	26.87
7L-c[c,e]	17.8	47.2	1.58	5.33	2.04	0.958	19.66
7R-a[a,c,d]	30.4	123.1	2.12	3.80	1.78	0.960	16.57
7R-b[c,e]	24.3	165.6	2.71	6.88	2.07	0.274	43.06
8L-a[c]	25.3	113.9	1.18	7.75	2.29	0.907	32.44
8L-b[a,d]	22.8	109.7	2.05	3.43	1.22	0.974	10.28
8L-c[c]	28.8	134.0	2.75	3.04	1.57	0.944	40.47
8L-d[d]	23.6	78.9	0.64	3.06	1.55	0.950	6.78
8L-e[c]	26.4	208.8	1.91	3.62	1.50	0.810	44.27
8L-f[a,d]	28.5	169.9	1.79	5.02	1.95	0.916	10.70
8L-g[c]	27.6	210.8	1.40	3.36	1.35	0.892	44.22
8R-c[b,c]	24.9	81.4	2.08	2.76	1.25	0.962	44.32

[a] Small intercostal spaces.
[b] Cancellous bone.
[c] Cortical bone and cartilage.
[d] Strong rib reflections.
[e] Cortical bone within cartilage.

Distortion and attenuation statistics for a variety of simulations employing rib-influenced paths are shown in Table III. Footnotes in Table III indicate physical causes of distortion present within each path. A variety of distortion and attenuation mechanisms are illustrated. Propagation through small intercostal spaces (paths 4L-a, 8L-b, 8L-f, and 7R-a) causes diffraction effects that introduce substantial curvature into the wavefront, as seen in Fig. 5. This large-scale wavefront curvature is associated with large arrival time fluctuation values although the wavefronts generally appear to be locally smooth. Interference between directly-transmitted and rib-reflected wavefronts (paths 4L-a, 8L-b, 8L-d, 8L-f, and 7R-a) introduces arrival time, energy level, and waveform distortion substantially greater than that for soft tissue paths without ribs. Propagation through cancellous bone (paths 4L-a, 4L-b, 5L-b, and 8R-c) results in considerable attenuation and large waveform distortion, while propagation through cortical bone and cartilage (paths 4L-a, 4L-b, 8L-a, 8L-c, 8L-e, 8L-g, 7L-c, 7R-a, 7R-b, and 8R-c) results in even larger attenuation but smaller distortion. Where bone is embedded within cartilage (paths 7L-c and 7R-b), additional scattering also occurs. For the path including a large bone inclusion (path 7R-b), this scattering results in an extremely high energy level and waveform distortion.

Computed frequency-dependent wavefront distortion statistics are summarized in Fig. 6. Tissue paths used for these computations, none of which include rib structures, are those labeled 4L-d, 4L-f, 5L-a, 5L-c, 8R-a, 8R-b, 7L-a, and 7L-b in Fig. 1. The results shown in Fig. 6 indicate that arrival time fluctuations, energy level fluctuations, and waveform distortion all become more severe with increasing pulse frequency. The most dramatic change is in the energy level distortion; on average, the rms energy level fluctuations for the 3.0-MHz signals are 2.3 times those for the 1.6-MHz signals. Correlation lengths of both arrival time and energy level fluctuations decrease with frequency, so that the predominant length scales of ultrasonic wavefront distortion are seen to decrease with the ultrasonic wavelength. As with the rms distortion statistics, the most dramatic frequency-dependent change is in the energy level fluctuations. Still, even the high-frequency pulses here show substantially

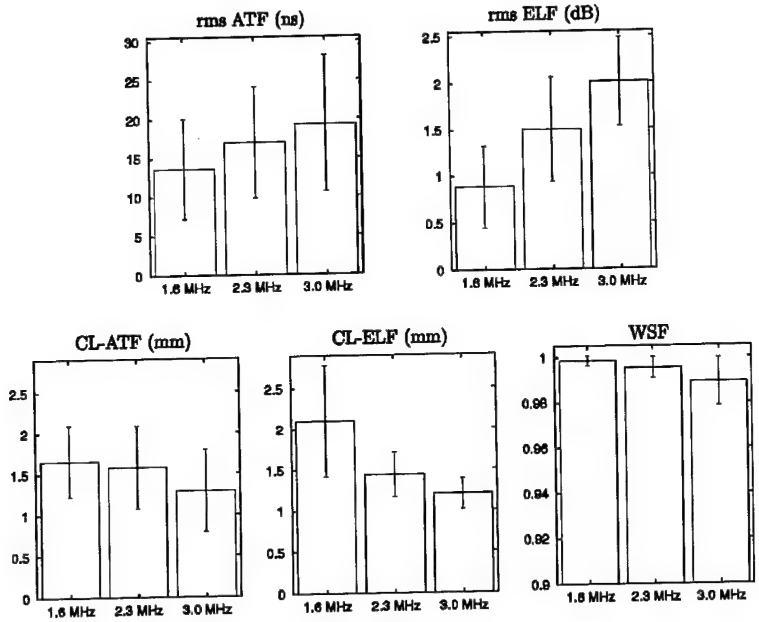

FIG. 6. Summary of simulated frequency-dependent distortion results. Mean rms arrival time fluctuations (ATF), energy level fluctuations (ELF), correlation lengths (CL) of these fluctuations, and waveform similarity factors (WSF) are shown for each of the three pulse frequencies investigated. Error bars indicate a range of plus or minus one standard deviation from the mean.

smaller distortion than that previously observed in experiments and simulations for the human abdominal wall.[10–12,38]

IV. DISCUSSION

As with earlier simulations of propagation through tissue,[10,12] the current study shows qualitative agreement with measured wavefront distortion results for similar specimens.[8] However, the accuracy of the present model is limited by simplifications of true tissue structure. In particular, the computational model here does not account for property variations within tissue types, tissue microstructure, or three-dimensional tissue structure. Each of these simplifications limits the ability of the present model to precisely mimic experimentally measured ultrasonic wavefront distortion. These limitations are discussed, with respect to soft tissues, in Ref. 10.

The modeling of ribs adds additional complication. In the current study, individual trabeculae were assumed to be composed of tissue having properties identical to cortical bone, an assumption known as Wolff's hypothesis.[39] The validity of this hypothesis has been questioned;[40,41] however, measured elastic properties of individual trabeculae vary widely[40,41] and recent work[42] has provided support for Wolff's hypothesis. Thus, the properties employed here for trabecular bone can be regarded as reasonable order-of-magnitude estimates. Likewise, the modeling of marrow as fat tissue is a simplifying assumption that may have limited validity, although available data suggest that the density and sound speed of marrow are close to those for other adipose tissues.[31] In addition, the present model for cartilage is based on measurements of normal cartilage, while the cartilage present in the specimens employed here was calcified due to the age of the donors. However, density measurements made on eight representative samples of calcified cartilage (two from specimen 7R, four from specimen 1R,[8] and two from an unused specimen) resulted in an average density of 0.00111 $\mathrm{kg/m}^3$, which is different by only 1% from the density assumed here. Since sound speed in calcified tissue has been empirically shown to be directly related to density,[43,44] this small change in density suggests that the acoustic properties of the calcified cartilage in our specimens is close to that for normal cartilage.

The computations reported here model the chest wall as a fluid of variable sound speed, density, and compressibility. This model implicitly neglects shear wave propagation. The neglect of shear waves in soft tissues is believed to be justified because the absorption of shear waves in soft tissues is much greater than absorption of longitudinal waves.[45,46] In calcified tissues, however, significant shear waves are known to be generated.[47,48] In the current scattering configuration, some shear waves are likely generated wherever the rib surface is far from parallel to the wavefront. However, since shear wave absorption has been found to be somewhat larger than longitudinal wave absorption for ultrasonic propagation in bone,[47] the significance of shear-wave propagation within bone on transmitted ultrasonic wavefronts is questionable. For this reason, omission of nonlongitudinal waves in the present study, as in another computational study of ultrasonic scattering from bone,[49] is believed to be justified; however, further study would be required to confirm this assumption.

The absence of frequency-dependent absorption is a possible source of error in the present estimates of total tissue attenuation, energy level fluctuations, and waveform distortion. However, since absorption in tissue increases approximately linearly with frequency, lower absorption for frequency components below the pulse center frequency would nearly cancel higher absorption for frequency components above the center frequency, so that the average absorption incurred by a wideband pulse should still be computed with fair accuracy. For this reason, the absence of frequency-dependent absorption in the calculations reported here is not considered to be a significant source of error in the computed attenuation or energy level fluctuation curves. Still, the inclusion of frequency-dependent absorption would result in additional waveform distortion effects. The lack of this effect is a likely reason for the lower waveform distortion (higher waveform similarity factors) obtained from simulations as compared to measurements. However, the absence of frequency-dependent absorption effects allowed frequency-dependent scattering effects to be clearly quantified separately from absorption effects.

Although the simulations were planned to match the measurements of Ref. 8 closely, a number of differences remain. The most important of these, as discussed in Ref. 10, is that the simulations were performed using a two-dimensional tissue model while the measurements were inherently three-dimensional. Other differences include details of the source waveform and wavefront shape, variations in the specimen orientations and the regions interrogated, and variations in the distance between the specimen and the real or simulated receiving aperture. All of these differences could contribute to discrepancies between measurements and simulations.

In general, most of the simplifying assumptions in the present tissue model are likely to result in underestimation of wavefront distortion produced by the human chest wall. The incorporation of tissue microstructure, spatially-dependent acoustic properties for each tissue type, shear wave propagation in bone and cartilage, three-dimensional propagation, and frequency-dependent absorption could all result in greater spatial and temporal variations in the propagating acoustic fields, so that these features could produce simulated distortion with characteristics closer to measurements. For this reason, distortion statistics computed using the present tissue model should be interpreted as lower limits for the statistics of distortion occurring in real chest wall tissue.

Additionally, some of the discrepancy between simulated and measured distortion may be explained by the nonuniform characteristics of the receiving transducer employed in the measurements.[8] The water-path measurements reported in Ref. 8 show arrival time fluctuations (mean 2.21 ns) and energy level fluctuations (mean 0.36 dB); although small, these fluctuations are comparable to the difference between the average measured and simulated fluctuations. Thus, compensation for arrival time and energy level fluctuations due to transducer irregularities could reduce measured distortion to levels closer to the simulations. Also, the waveform similarity factor for water path measurements was 0.991,[8] which indicates greater waveform distortion than the average value of 0.995 computed here for soft tissue paths. Thus, compensation of the measured data for transducer impulse-response variations could raise the measured waveform similarity factor to a value in closer agreement with simulations.

Previous experimental measurements of wavefront distortion caused by the human chest wall[8] have suggested that distortion caused by chest wall soft tissues is less severe than that caused by the human abdominal wall.[11,38] This difference has been observed to occur even though average specimen thicknesses were comparable in chest wall[8] and abdominal wall[11,38] measurements. The present results provide support for these results; arrival time and energy level distortion by the chest wall was found here to be smaller than that produced by the abdominal wall in previous simulation studies.[10,12] For the simulations, this difference may be partially explained by the fact that the chest wall specimens employed here are thinner on average (mean thickness 17.5 mm) than the abdominal wall cross sections employed in Refs. 10 and 12 (mean thickness 26.7 mm). Another possible partial explanation is that the pulse center frequency employed in abdominal wall measurements and simulations was 3.75 MHz, significantly higher than the center frequency of 2.3 MHz for the chest wall measurements and simulations. Differences in pulse frequency and specimen thickness may explain the discrepancy in energy level distortion between the abdominal wall and chest wall, but do not fully explain the discrepancy in arrival time distortion results. For instance, the mean arrival time and energy level fluctuations per unit length are 1.02 ns/mm and 0.083 dB/mm for the present study vs 1.96 ns/mm and 0.105 dB/mm for the abdominal wall cross sections of Ref. 10 and 12. Arrival time distortion was shown here to increase only subtly with increasing pulse frequency, so that this discrepancy in arrival time fluctuations is not fully explained by pulse frequency differences. However, energy level fluctuations increase markedly with frequency for chest wall tissue. Thus, for equal ultrasonic pulse frequencies, chest wall tissue should cause energy level distortion per unit length comparable to that caused by abdominal wall tissue.

It was suggested in Ref. 8 that chest wall morphology may differ from abdominal morphology in a manner that results in smaller ultrasonic wavefront distortion. The cross sections employed here can be compared with those employed in Refs. 10 and 12 to evaluate the importance of morphological differences between chest wall and abdominal wall tissue. One difference between the two groups of cross sections is the nature of the subcutaneous fat layers. The abdominal wall cross sections generally contain thicker fat layers, containing many more lobular structures than the chest wall cross sections. Since the high contrast between septa and fat causes substantial ultrasonic scattering,[10–12] this morphological difference is likely to result in lower overall energy level and waveform distortion for chest wall tissue (although, as discussed above, the energy level distortion per unit propagation length should be comparable). Also, the abdominal wall and chest wall cross sections have a markedly different structure within the muscle layers that occur below the subcutaneous fat. The abdominal wall cross sections have many large-scale features due to aponeuroses (interfaces between muscle groups, composed of connective tissue and fat) and large fatty regions. These large-scale features cause large wavefront fluctuations that are associated with large rms arrival time fluctuations.[10,12] In contrast, muscle layers of the chest wall cross sections considered here contain primarily smaller-scale structures associated with small islands of interlaced fatty tissue. This morphological difference may result in lower large-scale arrival time fluctuations but significant energy level fluctuations associated with scattering, consistent with the differences between distortion caused by soft tissues in the abdominal wall and the chest wall.

The present results for the frequency dependence of distortion provide further insight into the importance of scattering effects relative to large-scale structure in wavefront distortion caused by soft tissues. If wavefront distortion in the chest wall were caused only by large-scale tissue structures, the distortion would be roughly independent of frequency, since propagation effects are independent of frequency in the geometric acoustics limit. However, distortion caused by scattering effects should increase with the pulse frequency for inhomogeneities of size comparable to the wavelength. Previous simulation and experimental studies[10–12] on distortion caused by the human abdominal wall have suggested that energy level fluctuations and waveform distortion are generally associated with scattering effects, while arrival time fluctuations are predominantly caused by large-scale path length differences. The present results, while consistent with those conclusions, indicate that scattering plays a role in all types of distortion considered here. Since energy level fluctuations and waveform similarity factors exhibit more dramatic increases in distortion with increasing pulse frequency, the present results suggest that scattering is of primary importance in causing energy level and waveform distortion and of secondary importance in causing arrival time distortion.

These results can be employed to evaluate the potential of various approaches to improve echocardiographic imaging. Available acoustic windows for transthoracic imaging are severely limited by the presence of the ribs, so that image quality cannot be significantly improved by an increase of aperture size. The present results also indicate that use of higher-frequency probes may provide less benefit than expected because of frequency-dependent scattering in the chest wall.

For these reasons, aberration correction methods are potentially important in transthoracic echocardiography, particularly for higher-frequency imaging. The frequency-dependent distortion results reported here suggest that distortion models employing single phase screens may be of some benefit for aberration correction in echocardiography through soft tissue paths. The relatively weak dependence of arrival time fluctuations on pulse frequency suggests that a large portion of arrival time variations are caused by tissue structures too large to cause significant frequency-dependent scattering effects. Similar conclusions regarding the importance of large-scale structures to arrival time fluctuations have also been drawn from results presented in Refs. 10 and 12.

Still, the present results, like those from earlier studies,[10–12] suggest that single phase screens will not provide complete correction for distortion caused by soft tissues. In particular, methods employing single phase screens will not completely remove distortion caused by scattering. The sharp increase of amplitude and waveform distortion with frequency, as well as the moderate increase of arrival time distortion with frequency, indicate that scattering effects become much more important to ultrasonic aberration as imaging frequencies increase. Furthermore, phase screen models do not inherently account for distortion caused by rib structures, shown here to produce diffraction, reflection, and scattering. Thus, any attempted correction using only phase screen models is likely to provide little improvement in the presence of strong rib-induced effects.

Other correction models that incorporate rib structures may provide greater image improvements for the distortions most important to echocardiography. Processing wavefronts with techniques such as angular spectrum filtering can remove some spurious arrivals,[50] although such computations may be difficult to incorporate into a general correction algorithm. Other possible methods include those incorporating models of tissue structure. Models incorporating ray acoustics[9] may provide improvement, but implicitly neglect diffraction and scattering effects, so that aberration correction would be incomplete, particularly for small intercostal spaces. A more complete aberration correction method could employ synthetic focusing using full-wave numerical computation of acoustic fields within sufficiently accurate models of tissue structure. This method has been implemented, within the context of a quantitative frequency-domain inverse scattering method, in Ref. 51. However, the results presented here indicate that distortion caused by soft tissue and rib structures varies widely based on morphological variations between (and within) individuals. Thus, for any general correction method employing models of tissue structure, separate models of tissue structure must be constructed for each region of interest.

V. CONCLUSIONS

A computational study of ultrasonic propagation through the chest wall, including tissue-dependent absorption as well as detailed anatomical cross sections, has been presented. For soft tissue paths, computational results for arrival time distortion, energy level distortion, and correlation lengths of these distortions are comparable to those reported in previous chest wall measurements. Both simulations and measurements indicate that arrival time distortion and energy level distortion caused by soft tissues in the human chest wall is smaller than that caused by the human abdominal wall. Differences in morphology between the abdominal wall and the chest wall provide a probable explanation for this difference.

Distortion caused by rib structures is much more severe than that caused by soft tissues. Reflections and diffraction from rib structures complicate wavefronts that travel through soft tissue paths adjacent to ribs and can cause arrival time and energy level fluctuations much greater than those induced by soft tissue structures. Wavefronts propagating directly through rib structures are attenuated by both internal absorption and reflection at interfaces between bone, cartilage, and soft tissue. Internal scattering within rib structures causes distortion phenomena that include severe waveform and energy level distortion, additional attenuation, and lowering of the effective frequency for the transmitted pulse. The strong dependence of distortion on the morphological details of rib structures presents a major challenge for aberration correction in echocardiography.

Simulation of propagation through soft tissue paths using three different pulse frequencies has indicated that the distortion types investigated here have different frequency dependence. Arrival time fluctuations increase subtly with frequency, while energy level and waveform distortion increase greatly. Thus, a substantial portion of arrival time fluctuations produced by the chest wall may be explained by large-scale tissue variations, but some arrival time distortion and most energy level and waveform distortion apparently result from scattering. Thus, correction of wavefront distortion caused by soft tissues should become both more important and more challenging as pulse frequencies employed in imaging systems are increased.

ACKNOWLEDGMENTS

The authors thank Cari Kelly, Tara Jones, Tracy David, and Michael Pirri for assistance in creating accurate tissue maps of the chest wall cross sections. The original two-dimensional version of the distortion estimation software using the reference waveform method was developed by D.-L. Donald Liu. Funding for this investigation was provided by NIH grants No. DK 45533, No. HL 50855, and No. CA 74050, U.S. Army Grant No. DAMD17-98-1-8141, DARPA Grant N00014-96-0749, and the University of Rochester Diagnostic Ultrasound Research Laboratory Industrial Associates. Some computations were performed at the Cornell National Supercomputing Facility, which was supported in part by the National Science Foundation, New York State, and the IBM Corporation.

[1] H. Feigenbaum, *Echocardiography* (Lea and Febiger, Philadelphia, 1994).

[2] A. E. Weyman, *Principles and Practice of Echocardiography,* 5th ed. (Lea and Febiger, Philadelphia, 1994).

[3] J. T. T. Chen, *Essentials of Cardiac Imaging*, 2nd ed. (Lippincott-Raven, Philadelphia, 1997).

[4] F. M. Clements and N. P. de Bruijn, *Transesophageal Echocardiography* (Little, Brown, and Company, Boston, 1991).

[5] K.-L. Chan, G. I. Cohen, R. A. Sochowski, and M. G. Baird, "Complications of transesophageal echocardiography in ambulatory adult patients: analysis of 1500 consecutive examinations," J. Am. Soc. Echocardiogr. **4**, 577–582 (1991).

[6] W. G. Daniel, R. Erbel, W. Kasper, C. A. Visser, R. Engberding, G. R. Sutherland, E. Grube, P. Hanrath, B. Maisch, K. Dennig, M. Schartl, P. Kremer, C. Angermann, S. Iliceto, J. M. Curtius, and A. Mügge, "Safety of transesophageal echocardiography: a multicenter survey of 10,419 examination," Circulation **83**, 817–821 (1991).

[7] A. D. Savakus, K. K. Shung, and N. B. Miller, "Distortions of ultrasonic field introduced by the rib cage in echocardiography," J. Clin. Ultrasound **10**, 413–419 (1982).

[8] L. M. Hinkelman, T. L. Szabo, and R. C. Waag, "Measurements of ultrasonic pulse distortion produced by the human chest wall," J. Acoust. Soc. Am. **101**, 2365–2373 (1997).

[9] Y. Y. Botros, E. S. Ebbini, and J. L. Volakis, "Two-step hybrid virtual array-ray (VAR) technique for focusing through the rib cage," IEEE Trans. Ultrason. Ferroelectr. Freq. Control **45**, 989–999 (1998).

[10] T. D. Mast, L. M. Hinkelman, M. J. Orr, V. W. Sparrow, and R. C. Waag, "Simulation of ultrasonic pulse propagation through the abdominal wall," J. Acoust. Soc. Am. **102**, 1177–1190 (1997).

[11] L. M. Hinkelman, T. D. Mast, L. A. Metley, and R. C. Waag, "The effect of abdominal wall morphology on ultrasonic pulse distortion. Part I: Measurements," J. Acoust. Soc. Am. **104**, 3635–3649 (1998).

[12] T. D. Mast, L. M. Hinkelman, M. J. Orr, and R. C. Waag, "The effect of abdominal wall morphology on ultrasonic pulse distortion. Part II: Simulations," J. Acoust. Soc. Am. **104**, 3651–3664 (1998).

[13] H. Kolsky, *Stress Waves in Solids* (Clarendon, Oxford, UK, 1953), pp. 106–129.

[14] S. Leeman, L. Hutchins, and J. P. Jones, "Bounded pulse propagation," in *Acoustical Imaging*, edited by P. Alais and A. F. Metherell (Plenum, New York, 1982), Vol. 10, pp. 427–435.

[15] S. Finette, "Computational methods for simulating ultrasound scattering in soft tissue," IEEE Trans. Ultrason. Ferroelectr. Freq. Control **34**, 283–292 (1987).

[16] C. W. Manry and S. L. Broschat, "FDTD simulations for ultrasound propagation in a 2-D breast model," Ultrason. Imaging **118**, 25–34 (1996).

[17] V. W. Sparrow and R. Raspet, "A numerical method for general finite amplitude wave propagation and its application to spark pulses," J. Acoust. Soc. Am. **90**, 2683–2691 (1991).

[18] R. W. MacCormack, *Lecture Notes in Physics* (Springer-Verlag, Berlin, 1971), Vol. 8, p. 151.

[19] D. Gottlieb and A. Turkel, "Dissipative two-four methods for time-dependent problems," Math. Comput. **30**, 703–723 (1976).

[20] E. Turkel, "On the practical use of high-order methods for hyperbolic systems," J. Comput. Phys. **35**, 319–340 (1980).

[21] L. M. Hinkelman, L. A. Metlay, C. J. Churukian, and R. C. Waag, "Modified Gomori trichrome stain for macroscopic tissue slices," J. Histotech. **19**, 321–323 (1996).

[22] H. Gray, *Gray's Anatomy*, edited by T. P. Pick and R. Howden (Gramercy, New York, 1977), pp. 358–364 (facsimile of 1901 American edition of *Anatomy, Descriptive and Surgical*).

[23] R. Warwick and P. L. Williams, *Gray's Anatomy*, 35th ed. (Saunders, Philadelphia, 1973), pp. 488–490, 519–527.

[24] A. Elkeles, "Sex differences in the calcification of the costal cartilages," J. Am. Geriat. Soc. **14**, 456–461 (1966).

[25] N. Bilaniuk and G. S. K. Wong, "Speed of sound in pure water as a function of temperature," J. Acoust. Soc. Am. **93**, 1609–1612 (1993).

[26] *Handbook of Chemistry and Physics*, edited by R. C. Weast (CRC Press, Boca Raton, 1985), p. F-10.

[27] S. A. Goss, R. L. Johnston, and F. Dunn, "Comprehensive compilation of empirical ultrasonic properties of mammalian tissues," J. Acoust. Soc. Am. **64**, 423–457 (1978).

[28] S. A. Goss, R. L. Johnston, and F. Dunn, "Compilation of empirical ultrasonic properties of mammalian tissues II," J. Acoust. Soc. Am. **68**, 93–108 (1980).

[29] J. E. Olerud, W. O'Brien, M. A. Riederer-Henderson, D. Steiger, F. K. Forster, C. Daly, D. J. Ketterer, and G. F. Odland, "Ultrasonic assessment of skin and wounds with the scanning laser acoustic microscope," J. Invest. Dermatol. **8**, 615–623 (1987).

[30] R. E. Neuman and M. A. Logan, "The determination of collagen and elastin in tissues," J. Biol. Chem. **186**, 549–556 (1950).

[31] F. A. Duck, *Physical Properties of Tissue: A Comprehensive Reference Book* (Academic, New York, 1990).

[32] K. T. Dussik and D. J. Fritch, "Determination of sound attenuation and sound velocity in the structure constituting the joints, and of the ultrasonic field distribution within the joints on living tissues and anatomical preparations, both in normal and pathological conditions," Progress Report to Public Health Service, National Institutes of Health Project A454, 15 September 1956.

[33] H. Q. Woodard and D. R. White, "The composition of body tissues" Br. J. Radiol. **59**, 1209–1219 (1986).

[34] International Commission on Radiation Units and Measurements, *ICRU Report 61: Tissue Substitutes, Phantoms, and Computational Modelling in Medical Ultrasound* (ICRU, Bethesda, MD, 1998), pp. 43–51.

[35] K. H. Herzfeld and T. A. Litovitz, *Absorption and Dispersion of Ultrasonic Waves* (Academic, New York, 1959), pp. 353–361.

[36] Simulations were performed on a Linux workstation with an AMD K6 processor running at 200 MHz and 128 MB of random-access memory. The simulation code was written in Fortran 77 and compiled using the front end fort77 and the Fortran-to-C converter f2c with the Gnu C compiler gcc.

[37] D.-L. Liu and R. C. Waag, "Correction of ultrasonic wavefront distortion using backpropagation and a reference waveform method for time-shift compensation," J. Acoust. Soc. Am. **96**, 649–660 (1994).

[38] L. M. Hinkelman, D.-L. Liu, L. A. Metlay, and R. C. Waag, "Measurements of ultrasonic pulse arrival time and energy level variations produced by propagation through abdominal wall," J. Acoust. Soc. Am. **95**, 530–541 (1994).

[39] J. Wolff, *Das Gesetz der Transformation der Knochen* (Hirschwald, Berlin, 1982).

[40] J. C. Rice, S. C. Cowin, and J. A. Bowman, "On the dependence of the elasticity and strength of cancellous bone on apparent density," J. Biomech. **21**, 155–168 (1988).

[41] J. Y. Rho, R. B. Ashman, and C. H. Turner, "Young's modulus of trabecular and cortical bone material: ultrasonic and tensile measurements," J. Biomech. **26**, 111–119 (1993).

[42] C. H. Turner, J. Rho, Y. Takano, T. Y. Tsui, and G. M. Pharr, "The

elastic properties of trabecular and cortical bone tissues are similar: results from two microscopic measurement techniques," J. Biomech. **32**, 437–441 (1999).

[43] S. Lees, J. M. Ahern, and M. Leonard, "Parameters influencing the sonic velocity in compact calcified tissues of various species," J. Acoust. Soc. Am. **74**, 28–33 (1983).

[44] S. Lees, "Sonic properties of mineralized tissues," in *Tissue Characterization with Ultrasound*, edited by J. F. Greenleaf (CRC Press, Boca Raton, 1986), pp. 207–226.

[45] L. A. Frizzell, E. L. Carstensen, and J. F. Dyro, "Shear properties of mammalian tissues at low MHz frequencies," J. Acoust. Soc. Am. **60**, 1409–1411 (1976).

[46] E. L. Madsen, H. J. Sathoff, and J. A. Zagzebski, "Ultrasonic shear wave properties of soft tissues and tissuelike materials," J. Acoust. Soc. Am. **74**, 1346–1355 (1983).

[47] L. Adler and K. V. Cook, "Ultrasonic properties of freshly frozen dog tibia," J. Acoust. Soc. Am. **58**, 1107–1108 (1975).

[48] S. S. Kohles, J. R. Bowers, A. C. Vailas, and R. Vanderby, "Ultrasonic wave velocity measurement in small polymeric and cortical bone specimens," J. Biomech. Eng. **119**, 232–236 (1997).

[49] K. Chandra and C. Thompson, "Ultrasonic characterization of fractal media," Proc. IEEE **81**, 1523–1533 (1993).

[50] L. M. Hinkelman and D.-L. Liu, "Measurement and analysis of ultrasonic pulse wavefront distortion produced by chest wall," *Proceedings of the 12th Annual University of Rochester Diagnostic Ultrasound Research Laboratory Industrial Associates Meeting*, 1995, pp. 8–25.

[51] T. D. Mast, A. I. Nachman, and R. C. Waag, "Focusing and imaging using eigenfunctions of the scattering operator," J. Acoust. Soc. Am. **102**, 715–725 (1997).

APPENDIX E

IEEE TRANSACTIONS ON ULTRASONICS, FERROELECTRICS, AND FREQUENCY CONTROL, VOL. 48, NO. 2, MARCH 2001

A k-Space Method for Large-Scale Models of Wave Propagation in Tissue

T. Douglas Mast, *Member, IEEE,* Laurent P. Souriau, D.-L. Donald Liu, *Member, IEEE,*
Makoto Tabei, *Member, IEEE,* Adrian I. Nachman, and Robert C. Waag, *Fellow, IEEE*

***Abstract*—Large-scale simulation of ultrasonic pulse propagation in inhomogeneous tissue is important for the study of ultrasound-tissue interaction as well as for development of new imaging methods. Typical scales of interest span hundreds of wavelengths; most current two-dimensional methods, such as finite-difference and finite-element methods, are unable to compute propagation on this scale with the efficiency needed for imaging studies. Furthermore, for most available methods of simulating ultrasonic propagation, large-scale, three-dimensional computations of ultrasonic scattering are infeasible. Some of these difficulties have been overcome by previous pseudospectral and *k*-space methods, which allow substantial portions of the necessary computations to be executed using fast Fourier transforms. This paper presents a simplified derivation of the *k*-space method for a medium of variable sound speed and density; the derivation clearly shows the relationship of this *k*-space method to both past *k*-space methods and pseudospectral methods. In the present method, the spatial differential equations are solved by a simple Fourier transform method, and temporal iteration is performed using a *k-t* space propagator. The temporal iteration procedure is shown to be exact for homogeneous media, unconditionally stable for "slow" ($c(x) \leq c_0$) media, and highly accurate for general weakly scattering media. The applicability of the *k*-space method to large-scale soft tissue modeling is shown by simulating two-dimensional propagation of an incident plane wave through several tissue-mimicking cylinders as well as a model chest wall cross section. A three-dimensional implementation of the *k*-space method is also employed for the example problem of propagation through a tissue-mimicking sphere. Numerical results indicate that the *k*-space method is accurate for large-scale soft tissue computations with much greater efficiency than that of an analogous leapfrog pseudospectral method or a 2-4 finite difference time-domain method. However, numerical results also indicate that the *k*-space method is less accurate than the finite-difference method for a high contrast scatterer with bone-like properties, although qualitative results can still be obtained by the *k*-space method with high efficiency. Possible extensions to the method, including representation of absorption effects, absorbing boundary conditions, elastic-wave propagation, and acoustic nonlinearity, are discussed.**

I. Introduction

Computation of a scattered acoustic field, given an incident wavefield and complete specification of an inhomogeneous medium, is known as the forward scattering problem. Numerical solution of the forward scattering problem is central to many aspects of ultrasonic imaging, including inverse scattering methods, numerical studies of wavefront distortion, and development of new methods for adaptive focusing. Most methods for numerical solution of the forward scattering problem fall into one of three categories: finite difference methods, finite element methods, and spectral methods.

Finite difference and finite element methods are known as local because the wave propagation equations of interest are solved at each point based only on conditions at nearby points. In contrast, spectral methods, such as the k-space method [1]–[7] and the pseudospectral approach [8]–[14], are called global because information from the entire wavefield is employed to solve the wave propagation equations at each point. In part because of their global nature, spectral methods can be more accurate than local methods—for instance, pseudospectral methods applied to periodic problems have been shown to be equivalent to finite difference methods of infinite order [12].

Spectral methods also have considerable advantages for large-scale forward solvers because the required storage and the number of operations per iteration can be dramatically reduced compared with local methods. This advantage occurs principally because spectral methods can allow computations to be performed on coarser grids while maintaining accuracy. For example, finite element methods and high-order finite difference methods typically require grid spacings on the order of 10 points per minimum wavelength; second-order finite difference methods can require 20 points per wavelength [10]. Spectral methods, in theory, require only two points per wavelength (spatial Nyquist sampling), although for computations of propagation in inhomogeneous media, greater accuracy is achieved with grid spacings on the order of four points per wavelength [10], [11], [14].

This report addresses the problem of large-scale ultrasonic wave propagation in biological media, such as human

Manuscript received February 26, 1999; accepted August 9, 2000. This research was funded by NIH Grants DK 45533, HL 50855, CA 74050, and 1R29CA81688; US Army Grant DAMD-17-98-1-8141; DARPA Grant N00014-96-0749; and the University of Rochester Diagnostic Ultrasound Research Laboratory Industrial Associates.

T. D. Mast is with the Applied Research Laboratory, The Pennsylvania State University, University Park, PA 16802 (e-mail: mast@sabine.acs.psu.edu).

D.-L. Donald Liu is with the Ultrasound Group, Siemens Medical Systems, Issaquah, WA 98027.

L. P. Souriau, M. Tabei, and R. C. Waag are with the Department of Electrical and Computer Engineering, University of Rochester, Rochester, NY 14627. R. C. Waag is also with the Department of Radiology.

A. I. Nachman is with the Department of Mathematics, University of Rochester, Rochester, NY 14627.

0885–3010/$10.00 © 2001 IEEE

tissue. For problems of interest in medical ultrasound, domain sizes can often exceed the capabilities of conventional forward solvers. For example, one computation of realistic scale would be the simulated propagation of a pulse with an upper bandwidth limit of 5 MHz in a volume of dimensions 30 mm on each side and a nominal sound speed of 1.5 mm/μs, so that the minimum wavelength is 0.3 mm. For this computation, a second-order finite difference method (using 20 points per wavelength) would require a three-dimensional grid containing 8×10^9 nodes; a finite element or fourth-order finite difference method (using 10 points per wavelength) would require 1×10^9 nodes; and a spectral method (using four points per wavelength) would require 6.4×10^7 nodes. Because a grid of 6.4×10^7 single precision complex numbers requires storage of 512 megabytes, only spectral methods are feasible for realistic three-dimensional computations on present-day computers that typically have a maximum random-access memory storage of several gigabytes. The efficiency provided by fast Fourier transform implementations of spectral algorithms is a further reason why spectral methods are a practical approach to large-scale and three-dimensional computations of ultrasonic wave propagation.

Previous spectral approaches have included pseudospectral methods, in which spatial derivatives are evaluated globally by Fourier transformation and wavefields are advanced in time using various numerical integration techniques [8]–[14]. This method has provided high accuracy in many cases; however, temporal iteration techniques that provide good accuracy for large-scale models typically require small time steps, significant additional computations, or storage of wavefields from additional time steps [13], so that the efficiency advantages of the pseudospectral approach are less than might first be expected. The k-space family of methods [1]–[7] can overcome this problem by providing explicit temporal propagators related to the Green's function for wave propagation in k-t (spatial frequency and time) space.

The present paper presents a simplified derivation of the k-space method using a differential representation of the wave propagation equations. The spatial part of the wave propagation equations is solved by Fourier transformation in a manner analogous to past pseudospectral methods; this derivation is shown to be theoretically equivalent to previous integral formulations of the k-space method. Temporal iteration is performed using a k-t space propagator [2], which is shown to be exact for homogeneous media and, in general, provides much greater accuracy and stability than leapfrog iteration (in which temporal derivatives are evaluated using second-order accurate finite differences) without significant additional computation or storage requirements. Thus, the k-space method provides spatial and temporal accuracy ideal for large-scale models of acoustic propagation in weak scattering media.

Subsequently, a derivation of the k-space method is presented for propagation in fluid media with spatially dependent sound speed and density. For several canonical forward problems relevant to ultrasonic imaging, the accuracy and efficiency of the k-space method is compared with a pseudospectral method employing leapfrog iteration and also with a 2-4 finite difference time-domain method. The k-space and finite difference methods are also used in an example computation for a large-scale, two-dimensional tissue model. Another example computation illustrates the efficiency of the k-space method for three-dimensional scattering computations. Possible extensions of the present k-space method, including multiple relaxation effects for absorption, absorbing boundary conditions, inclusion of elastic and nonlinear acoustic effects, and parallelization, are discussed.

II. THEORY

A. Derivation of the k-Space Method

The k-space method for solving the acoustic scattering problem is briefly derived subsequently. The derivation is simpler than those previously published and also provides some new insight regarding the remarkable accuracy and stability characteristics of the k-space method.

The method is applicable to large-scale modeling of linear ultrasonic propagation in soft tissues, which are modeled here as fluid media with spatially dependent sound speed and density. Although the k-space method described subsequently can be extended to include absorption effects, acoustic nonlinearity, and shear-wave propagation, these effects are neglected in this derivation for simplicity.

For a fluid medium with spatially dependent sound speed and density, the linear acoustic wave equation is [15]

$$\nabla \cdot \left(\frac{1}{\rho(\mathbf{x})} \nabla p(\mathbf{x},t) \right) - \frac{1}{\rho(\mathbf{x})\, c(\mathbf{x})^2} \frac{\partial^2 p(\mathbf{x},t)}{\partial t^2} = 0 \tag{1}$$

where $p(\mathbf{x},t)$ is the acoustic perturbation in pressure, $\rho(\mathbf{x})$ is the spatially dependent density, and $c(\mathbf{x})$ is the spatially dependent sound speed.

By defining the normalized wavefield $f(\mathbf{x},t) \equiv p(\mathbf{x},t)/\sqrt{\rho(\mathbf{x})}$, as performed in a number of previous studies (e.g., [16], [17]), the first-order derivative term can be eliminated from (1). Details of this step are given in [6]. When the wavefield is also split into incident and scattered parts, such that $f(\mathbf{x},t) = f_i(\mathbf{x},t) + f_s(\mathbf{x},t)$, a wave equation for the scattered field can be written

$$\nabla^2 f_s(\mathbf{x},t) - \frac{1}{c_0^2} \frac{\partial^2 f_s(\mathbf{x},t)}{\partial t^2} = \frac{1}{c_0^2} \left(q(\mathbf{x},t) + \frac{\partial^2 v(\mathbf{x},t)}{\partial t^2} \right). \tag{2}$$

The terms on the right-hand side are effective sources associated with density and sound speed variations, which are defined as

$$q(\mathbf{x},t) = c_0^2 \sqrt{\rho(\mathbf{x})}\, \nabla^2 \left(1/\sqrt{\rho(\mathbf{x})} \right) f(\mathbf{x},t) \tag{3}$$

and

$$v(\mathbf{x},t) = \left(\frac{c_0^2}{c(\mathbf{x})^2} - 1\right) f(\mathbf{x},t). \tag{4}$$

The incident wavefield $f_i(\mathbf{x},t)$ is required to satisfy the usual wave equation without any source terms [i.e., the D'Alembertian operator from the left-hand side of (2), applied to $f_i(\mathbf{x},t)$, is equal to zero]. Thus, the total wavefield $f(\mathbf{x},t)$ also satisfies (2) identically, so that the numerical algorithm developed for the scattered field is equally applicable to the total field.

With the additional definition of an auxiliary field $w(\mathbf{x},t) = f_s(\mathbf{x},t) + v(\mathbf{x},t)$, (2) can be rewritten in k-space as the coupled set of equations

$$\frac{\partial^2 W(\mathbf{k},t)}{\partial t^2} = (c_0 k)^2 \left[V(\mathbf{k},t) - W(\mathbf{k},t)\right] - Q(\mathbf{k},t), \tag{5}$$

$$V(\mathbf{k},t) = \mathbf{F}\left[\left(1 - \frac{c(\mathbf{x})^2}{c_0^2}\right)\left[f_i(\mathbf{x},t) + w(\mathbf{x},t)\right]\right], \tag{6}$$

$$Q(\mathbf{k},t) = c_0^2\, \mathbf{F}\left[\sqrt{\rho(\mathbf{x})}\, \nabla^2 \left(\sqrt{\frac{1}{\rho(\mathbf{x})}}\right)\left[f_i(\mathbf{x},t) + w(\mathbf{x},t) - v(\mathbf{x},t)\right]\right] \tag{7}$$

where $\mathbf{F}$ denotes spatial Fourier transformation, and capital letters indicate spatially Fourier transformed quantities.

For each point in k-space, (5) represents an independent ordinary differential equation equivalent to the standard simple harmonic oscillator equation with the source terms $(c_0 k)^2 V$ and $-Q$. This ordinary differential equation can be discretized in several ways. For instance, a second-order accurate finite difference representation of the second-order time derivative allows (5) to be written as

$$W(\mathbf{k},t+\Delta t) - 2\,W(\mathbf{k},t) + W(\mathbf{k},t-\Delta t) \approx (c_0 k \Delta t)^2 \left[V(\mathbf{k},t) - W(\mathbf{k},t) - \frac{Q(\mathbf{k},t)}{(c_0 k)^2}\right] \tag{8}$$

where Δt is the time step. This is known as leapfrog iteration; use of (8) in the current method is analogous to commonly used pseudospectral approaches [13], [14]. (Although increased accuracy can be achieved by higher order methods such as fourth-order Adams-Bashforth or Adams-Moulton iteration, these methods have the disadvantage of requiring storage of the entire computational grid for additional time steps [12], [13]).

A more accurate form of the temporal iterator is obtained using a nonstandard finite difference approach. For the homogeneous simple harmonic oscillator equation, an exact discretization is known [18]. (That is, for any temporal and spatial step sizes, the discrete difference equations yield exactly the same solutions as the continuous differential equations. A similar exact discretization for the linear part of the Korteweg-de Vries equation was presented in [19].) Use of this nonstandard discretization leads to the following discrete form of (5):

$$W(\mathbf{k},t+\Delta t) - 2\,W(\mathbf{k},t) + W(\mathbf{k},t-\Delta t) = 4\sin^2\left(\frac{c_0 k \Delta t}{2}\right)\left[V(\mathbf{k},t) - W(\mathbf{k},t) - \frac{Q(\mathbf{k},t)}{(c_0 k)^2}\right]. \tag{9}$$

Because the discretization employed is exact for the simple harmonic oscillator equation, (9) is exactly equivalent to the differential equation, (5), for the case of a homogeneous medium [i.e., $V(\mathbf{k},t) = Q(\mathbf{k},t) = 0$]. Numerical results shown subsequently indicate that high accuracy is also achieved for weak scattering media, in which case $V(\mathbf{k},t) \ll W(\mathbf{k},t)$ and $Q(\mathbf{k},t) \ll W(\mathbf{k},t)$. The present discretization method is equivalent to that employed by Bojarski (the form given in [2] follows after some trigonometric manipulation); however, previous derivations of this method have been based on approximations to an integral representation of (5) [2], [6]. It may also be noted that (8) and (9) are equivalent in the limit of small Δt. However, results shown subsequently indicate that, for weak scattering media, use of the k-t propagator (9) provides much greater accuracy for larger time steps.

In numerical implementation of the k-space algorithm, (5) is used to advance the auxiliary field $W(\mathbf{k},t)$ in time. Eq. (6) and (7) represent updates of the effective scattering sources v and q and their spatial Fourier transformation to yield the k-space effective sources V and Q. Notable is that the effective source v is directly proportional to the square of the sound speed variation of the medium, and the effective source q is directly proportional to the Laplacian of $1/\sqrt{\rho(\mathbf{x})}$. Thus, for a piecewise constant inhomogeneous medium, v may be non-zero everywhere, but q is nonzero (and singular) only on borders between regions.

The present k-space algorithm can now be summarized as follows:

Step 1: set any initial conditions for $w(\mathbf{x},t)$ and spatially Fourier transform [by fast Fourier transform (FFT)] to obtain initial conditions for $W(\mathbf{k},t)$

Step 2: define the incident wave $f_i(\mathbf{x},t)$ on the entire grid ($f_i(\mathbf{x},t)$ can be identically zero)

Step 3: compute $v(\mathbf{x},t)$ and transform to obtain $V(\mathbf{k},t)$ (6)

Step 4: compute $q(\mathbf{x},t)$ and transform to obtain $Q(\mathbf{k},t)$ (7)

Step 5: evaluate $W(\mathbf{k},t+\Delta t)$ (9) and inverse transform to obtain $w(\mathbf{x},t+\Delta t)$

Step 6: set $t \rightarrow t + \Delta t$ and go to step 2

This method requires three fast Fourier transform operations per time step (one each for steps 3, 4, and 5 of the algorithm enumerated above).

Also notable is that the algorithm is directly applicable to one-dimensional, two-dimensional, and three-dimensional propagation. This is possible because the k-t space Green's function has an identical form for any number of spatial dimensions [2]. For example, to implement the present methods for two-dimensional computations, the algorithm just outlined is simply employed using two-dimensional Fourier transforms. The three-dimensional version of the algorithm is formally identical but with three-dimensional Fourier transforms.

To distinguish between the standard leapfrog iteration method and the improved method used here, the following nomenclature is used in the present paper. The algorithm employing (9) is referred to as a k-space method, and the corresponding algorithm employing (8) for temporal iteration is referred to as a leapfrog pseudospectral method. This nomenclature is used because the algorithm employing (9) is mathematically equivalent to an extended form of Bojarski's k-space method [2] cast in terms of differential equations rather than integral equations. The algorithm employing (8) is referred to as pseudospectral because it is mathematically equivalent to a conventional "method of lines" pseudospectral algorithm with leapfrog iteration [12]. [A conventional pseudospectral algorithm of this form would employ the spatial inverse Fourier transform of (8) for temporal iteration.]

B. Temporal and Spatial Sampling Criteria

To determine the usable range of spatial and temporal sampling rates for the present k-space method, limits on the stability and accuracy of the method can be evaluated analytically.

The stability of the k-space and leapfrog pseudospectral methods derived previously can be evaluated using standard, linear von Neumann stability analysis [20]. Using this technique, the difference equations that comprise (8) and (9) are applied to a test function

$$W_{\text{test}}(\mathbf{k}, n\Delta t) = \vartheta(\mathbf{k})^n \, \psi(\mathbf{k}) \tag{10}$$

where $\psi(\mathbf{k})$ is a spatial-frequency domain eigenmode and $\vartheta(\mathbf{k})$ is a temporal amplification factor. If a difference equation admits solutions with $|\vartheta(\mathbf{k})| > 1$ for any vector wavenumber $\mathbf{k}$, errors may grow exponentially with time, and the solution is thus unstable. If $|\vartheta(\mathbf{k})| \leq 1$ for all wavenumbers, then the solution is numerically stable. For simplicity, the present stability computation is performed in the absence of density variations; the incident wave $f_i(\mathbf{x}, t)$ is assumed (without loss of generality) to be zero. To obtain limiting stability criteria, the worst case sound speed inhomogeneity $c(\mathbf{x}) = c_{\max}$ is also assumed.

Application of this technique to (8), which represents a leapfrog pseudospectral approach, yields a quadratic equation for $\vartheta(\mathbf{k})$. The resulting stability condition is

$$c_{\max} k_{\max} \Delta t \leq 2 \tag{11}$$

where $c_{\max}$ is the maximum sound speed in the region of computation; $k_{\max} = \pi/\Delta x$ is the maximum wavenumber in the discrete Fourier transforms used to compute $W(\mathbf{k}, \mathbf{t})$; and Δt and Δx, respectively, are the temporal and spatial steps employed. Using the standard definition for a Courant-Friedrichs-Lewy (CFL) number [21], the stability condition

$$\text{CFL} \equiv \frac{c_0 \Delta t}{\Delta x} \leq \frac{2}{\pi} \frac{c_0}{c_{\max}} \tag{12}$$

is obtained for the leapfrog pseudospectral method represented by (8).

Application of the same analysis to the k-space iterator of (9) yields the stability condition

$$\sin \frac{\pi \, \text{CFL}}{2} \leq \frac{c_0}{c_{\max}}. \tag{13}$$

This condition has the remarkable result that, for media with $c(\mathbf{x}) \leq c_0$ everywhere, the linear numerical stability of the k-space method is unconditional. However, for any medium, an upper limit on the time step still arises from the requirement of sampling at the Nyquist rate: that is, the time step should be sufficiently small to allow two samples per period for the highest frequency component of the computed field. Thus, the temporal sampling criterion can be written

$$\Delta t \leq \frac{1}{2 f_{\max}} = \frac{\pi}{c_{\max} k_{\max}} = \frac{\Delta x}{c_{\max}} \tag{14}$$

or simply $\text{CFL} \leq c_0/c_{\max}$. The stability criterion (13) is met whenever the Nyquist sampling criterion (14) is met; thus, the Nyquist sampling criterion is more restrictive.

For the spatial discretization, a Nyquist criterion based on the maximum spatial frequency $k_{\max} = \pi/\Delta x$ is met for any step size Δx. However, the inhomogeneous medium will be inaccurately represented (aliased) if its Fourier transform has significant spatial-frequency components beyond $k_{\max}$. Aliasing is a particular problem when the medium contains discontinuities, which correspond to infinite spatial frequency content; removal of errors associated with discontinuities is discussed in the following section.

C. Effects of Discontinuities

The Fourier transforms performed in the present k-space algorithm can lead to numerical artifacts (related to the Gibbs phenomenon) when the inhomogeneous medium contains discontinuities in sound speed or density. To avoid such artifacts, the scattering object can be spatially filtered to smooth any discontinuities. That is, the spatially dependent sound speed $c(\mathbf{x})$ and density $\rho(\mathbf{x})$ can be replaced by filtered functions of the form

$$u_{\text{filtered}}(\mathbf{x}) = \mathbf{F}^{-1}[U(\mathbf{k}) \, \phi(\mathbf{k})] \tag{15}$$

in which the Fourier transform $U(\mathbf{k})$ of the function $u(\mathbf{x})$ is multiplied by a low-pass spatial frequency filter $\phi(\mathbf{k})$. The function $U(\mathbf{k})$ should be represented as accurately as possible; for example, exact Fourier transforms of simply shaped inhomogeneities can be used when available. Subsequently, the exact Fourier transform of a two-dimensional disk is employed for filtered representations of an infinite cylinder.

In the present study, the filter employed is the half-band filter [22]

$$\phi_H(k) = \begin{cases} 1, & k/k_{\max} < 1/2 \\ f(k/k_{\max} - 1/2), & 1/2 \leq k/k_{\max} \leq 3/2 \end{cases} \tag{16}$$

where

$$f(\theta) = \frac{1}{2} + \frac{9}{16}\cos(\pi\theta) - \frac{1}{16}\cos(3\pi\theta) \tag{17}$$

and k is the magnitude of the spatial frequency vector $\mathbf{k}$.

This filter defines a smoothly tapered window that causes no attenuation of spatial frequencies below $k_{\max}/2$ and drops to one-half amplitude (-6 dB) at the spatial frequency $k_{\max}$. Zero amplitude is reached at the spatial frequency $3/2\,k_{\max}$, which exceeds the spatial frequency range of the discrete Fourier transforms employed in the k-space algorithm, so that aliasing error is not eliminated by the half-band filter. However, a strict bandlimiting filter was found to cause excessive loss of high spatial frequency components in the medium, so that scattering amplitude near the backscatter direction was greatly reduced. The half-band filter of (16) was found to greatly reduce Gibbs phenomenon artifacts and maintain enough high spatial frequency components of inhomogeneities to provide accurate backscatter results.

For inhomogeneous media, exact Fourier transforms are not generally available. However, artifacts associated with discontinuities can still be removed by the methods given previously. For example, a finely sampled representation of the medium could be filtered using (15) and then decimated to the desired spatial step size.

III. Numerical Methods

Numerical implementation of the k-space algorithm was accomplished using the algorithm described previously. The normalized incident wave $f_i(\mathbf{x}, t)$ was defined as a plane wave with Gaussian temporal shape:

$$f_i(\mathbf{x}, t) = \rho(\mathbf{x})^{-\frac{1}{2}} \sin(\omega_0 \tau)\, e^{-\tau^2/(2\sigma^2)} \tag{18}$$

where τ is the retarded time $\tau = t - (x - x_0)/c_0$ and x_0 is the initial central position of the wavefield. This incident wave was implicitly specified using initial conditions (as for the incident plane wave in [23]) rather than explicitly updated at each time step. Boundary conditions were implicitly periodic at each edge of the computational domain because of the inherent periodicity of the fast Fourier transforms employed.

Wavefields were computed on two-dimensional grids that were large enough to avoid influence of "wraparound" error within the temporal window of interest. All k-space computations were performed on square grids of size N by N. Prior to execution of the main computation loop, the Laplacian occurring in (7) was evaluated using second-order accurate, centered finite difference representations of the second derivative in each direction. Within the main computational loop, all spatial derivatives were evaluated by Fourier transformation, implemented using an FFT algorithm [24]. For maximum FFT efficiency, grid sizes N were chosen to be integers with prime factors no greater than three.

To reduce any spatial anistropy associated with the rectangular grid shape, the spatial frequency time-domain wavefield $W(\mathbf{k}, t + \Delta t)$ was windowed using the radially symmetric window

$$\phi(\mathbf{k}) = H(k_{\max} - k) \tag{19}$$

before inversion to yield $w(\mathbf{x}, t + \Delta t)$ (i.e., within step 5 in the algorithm enumerated previously). In (19), H is, as before, the Heaviside step function, $k_{\max}$ is the maximum wavenumber magnitude (equal to $\pi/\Delta x$ because the spatial frequency range sampled extends from $-\pi/\Delta x$ to $\pi/\Delta x$ in each direction), and k is the magnitude of the vector wavenumber $\mathbf{k}$. In some cases, the medium properties $c(\mathbf{x})$ and $\rho(\mathbf{x})$ were also smoothed by windowing in the spatial-frequency domain using (16) with a wavenumber cutoff of $k_{\max} = \pi/\Delta x$.

For comparison, wavefields were also computed using a second-order in time, fourth-order in space finite difference method, described in [21], [23], [25]–[27]. As for the k-space computations, the incident wave was specified by a single initial condition rather than updated at each time step. Periodic boundary conditions were applied on all sides of the grid. Time steps were determined using a CFL number of 0.25, which is a natural choice for this finite difference method [26]. As in [23] and [28], computations were performed at each time step only on portions of the grid where the wavefields were nonzero; this reduces the required computation time for the finite difference method by about one-half.

To test the k-space and finite difference methods quantitatively, benchmark computations were performed using an exact series solution for the scattering of a plane wave by a fluid cylinder [29]. The sampling rate and waveform shape were chosen to match the time-domain simulation data for the case of interest. The pressure field was then computed for each frequency component with relative magnitude within 60 dB of the peak magnitude. Each single frequency computation truncated the series at the term with a relative contribution less than 10^{-12} times the sum of all terms. The frequency-domain scattered fields were then inverted by FFT to obtain numerically exact solutions for the time-domain pressure fields at the simulated measurement points. An exact time-domain solution for scattering from a fluid sphere was also obtained using an analogous approach.

Benchmark studies of accuracy were performed using a cylinder with radius 2.0 mm and acoustic properties of human fat and a background medium with acoustic properties of water at body temperature. Rationale for use of these values is discussed in [23]. The cylinder had a sound speed of 1.478 mm/μs and a density of 0.950 g/cm^3; the background medium had a sound speed of 1.524 mm/μs

$$
\begin{aligned}
p_{\mathrm{interp}}(x,y) = \sum_{x_i}\sum_{y_i} & \frac{\sin(\pi(x-x_i)/\Delta x)}{\pi(x-x_i)/\Delta x}\,\frac{\mathrm{I}_0[\beta(1-[(x-x_i)/(m\Delta x)]^2)^{1/2}]}{\mathrm{I}_0[\beta]} \\
& \times\frac{\sin(\pi(y-y_i)/\Delta x)}{\pi(y-y_i)/\Delta x}\,\frac{\mathrm{I}_0[\beta(1-[(y-y_i)/(m\Delta x)]^2)^{1/2}]}{\mathrm{I}_0[\beta]}\times p(x_i,y_i), \\
& x-m\Delta x \le x_i < x+m\Delta x, \\
& y-m\Delta x \le y_i < y+m\Delta x
\end{aligned}
\tag{20}
$$

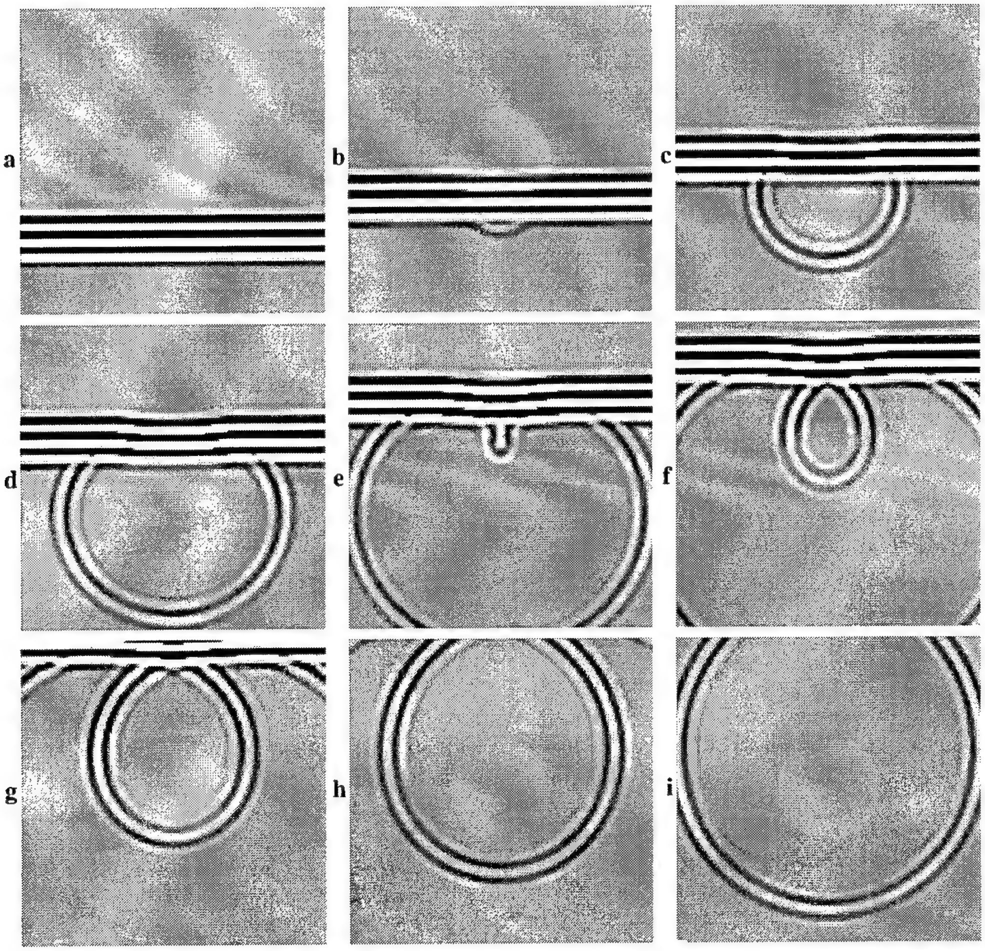

Fig. 1. Time history of total acoustic pressure computed by the k-space method for a cylinder with a 2.0-mm radius and fat-mimicking acoustic properties. The cylinder is sketched as a light gray region. The first panel shows the wavefield impinging on the cylinder at time $t = 0.98$ μs, and subsequent panels (progressing from left to right and top to bottom) show the total wavefield at intervals of 0.98 μs. The acoustic pressure is plotted in all panels using a bipolar logarithmic scale with a 60 dB dynamic range.

and a density of 0.993 g/cm^3. The scattering geometry is as shown in Fig. 1. The incident pulse was a plane wave with Gaussian temporal characteristics, a temporal Gaussian parameter $\sigma = 0.25$ μs, and a central starting position of $x = -4.5$ mm at time zero. For this pulse, a nominal maximum frequency is 4.43 MHz, corresponding to the spectral point 40 dB down from the center frequency (for the benchmark problem, this frequency corresponds to a minimum wavelength of 0.33 mm). The k-space, leapfrog pseudospectral, finite difference, and exact methods described previously were used to compute time histories of the total pressure field at 128 equally spaced "measurement" points spanning a circle of radius 2.5 mm concentric to the cylinder. The pressure was interpolated using a two-dimensional low-pass interpolation filter implemented by the formula [30] [(20), see above], where I_0 is the zero-order modified Bessel function of the first kind, and β is the Kaiser window coefficient, taken here to be 7.0. This choice of β provides a filter with flat response up to about $0.6\,k_{\max}$ and sidelobes at the -70 dB level.

The domain size for each k-space, pseudospectral, and finite difference computation employing this cylinder was 18×18 mm^2.

Further studies of accuracy were performed using a cylinder of radius 10 mm. Other parameters were as described previously for the small problem, except that the radius of the measurement circle was 12.5 mm and the starting position of the wavefront was $x = -14.5$ mm. The k-space method was employed to compute two cases corresponding to unsmoothed and smoothed contrast functions, using a spatial step of four points per minimum wavelength and a CFL number of 0.5. In each k-space computation for this cylinder, the domain size employed was 72×72 mm^2. The finite difference method was employed to compute a single case using a spatial step of 14 points per minimum wavelength, a CFL number of 0.25, and a domain size of 72×60 mm.

To evaluate the relative accuracy and efficiency of the k-space and finite difference methods for a high contrast scatterer, computations were also performed using a cylinder of radius 2.0 mm with the sound speed and density of human bone. The values employed were a sound speed of 3.54 mm/μs and a density of 1.99 g/cm^3 as in [28]. The incident pulse, receiver, and computational domain characteristics were identical to those for the 2.0 mm "fat" cylinder case described previously.

In all of the previously mentioned accuracy tests, a quantitative measure of the accuracy was obtained using the time-domain L^2 error of each numerically computed pressure field $p_{\text{num}}(\mathbf{x}, t)$ versus the corresponding exact series solution $p_{\text{exact}}(\mathbf{x}, t)$. This quantity has the definition

$$\epsilon = \frac{\|p_{\text{num}}(\mathbf{x}_r, t) - p_{\text{exact}}(\mathbf{x}_r, t)\|}{\|p_{\text{exact}}(\mathbf{x}_r, t)\|} \tag{21}$$

where $\|p(\mathbf{x}_r, t)\|$ is the L^2 norm [31] of a matrix composed of the time-domain signal $p(\mathbf{x}, t)$ for all receiver points $\mathbf{x}_r$ and all time samples computed. Eq. (21) represents an accuracy criterion that is much stricter than more general criteria, such as comparison of the rms waveform amplitude or the amplitude and phase at the center frequency. To achieve a low L^2 error by the definition of (21), both the waveform amplitude and phase must be accurately computed for all significant frequency components of the field.

The use of the present k-space method in a more realistic two-dimensional simulation of ultrasonic propagation was also tested. For this purpose, a cross-sectional tissue map of the human chest wall [28] was used as the simulated medium. A pulse center frequency of 3.0 MHz was employed together with a temporal Gaussian parameter of 0.3127 μs; these parameters correspond to the highest center frequency employed in the simulation study reported in [28]. The corresponding nominal minimum wavelength is 0.34 mm. The k-space computation employed four points per minimum wavelength, a CFL number of 0.5, and a grid size of 54.9×54.9 mm^2. The finite difference computation employed 14 points per minimum wavelength, a CFL number of 0.25, and a grid size of 38.5×29.7 mm^2. As in [23] and [28], periodic boundary conditions were applied on the sides perpendicular to the wavefront; first-order radiation boundary conditions [23] were applied on the sides parallel to the wavefront.

Finally, to illustrate the efficiency and accuracy of the present k-space method for three-dimensional computations, scattering from a penetrable sphere with acoustic properties of human muscle (speed, 1.547 mm/μs; density, 1.090 g/cm^3 [23]) was computed. The sphere radius was 1.5 mm; time-domain pressure waveforms were recorded at 128 equally spaced measurement points on the sphere surface (in the $\phi = 0$ plane). The computation employed an incident pulse identical to that for the cylinder simulations described previously, a spatial step of four points per minimum wavelength and a CFL number of 0.5. The total pressure wavefield was computed for a time duration of 7.3 μs on a three-dimensional grid of dimensions $10.66 \times 10.66 \times 10.66$ mm^3. The accuracy of this computation was assessed by evaluating the L^2 error between the k-space and exact solutions using (21).

IV. Numerical Results

An example k-space computation, performed using the 2.0-mm cylinder with acoustic properties of human fat, is illustrated in Fig. 1. The cylinder is also sketched in each panel. For the computation shown, smoothed sound speed and density functions were obtained by filtering the analytic spatial Fourier transform of the cylinder using (16). The time history of the total wavefield is shown as computed by the k-space method for a spatial step size of four points per minimum wavelength and a CFL number of 0.5. Details visible include a scattered wave from the edge nearest the initial wavefront (c), weak focusing near the trailing edge of the cylinder (e), scattering from the trailing edge [(f)–(i)], and low level multiple scattering [(g)–(h)].

Results of accuracy benchmarks for the k-space and leapfrog pseudospectral methods described previously are shown in Fig. 2. Each of these computations was made using the 2.0-mm cylinder described previously and a spatial step size of four points per maximum wavelength. The results show that the k-space method employing the k-t space propagator of (9) provides much higher accuracy than the pseudospectral method employing the leapfrog propagator of (8). The two methods provide equivalent results for very small time steps (CFL numbers less than about 0.1), but the k-space method maintains its highest accuracy up to a CFL number of about 0.4. In contrast, the pseudospectral method rapidly increases in error for CFL numbers above 0.1.

Error results for the pseudospectral computations shown in Fig. 2 are not given for CFL numbers above 0.6 because the computation was unstable for higher CFL numbers i.e., computed fields incurred spurious exponen-

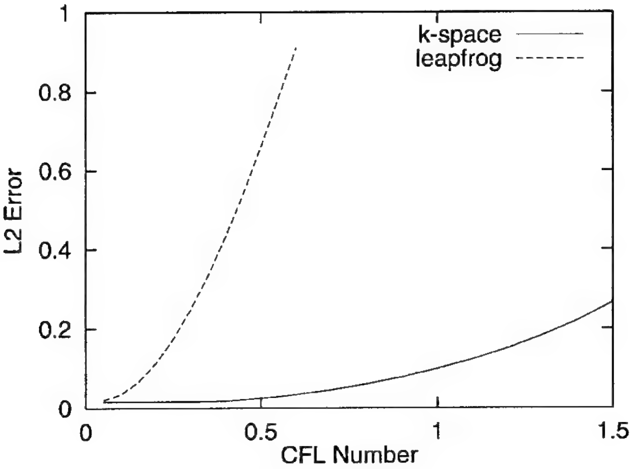

Fig. 2. Time-domain comparison of accuracy for the k-space and leapfrog pseudospectral methods as a function of Courant-Friedrichs-Lewy (CFL) number. Each test used the "fat" cylinder (2.0-mm radius) and a spatial step size of four points per minimum wavelength.

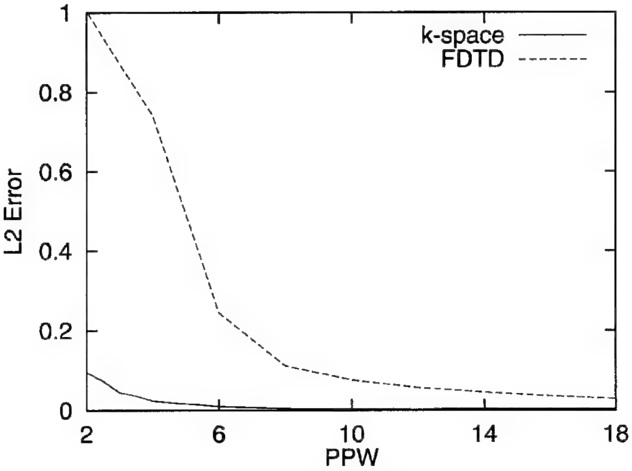

Fig. 3. Time-domain comparison of accuracy for the k-space and 2-4 finite difference time-domain methods as a function of the spatial step size in points per minimum wavelength (PPW). Each test used the "fat" cylinder (2.0-mm radius). Courant-Friedrichs-Lewy (CFL) numbers were 0.5 for the k-space method and 0.25 for the finite difference time-domain method.

tial growth, resulting in numerical overflow. This observation of instability is consistent with the linear stability limit of 0.6366 given by (12) for this case. The k-space method did not incur any numerical instability for the range of CFL numbers investigated, so that the method is observed to be unconditionally stable as predicted for $c(\mathbf{x}) \leq c_0$. However, the error of this method grows as the CFL number approaches and exceeds unity, consistent with the Nyquist sampling criterion given by (14).

Pseudospectral methods employing higher order time integration achieve higher accuracy than the leapfrog iteration used as a comparison here. However, tests of the present k-space method and a pseudospectral method employing fourth-order Adams-Bashforth time integration have shown trends similar to that seen in Fig. 2 [32]. Specifically, for weak scattering media, the k-space method yields similar accuracy for time steps two to three times larger than those required by the higher order pseudospectral method described in [13].

The relative accuracy of the k-space method and the 2-4 finite difference method are compared in Fig. 3 as a function of the spatial step size. For these computations, the CFL number of the k-space computations was held constant at 0.5, consistent with the CFL-accuracy relationship shown in Fig. 2; the CFL number of the finite difference computations was held at 0.25 [26]. Both methods achieve high accuracy for finer grid spacings; however, the k-space method achieves higher accuracy for much larger spatial step sizes. The L^2 error drops below 0.05 for k-space computations, employing only three points per minimum wavelength; achievement of the same accuracy criterion requires 14 points per minimum wavelength for the finite difference computations. This difference suggests that storage requirements for k-space computations can be much smaller than those for finite difference computations of comparable accuracy, on the order of 12 times smaller for two-dimensional computations and 43 times smaller for three-dimensional computations.

Visual comparison of simulated waveforms for the 2.0-mm cylinder is shown in Fig. 4. Waveforms in this figure are those computed using the k-space (four points per minimum wavelength; CFL number, 0.5; both unsmoothed and smoothed contrast functions), finite difference time-domain (14 points per minimum wavelength; CFL number, 0.25), and exact methods. The k-space solution for the unsmoothed cylinder shows a small time-domain L^2 error (0.0243) but also exhibits spurious waves (nearly 60 dB down from the peak pressure amplitude) between the two main arrivals. These spurious waves are removed by use of the k-space method with smoothed medium parameters [i.e., $\rho(\mathbf{x})$ and $c(\mathbf{x})$ smoothed using (16) with $k_{\max} = \pi/\Delta x$]; the L^2 error is decreased to 0.0214 by this smoothing. The finite difference result bears a strong qualitative resemblance to the exact solution, but the larger L^2 error (0.0454) indicates that phase errors have been introduced by the dispersion inherent to the finite difference method. Computation times [33] were 2.31 min for the k-space method and 1.55 h for the finite difference method, so that the k-space method yields greater accuracy at much less computational cost.

Waveforms for the 10-mm cylinder are shown in Fig. 5 in a format analogous to that of Fig. 4. These results indicate that, as for the smaller cylinder, smoothing of the contrast functions produces a reduction in spurious low amplitude waves. For this problem, unlike the 2.0-mm cylinder discussed previously, this smoothing slightly decreases the overall accuracy. (The time-domain L^2 error is 0.1292 for the smoothed case vs. 0.1288 for the unsmoothed case.) The finite difference solution, using 14 points per wavelength and a CFL number of 0.25, requires much greater storage and computational time and produces waveforms

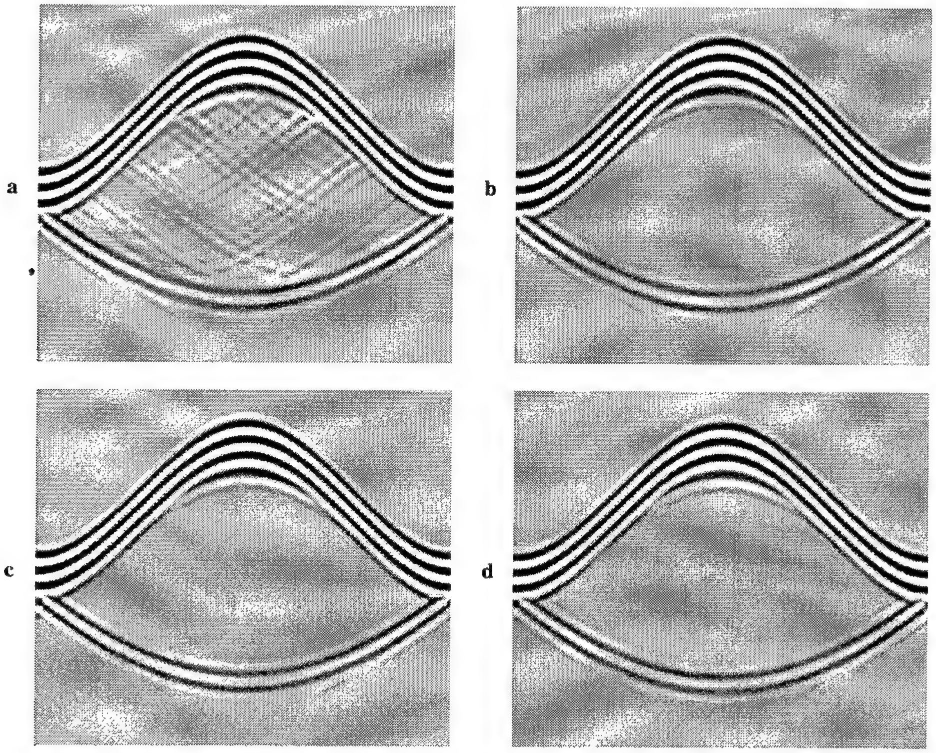

Fig. 4. Computed waveforms for the "fat" cylinder at a radius of 2.5 mm for a cylinder of radius 2.0 mm and a pulse center frequency of 2.5 MHz. The acoustic pressure is shown on a bipolar logarithmic scale with 60 dB dynamic range. The horizontal range of each plot is 360 degrees, covering the entire measurement circle starting with angle 0 (forward propagation). The vertical range of each panel corresponds to a temporal duration of 9 μs, with $t = 0$ at the top of each plot. a) Unsmoothed object: k-space solution with four points per minimum wavelength, L^2 error = 0.0243; b) smoothed object: k-space solution with four points per minimum wavelength, L^2 error = 0.0214; c) finite-difference solution with 14 points per minimum wavelength, L^2 error = 0.0454; and d) exact solution.

with poorer accuracy (an L^2 error of 0.1794) than the k-space method.

Results for the 2-mm "bone" cylinder are shown in Fig. 6. In this case, the k-space method using a CFL number of 0.5 exhibited numerical instability. This instability is expected because this CFL number exceeds the limit of 0.2833 set by (13). To obtain an appropriate temporal sampling rate, the time step was reduced in proportion to the increase in $c_{\max}$, resulting in a CFL number of 0.2153. Required computation time for the k-space method was 5.34 min[1]; the time-domain L^2 error was 0.3061 for the unsmoothed case and 0.2687 for the smoothed case.

The finite difference method, employing 14 points per wavelength and a CFL number of 0.1076 (also changed in proportion to $c_{\max}$), achieved an L^2 error of 0.0350 in a computation time of 3.99 h[1]. This result indicates that finite difference methods can be much more accurate than k-space methods for scattering problems involving very high contrast inhomogeneities such as bone within soft tissue. However, the k-space solution, as seen in Fig. 6, still shows good qualitative agreement with the exact solution.

The relative inaccuracy of the k-space method for high contrast scatterers may be associated with aliasing effects, as suggested in [5]. That is, large jumps in spatial contrast functions are associated with significant high frequency components of the corresponding k-space spectra. If the spatial frequency range employed in the k-space algorithm is not sufficiently large, aliasing errors result. Low-pass filtering of the contrast functions would remove this aliasing, but this also introduces additional errors because high spatial frequency components of the scattering medium are lost. The half-band filtering employed here is a compromise that greatly reduces aliasing errors but maintains some contributions from high spatial frequencies (up to the spatial Nyquist rate).

Computational results for a large scale, two-dimensional tissue model are shown in Fig. 7. Waveforms computed by the k-space (four points per minimum wavelength; CFL number, 0.5; no smoothing) and the finite difference models (10 points per minimum wavelength; CFL number, 0.25) were recorded at 130-element apertures composed of simulated point receivers separated by a pitch of 0.21 mm. The results produced by the finite difference method and the k-space method are visually indistinguishable. However, despite the reduced grid size and limited computations employed for the finite difference method, the k-space method was more efficient by about a factor

---

[1] All CPU timings reported in this paper were obtained using a Linux workstation with a 200-MHz AMD K6 processor and 128 MB RAM.

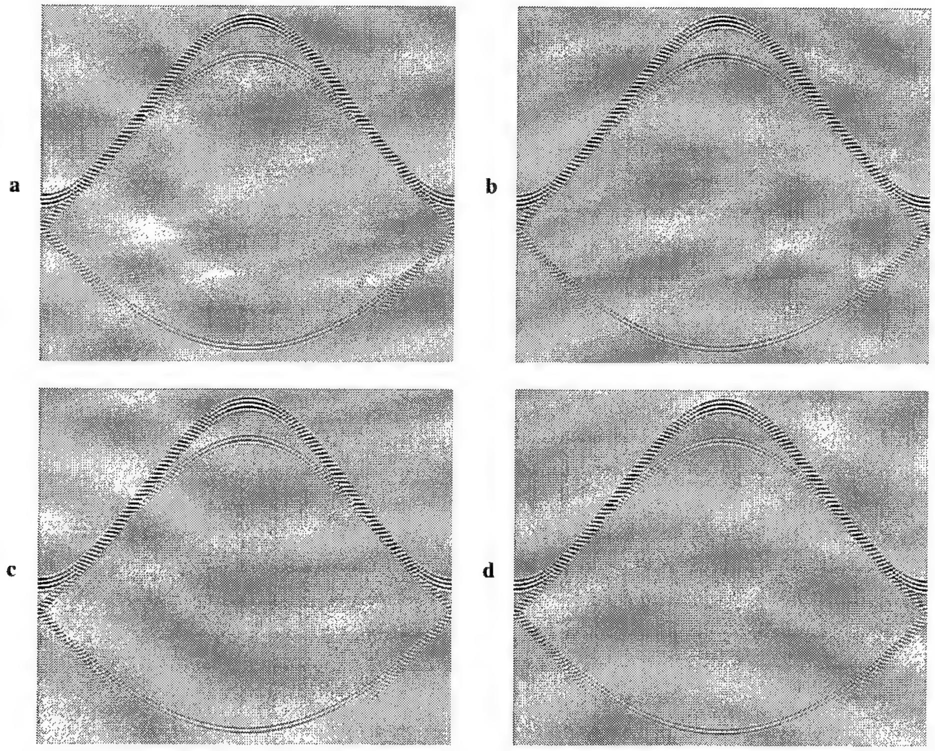

Fig. 5. Computed waveforms at a radius of 12.5 mm for a "fat" cylinder of radius 10.0 mm and a pulse center frequency of 2.5 MHz. The acoustic pressure is shown in each panel using a bipolar logarithmic scale with a 60 dB dynamic range. The horizontal range of each panel is 360 degrees, and the vertical range is 33 μs. a) Unsmoothed object: k-space solution, L^2 error = 0.1288; b) smoothed object: k-space solution, L^2 error = 0.1292; c) finite-difference solution, L^2 error = 0.1794; and d) exact solution.

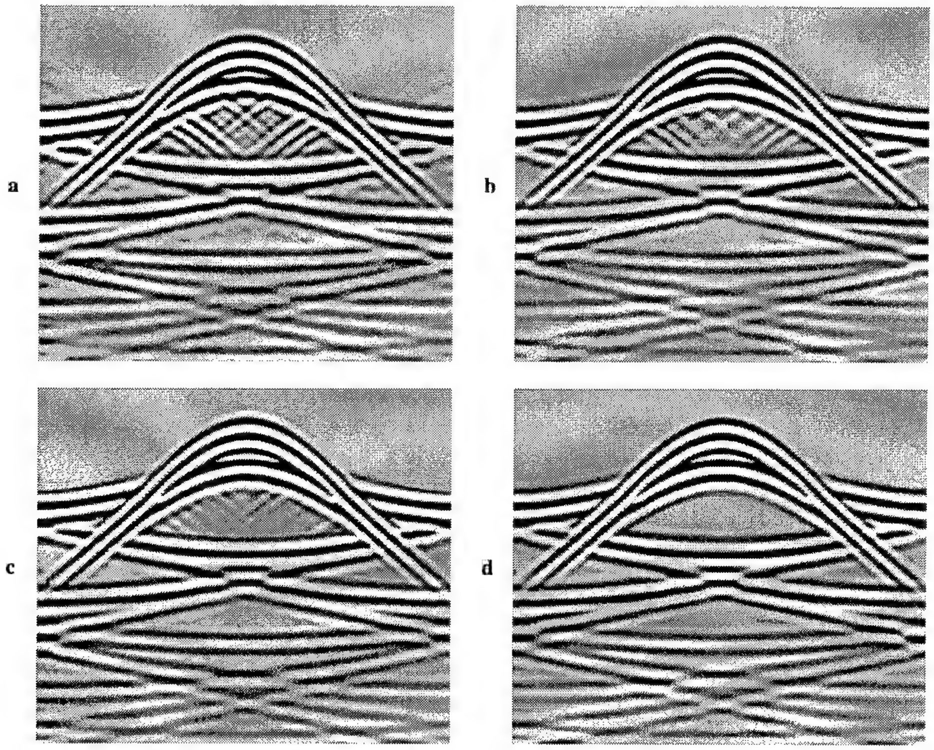

Fig. 6. Computed pressure waveforms at a receiver radius of 2.5 mm for a "bone" cylinder of radius 2.0 mm and a pulse center frequency of 2.5 MHz. The format is the same as in Fig. 4. a) Unsmoothed object: k-space solution, L^2 error = 0.3061; b) smoothed object: k-space solution, L^2 error = 0.2687; c) finite-difference solution, L^2 error = 0.0380; and d) exact solution.

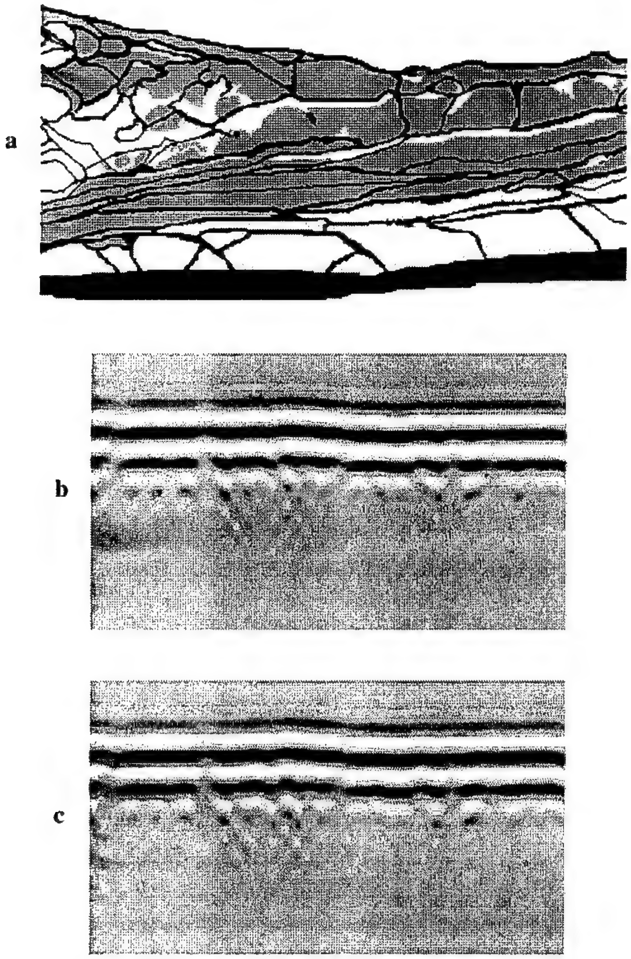

Fig. 7. Comparison of k-space and finite difference methods for a tissue cross-sectional model. a) Chest wall cross section (taken from [24]), with black indicating connective tissue, dark gray indicating muscle, and light gray indicating fat. The region is 33.5 mm wide and 17.2 mm high. b) Transmitted waveforms computed by the k-space method using four points per minimum wavelength and a Courant-Friedrichs-Lewy (CFL) number of 0.5, shown on a bipolar linear gray scale with white indicating maximum positive pressure and black indicating maximum negative pressure. The horizontal range shown is 27.3 mm at the same scale as a. The vertical range is 3.29 μs. c) Transmitted waveforms computed by the finite difference time-domain method using 10 points per minimum wavelength and a CFL number of 0.25, shown using the same format as b.

of four; the required CPU time for the k-space method was 0.90 CPU h; the corresponding time for the finite difference time-domain method was 4.58 CPU h^1. This discrepancy in efficiency is even more impressive when note is made that the k-space method using four points per minimum wavelength provides significantly higher accuracy than the finite difference method using 14 points per minimum wavelength (as illustrated in Fig. 3). Thus, the present k-space method is suggested to be an appropriate replacement for finite difference methods previously employed to compute propagation through large scale, soft tissue models [23]–[28].

Results of the example three-dimensional computation are shown in Fig. 8. Three-dimensional isosurface renderings of the total pressure wavefield are shown at three instants separated by 0.79 μs. For the three-dimensional computation, the total computation time required was 1.51 h^1. The L^2 error of the computed waveforms, relative to the exact time-domain solution for scattering from a sphere [29], was 0.0186.

V. EXTENSIONS TO THE k-SPACE METHOD

The present method can be extended in a number of ways to increase its range of applicability in computations of ultrasound tissue interactions.

Absorption effects could be added to the present algorithm in several ways. The most straightforward method for including absorption is to include an ad hoc damping term proportional to $\partial f_s/\partial t$ in (2) [3]–[5]. This approach yields absorption coefficients roughly independent of frequency. Similarly, inclusion of a damping term proportional to $\partial^3 f_s/\partial t^3$ (a thermoviscous approximation) would lead to absorption roughly proportional to the frequency squared [33]. However, neither of these approaches has a rigorous justification for use in models of ultrasound propagation in biological tissue.

A physically justifiable approach for inclusion of absorption in the present algorithm is to consider absorption associated with multiple relaxation processes. The theoretical basis for this approach is presented in [34]; one implementation of this method in a finite difference time-domain algorithm is given in [35]. Because multiple relaxation processes can lead to a variety of frequency-dependent absorption characteristics, this approach provides a possibility of modeling realistic frequency-dependent attenuation in tissue without introduction of nonphysical dispersion or violation of causality. Following the methods presented in [35], absorption caused by multiple relaxation processes can be implemented in a computationally efficient form. Possible alternatives include the time-causal power law absorption formulation of [36].

Another possible extension to the present method is to incorporate the full elastic wave propagation equations. This extension would account for shear wave propagation, which may substantially affect results for propagation models, including bone and other calcified tissue. By applying methods similar to those outlined in [7] to the algorithm described previously, a full elastic k-space method incorporating Fourier space evaluation of spatial derivatives and a k-t space propagator could be derived. Such a method would, as in [7], include separate k-t space propagators for compressional and shear waves.

Boundary conditions of k-space and pseudospectral methods are inherently periodic, so that simple radiation boundary conditions cannot be straightforwardly implemented. One option for absorbing boundary conditions is to include tapered (artificial) absorption functions at each boundary [37]. The technique of perfectly matched layers

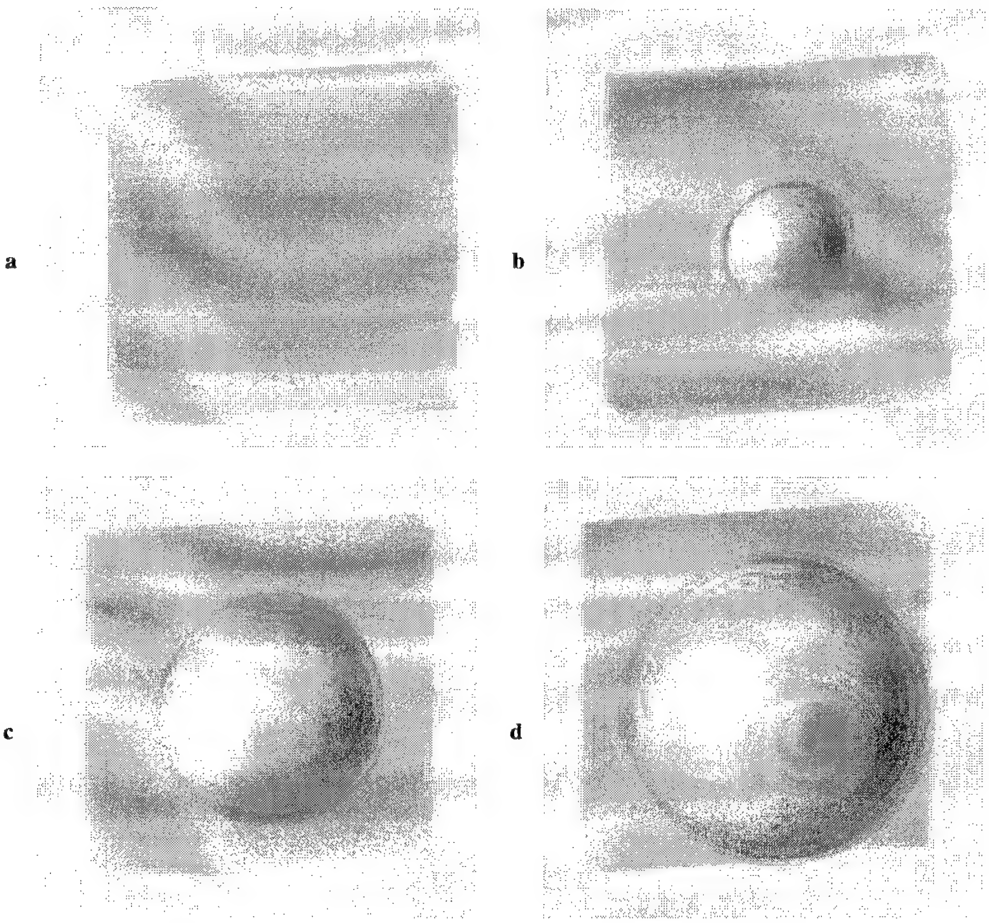

Fig. 8. Isosurface renderings of the total (logarithmically scaled) pressure wavefield associated with scattering from a "muscle" sphere of radius 1.5 mm. Incident pulse parameters were the same as in Fig. 4–6. Panels a–d show the wavefield at four instants separated by 0.79 μs. The view shown is such that the incident wave is traveling into the page, so that the visible wavefield includes the backscattered component. The lowest amplitude isosurface shown is 67.5 dB down from the incident wave amplitude. Each panel shows a rendering of the entire computational domain (10.66 mm on each side). In panel a, the incident wavefront is just impinging on the sphere; in panel d, the scattered wavefront has just passed the computational boundary.

(PML) [38] can provide true radiation boundary conditions; however, present PML implementations are not applicable to the second-order wave equation employed here. Combination of a k-space method with PML boundary conditions may require derivation of a new k-t space time integrator for the first-order wave propagation equations.

The present derivation was based on the linear (small amplitude) acoustic propagation equations. The k-space method could be easily extended to incorporate finite amplitude acoustic effects. For example, the nonlinear terms of the Westervelt propagation equation (used in [33] for modeling of ultrasonic propagation in tissue) could be included as effective source terms additional to the effective sources v and q defined previously. The numerical results obtained suggest that the k-space method is most accurate when the effective source terms are fairly small; thus, a nonlinear extension to the k-space method should be highly accurate for weak nonlinear effects.

Computation times for the k-space method can be reduced easily by parallelization. The primary computational burden of the method is incurred in the multidimensional FFT taken at each time step. Because FFTs can be efficiently executed on parallel processors [24], [39], the present k-space method should scale efficiently to large problems that require parallel processing.

VI. Conclusions

A simplified derivation of the k-space method for computation of ultrasonic wave propagation has been presented. The method efficiently accounts for sound speed and density variations and can be extended to include realistic absorption effects and absorbing boundary conditions. Three-dimensional computations can also be performed without change to the algorithm as derived here.

Analytic and numerical results have shown that the present k-space method provides superior stability and accuracy over both a similar leapfrog pseudospectral method and a fourth-order space, second-order time, finite difference method. This improved accuracy allows larger spatial and time steps to be employed, so that large-scale multidimensional computations are more feasible. Computations using a realistic two-dimensional tissue model support the conclusion that the k-space method provides high accuracy and low computational cost for large-scale computations.

The results also indicate that care should be taken when choosing and implementing a forward solver for a particular scattering problem. For instance, in the present k-space method, one can suppress spurious waves by smoothing sound speed and density variations; however, this smoothing does not decrease the time-domain L^2 error in some cases. Similarly, the finite difference time-domain method employed here is less accurate than the k-space method in most cases examined here, but the method achieved higher accuracy for a test case with a bone-like scatterer. In general, the k-space method proposed here should be most applicable to large-scale scattering problems involving low contrast inhomogeneities, such as soft tissue structures.

ACKNOWLEDGMENT

The authors thank Fadil Santosa and Bengt Fornberg for helpful discussions.

REFERENCES

[1] N. N. Bojarski, "The k-space formulation of the scattering problem in the time domain," *J. Acoust. Soc. Amer.*, vol. 72, no. 2, pp. 570–584, 1982.
[2] ——, "The k-space formulation of the scattering problem in the time domain: An improved single propagator formulation," *J. Acoust. Soc. Amer.*, vol. 77, no. 3, pp. 826–831, 1985.
[3] B. Compani-Tabrizi, "K-space formulation of the absorptive full fluid elastic scalar wave equation in the time domain," *J. Acoust. Soc. Amer.*, vol. 79, no. 4, pp. 901–905, 1986.
[4] S. Finette, "A computer model of acoustic wave scattering in soft tissue," *IEEE Trans. Biomed. Eng.*, vol. 34, no. 5, pp. 336–344, 1987.
[5] S. Finette, "Computational methods for simulating ultrasound scattering in soft tissue," *IEEE Trans. Ultrason., Ferroelect., Freq. Contr.*, vol. 34, no. 3, pp. 283–292, 1987.
[6] S. Pourjavid and O. J. Tretiak, "Numerical solution of the direct scattering problem through the transformed acoustical wave equation," *J. Acoust. Soc. Amer.*, vol. 91, no. 2, pp. 639–645, 1992.
[7] Q. H. Liu, "Generalization of the k-space formulation to elastodynamic scattering problems," *J. Acoust. Soc. Amer.*, vol. 97, no. 3, pp. 1373–1379, 1995.
[8] H.-O. Kreiss and J. Oliger, "Comparison of accurate methods for the integration of hyperbolic equations," *Tellus*, vol. 24, no. 3, pp. 199–215, 1972.
[9] B. Fornberg, "On a Fourier method for the integration of hyperbolic," *SIAM J. Numer. Anal.*, vol. 12, no. 4, pp. 509–528, 1975.
[10] D. Gottlieb and S. A. Orszag, *Numerical Analysis of Spectral Methods.* Philadelphia, PA: SIAM, 1977.
[11] D. C. Witte and P. G. Richards, "The pseudospectral method for simulating wave propagation," in *Computational Acoustics.* vol. 3, D. Lee, A. Cakmak, and R. Vichnevetsky, Eds. New York: North-Holland, 1990, pp. 1–18.
[12] B. Fornberg, "Introduction to PS method via finite differences," in *A Practical Guide to Pseudospectral Methods.* Cambridge: Cambridge University Press, 1996, ch. 3.
[13] G. Wojcik, B. Fornberg, R. Waag, L. Carcione, J. Mould, L. Nikodym, and T. Driscoll, "Pseudospectral methods for large-scale bioacoustic models," in *Proc. IEEE Ultrason. Symp.*, 1997, vol. 2, pp. 1501–1506.
[14] Q. H. Liu, "The pseudospectral time-domain (PSTD) algorithm for acoustic waves in absorptive media," *IEEE Trans. Ultrason., Ferroelect., Freq. Contr.*, vol. 45, no. 4, pp. 1044–1055, 1998.
[15] A. D. Pierce, "The wave theory of sound," in *Acoustics: An Introduction to Its Physical Principles and Applications*, 2nd ed., Woodbury, NY: Acoustical Society of America, 1989, ch. 1.
[16] S. A. Johnson and M. L. Tracy, "Inverse scattering solutions by a sinc basis moment method—Part I: Theory," *Ultrason. Imag.*, vol. 5, no. 4, pp. 361–375, 1983.
[17] A. Nachman, "Reconstructions from boundary measurements," *Ann. Math.*, vol. 128, no. 3, pp. 531–576, 1988.
[18] R. E. Mickens, *Nonstandard Finite Difference Models of Differential Equations.* Singapore: World Scientific, 1994.
[19] B. Fornberg and G. B. Whitham, "A numerical and theoretical study of certain nonlinear wave phenomena," *Phil. Trans. R. Soc. London*, vol. 289, no. 1361, pp. 373–404, 1978.
[20] E. H. Twizell, *Computational Methods for Partial Differential Equations.* New York: Ellis Horwood Limited, 1984.
[21] E. Turkel, "On the practical use of high-order methods for hyperbolic systems," *J. Comp. Phys.*, vol. 35, no. 3, pp. 319–340, 1980.
[22] R. E. Crochiere and L. R. Rabiner, *Multirate Digital Signal Processing.* Englewood Cliffs, NJ: Prentice-Hall, 1983.
[23] T. D. Mast, L. M. Hinkelman, M. J. Orr, V. W. Sparrow, and R. C. Waag, "Simulation of ultrasonic pulse propagation through the abdominal wall," *J. Acoust. Soc. Amer.*, vol. 102, no. 2, pp. 1177–1190, 1998. [Erratum: *J. Acoust. Soc. Amer.*, vol. 104, no. 2, pp. 1124–1125, 1998.].
[24] M. Frigo and S. G. Johnson, "FFTW: An adaptive software architecture for the FFT," in *Proc. of the ICASSP*, 1998, vol. 3, pp. 1381–1384.
[25] R. W. MacCormack, "Numerical solution of the interaction of a shock wave with a laminar boundary layer," in *Lecture Notes in Physics*, vol. 8, J. Ehlers, K. Hepp, and H. A. Weidenmüller, Eds. Berlin: Springer-Verlag, 1971, pp. 151–163.
[26] D. Gottlieb and A. Turkel, "Dissipative two-four methods for time-dependent problems," *Math. Comp.*, vol. 30, no. 136, pp. 703–723, 1976.
[27] V. W. Sparrow and R. Raspet, "A numerical method for general finite amplitude wave propagation and its application to spark pulses," *J. Acoust. Soc. Amer.*, vol. 90, no. 5, pp. 2683–2691, 1991.
[28] T. D. Mast, L. M. Hinkelman, M. J. Orr, and R. C. Waag, "Simulation of ultrasonic pulse propagation, distortion, and attenuation in the human chest wall," *J. Acoust. Soc. Amer.*, vol. 106, no. 6, pp. 3665–3677, 1999.
[29] P. M. Morse and K. U. Ingard, "The scattering of sound," in *Theoretical Acoustics.* New York: McGraw-Hill, 1968, ch. 8.
[30] A. V. Oppenheim and R. W. Schafer, "Filter design techniques," in *Discrete-Time Signal Processing*, Englewood Cliffs, NJ: Prentice Hall, 1989, ch. 7.
[31] R. L. Burden, J. D. Faires, and A. C. Reynolds, "Iterative techniques in matrix algebra," in *Numerical Analysis.* Boston, MA: Prindle, Weber, and Schmidt, 1978, ch. 8.
[32] J. C. Mould, G. L. Wojcik, L. M. Carcione, M. Tabei, T. D. Mast, and R. C. Waag, "Validation of FFT-based algorithms for large-scale modeling of wave propagation in tissue," in *Proc. IEEE Ultrason. Symp.*, 1999, pp. 1551–1556.
[33] I. M. Hallaj and R. O. Cleveland, "FDTD simulation of finite-amplitude pressure and temperature fields for biomedical ultrasound," *J. Acoust. Soc. Amer.*, vol. 105, no. 5, pp. L7–L12, 1999.
[34] A. I. Nachman, J. Smith, and R. C. Waag, "An equation for acoustic propagation in inhomogeneous media with relaxation losses," *J. Acoust. Soc. Amer.*, vol. 88, no. 3, pp. 1584–1595, 1990.
[35] X. Yuan, D. Borup, J. Wiskin, M. Berggren, and S. Johnson, "Simulation of acoustic wave propagation in dispersive media with relaxation losses by using FDTD method with PML absorbing boundary condition," *IEEE Trans. Ultrason., Ferroelect., Freq. Contr.*, vol. 46, no. 1, pp. 14–23, 1999.
[36] T. L. Szabo, "Time domain wave equations for lossy media obeying a frequency power law," *J. Acoust. Soc. Amer.*, vol. 96, no. 1, pp. 491–500, 1994.
[37] C. Cerjan, D. Kosloff, R. Kosloff, and M. Reshef, "A nonreflecting boundary condition for discrete acoustic and elastic wave equations," *Geophysics*, vol. 50, no. 4, pp. 705–708, 1985.
[38] J.-P. Berenger, "A perfectly matched layer for the absorption of electromagnetic waves," *J. Comput. Phys.*, vol. 114, no. 2, pp. 185–200, 1994.

[39] P. N. Swarztrauber, "Multiprocessor FFTs," *Parallel Computing*, vol. 5, no. 1, pp. 197–210, 1987.

T. Douglas Mast (M'98) was born in St. Louis, Missouri in 1965. He received a B.A. in physics and mathematics from Goshen College in 1987 and a Ph.D. in acoustics from The Pennsylvania State University in 1993. From 1993 until 1996, he was Postdoctoral Research Associate with the University of Rochester's Ultrasound Research Laboratory. Since 1996, he has been with the Applied Research Laboratory of The Pennsylvania State University, where he currently is Research Associate and Assistant Professor of Acoustics. His research interests include propagation and scattering in inhomogeneous media, inverse scattering, tissue characterization, and nondestructive testing.

Laurent P. Souriau was born in Saint Maur, near Paris, France in 1964. He received the Engineer degree in physics from the Ecole Nationale Supérieure de Physique de Marseille in 1988 and the Ph.D. degree at the Universite d'Orsay in 1996. He joined the Ultrasound Research Laboratory, the University of Rochester, Rochester, NY, as Research Associate in 1996. His research interests include submarine detection, biomedical acoustic imaging, and inverse problem theory.

D.-L. Donald Liu (M'93) obtained his Bachelor of Engineering degree in 1984 from the Department of Automatic Control, Qinghua University, Beijing, China and Master of Engineering degree and Doctor of Engineering degree in 1988 and 1991, respectively, both from the Department of Electronic Engineering, University of Tokyo, Tokyo, Japan. He was Assistant Professor in the Department of Electrical and Electronic Engineering at Sophia University, Tokyo, Japan from April 1991 to March 1992. From April 1992 to March 1997, he was with the Department of Electrical Engineering at University of Rochester, Rochester, New York, where he was appointed Scientist and Assistant Professor. Since April 1997, he has been with Siemens Medical Systems, where he is currently Staff Systems Engineer. Dr. Liu's research interests include analysis and modeling of ultrasonic wavefront distortion, adaptive imaging through aberration correction, quantitative and 3-D ultrasonic imaging, spectral analysis, and digital signal processing.

Makoto Tabei (M'94) was born in Osaka, Japan in 1956. He received the B.E. degree in computer science from the University of Electro-Communications, Tokyo, Japan in 1979 and the M.E. and Dr.Eng. degrees in information processing from Tokyo Institute of Technology in 1981 and 1996, respectively. From 1981 to 1982, he was with Japan Atomic Energy Research Institute in Ibaraki, Japan, working as a research engineer. Since 1982, he has been Research Associate at the Precision and Intelligence Laboratory, Tokyo Institute of Technology. From 1989 to 1990, he was a visiting scientist at the Research Laboratory of Electronics of the Massachusetts Institute of Technology. He has been a visiting associate professor in the Department of Electrical and Computer Engineering, University of Rochester, since 1997. His research interests are in the areas of estimation theory, image reconstruction, and numerical analysis of acoustic wave propagation.

Adrian I. Nachman received his B.Sc. degree from McGill University in 1974 and the Ph.D. degree in mathematics from Princeton University in 1980. He was a J.W. Gibbs Instructor at Yale University from 1979 to 1981. In 1981, he joined the faculty of the University of Rochester, where he is now Professor in the Department of Mathematics. Dr. Nachman's recent research has involved the development of new nonlinear reconstruction methods for electric impedance imaging and other boundary value problems in two and three dimensions, multidimensional inverse scattering problems, and quantitative ultrasonic imaging. He is a member of the Society for Industrial and Applied Mathematics.

Robert C. Waag (S'59–M'66–SM'83–F'90) received his B.E.E., M.S., and Ph.D. degrees from Cornell University in 1961, 1963, and 1965, respectively. After completing his Ph.D. studies, he became a member of the technical staff at Sandia Laboratories, Albuquerque, NM and then served as an officer in the United States Air Force from 1966 to 1969 at the Rome Air Development Center, Griffiss Air Force Base, NY. In 1969, he joined the faculty of the University of Rochester, where he is now Arthur Gould Yates Professor in the Department of Electrical Engineering, School of Engineering and Applied Science and also holds an appointment in the Department of Radiology, School of Medicine and Dentistry. Prof. Waag's recent research has treated ultrasonic scattering, propagation, and imaging in medical applications. In 1992, he received the Joseph H. Holmes Pioneer Award from the American Institute of Ultrasound in Medicine. He is a Fellow of the Institute of Electrical and Electronics Engineers, the Acoustical Society of America, and the American Institute of Ultrasound in Medicine.

Validation of FFT-Based Algorithms for Large-Scale Modeling of Wave Propagation in Tissue

John C. Mould, Gregory L. Wojcik, Laura M. Carcione, Makoto Tabei*[†],
T. Douglas Mast[+], Robert C. Waag*[‡],
Weidlinger Associates, 4410 El Camino Real, Suite 110, Los Altos, CA 94022,
*University of Rochester, [†]Department of Electrical & Computer Engineering,
[‡]Departments of Electrical & Computer Engineering and Radiology, Rochester, NY 14642
[+]Applied Research Laboratory, The Pennsylvania State University, University Park, PA 16801

Abstract - We investigate accuracy of existing 2D pseudospectral and k-space formulations for simulating acoustic propagation in tissue or model scattering media. They are intended to provide insight into tissue-ultrasound interaction and a "test bed" for aberration correction schemes in medical imaging. Both methods employ FFT's to evaluate spatial derivatives to high accuracy on coarse grids. The primary difference lies in the approach to time integration. Scattering in large-scale, 2D, inhomogeneous media is included. We compare simulations against analytical solutions to illustrate spatial and temporal discretization required for acceptable solutions.

INTRODUCTION

The medium is represented by a uniform Cartesian grid where pressure/stiffness and velocity/density are unknowns/parameters at discrete points. Spectral operators in space enable accuracy and computational efficiency in very large models. However, inhomogeneities are often represented as piecewise constant from node to node, rather than smooth. The resulting stairstep can produce spurious diffractions at edges/corners, inaccurate reflections and transmissions at interfaces and local Gibbs phenomena, by approximating derivatives at a material discontinuity. Thus, the efficiency permitted by coarse spectral grids is compromised by the need to resolve interface derivatives.

For example, scattering by a soft cylinder requires only two nodes per wavelength inside and outside the cylinder for accurate propagation, but significantly more nodes per wavelength are necessary to reduce interface artifacts. Interface artifacts are quantified for a single interface, 1D multilayer models, and cylindrical scatterers. Abdominal wall cross sections with coarse and fine-scale inhomogenities are used to explore fidelity of wave propagation versus nodes per wavelength and tissue characteristic lengths. We show that the existing tools are useable in 2D.

The pseudospectral method is implemented in the *SpectralFlex* code. *Kbench* implements the k-space method.

PSEUDOSPECTRAL AND K-SPACE METHODS

The pseudospectral and k-space methods were formulated to provide efficient high-accuracy solutions to long range wave propagation problems. In fact, they debuted during the same year [1,2]. We briefly describe the two methods as implemented in [3,4], highlighting the major similarities and differences.

Both use FFT's to evaluate spatial derivatives to high accuracy on coarse grids. The primary difference lies in their respective approaches to time integration. Note that coarse spatial grids provide the primary incentive for FFT based (or any high order) method. The computational burden is linear in the number of timesteps per cycle, for both 2D and 3D. Including the timestep, computational burden is proportional to the number of Points Per Wave $(PPW)^3$ in 2D or $(PPW)^4$ in 3D.

SpectralFlex adopts a 4th order staggered Adams Bashforth ABS4 time integrator [5]. Among general purpose integrators, this is close to optimal for the current applications - 2-3 digits of accuracy for a wave propagating several hundred wavelengths on the coarsest possible grid. The stability limit for ABS4 in 2D is CFL = 0.3. The CFL number is defined as: $CFL = \Delta t/(\Delta x/c)$, where Δt is the timestep, c is the wavespeed and Δx is the cell size.

(c) 1999 IEEE

0-7803-5725-6/99/$10.00

Accuracy frequently requires a smaller timestep, say CFL = 0.1. *Kbench* implements a time integrator in k-space based on the exact solution for waves propagating in a homogeneous medium [4]. It outperforms the general purpose ABS4 time integrator for weak scatterers in a homogeneous linear acoustic medium. ABS4 becomes more efficient when the scattering objects have a larger impedance contrast.

LONG RANGE PROPAGATION

To illustrate the advantages of the FFT based approach for long range propagation, we propagate a 2.5 MHz pulse 200 wavelengths through water using both *SpectralFlex* and *PZFlex*, a finite element code that is second order accurate in both space and time. The center frequency is 2.5 MHz, but spectral content is observable up to 5 MHz. Thus, 4 PPW at 2.5 MHz is the minimum sampling capable of resolving the pulse.

Figure 1 compares exact, *PZFlex* and *SpectralFlex* solutions. *SpectralFlex* used 4 PPW at CFL = 0.1, whereas *PZFlex* used 20 PPW at CFL = 0.8. These discretizations in time and space are typical of those that would be used in real problems. The *SpectralFlex* signal looks good and can be made better by reducing the timestep. The *PZFlex* signal is delayed in time and badly dispersed. A much finer grid is required to achieve reasonable accuracy. Note that at CFL = 1., *PZFlex* becomes a characteristic method, and produces exact results, even at 2 PPW. Unfortunately, this only works for 1D linear problems.

Kbench produces exact results for this example because the time integrator is based on the exact solution for a homogeneous medium.

DISCONTINUITIES

Spectral methods compute highly accurate spatial derivatives of smooth fields. Thus, in homogeneous regions, 2 cells per minimum wavelength (ie, highest spatial frequency) suffice. However, at material interfaces both the pressure and velocity fields should exhibit slope discontinuities as given by (1), where n denotes the normal direction and the

$$\frac{\partial p^+}{\partial n}=\frac{\rho^+}{\rho^-}\frac{\partial p^-}{\partial n} \tag{1}$$

superscript defines the + or – side of the interface. The velocity field likewise exhibits slope discontinuities at interfaces.

Spectral methods enforce smoothness, approximating the jumps in normal derivatives with steep gradients over a few cells. This approximation is quite good at 10-20 cells per wavelength, but less accurate at 2 cells per wavelength. For a staggered grid, as in *SpectralFlex*, the material interfaces coincide with velocity nodes, so we average the density at these interface points. On a regular grid, all the nodes lie away from interfaces, so no averaging is necessary, but the accuracy is even worse than for the staggered grid.

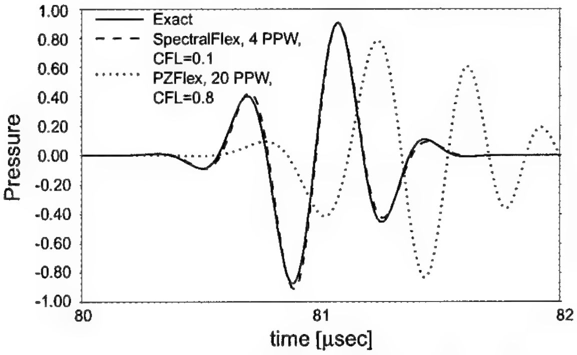

Figure 1. Long range pulse propagation through water.

1D versus exact solutions

Table 1 summarizes material properties used for the 1D benchmarks. Figure 2 illustrates the reflection/ transmission of a normally incident pulse at a water/fat interface as modeled by *SpectralFlex*. To plotting accuracy, the transmitted signals appear exact (because it has much larger amplitude than the reflected wave). However, the error in the reflected signal is readily apparent at 4 PPW, and barely visible at 6 PPW.

Figure 3 shows results for a water /bone interface. In this case, errors are visible in both the reflected and transmitted signals at 4 PPW. In both codes, the most pathological case is varying density/constant stiffness. Fortunately, most tissues have a higher contrast in stiffness than density [6], so this worst case is seldom encountered. As shown in Fig. 4 (density=1000, 928 kg/m^3) errors in the reflected wave are visible even at 12 PPW.

Table 1 – Material Properties for 1-D benchmarks

Material	Density [kg/m^3]	Wavespeed [m/sec]
Water	1000.	1500.
Fat	928.	1427.
Conn	1100.	1537.
Musl	1041.	1571.
Livr	1050.	1577.

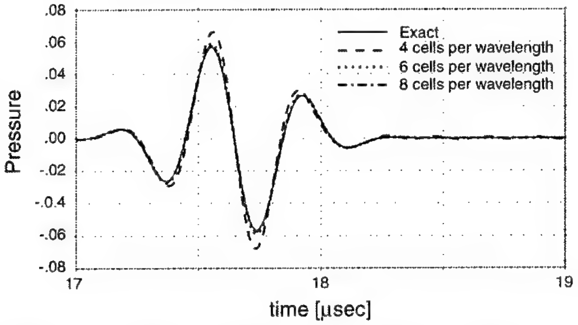

Figure 2. Reflected pulse at a water/fat interface.

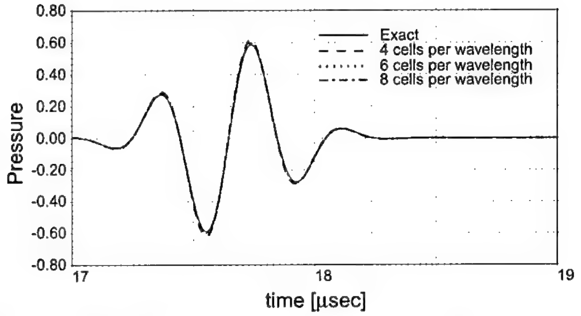

Figure 3. Reflected pulse at a water/bone interface.

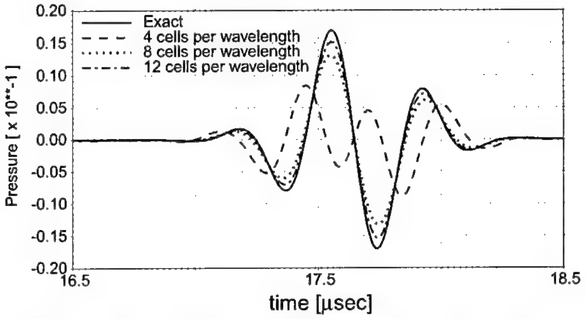

Figure 4. Reflected pulse from worst case interface.

The next benchmark examines propagation through a 1-D approximation of an abdominal cross section. Material parameters are again given in Table 1. Slight errors in the transmitted wave are apparent at 4 PPW (Fig. 5), but not at 8 PPW. Reflected signals (not shown) are similar. Figure 6 illustrates the effect of coarse non-conforming grids. At 4.1 PPW, cell boundaries are misaligned with actual material interfaces by up to ½ cell. This is, of course, the case for any real model with discontinuous material properties. Properties are assigned based on the center of the cell. The errors introduced by this sampling dwarf all others. More will be said about this in a later section.

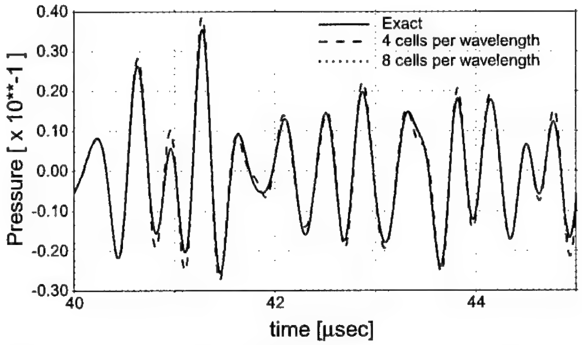

Figure 5. Pulse transmitted through 1-D abdominal wall model.

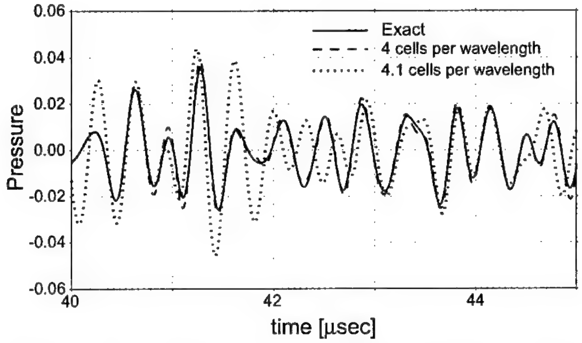

Figure 6. Pulse transmitted through 1-D approximation of abdominal wall. Non-conforming grid.

Scattering by cylinders

In addition to the numerical errors at interfaces, approximations are introduced by the stair-step representation of curved surfaces. To quantify these approximations, we consider 3 mm radius fat and bone cylinders immersed in water and insonified by the usual 2.5 MHz pulse. We compute the difference between exact and numerical signals for each timestep at 128 locations at 6 mm radius, and equal spacing in theta. We use the L^2 norm of this matrix as an error metric. Figure 7a shows the L^2 error vs PPW for *kbench* and *SpectralFlex* at CFL = 0.2.

The curves are similar, though *kbench* is slightly more accurate. For the larger contrast bone case in Figure 7b, similar trends are evident, but in this case *SpectralFlex* is more accurate. The error is tending to zero as the PPW increases. The rate of convergence is not quite quadratic. For context, Fig. 12 shows waveforms for L^2 error near 0.01.

Table 2 - Material Properties for Cylinders

Material	Wavespeed [m/sec]	Density [kg/m^3]
Water	1524.	993.
Fat	1478.	950.
Bone	3540.	1990.

Figure 7c illustrates that at low CFL, the error due to time integration tends to zero. For this problem, *kbench* permits reasonable accuracy at roughly double the *SpectralFlex* timestep. For the bone cylinder, the stability limit of *SpectralFlex* is 0.15 (0.3 in the bone) , and *kbench* can go up to 0.2.

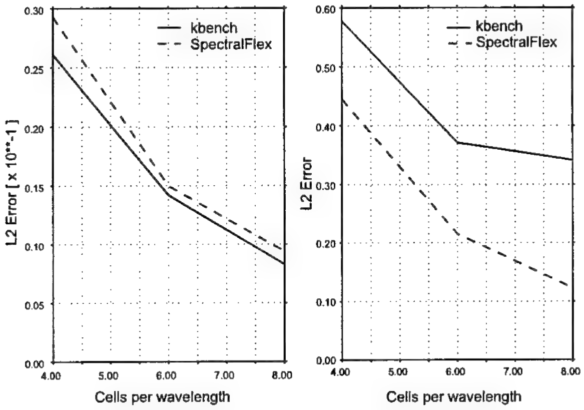

Fat Cylinder, CFL = 0.2 Bone Cylinder, CFL = 0.1

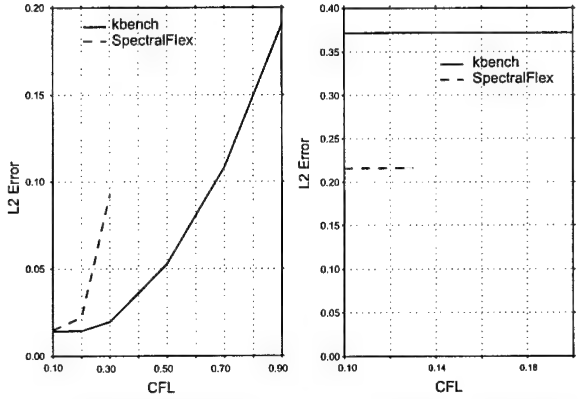

Fat Cylinder, 6 cells per wave Bone Cylinder, 6 cells per wave

Figure 7. Cylinder benchmarks. Convergence with increasing discretization.

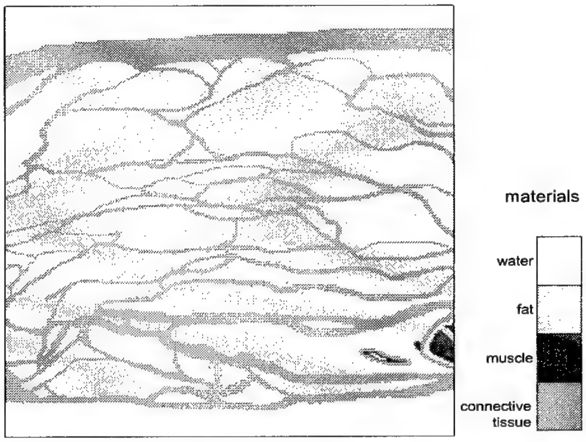

Figure 8. Abdominal wall model.

Tissue examples

Figure 8 shows an abdominal wall cross section [7,8]. This model is insonified by a 4.35 MHz plane wave pulse. Figure 9 displays typical reflected and transmitted signals computed by *SpectralFlex* at 4, 8 and 12 PPW. The grids were defined such that material boundaries always lie in exactly the same place. Again, it is confirmed that even the coarse 4 PPW model produces fairly accurate results.

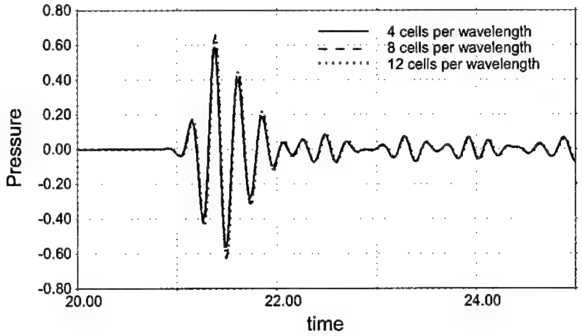

Figure 9. Transmitted pulse from Abdominal wall model.

INTERFACE TREATMENTS

Given that the largest numerical errors in the FFT based methods stem from material interfaces, we look at several interface treatments for reducing those errors.

Jump conditions

One possible method for improving the accuracy at interfaces is to split the solution into smooth and non-smooth parts, and apply the spectral method only to the smooth part. The idea is to introduce local corrections at material interfaces that enforce the jump conditions exactly. E.g., construct low order polynomials over the cells adjacent to the interface that have zero value and zero slope 1 cell away, and, when added to the continuous part satisfy the jump condition (1) at the interface. Obviously, the correction is not required to be local, but if it covers more than 1 cell, the algorithm will become much more complicated for multiple interfaces. LaVeque [9] discusses such an approach applied to finite difference models.

Figure 10 compares reflected and transmitted signals for coarse models of an interface with and without the jump correction for interface velocity. This example isolates the effects of density changes in that only the density is discontinuous. The bulk modulus is continuous. The correction term improves the computed result, but not to the level of a homogeneous material. A similar correction could be applied to the discontinuity in the velocity gradients. However, it will have a weaker effect on the staggered grid since the leading coefficients are already continuous.

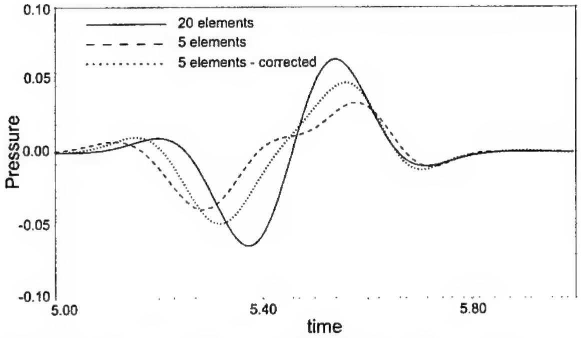

Figure 10. Jump treatment applied to interfaces.

Smoothing (Bandlimitation)

Another approach to improving accuracy at discontinuities is to smooth or bandlimit the model before sampling. This removes unresolvable high spatial frequencies from the model itself. We found that perfect bandlimitation reduced computed signals too much, but a "halfband" filter improves accuracy. The halfband filter is smooth with an amplitude of 0.5 at half the sampling frequency. Figure 11 shows direct and halfband filtered *kbench* models of a 3 mm cylinder using the same number of PPW. The corresponding pressure fields are plotted using a 60 dB bipolar log scale.

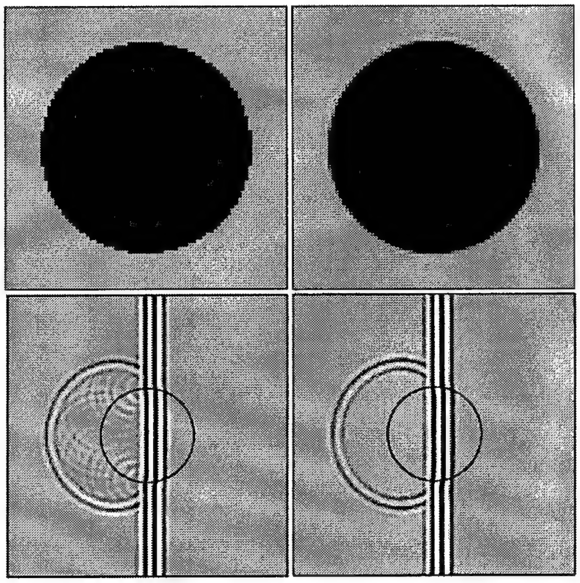

a) Unsmoothed b) Halfband Filtered

Figure 11. Direct sampled & bandlimited cylinders. Models and pressure, 60 dB bipolar log scale.

The staircase representation of the cylinder generates diffracted signals at each corner in 11a, but these have disappeared in 11b. Figure 12 shows selected waveforms from the direct and halfband sampled models. The late time diffractions have been removed, and overall L^2 error was reduced from 0.0155 to 0.0105. This exercise demonstrates that smoothing can be useful. However, there are some practical complications. The current procedure computes the smoothed object as the inverse transform of the object's analytical spectrum multiplied by the filter, and is thus defined only for objects with a known analytical spectrum. The extension to more general models defined on a pixel by pixel level has not yet been demonstrated. Also, continuous variations of material properties produce a large number of distinct materials. In the limit, each cell of the model has different properties. For the purely acoustic case, this presents little difficulty, but when material nonlinearity or viscoacoustic damping is added, the complexity intensifies. E.g., for each wavespeed/damping set, an optimization problem must be solved to compute the appropriate relaxation constants, and these constants must be stored.

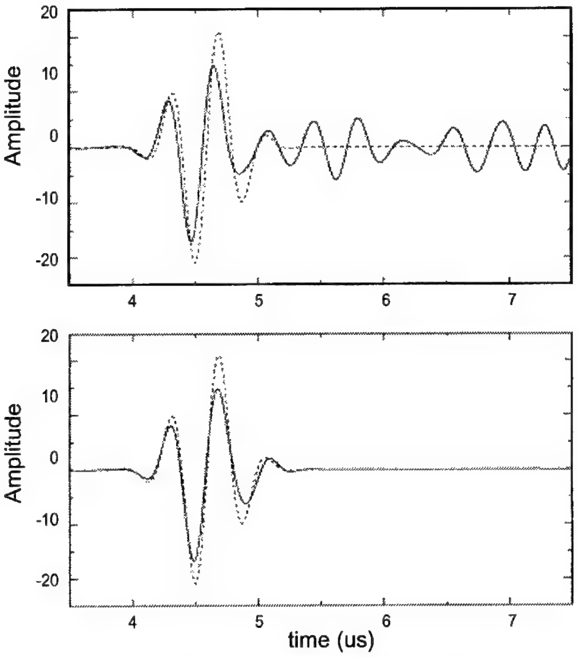

Figure 12. Backscattered signals from direct (top) and bandlimited (bottom) models.

Note that this procedure adds information to the model compared to the unsmoothed case. Because smoothing is applied to the analytical cylinder, the continuous variation of material constants provides a richer set of parameters than is available in the unsmoothed representation. As long as the model is known to higher resolution than the grid, information will be added. It is an interesting question whether smoothing would be beneficial on a grid finer than the pixel by pixel model definition. For example, the UOR tissue cross sections [7,8] are the most detailed models we know of. These are represented as piecewise constant with a pixel size 0.085 mm (about 7 PPW for a 2.5 MHz pulse). For a 5 MHz pulse, the coarsest grid would have finer resolution than the model.

Volume averaging of material constants has also been shown effective [10]. This adds additional information compared to the unsmoothed case, and the correction is more local than smoothing. However, the practical difficulties are the same.

As a last resort, increased discretization (brute force) will always converge to an accurate solution. This is a practical solution in 2D, as the above tissue examples indicate.

CONCLUSIONS

Model parameterization is a critical issue and puts all the above results in practical perspective. As shown above, differences in material constants or interface locations cause much larger differences in reflected/transmitted signals than any numerical errors in the FFT based methods. For gaining insight, or as a test-bed for aberration correction schemes, a 4 PPW model is sufficient at frequencies of 2.5 MHz or greater. Fine grids or cell-by-cell representation of material properties are needed only for more accurate rendition of model geometry.

ACKNOWLEDGEMENTS

Sponsored in part (JCM, GLW, LMC) by DARPA and ONR, and monitored by Dr. Wallace A. Smith.

REFERENCES

[1] N.N. Bojarski, "k-space formulation of the acoustic scattering problem, *J. Acoust. Soc. Am.,* Vol. 53, 374, 1973, presented 84th mtg. ASA, 1972.

[2] O. Kreiss and J. Oliger, "Comparison of accurate methods for the integration of hyperbolic equations," *Tellus*, vol. 24, 199-215, 1972.

[3] G. Wojcik, B. Fornberg, R. Waag, L. Carcione, J. Mould, L. Nikodym, T. Driscoll, "Pseudospectral methods for large-scale bioacoustic models," *IEEE Ultrasonics Symp.* 1501-1506, 1997.

[4] L.P. Souriau, T.D. Mast, D.L. Liu, A. Nachman and R.C. Waag, "A k-space method for large-scale models of wave propagation in tissue," IEEE Trans. UFFC, Submitted for publication, Feb. 1999.

[5] M.B. Ghrist, B. Fornberg and T. Driscoll, "Staggered time integrators for wave equations," Preprint No. 394, Dept of Applied Math., Univ. of Colorado, Boulder, CO., 1998.

[6] F.A. Duck, 1990, Physical Properties of Tissue, Academic Press.

[7] L.M. Hinkelman, T.D. Mast, M.J. Orr, and R.C. Waag, "Effects of abdominal wall morphology on ultrasonic pulse distortion," *Proc. IEEE Ultrason. Symp.*, 1493-1496, 1997.

[8] T.D. Mast, L.M. Hinkelman, M.J. Orr, V.W. Sparrow and R.C. Waag, "Simulation of ultrasonic pulse propagation through the abdominal wall," *J. Acoust. Soc. Am.*, 102, 1177-1190, 1997.

[9] R. LaVeque, C. Zhang, "The Immersed Interface Method for Wave Equations with Discontinuous Coefficients," Univ. of Wash., Seattle WA, 1994.

[10] F. Muir, J. Dellinger, J. Etgen and D. Nichols, "Modeling elastic fields across irregular boundaries," Geophysics, Vol. 57, No. 9, 1992.

A *k*-space method for coupled first-order acoustic propagation equations

Makoto Tabei
Department of Electrical and Computer Engineering
University of Rochester
Rochester, NY 14627

T. Douglas Mast
Applied Research Laboratory
The Pennsylvania State University
University Park, PA 16801

Robert C. Waag
Departments of Electrical and Computer Engineering and Radiology
University of Rochester
Rochester, NY 14627

Abbreviated title: A first-order *k*-space method

ABSTRACT

A k-space method for large-scale simulation of ultrasonic pulse propagation is presented. The present method, which solves the coupled first-order differential equations for wave propagation in inhomogeneous media, is derived in a simple form analogous to previous finite-difference methods with staggered spatial and temporal grids. Like k-space methods based on second-order wave equations, the present method is exact for homogeneous media, unconditionally stable for "slow" ($c(\mathbf{r}) \leq c_0$) media, and highly accurate for general weakly scattering media. In addition, unlike previous k-space methods, the form of the method allows straightforward inclusion of relaxation absorption and perfectly matched layer (PML) nonreflecting boundary conditions. Numerical examples illustrate the capabilities of the present k-space method. For weakly inhomogeneous media, accurate results are obtained using coarser temporal and spatial steps than possible with comparable finite-difference and pseudospectral methods. The low dispersion of the k-space method allows accurate representation of frequency-dependent attenuation and phase velocity associated with relaxation absorption. A technique for reduction of Gibbs phenomenon artifacts, in which compressibility and exponentially-scaled density functions are smoothed by half-band filtering, is introduced. When employed together with this smoothing technique, the k-space method provides high accuracy for media including discontinuities, high-contrast inhomogeneities, and scattering structures smaller than the spatial grid resolution.

PACS numbers: 43.20.Fn, 43.80.Qf, 43.20.Px

I. INTRODUCTION

This paper presents a method for computation of acoustic propagation in inhomogeneous media. The present method is an adaptation of the k-space method originally derived by Bojarski[1,2] and extended by several others.[3–5] As shown in Ref. 6, the k-space method has considerable advantages for large-scale simulations of ultrasonic propagation in soft tissues. The k-space method combines accurate spectral evaluation of spatial derivatives with a temporal iteration procedure that is exact for homogeneous media. For soft tissues, in which local medium properties show small variations around nominal background properties, this method provides excellent efficency and accuracy compared to other approaches such as finite-difference and pseudospectral methods.[6,7]

Previous formulations of the k-space method for acoustic propagation have numerically solved second-order differential wave equations. Such formulations have some advantages, including conceptual simplicity and computational efficiency, since the acoustic fields are defined only by one independent variable, the acoustic pressure fluctuation, instead of acoustic pressure and vector particle velocity fluctuations. Propagation in inhomogeneous media including density variations can be computed using a simple transformation of the pressure variable (*e.g.*, as in Refs. 5 and 6).

However, several desirable extensions to the k-space method are not possible using the usual second-order formulation. In particular, perfectly matched layer (PML) absorbing boundary conditions are not readily incorporated into current second-order k-space methods, while PML's are easily formulated for coupled first-order acoustic propagation equations. Additionally, as derived in Ref. 8, the full wave equation incorporating relaxation absorption effects is of order $2 + N$, where N is the number of relaxation processes employed. Relaxation effects can be incorporated more simply into numerical methods using coupled first-order acoustic propagation equations.[9]

Here, a k-space method is derived based on the coupled first-order differential equations for linear acoustic propagation. The method accounts for spatially-varying sound speed, density, and relaxation absorption processes, and includes PML absorbing boundary conditions. The formulation of this method shows that the k-space method can be regarded as a finite-difference method containing linear correction operators. Use of staggered spatial and temporal grids increases the range of applicability for the method, and facilitates inclusion of relaxation absorption and PML boundary conditions. The close analogy between the method presented here and existing finite-difference methods allows extensions developed for finite-difference methods to be easily applied to the k-space method, and also allows current finite-difference algorithms to be improved by inclusion of the k-space operators introduced here.

The present k-space method is, like previous k-space methods based on second-order wave equations,[6] temporally exact for homogeneous media. For general media, the present method also has accuracy and efficiency advantages similar to previous k-space methods. Numerical results presented here show that the k-space method presented here has the high accuracy and stability characteristics of the original k-space method, including unconditional stability for media with $c(\mathbf{r}) \leq c_0$. The low numerical dispersion inherent to the k-space method allows the frequency-dependent absorption and physical dispersion associated with relaxation-process absorption to be accurately modeled.

A method for smoothing of discontinuous scattering media is also presented here. Together with the k-space method, this smoothing method is shown to provide accurate results for strongly scattering media and for media with structures smaller than the grid resolution. Numerical examples also demonstrate the efficiency of the present k-space method for large-scale computations of interest in ultrasonic imaging studies.

II. THEORY

A. Second-order and first-order k-space methods

The k-space method derived below is based on the coupled first-order linear acoustic propagation equations for a fluid medium of variable sound speed and density. For a lossless two-dimensional medium, these are:[10]

$$\begin{aligned} \rho(\mathbf{r})\,\frac{\partial \mathbf{u}(\mathbf{r},t)}{\partial t} &= -\nabla p(\mathbf{r},t) \\ \frac{1}{\rho(\mathbf{r})\,c(\mathbf{r})^2}\,\frac{\partial p(\mathbf{r},t)}{\partial t} &= -\nabla\cdot\mathbf{u}(\mathbf{r},t), \end{aligned} \tag{1}$$

where $\mathbf{u}$ is the (vector) acoustic particle velocity fluctuation with components u_x and u_y, p is the acoustic pressure fluctuation, $\rho(\mathbf{r})$ is the density of the medium, $c(\mathbf{r})$ is the sound speed of the medium, and $\mathbf{r}$ denotes the vector coordinate (x, y).

Many numerical methods for acoustic wave propagation have been based on Eqs. (1). For example, in Ref. 11, ultrasonic propagation in an abdominal model was computed using a finite-difference method applied directly to the coupled equations.

The second-order wave equation corresponding to Eqs. (1) is[10]

$$\nabla\cdot\left(\frac{1}{\rho(\mathbf{r})}\,\nabla p(\mathbf{r},t)\right) - \frac{1}{\rho(\mathbf{r})\,c(\mathbf{r})^2}\,\frac{\partial^2 p(\mathbf{r},t)}{\partial t^2} = 0. \tag{2}$$

This equation can be solved numerically by the k-space method. Below, a brief sketch of the k-space solution to Eq. (2) will be given and this solution will be analyzed to obtain a corresponding k-space method for coupled first-order propagation equations. For simplicity, the derivation will assume sound speed and density are constant, *i.e.*, $\rho(\mathbf{r}) = \rho_0$ and $c(\mathbf{r}) = c_0$. A general derivation of the second-order k-space method is given in Ref. 6, while the first-order k-space method is straightforwardly extended to inhomogeneous media, as seen below.

For bandlimited signals such as typical ultrasonic pulses, very accurate spatial derivatives can be obtained by Fourier transformation of the pressure field.[12] This is the principle behind pseudospectral methods like that described in Ref. 13, in which the spatial derivatives from Eqs. (1) are evaluated using discrete Fourier transformation and temporal iteration is performed using a fourth-order Adams-Bashforth/Adams-Moulton scheme. For the case of homogeneous sound speed and density, Eq. (2) can be written in the spatial-frequency domain as

$$\frac{\partial^2 \hat{p}(\mathbf{k},t)}{\partial t^2} = -c_0^2 k^2 \hat{p}(\mathbf{k},t), \tag{3}$$

where $\hat{p}(\mathbf{k}, t)$ is the two-dimensional spatial Fourier transform of the acoustic pressure fluctuation $p(\mathbf{r}, t)$.

A discrete form of the left-hand-side of Eq. (3), obtained using a second-order-accurate finite-difference scheme, yields a crude pseudospectral method, expressed as

$$\frac{p(\mathbf{r}, t+\Delta t) - 2p(\mathbf{r}, t) + p(\mathbf{r}, t-\Delta t)}{(\Delta t)^2} = -c_0^2\, \mathbf{F}^{-1}\left[k^2\, \mathbf{F}\left[p(\mathbf{r}, t)\right]\right], \tag{4}$$

where $\mathbf{F}$ represents the two-dimensional spatial Fourier transform. In numerical implementations of Eq. (4), the spatial derivatives from the right-hand side of Eq. (3) are accurately represented using discrete Fourier transformation. Still, the discrete representation of the temporal derivative on the left-hand-side is significantly dispersive. Current pseudospectral methods[12, 13] typically use higher-order temporal integration schemes to decrease dispersion errors. However, for the homogeneous-medium case, temporal iteration can be performed exactly (*e.g.*, without any dispersion) using the *k*-*t* space scheme[6]

$$\frac{\hat{p}(\mathbf{k}, t+\Delta t) - 2\,\hat{p}(\mathbf{k}, t) + \hat{p}(\mathbf{k}, t-\Delta t)}{(\Delta t)^2\, \mathrm{sinc}\,(c_0 \Delta t\; k/2)^2} = -(c_0 k)^2 \hat{p}(\mathbf{k}, t), \tag{5}$$

where $\mathrm{sinc}(\mu) \equiv \sin(\mu)/(\mu)$. The temporal iteration scheme of Eq. (5) is mathematically equivalent to the scheme originally presented in Ref. 2. The temporal exactness of this scheme follows from an exact discrete representation of the harmonic-oscillator differential equation, described in Ref. 14. Temporal iteration can be performed in the spatial-frequency domain, as done in Ref. 6 using a generalized form of Eq. (5). Alternatively, the same iteration can be accomplished in real space by inverse Fourier transformation of Eq. (5). This results in the procedure

$$\frac{p(\mathbf{r}, t+\Delta t) - 2\,p(\mathbf{r}, t) + p(\mathbf{r}, t-\Delta t)}{(\Delta t)^2} = -c_0^2\, \mathbf{F}^{-1}\Big[k^2\, \mathrm{sinc}\,(c_0 \Delta t\, k/2)^2\; \mathbf{F}[p(\mathbf{r}, t)]\Big]. \tag{6}$$

Below, the operation on the right-hand side of Eq. (6) is called the second-order *k*-space operator. This operator is defined as

$$\left[\nabla^{(c_0 \Delta t)}\right]^2 p(\mathbf{r}, t) \equiv -\mathbf{F}^{-1}\left[k^2\, \mathrm{sinc}\,(c_0 \Delta t\, k/2)^2\, \mathbf{F}\left[p(\mathbf{r}, t)\right]\right]. \tag{7}$$

The form of Eq. (6) suggests that the second-order *k*-space method can be considered a corrected finite-difference method in which the spatial Laplacian is replaced by the *k*-space operator. However, the *k*-space operator of Eq. (7) incorporates not only spectral evaluation of the Laplacian, but also a temporal correction term associated with the *k*-*t* space iterator of Eq. (5).

To construct a k-space method for coupled first-order wave propagation equations, the second-order k-space operator can be factored into parts associated with each spatial direction. Below, this procedure is carried out for the two-dimensional case. An appropriate factorization is given by the first-order k-space operators

$$\begin{aligned}
\frac{\partial p(\mathbf{r},t)}{\partial^{(c_0\Delta t)^+}x} &\equiv \mathbf{F}^{-1}\Big[ik_x\, e^{ik_x\Delta_x/2}\,\mathrm{sinc}\,(c_0\Delta t\, k/2)\,\mathbf{F}[p(\mathbf{r},t)]\Big],\\
\frac{\partial p(\mathbf{r},t)}{\partial^{(c_0\Delta t)^+}y} &\equiv \mathbf{F}^{-1}\Big[ik_y\, e^{ik_y\Delta_y/2}\,\mathrm{sinc}\,(c_0\Delta t\, k/2)\,\mathbf{F}[p(\mathbf{r},t)]\Big],\\
\frac{\partial p(\mathbf{r},t)}{\partial^{(c_0\Delta t)^-}x} &\equiv \mathbf{F}^{-1}\Big[ik_x\, e^{-ik_x\Delta_x/2}\,\mathrm{sinc}\,(c_0\Delta t\, k/2)\,\mathbf{F}[p(\mathbf{r},t)]\Big],\\
\frac{\partial p(\mathbf{r},t)}{\partial^{(c_0\Delta t)^-}y} &\equiv \mathbf{F}^{-1}\Big[ik_y\, e^{-ik_y\Delta_y/2}\,\mathrm{sinc}\,(c_0\Delta t\, k/2)\,\mathbf{F}[p(\mathbf{r},t)]\Big],
\end{aligned} \tag{8}$$

so that

$$\left(\frac{\partial}{\partial^{(c_0\Delta t)^+}x}\frac{\partial}{\partial^{(c_0\Delta t)^-}x}+\frac{\partial}{\partial^{(c_0\Delta t)^+}y}\frac{\partial}{\partial^{(c_0\Delta t)^-}y}\right)p(\mathbf{r},t)=\left[\nabla^{(c_0\Delta t)}\right]^2 p(\mathbf{r},t). \tag{9}$$

The spatial-frequency components k_x and k_y are defined such that $k^2 = k_x^2 + k_y^2$.

Using the operators of Eqs. (8) within Eqs. (1) enables construction of a first-order k-space method equivalent to Eq. (6). Application of the exponential coefficients from Eqs. (8) requires the acoustic particle velocity variables u_x and u_y to be evaluated on grid points staggered by distances of $\Delta x/2$ and $\Delta y/2$, respectively. The resulting algorithm is

$$\begin{aligned}
\frac{u_x(\mathbf{r}_1,t^+)-u_x(\mathbf{r}_1,t^-)}{\Delta t} &= -\frac{1}{\rho(\mathbf{r}_1)}\frac{\partial p(\mathbf{r},t)}{\partial^{(c_0\Delta t)^+}x},\\
\frac{u_y(\mathbf{r}_2,t^+)-u_y(\mathbf{r}_2,t^-)}{\Delta t} &= -\frac{1}{\rho(\mathbf{r}_2)}\frac{\partial p(\mathbf{r},t)}{\partial^{(c_0\Delta t)^+}y},\\
\frac{p(\mathbf{r},t+\Delta t)-p(\mathbf{r},t)}{\Delta t} &= -\rho(\mathbf{r})\,c(\mathbf{r})^2\left(\frac{\partial u_x(\mathbf{r}_1,t^+)}{\partial^{(c_0\Delta t)^-}x}+\frac{\partial u_y(\mathbf{r}_2,t^+)}{\partial^{(c_0\Delta t)^-}y}\right),
\end{aligned} \tag{10}$$

where

$$\begin{aligned}
\mathbf{r}_1 &\equiv (x+\Delta x/2,y),\;\; \mathbf{r}_2 \equiv (x,y+\Delta y/2),\\
t^+ &\equiv t+\Delta t/2,\;\; \text{and}\;\; t^- \equiv t-\Delta t/2.
\end{aligned} \tag{11}$$

In Eqs. (10), the coefficients c_0 and ρ_0 have been replaced by the spatially-varying sound speed and density $c(\mathbf{r})$ and $\rho(\mathbf{r})$. Spatial staggering in Eqs. (10) is implicitly incorporated into the spatial derivative operators employed. For example, the operators $\partial/\partial^{(c_0\Delta t)^+}x$ and $\partial/\partial^{(c_0\Delta t)^-}x$ defined by

Eqs. (8) correspond, by the shift property of Fourier transformation, to derivatives evaluated after spatial shifts of $\Delta x/2$ and $-\Delta x/2$, respectively.

Staggered temporal grids, discussed in the following section, have also been employed in Eqs. (10). Notable is that the ordering of $(c_0\Delta t)^+$ and $(c_0\Delta t)^-$ operators is arbitrary depending on how the staggered grids are configured; however, for solution of coupled equations, the operators should be used in pairs such that the spatial shifting operations cancel out over any temporal interval of length Δt. Rationale for the use of spatial and temporal staggering is given in the folowing section.

The k-space method of Eqs. (10) is straightforwardly shown to be equivalent to Eq. (5) for $c(\mathbf{r}) = c_0$ and $\rho(\mathbf{r}) = \rho_0$. Thus, this first-order k-space scheme is temporally exact for homogeneous media. As shown below, the method also provides high accuracy for media with properties are close to the background values, and in conjunction with an appropriate smoothing algorithm, yields high accuracy even for media including high-contrast discontinuities.

Theoretical stability limits for the present k-space method can be computed as described in Ref. 6; given neglect of density variations and assumption of a worst-case sound-speed variation $c(\mathbf{r}) = c_{\max}$, the results are identical to those for the second-order k-space method. The resulting theoretical stability boundary is

$$\sin\frac{\pi\,\mathrm{CFL}}{2} \le \frac{c_0}{c_{\max}}, \tag{12}$$

where CFL denotes the Courant-Friedrichs-Lewy number $c_0\Delta t/\Delta x$. Thus, like the original k-space method,[6] the k-space method derived above is also expected to be unconditionally stable for media with $c(\mathbf{r}) \le c_0$ everywhere.

As with the second-order k-space method, the first-order method of Eqs. (10) can be regarded as a finite-difference method with correction factors that appear within the spatial derivative terms. The k-space algorithm of Eqs. (10) is analogous to standard second-order-accurate finite-difference methods for computation of acoustic wave propagation[9, 15] except that second-order-accurate spatial derivatives have been replaced by the k-space operators of Eqs. (8) that incorporate spectral spatial accuracy as well as corrected temporal iteration.

B. Properties of staggered spatial and temporal grids

The temporal and spatial sampling configuration employed in the k-space method of Eqs. (10) is directly analogous to staggered-space, staggered-time schemes employed in previous finite-difference methods.[9,15] Such staggered configurations are known to increase accuracy and stability for discrete representations of odd-order spatial and temporal derivatives.[12] For example, because the discrete Fourier transform is implicitly periodic, Gibbs phenomenon (ringing) artifacts result if the coefficients on the right-hand side of Eq. (8) have different values at the maximum spatial frequency $\pi/\Delta x$ and the minimum negative spatial frequency $-\pi/\Delta x$. The coefficient ik (which would correspond to a nonstaggered spatial grid) has a jump discontinuity of magnitude $2\pi/\Delta x$ at the transition between $k = \pi/\Delta x$ and $k = -\pi/\Delta x$. Coefficients of the form used in Eqs. (8) remove this discontinuity and, thus, can substantially reduce numerical artifacts in some cases, such as when the wavefield is spatially undersampled. Accuracy and stability are particularly increased for media containing large discontinuities.[16]

Although staggering slightly increases the complexity of the k-space algorithm, the benefit from spatial staggering can be easily understood by examining the physical relationship between sound pressure and particle velocity. Figure 1(a) represents the spatial sampling locations for sound pressure and particle velocity in the present staggered grid. The arrow at each sampling location indicates the direction of particle motion represented by each parameter. In this configuration, a local change in sound pressure $p(x, y)$ immediately affects the adjacent particle velocities. On the contrary, in a nonstaggered grid configuration, in which p, u_x, and u_y are all sampled at the same grid points, symmetry prohibits a local change in sound pressure from immediately affecting the particle velocity components sampled at the same position. This effect limits the accuracy of computations for high-spatial-frequency components of the wavefield.

Figure 1(b) shows the spatial-frequency response of the second-order-accurate discrete finite-difference operators for the first-order spatial derivative. Curve (i) shows the response for a nonstaggered center difference configuration, curve (ii) shows the corresponding response for the staggered grid center difference configuration, and curve (iii) shows the ideal frequency response for the continuous first-order derivative. Finite-difference schemes with higher-order accuracy show improved high-spatial-frequency response. Spectral computation of the first derivative on a staggered spatial grid, performed implicitly within the present k-space method, achieves this ideal frequency response up to the spatial Nyquist frequency $\pi/\Delta x$.

Figure 2 illustrates the characteristics of the temporal scheme employed. In panel (a), the temporal iteration process is shown for the staggered-time marching scheme. Because the time step is interleaved, time derivatives are evaluated based on values of spatial derivatives at the center of each time step. This staggering minimizes error when a crude time integration (Euler) scheme is employed. Panel (b) shows the difference between the true derivative in the center of the time step (slopes of the tangential lines) and a standard forward difference (slopes of the straight lines between A, B and C). Although time staggering reduces the error between the finite difference and the actual derivative, staggered finite-difference schemes still incur significant error with large time steps. This error is compensated in the k-space method by introducing a correction factor that leads to a temporally exact solution for a medium with constant sound speed. Although a temporally exact discrete solution can also be obtained using a nonstaggered grid,[14] staggered grids allow the necessary compensation to be performed using a single multiplicative factor. Use of a staggered time scheme also facilitates modeling of absorption, as shown in the next section. Thus, temporal staggering is important to the first-order k-space method.

C. Relaxation absorption and perfectly-matched layers

The close analogy between the k-space method of Eqs. (10) and standard finite-difference techniques[15] allows easy addition of features such as perfectly-matched layer (PML) absorbing boundary conditions and relaxation-process absorption to the present k-space method.

In the following, the acoustic pressure fluctuation $p(\mathbf{r}, t)$ is split into x and y components, $p(\mathbf{r}, t) = p_x(\mathbf{r}, t) + p_y(\mathbf{r}, t)$. This splitting is necessary for incorporation of the PML. Following the procedure applied to the finite-difference method in Ref. 9, the field equations are then written as a group of coupled first-order equations, with decay terms corresponding to relaxation absorption and to the PML. Discrete forms of these field equations are defined in a manner that provides high accuracy in the presence of large absorption.[9]

The (continuous) field equations for a PML medium with relaxation absorption can be written as

$$\rho(\mathbf{r}) \left(\frac{\partial u_x(\mathbf{r}, t)}{\partial t} + \alpha_x(\mathbf{r})\, u_x(\mathbf{r}, t) \right) = -\frac{\partial \left(p_x(\mathbf{r}, t) + p_y(\mathbf{r}, t) \right)}{\partial x}, \tag{13}$$

$$\rho(\mathbf{r}) \left(\frac{\partial u_y(\mathbf{r}, t)}{\partial t} + \alpha_y(\mathbf{r})\, u_y(\mathbf{r}, t) \right) = -\frac{\partial \left(p_x(\mathbf{r}, t) + p_y(\mathbf{r}, t) \right)}{\partial y}, \tag{14}$$

$$\kappa(\mathbf{r}, t) \otimes \left(\frac{\partial p_x(\mathbf{r}, t)}{\partial t} + \alpha_x(\mathbf{r})\, p_x(\mathbf{r}, t) \right) = -\frac{\partial u_x(\mathbf{r}, t)}{\partial x}, \tag{15}$$

$$\kappa(\mathbf{r}, t) \otimes \left(\frac{\partial p_y(\mathbf{r}, t)}{\partial t} + \alpha_y(\mathbf{r})\, p_y(\mathbf{r}, t) \right) = -\frac{\partial u_y(\mathbf{r}, t)}{\partial y}, \tag{16}$$

where $\alpha_x(\mathbf{r})$ and $\alpha_y(\mathbf{r})$ are absorption parameters employed only within the PML and the $\otimes$ operator denotes temporal convolution. Equations (15) and (16) contain a generalized compressibility,[8] defined as

$$\kappa(\mathbf{r},t) \;\equiv\; \kappa_\infty(\mathbf{r})\,\delta(t) + \sum_{i=1}^{N} \frac{\kappa_i(\mathbf{r})}{\tau_i(\mathbf{r})}\, e^{-t/\tau_i(\mathbf{r})}\, H(t), \tag{17}$$

where $\kappa_\infty(\mathbf{r})$ is the usual compressibility $1/[\rho(\mathbf{r})c(\mathbf{r})^2]$, $\tau_i(\mathbf{r})$ is the relaxation time for the ith relaxation process, $\kappa_i(\mathbf{r})$ is the relaxation modulus for the ith-order relaxation process, with units of compressibility, and $H(t)$ is the Heaviside step function. The integration (convolution) terms in Eqs. (15) and (16) make these equations equivalent to second-order differential equations in time. The convolution terms can be simplified using properties of the Dirac δ function and Heaviside step function that appear in the generalized compressibility (17) as well as identities for convolutions involving time derivatives.[9] Thus, for example, the left-hand side of Eq. (15) can be written as

$$\kappa_\infty(\mathbf{r}) \left(\frac{\partial p_x(\mathbf{r},t)}{\partial t} + \alpha_x(\mathbf{r})\, p_x(\mathbf{r},t) \right) + \sum_{i=1}^{N} \frac{\kappa_i(\mathbf{r})}{\tau_i(\mathbf{r})}\, p_x(\mathbf{r},t)$$
$$+ \left[\sum_{i=1}^{N} \frac{\kappa_i(\mathbf{r})}{\tau_i(\mathbf{r})}\, e^{-t/\tau_i(\mathbf{r})}\, H(t) \left(-\frac{1}{\tau_i(\mathbf{r})} + \alpha_x(\mathbf{r}) \right) \right] \otimes p_x(\mathbf{r},t).$$

The last term in this latter expression is still a convolution of two time-dependent functions, and this form presents difficulties for numerical implementation. The difficulties can be resolved by introducing a state variable, which allows Eqs. (13)–(16) to be rewritten as a set of simultaneous first-order differential equations. The state variable employed here is a filtered version of the acoustic pressure fluctuation, defined as

$$S_i^{(\cdot)}(\mathbf{r},t) \;\equiv\; \left(\frac{e^{-t/\tau_i(\mathbf{r})}}{\tau_i(\mathbf{r})} H(t) \right) \otimes p_{(\cdot)}(\mathbf{r},t), \tag{18}$$

where $(\cdot)$ denotes x or y.

Using the state variables defined by Eq. (18), the continuous field equations are rewritten as the coupled first-order differential equations

$$\begin{aligned}
\frac{\partial u_x(\mathbf{r},t)}{\partial t} + \alpha_x(\mathbf{r})\, u_x(\mathbf{r},t) &= -\frac{1}{\rho(\mathbf{r})} \frac{\partial\left(p_x(\mathbf{r},t) + p_y(\mathbf{r},t) \right)}{\partial x}, \\
\frac{\partial u_y(\mathbf{r},t)}{\partial t} + \alpha_y(\mathbf{r})\, u_y(\mathbf{r},t) &= -\frac{1}{\rho(\mathbf{r})} \frac{\partial\left(p_x(\mathbf{r},t) + p_y(\mathbf{r},t) \right)}{\partial y}, \\
\frac{\partial p_x(\mathbf{r},t)}{\partial t} + \mu_x(\mathbf{r})\, p_x(\mathbf{r},t) &= -\frac{1}{\kappa_\infty(\mathbf{r})} \left[\frac{\partial u_x(\mathbf{r},t)}{\partial x} - \sum_{i=1}^{N} \nu_i^x(\mathbf{r})\, S_i^x(\mathbf{r},t) \right],
\end{aligned}$$

$$\begin{aligned}
\frac{\partial p_y(\mathbf{r},t)}{\partial t} + \mu_y(\mathbf{r})\, p_y(\mathbf{r},t) &= -\frac{1}{\kappa_\infty(\mathbf{r})}\left[\frac{\partial u_y(\mathbf{r},t)}{\partial y} - \sum_{i=1}^{N} \nu_i^y(\mathbf{r}) S_i^y(\mathbf{r},t)\right], \\
\frac{\partial S_i^x(\mathbf{r},t)}{\partial t} + \frac{1}{\tau_i(\mathbf{r})} S_i^x(\mathbf{r},t) &= \frac{p_x(\mathbf{r},t)}{\tau_i(\mathbf{r})}, \\
\frac{\partial S_i^y(\mathbf{r},t)}{\partial t} + \frac{1}{\tau_i(\mathbf{r})} S_i^y(\mathbf{r},t) &= \frac{p_y(\mathbf{r},t)}{\tau_i(\mathbf{r})},
\end{aligned} \tag{19}$$

where

$$\mu_{(\cdot)}(\mathbf{r}) \equiv \frac{1}{\kappa_\infty(\mathbf{r})} \sum_{i=1}^{N} \frac{\kappa_i(\mathbf{r})}{\tau_i(\mathbf{r})} + \alpha_{(\cdot)}(\mathbf{r}) \tag{20}$$

and

$$\nu_i^{(\cdot)}(\mathbf{r}) \equiv \frac{\kappa_i(\mathbf{r})}{\tau_i(\mathbf{r})} - \kappa_i(\mathbf{r})\, \alpha_{(\cdot)}(\mathbf{r}). \tag{21}$$

Each of Eqs. (19) has the form

$$\frac{\partial R(\mathbf{r},t)}{\partial t} + \beta R(\mathbf{r},t) = Q(\mathbf{r},t), \tag{22}$$

where β is a constant that controls the decay of a field variable R. Following Ref. 9, the field equations can be transformed into a form that allows larger attenuations without numerical instability. This form is

$$\frac{\partial \left(e^{\beta t} R(\mathbf{r},t)\right)}{\partial t} = e^{\beta t} Q(\mathbf{r},t). \tag{23}$$

Equations of this form can be discretized using the time-staggered scheme

$$\frac{e^{\beta(t+\Delta t)} R(\mathbf{r},t+\Delta t) - e^{\beta t} R(\mathbf{r},t)}{\Delta t} = e^{\beta(t+\Delta t/2)} Q(\mathbf{r},t+\Delta t/2) \tag{24}$$

and the equivalent form

$$R(\mathbf{r},t+\Delta t) = e^{-\beta\Delta t/2}\left(e^{-\beta\Delta t/2} R(\mathbf{r},t) + \Delta t\, Q(\mathbf{r},t+\Delta t/2)\right). \tag{25}$$

To obtain the final k-space scheme including PML and relaxation absorption, Eq. (25) is applied directly to Eqs. (19). The spatial derivatives are replaced by the k-space operators (8), and the particle velocity variables u_x and u_y are evaluated on staggered spatial and temporal grids, as in the lossless algorithm of Eqs. (10). The state variables $S_i^{(\cdot)}$ are evaluated using a staggered-time scheme. The final discrete field equations, written in a form suitable for direct numerical implementation, are

$$
\begin{aligned}
u_x(\mathbf{r}_1, t^+) &= e^{-\alpha_x(\mathbf{r}_1)\Delta t/2}\left[e^{-\alpha_x(\mathbf{r}_1)\Delta t/2}\, u_x(\mathbf{r}_1, t^-) - \frac{\Delta t}{\rho(\mathbf{r}_1)}\left(\frac{\partial\left(p_x(\mathbf{r}, t) + p_y(\mathbf{r}, t)\right)}{\partial^{(c_0\Delta t)^+} x}\right)\right], \\
u_y(\mathbf{r}_2, t^+) &= e^{-\alpha_y(\mathbf{r}_2)\Delta t/2}\left[e^{-\alpha_y(\mathbf{r}_2)\Delta t/2}\, u_y(\mathbf{r}_2, t^-) - \frac{\Delta t}{\rho(\mathbf{r}_2)}\left(\frac{\partial\left(p_x(\mathbf{r}, t) + p_y(\mathbf{r}, t)\right)}{\partial^{(c_0\Delta t)^+} y}\right)\right], \\
p_x(\mathbf{r}, t + \Delta t) &= e^{-\mu_x(\mathbf{r})\Delta t/2}\left[e^{-\mu_x(\mathbf{r})\Delta t/2}\, p_x(\mathbf{r}, t) - \frac{\Delta t}{\kappa_\infty(\mathbf{r})}\left(\frac{\partial u_x(\mathbf{r}_1, t^+)}{\partial^{(c_0\Delta t)^-} x} - \sum_1^N \nu_i^x(\mathbf{r})\, S_i^x(\mathbf{r}, t^+)\right)\right], \\
p_y(\mathbf{r}, t + \Delta t) &= e^{-\mu_y(\mathbf{r})\Delta t/2}\left[e^{-\mu_y(\mathbf{r})\Delta t/2}\, p_y(\mathbf{r}, t) - \frac{\Delta t}{\kappa_\infty(\mathbf{r})}\left(\frac{\partial u_y(\mathbf{r}_2, t^+)}{\partial^{(c_0\Delta t)^-} y} - \sum_1^N \nu_i^y(\mathbf{r})\, S_i^y(\mathbf{r}, t^+)\right)\right], \\
S_i^x(\mathbf{r}, t^+) &= e^{-\Delta t/[2\tau_i(\mathbf{r})]}\left[e^{-\Delta t/[2\tau_i(\mathbf{r})]}\, S_i^x(\mathbf{r}, t^-) + \Delta t\, \frac{p_x(\mathbf{r}, t)}{\tau_i(\mathbf{r})}\right], \\
S_i^y(\mathbf{r}, t^+) &= e^{-\Delta t/[2\tau_i(\mathbf{r})]}\left[e^{-\Delta t/[2\tau_i(\mathbf{r})]}\, S_i^y(\mathbf{r}, t^-) + \Delta t\, \frac{p_y(\mathbf{r}, t)}{\tau_i(\mathbf{r})}\right],
\end{aligned}
\qquad (26)
$$

where the quantities μ and ν are defined by Eqs. (20) and (21), respectively.

This scheme provides spatial derivatives with spectral accuracy, temporal iteration that is exact for a homogeneous, lossless medium, and additional corrections that allow stable computations to be made in the presence of large absorption coefficients. The incorporation of relaxation processes allows simulation of realistic absorption in tissue, while use of the PML allows accurate computations to be carried out using small grid sizes. As shown below, the combination of these characteristics results in a powerful and flexible method for computation of ultrasonic propagation over long distances in inhomogeneous media such as soft tissues.

III. NUMERICAL METHODS

Numerical implementation of the present k-space method was accomplished using Eqs. (26) directly. The k-space operators of Eqs. (8) were evaluated using two-dimensional discrete Fourier transforms, implemented using a fast Fourier transform (FFT) method.[17]

Initial conditions were chosen to specify a pulsatile incident plane wave with sinusoidal time variation and a Gaussian envelope. Boundary conditions were given by the perfectly-matched layer (PML) on all sides of the grid. The absorption parameters α_x and α_y were tapered within the PML's using formulas of the form[18]

$$\alpha_x = A \frac{c_0}{\Delta x} \left(\frac{x - x_0}{x_{\max} - x_0} \right)^4, \tag{27}$$

where x_0 is the coordinate at the inner edge of the PML, $x_{\max}$ is the coordinate at the outer edge of the grid, and A is the maximum absorption per cell, in nepers, within the PML. A PML thickness of 9 grid points, together with a maximum PML absorption A of 4 nepers per cell, were found to be sufficient to reduce boundary reflection and transmission coefficients below -90 dB for normally-incident waves.

Relaxation-process absorption was implemented using two relaxation processes. The parameters κ_i and τ_i were chosen to approximate a linear dependence of absorption on frequency over the pulse bandwidth, using the formula for frequency-dependent absorption given in Ref. 8. The relaxation times chosen were

$$\tau_1 = \frac{1}{5 f_{\max}}, \quad \tau_2 = \frac{2}{f_{\max}}, \tag{28}$$

where $f_{\max}$ is the nominal maximum frequency of interest. For a maximum frequency of 5 MHz, these are $\tau_1 = 40$ ns and $\tau_2 = 400$ ns. Given this choice of relaxation times, an absorption frequency dependence of 0.5 dB/cm/MHz is best approximated (in a least-squares sense) for the frequency range $0 < f < 5$ MHz by the compressibility coefficients $\kappa_1 = 0.004749\,\kappa_\infty$ and $\kappa_2 = 0.004562\,\kappa_\infty$.

Benchmark computations analogous to those described in Ref. 6 were carried out to test the accuracy and stability of the present k-space method. As in Ref. 6, time-domain scattered fields for cylindrical test objects were computed and quantitatively compared to an exact solution[19] using an L^2 error metric.[20] The primary test object was, as in Ref. 6, a cylinder with radius 2.0 mm and acoustic properties of human fat ($c = 1.478$ mm/μs, $\rho = 0.950$ g/cm^3)[11] in a background medium with acoustic properties of water at body temperature ($c = 1.524$ mm/μs, $\rho = 0.993$ g/cm^3). The incident pulse was a plane wave with Gaussian temporal characteristics, a temporal Gaussian parameter $\sigma = 0.25\ \mu$s, which corresponds to a -6 dB bandwidth of 1.5 MHz, and a central starting position of $x = -4.5$ mm at time zero. Time histories of the total pressure field were recorded, at 128 equally-spaced "measurement" points spanning a circle of radius 2.5 mm concentric to the cylinder, using the interpolation method described in Ref. 6. Another benchmark employed the same configuration except that the cylinder had the density and sound speed of human bone ($c = 3.540$ mm/μs, $\rho = 1.990$ g/cm^3).[11]

In some cases, model media were smoothed before the computation to reduce errors associated with aliasing caused by discontuities. Smoothing was applied by filtering analytic Fourier transforms of the inhomogeneities considered using the half-band spatial-frequency filter described in Ref. 6. This filter was found to give the most satisfactory results when applied to the quantities $\kappa_\infty(\mathbf{r})$ and $\rho(\mathbf{r})^{-\beta}$, where β is a small coefficient. The accuracy of computations was found not to depend strongly on the value of β employed; the value $\beta = 1/6$ was used in the computations reported here.

A specific test of the smoothing method was implemented by computing scattering from a point (wire) scatterer with dimensions less than the grid resolution. The test object employed in this case was a point scatterer with acoustic properties of human bone ($c = 3540$ m/s, $\rho = 1.990$ g/cm^3) and a radius of 20 μm. Computations were performed with a spatial step of $\Delta x = 0.0833$ mm (four points per nominal minimum wavelength of .333 mm) and a Courant-Friedrichs-Lewy number (CFL $\equiv c_0 \Delta t / \Delta x$) of 0.1. For a k-space computation with smoothing, the model medium was obtained by the spatial-frequency filtering procedure described above applied to the analytic Fourier transform of the subresolution scatterer. For comparison, a computation using a discrete single-point scatterer was also carried out. In this case, the scatterer sound speed and density were decreased so that the compressibility contrast γ_κ and the density contrast γ_ρ decreased in proportion to the relative increase in area, which corresponds (for a scatterer of dimensions much smaller than the wavelength) to constant scattering strength.[19] For a scatterer area of 0.0833×0.0833 mm^2 (one grid point), this corresponds to a sound speed of 1.5897 mm/μs and a density of 1.0921 g/cm^3. Computational configurations were the same as for the 2.0 mm radius cylinder benchmarks, except that scattered fields (determined by subtracting the computed incident field in the absence of the scatterer) instead of total fields were compared to the corresponding exact solutions.

Implementation of relaxation absorption was tested in the k-space method by computing propagation of a plane-wave pulse in an absorbing medium. The pulse employed was a Gaussian-modulated sinusoid with a temporal Gaussian parameter of 0.25 μs. Propagation of this pulse was computed for a medium with absorption of 0.5 dB/cm/MHz (parameters τ_0, τ_1, κ_0, and κ_1 as given above), using a spatial step of $\Delta x = 0.0833$ mm (four points per nominal minimum wavelength). Waveforms were recorded at virtual measurement locations separated by 5 mm along the direction of propagation. The attenuation and for the computed propagation was determined numerically as a function of frequency from the ratio of the two pulse spectra, while the phase speed was determined numerically from the frequency-dependent phase change between the two pulses. These computed values were then compared with theoretical values, given by formulas available in Ref. 8.

An example computation, illustrating the performance of the present k-space method for large-scale problems relevant to ultrasonic imaging, was undertaken using a model tissue-mimicking phantom. This phantom is a 48 mm diameter cylinder ($c = 1.567$ mm/μs, $\rho = 1.040$ g/cm^3) with two internal 10 mm diameter cylinders ($c = 1.465$ mm/μs, $\rho = 0.0940$ g/cm^3) and three internal 0.2 mm diameter wires ($c = 2.600$ mm/μs, $\rho = 1.120$ g/cm^3) in a background medium with properties of water ($c = 1.509$ mm/μs, $\rho = 0.997$ g/cm^3). The 48 mm cylinder also contained simulated random scatterers, implemented by applying a Gaussian random perturbation with RMS amplitude 1% to the compressibility. The internal 10 mm cylinders and wires were not perturbed in this manner. The incident plane wave had a center frequency of 2.5 MHz, a -6 dB bandwidth of 1.7 MHz, and a propagation direction of 37° from the x axis, and was apodized using the window

$$A(\xi) = \frac{\mathrm{erf}\,[5(\xi + w_1/2 + w_2/2)/w_2] - \mathrm{erf}\,[5(\xi - w_1/2 - w_2/2)/w_2]}{2}, \tag{29}$$

where erf is the error function and ξ is an azimuthal distance along the initial wavefront. This window approximates a spatially-limited plane wave of the width w_1 with tapered ends of width w_2. The window parameters employed for this example were $w_1 = 48$ mm (the diameter of the phantom) and $w_2 = 6$ mm. The grid size employed was 768 × 768 with a spatial step of 0.12 mm and a time step of 0.02 μs (CFL $= 0.25$ based on the background sound speed).

IV. NUMERICAL RESULTS

The previous k-space method based on the second-order wave equation[2,5,6] has been shown in Refs. 6 and 7 to provide high accuracy for weakly-scattering media. Spectral evaluation of spatial derivatives provides much higher accuracy than typical finite difference methods for comparable spatial steps. The k-t space iteration scheme of Ref. 2 provides unconditionally stable computations for media with $c(\mathbf{r}) \leq c_0$[6] and allows large time steps to be employed while maintaining accuracy higher than comparable pseudospectral methods.[6,7]

Not surprisingly, the k-space method described here, which is based on coupled first-order wave propagation equations, has numerical properties very similar to those of the original k-space method. Figures 3 and 4, similar to Figs. 2 and 3 of Ref. 6, show the time-domain L^2 error as a function of the spatial and temporal sampling parameters. Figure 3, which shows computations made using the 2.0 mm radius "fat" cylinder described above and a spatial step size of four points per minimum wavelength, show that the present k-space method exhibits temporal accuracy almost identical to the k-space method of Ref. 6. Figure 3 also shows that both k-space methods provide much higher accuracy than a comparable pseudospectral method employing a leapfrog propagator (described in Ref. 6). All three methods provide equivalent results for very small time steps (CFL numbers less than about 0.1), but the k-space methods maintain high accuracy up to a CFL number of about 0.4. In contrast, the pseudospectral method rapidly increases in error for CFL numbers above 0.1.

The spatial accuracy of the present k-space method is compared to the previous k-space method[6] and to a 2-4 finite-difference method[11] in Fig. 4. Time-domain L^2 errors are shown, for the 2.0 mm radius "fat" cylinder, as a function of the spatial step size (in points per wavelength, based on a nominal minimum wavelength of 0.333 mm). For these computations, the CFL number of the k-space computations was held constant at 0.5, consistent with the CFL-accuracy relationship shown in Fig. 3, while the CFL number of the finite-difference computations was held at an optimal value of 0.25.[21] Again, the present k-space method yields accuracy almost identical to that of the previous k-space method of Ref. 6. All three methods achieve high accuracy for finer grid spacings; however, the k-space methods achieve higher accuracy for much larger spatial step sizes. The L^2 error drops below 0.05 for k-space computations employing only three points per minimum wavelength, while achievement of the same accuracy criterion requires 14 points per minimum wavelength for the finite-difference computations.

Although the present k-space method and that of Ref. 6 yield nearly equivalent results for the benchmark case illustrated in Figs. 3 and 4, the use of coupled first-order equations in the present k-space method can provide greater accuracy for strongly-scattering media. These advantages are illustrated using a benchmark computation for a 2 mm "bone" cylinder, introduced in Ref. 6. Since computations became unstable in this case for CFL numbers above about 0.2 [comparable to the theoretical upper stability limit of 0.2833 given by Eq. (12)], a CFL number of 0.1 was employed for the benchmark. Simulated waveforms obtained using the present k-space method and the previous k-space method of Ref. 6 are presented in Fig. 5 (computations carried out using the method of Ref. 6 were identical to those described in Ref. 6 except that the CFL number was reduced to 0.1.). Both before and after smoothing of the model medium, the present k-space method achieves much higher accuracy than the previous method (L^2 error, relative to an exact series solution, was 0.2292 vs. 0.3060 before smoothing; 0.0263 vs. 0.2687 after smoothing). In addition, artifacts are greatly reduced in the computations employing the present k-space method. The waveforms obtained using the present k-space method with smoothing [panel (b)] are visually identical to those obtained from the exact series solution, shown in Ref. 6.

Further demonstration of the effectiveness of the present k-space algorithm, in conjunction with the smoothing methods used here, is given by Fig. 6. This figure illustrates numerical results for scattering from a bone-mimicking cylinder of sub-grid-resolution size (radius 0.02 mm [20 μm] compared to a spatial step of $\Delta x = 0.0833$ mm). The model medium obtained by smoothing this subresolution cylinder results in a scattered amplitude that is nearly identical to the exact solution. The corresponding discrete computation, which attempts to represent the subresolution scatterer using a single pixel with adjusted acoustic parameters, accurately obtains the waveform shape and delay, but incorrectly predicts the angle-dependent scattered amplitude. This result indicates that the present k-space method, with smoothing of the kind used here, can accurately account for structures with dimensions much smaller than the spatial step employed.

Results of the numerical test of relaxation absorption are illustrated in Fig. 7. Panel (a) shows theoretical and simulated attenuation values, while panel (b) shows theoretical and simulated values of the phase speed. The simulations are for two sizes of the time step corresponding to CFL $=$ 0.25 and CFL $=$ 0.5. The case with a smaller time step (CFL $=$ 0.25) agrees very well with the theory, while the case with a larger time step (CFL $=$ 0.5, as employed in the soft-tissue benchmark computations described above) shows good qualitative agreement. These results illustrate that the present k-space method with relaxation absorption can realistically simulate attenuation caused by soft tissues even for relatively coarse time steps.

Numerical results for the tissue-mimicking phantom example, described in the previous section, are illustrated in Fig. 8. This figure shows four snapshots of the spatially-limited plane wave propagating through the phantom, causing coherent reflection from boundaries and wires as well as incoherent scattering from the random structure within the background cylinder. Notable is that smoothing of the medium has reduced any ringing artifacts to a level far below the low-level random scattering within the cylinder. Also notable is that the use of PML absorbing boundary conditions allows the computation shown to be performed efficiently (4063 CPU s on a 650 MHz Athlon processor for a simulation of duration 360 μs on a 768×768 grid). A hypothetical computation without absorbing boundaries, in which the grid size would be expanded to eliminate wraparound error within the region shown in Fig. 8, would require a grid size of approximately 4600×4600 points, resulting in a 35-fold increase in storage and computation time requirements.

V. DISCUSSION

The starting point for the k-space method introduced here is the previous k-space method based on the second-order wave equation.[2,6] Thus, a brief discussion of similarities and differences between these two methods is appropriate.

The two methods show identical accuracy for homogeneous media, since they are mathematically identical in this case. For weakly inhomogeneous media, both methods have similar performance in accuracy and stability. However, for stronger inhomogeneities such as the bone-mimicking cylinder benchmark described here, the two k-space methods differ significantly. The present method, based on the coupled first-order wave propagation equations, achieves much higher accuracy, although numerical evidence suggests that the present method has a lower stability threshold than the method of Ref. 6. The increased accuracy of the present k-space method for high-contrast media, relative to previous k-space methods based on second-order wave equations,[6] occurs for several likely reasons. Since the k-space method for coupled first-order propagation equations can be written in a form involving no Fourier transforms of medium properties [Eq. (10)], some aliasing errors may be eliminated. In addition, the coupled first-order equations incorporate the density directly rather than within a derivative term, so that errors associated with inaccuracies in discrete derivatives of the density are also reduced.

The two methods also differ somewhat in computation and storage requirements. The method of Ref. 6 requires computation and storage of only one acoustic variable (the acoustic pressure fluctuation), while the present method requires computation of the pressure fluctuation as well as each vector component of the acoustic particle velocity fluctuation. Thus, for a constant grid size, the present k-space method requires somewhat greater storage and computation time than the method of Ref. 6. However, this difference is offset by the capability of the present k-space method to incorporate PML absorbing boundary conditions. For large computations, the high performance of the PML allows the grid size to be substantially reduced without introduction of wraparound or boundary-reflection errors, so that the present k-space method is often more efficient for practical problems. This advantage is potentially even more important for three-dimensional computations.

The present k-space method can also be compared with pseudospectral methods for coupled first-order propagation equations (*e.g.*, Refs. 12, 13, and 16). Although both methods use Fourier transforms to accurately evaluate the spatial first order derivative, the present k-space method also includes temporal correction terms, which were obtained by factoring the second-order k-

space operator of Eq. (7) into the first-order operators of Eqs. (8). As a result, the present k-space method utilizes two-dimensional Fourier transforms, while pseudospectral methods employ one-dimensional Fourier transforms for calculation of spatial derivatives. This difference leads to a slight increase in computational requirements associated with Fourier transforms. Typically, pseudospectral methods require eight one-dimensional Fourier transforms per time step, while the present k-space method requires seven two-dimensional Fourier transforms per time step. However, the temporal correction provided by the k-space method eliminates the need for higher-order time schemes such as Adams-Bashforth and Adams-Moulton iteration, so that the k-space method may provide improved overall efficiency. This advantage occurs in part because the k-space method can provide accurate results for larger time steps (higher CFL numbers) than pseudospectral methods employing higher-order temporal iteration.[7]

Another advantage of the present k-space method is the close analogy between this method and the standard finite-difference time-domain method of Ref. 15. The present k-space method is algorithmically identical to the method of Ref. 15 except that second-order-accurate spatial derivatives have been replaced by the k-space operator of Eqs. (8), which provides spectral accuracy in space, exact temporal iteration for homogeneous media, and high accuracy for general media. This close analogy has allowed relaxation absorption and PML's, previously adapated to the corresponding finite-difference method,[9] to be straightforwardly incorporated into the present k-space method. The analogy allows great improvements in the performance and accuracy of existing finite-difference codes employing algorithms similar to those of Refs. 9 and 15 by the straightforward replacement of finite-difference spatial derivatives with the k-space operators of Eqs. (8).

VI. CONCLUSIONS

The present *k*-space method, which numerically solves the coupled first-order differential equations for wave propagation in inhomogeneous fluid media, has been shown to hold a number of advantages for large-scale simulation of ultrasound-tissue interaction.

The method maintains the major advantages of previous *k*-space methods;[6] like those, the present method is spectrally accurate in space, temporally exact for homogeneous media, and highly accurate for modest medium variations. Furthermore, the form of the present method has allowed it to be extended with PML absorbing boundary conditions, relaxation absorption, and an effective approach to smoothing discontinuous scattering media. Since the present method can be interpreted as a finite-difference method with correction terms, existing finite-difference codes may be easily modified to take advantage of the accuracy available from the *k*-space method.

Numerical examples presented here have shown that the present *k*-space method has remarkable accuracy and stability characteristics, similar to previous *k*-space methods,[6] for computations involving weakly scattering media. The method, together with the smoothing approach presented here, provides higher accuracy for strongly scattering media. Since *k*-space methods allow highly accurate results to be obtained using coarse spatial and temporal sampling, the present *k*-space method, with the incorporation of PML absorbing boundary conditions and relaxation absorption, is particularly well-suited to realistic large-scale simulations for applications including ultrasonic imaging studies.

ACKNOWLEDGMENTS

This research was funded by NIH Grants HL 50855, CA 74050, and CA 81688, US Army Grant DAMD-17-98-1-8141, DARPA Grant N00014-96-0749, and the University of Rochester Diagnostic Ultrasound Research Laboratory Industrial Associates.

REFERENCES

[1] N. N. Bojarski, "The *k*-space formulation of the scattering problem in the time domain," J. Acoust. Soc. Am. **72**, 570–584 (1982).

[2] N. N. Bojarski, "The *k*-space formulation of the scattering problem in the time domain: an improved single propagator formulation," J. Acoust. Soc. Am. **77**, 826–831 (1985).

[3] B. Compani-Tabrizi, "K-space formulation of the absorptive full fluid elastic scalar wave equation in the time domain," J. Acoust. Soc. Am. **79**, 901–905 (1986).

[4] S. Finette, "Computational methods for simulating ultrasound scattering in soft tissue," IEEE Trans. Ultrason., Ferroelect., Freq. Contr. **34**, 283–292 (1987).

[5] S. Pourjavid and O. J. Tretiak, "Numerical solution of the direct scattering problem through the transformed acoustical wave equation," J. Acoust. Soc. Am., **91**, 639–645 (1992).

[6] T. D. Mast, L. P. Souriau, D.-L. Liu, M. Tabei, A. I. Nachman, and R. C. Waag, "A *k*-space method for large-scale models of wave propagation in tissue," IEEE Trans. Ultrason., Ferroelect., Freq. Contr. **48**, 341–354 (2001).

[7] J. C. Mould, G. L. Wojcik, L. M. Carcione, M. Tabei, T. D. Mast, and R. C. Waag, "Validation of FFT-based algorithms for large-scale modeling of wave propagation in tissue," Proc. IEEE Ultrason. Symp. 1999 **2**, 1551–1556 (1999).

[8] A. I. Nachman, J. Smith, and R. C. Waag, "An equation for acoustic propagation in inhomogeneous media with relaxation losses," J. Acoust. Soc. Am. **88**, 1584–1595 (1990).

[9] X. Yuan, D. Borup, J. Wiskin, M. Berggren, and S. Johnson, "Simulation of acoustic wave propagation in dispersive media with relaxation losses by using FDTD method with PML absorbing boundary condition," IEEE Trans. Ultrason., Ferroelect., Freq. Contr. **46**, 14–23 (1999).

[10] A. D. Pierce, *Acoustics: an Introduction to its Physical Principles and Applications*, Second Edition (Acoustical Society of America, Woodbury, New York, 1989), ch. 1.

[11] T. D. Mast, L. M. Hinkelman, M. J. Orr, V. W. Sparrow, and R. C. Waag, "Simulation of ultrasonic pulse propagation through the abdominal wall," J. Acoust. Soc. Am. **102**, 1177–1190 (1998).

[12] B. Fornberg, *A Practical Guide to Pseudospectral Methods*, (Cambridge University Press, Cambridge, 1996).

[13] G. Wojcik, B. Fornberg, R. Waag, L. Carcione, J. Mould, L. Nikodym, and T. Driscoll, "Pseudospectral methods for large-scale bioacoustic models," Proc. IEEE Ultrason. Symp. 1997, **2**, 1501–1506 (1997).

[14] Ronald A. Mickens, *Nonstandard Finite Difference Models of Differential Equations* (World Scientific, Singapore, 1994).

[15] K. S. Yee, "Numerical solution of initial boundary value problems involving Maxwell's equations in isotropic media," IEEE Trans. Antennas Propagat. **14**, 302–307 (1966).

[16] H.-W. Chen, "Staggered-grid pseudospectral viscoacoustic wave field simulation in two-dimensional media," J. Acoust. Soc. Am., **100**, no. 1, 120–131 (1996).

[17] M. Frigo and S. G. Johnson, “FFTW: An adaptive software architecture for the FFT,” Proc. ICASSP, **3**, 1381–1384 (1998).

[18] J. Mould, D. K. Vaughan, and L. Carcione, *SpectralFlex User's Manual* (Weidlinger Associates, Los Altos, California, 1999).

[19] P. M. Morse and K. U. Ingard, *Theoretical Acoustics* (McGraw-Hill, New York, 1968), ch. 8.

[20] R. L. Burden, J. D. Faires, and A. C. Reynolds, *Numerical Analysis* (Prindle, Weber, and Schmidt, Boston, 1978), ch. 8.

[21] E. Turkel, “On the practical use of high-order methods for hyperbolic systems,” J. Comp. Phys. **35**, 319–340 (1980).

FIGURE CAPTIONS

1 Characteristics of discrete spatial derivative operators. (a) Sampling locations for spatially-staggered grid. (b) Spatial-frequency response of first-derivative operators: (i) nonstaggered grid; (ii) staggered grid; (iii) ideal. 27

2 Characteristics of discrete time derivative operators. (a) Time-staggered sampling for acoustic pressure and particle velocity. (b) Derivatives estimated using a nonstaggered time scheme and true derivatives evaluated at the center of the time step. 28

3 Time-domain comparison of accuracy for the k-space and leapfrog pseudospectral methods as a function of CFL number. Each test used the “fat” cylinder of 2.0 mm radius and a spatial step size of four points per minimum wavelength. 29

4 Time-domain comparison of accuracy for the k-space and 2-4 finite-difference time-domain methods as a function of the spatial step size in points per minimum wavelength (PPW). Each test used the “fat” cylinder of 2.0 mm radius. CFL numbers were 0.5 for the k-space methods and 0.25 for the finite-difference time-domain method. 30

5 Computed pressure waveforms at a receiver radius of 2.5 mm for a “bone” cylinder of radius 2.0 mm and a pulse center frequency of 2.5 MHz. The acoustic pressure is shown on a bipolar logarithmic scale with a 60 dB dynamic range. The horizontal range of each plot is 360 degrees, covering the entire measurement circle starting with angle 0 (forward propagation). The vertical range of each panel corresponds to a temporal duration of 9 μs, with $t = 0$ at the top of each plot. (a) Unsmoothed object; present k-space method, L^2 error 0.2292. (b) Smoothed object; present k-space method, L^2 error 0.0263. (c) Unsmoothed object; previous k-space method,[6] L^2 error 0.3060. (d) Smoothed object; previous k-space method,[6] L^2 error 0.2687. 31

6 Simulated scattering from a point (wire) scatter with radius 20 μm and acoustic properties of human bone. Each plot shows results for an exact series solution, a k-space solution using a half-band filtered representation of the subresolution scatterer (“smoothed”), and a single-pixel representation with equal scattering strength. (a) Backscattered signals. (b) RMS waveform amplitudes. 32

7 Attenuation and phase speed for propagation of a pulse in a medium with two relaxation processes. Each panel shows theoretical values[8] and values obtained using the present k-space method for two values of the CFL number. (a) Frequency-dependent attenuation. (b) Frequency-dependent phase speed. 33

8 Computed pressure fields for a 48 mm diameter tissue-mimicking phantom. Panels (a)–(d) show the total acoustic pressure at intervals of 12 μs, superimposed on an image of the phantom. The area shown in each panel is 61 mm × 61 mm. Wavefields are plotted using a bipolar logarithmic scale with a dynamic range of 60 dB. 34

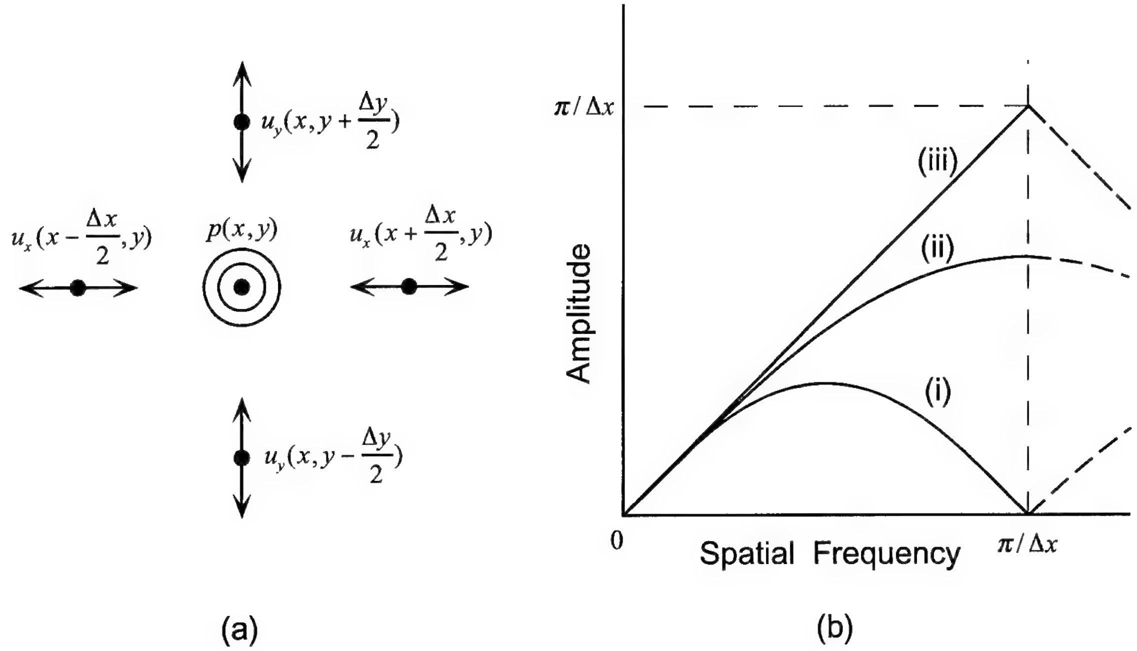
$u_y(x, y+\frac{\Delta y}{2})$
$u_x(x-\frac{\Delta x}{2}, y)$
$p(x,y)$
$u_x(x+\frac{\Delta x}{2}, y)$
$u_y(x, y-\frac{\Delta y}{2})$
$\pi/\Delta x$
(iii)
(ii)
(i)
Amplitude
0
Spatial Frequency
$\pi/\Delta x$
(a)
(b)

Figure 1: Characteristics of discrete spatial derivative operators. (a) Sampling locations for spatially-staggered grid. (b) Spatial-frequency response of first-derivative operators: (i) nonstaggered grid; (ii) staggered grid; (iii) ideal.

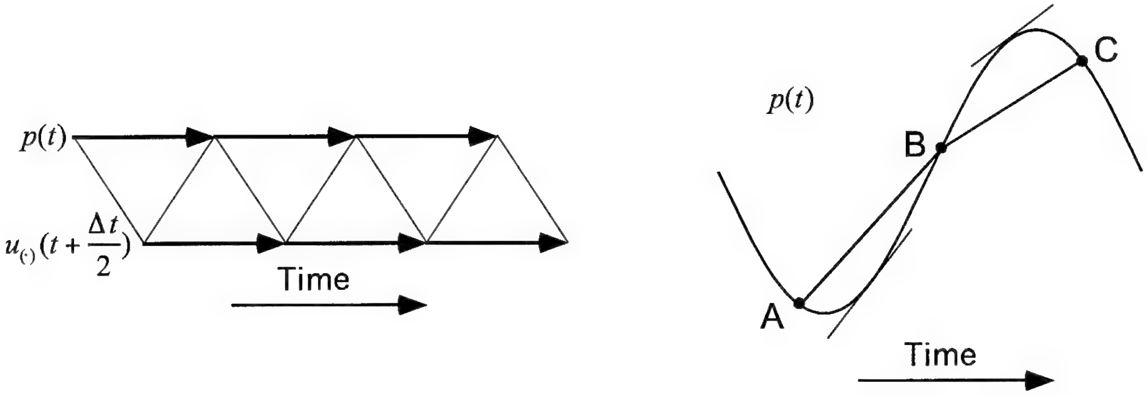

(a)

(b)

Figure 2: Characteristics of discrete time derivative operators. (a) Time-staggered sampling for acoustic pressure and particle velocity. (b) Derivatives estimated using a nonstaggered time scheme and true derivatives evaluated at the center of the time step.

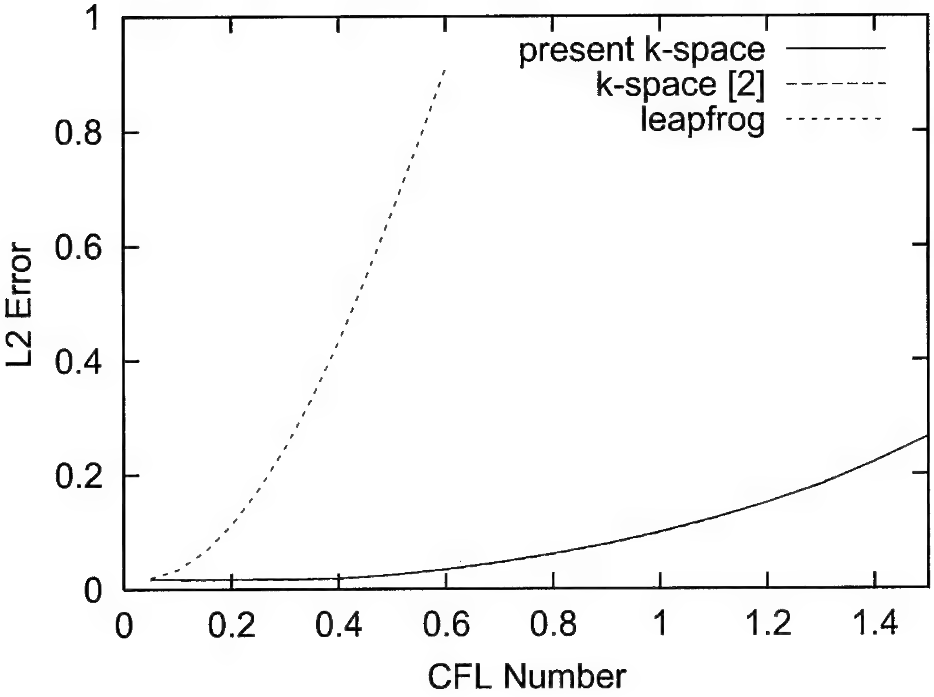

Figure 3: Time-domain comparison of accuracy for the *k*-space and leapfrog pseudospectral methods as a function of CFL number. Each test used the "fat" cylinder of 2.0 mm radius and a spatial step size of four points per minimum wavelength.

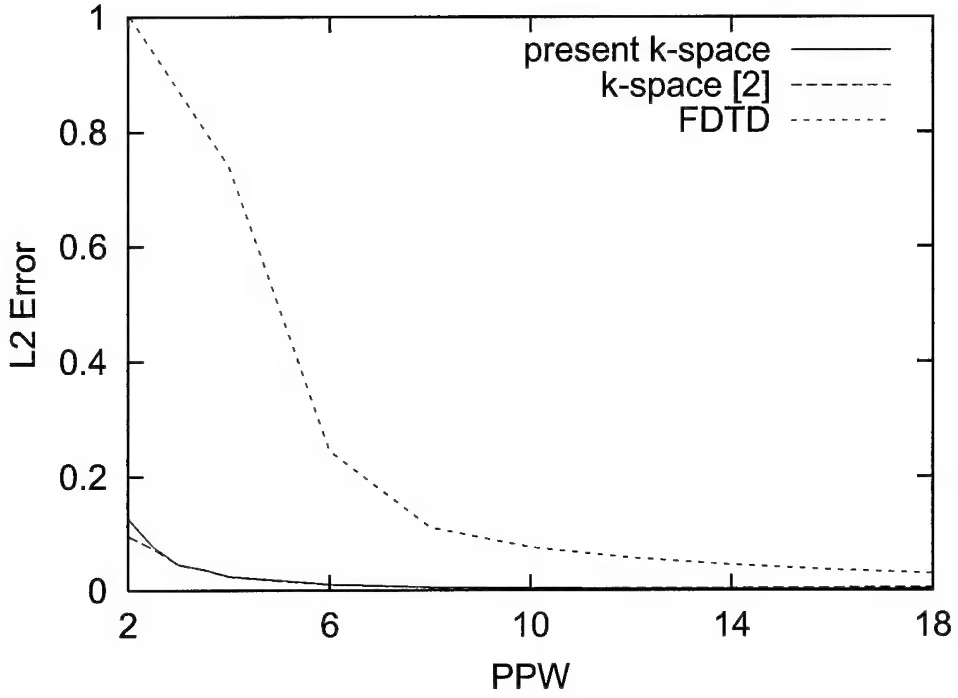

Figure 4: Time-domain comparison of accuracy for the *k*-space and 2-4 finite-difference time-domain methods as a function of the spatial step size in points per minimum wavelength (PPW). Each test used the "fat" cylinder of 2.0 mm radius. CFL numbers were 0.5 for the *k*-space methods and 0.25 for the finite-difference time-domain method.

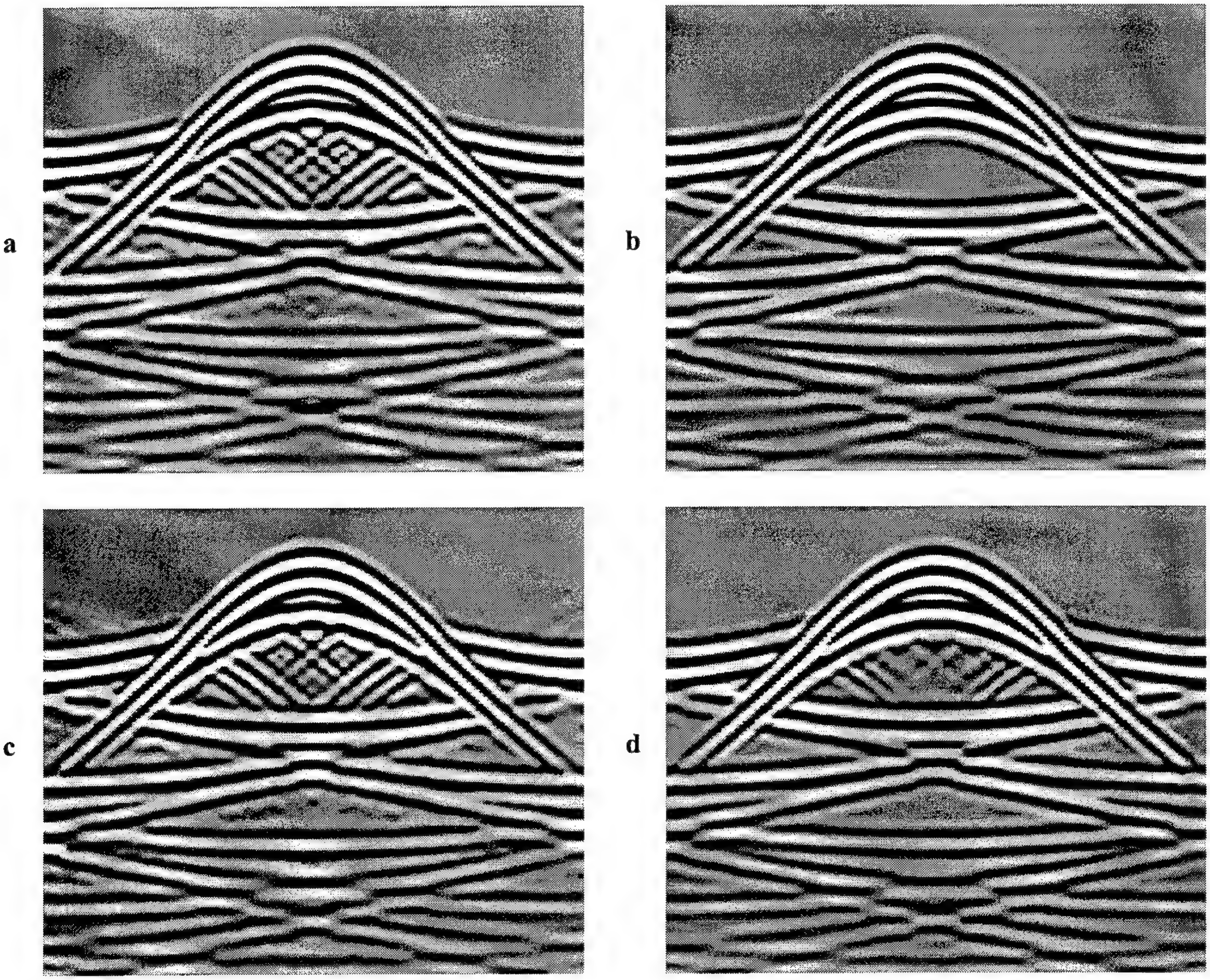

Figure 5: Computed pressure waveforms at a receiver radius of 2.5 mm for a "bone" cylinder of radius 2.0 mm and a pulse center frequency of 2.5 MHz. The acoustic pressure is shown on a bipolar logarithmic scale with a 60 dB dynamic range. The horizontal range of each plot is 360 degrees, covering the entire measurement circle starting with angle 0 (forward propagation). The vertical range of each panel corresponds to a temporal duration of 9 μs, with $t = 0$ at the top of each plot. (a) Unsmoothed object; present k-space method, L^2 error 0.2292. (b) Smoothed object; present k-space method, L^2 error 0.0263. (c) Unsmoothed object; previous k-space method,[6] L^2 error 0.3060. (d) Smoothed object; previous k-space method,[6] L^2 error 0.2687.

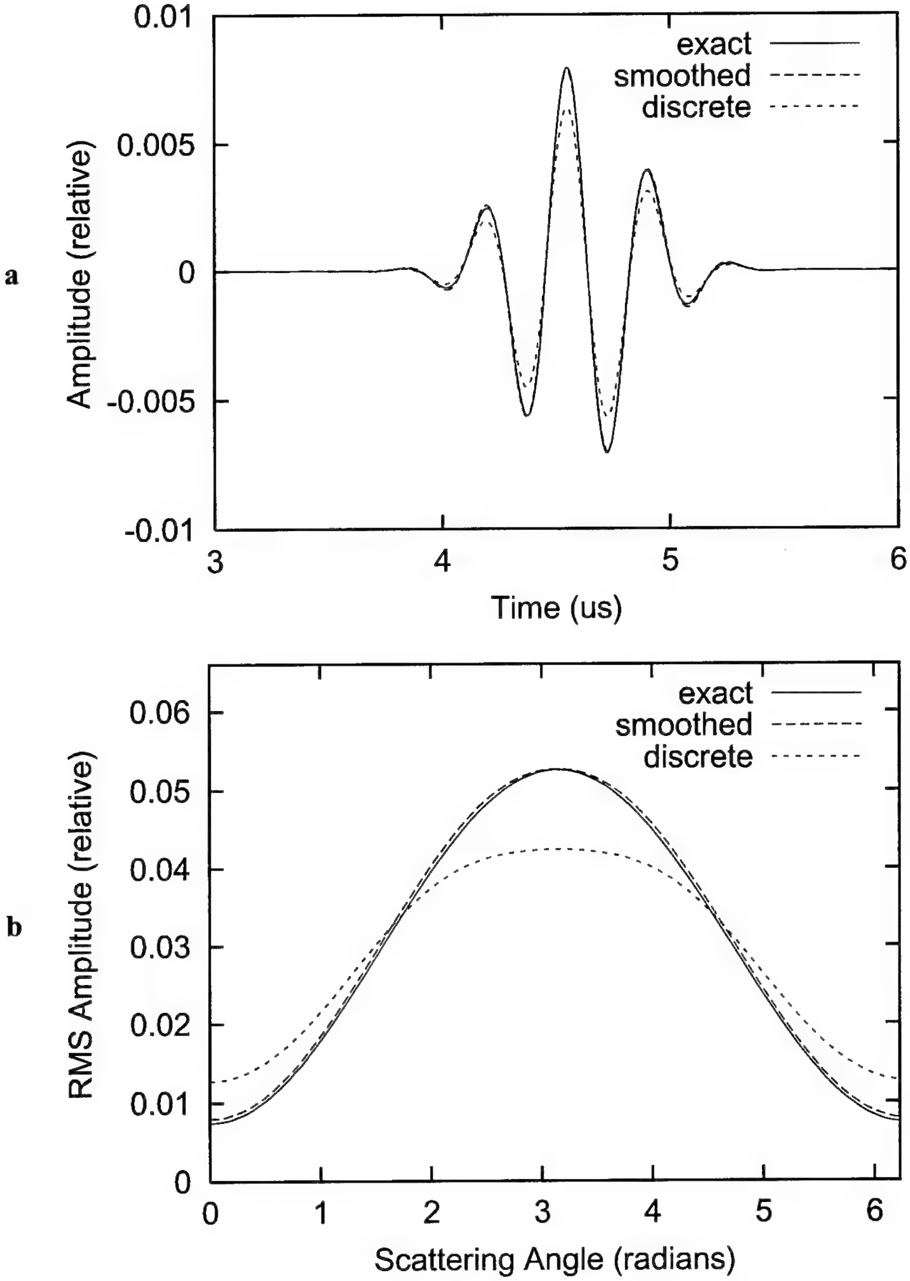

Figure 6: Simulated scattering from a point (wire) scatter with radius 20 μm and acoustic properties of human bone. Each plot shows results for an exact series solution, a k-space solution using a half-band filtered representation of the subresolution scatterer ("smoothed"), and a single-pixel representation with equal scattering strength. (a) Backscattered signals. (b) RMS waveform amplitudes.

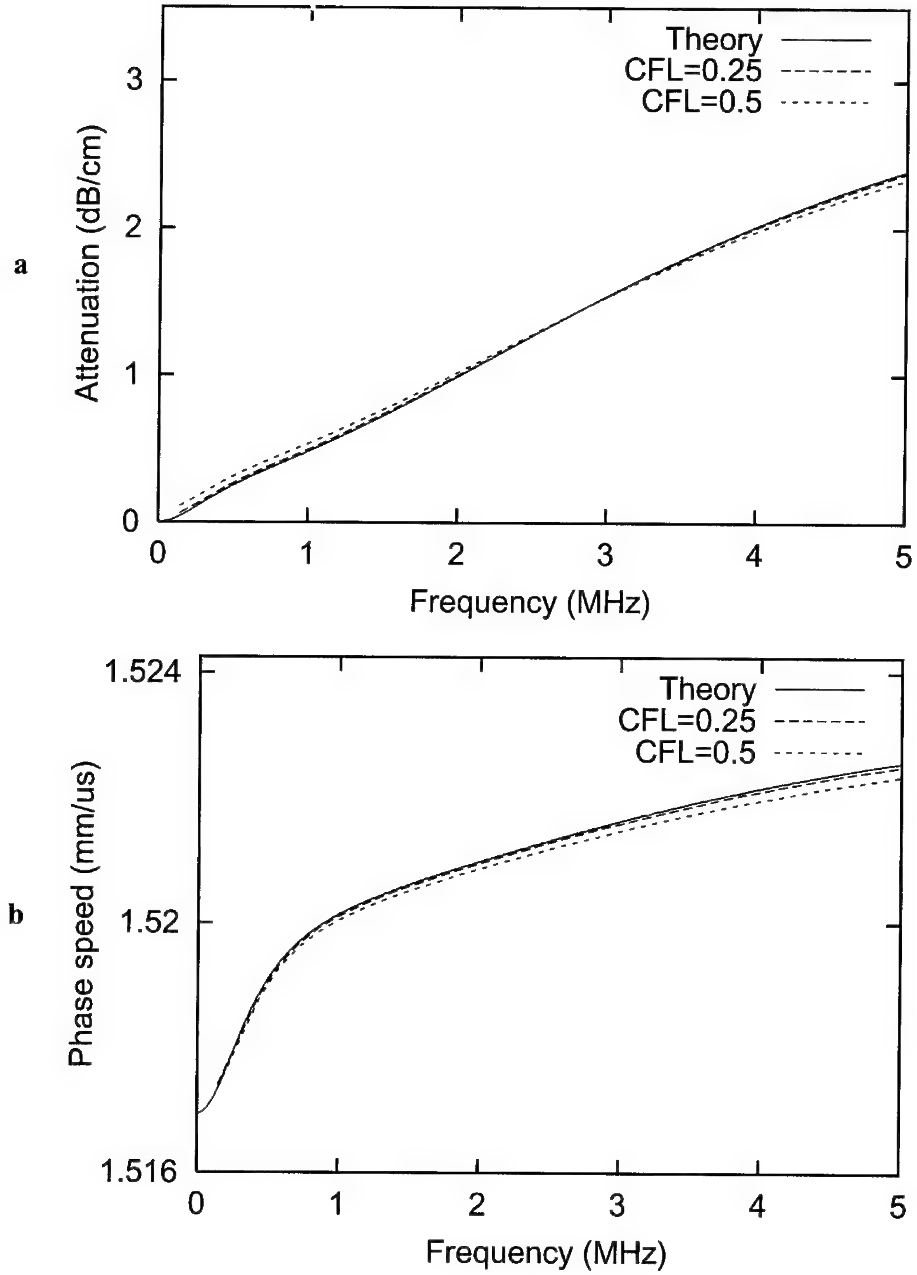

Figure 7: Attenuation and phase speed for propagation of a pulse in a medium with two relaxation processes. Each panel shows theoretical values[8] and values obtained using the present *k*-space method for two values of the CFL number. (a) Frequency-dependent attenuation. (b) Frequency-dependent phase speed.

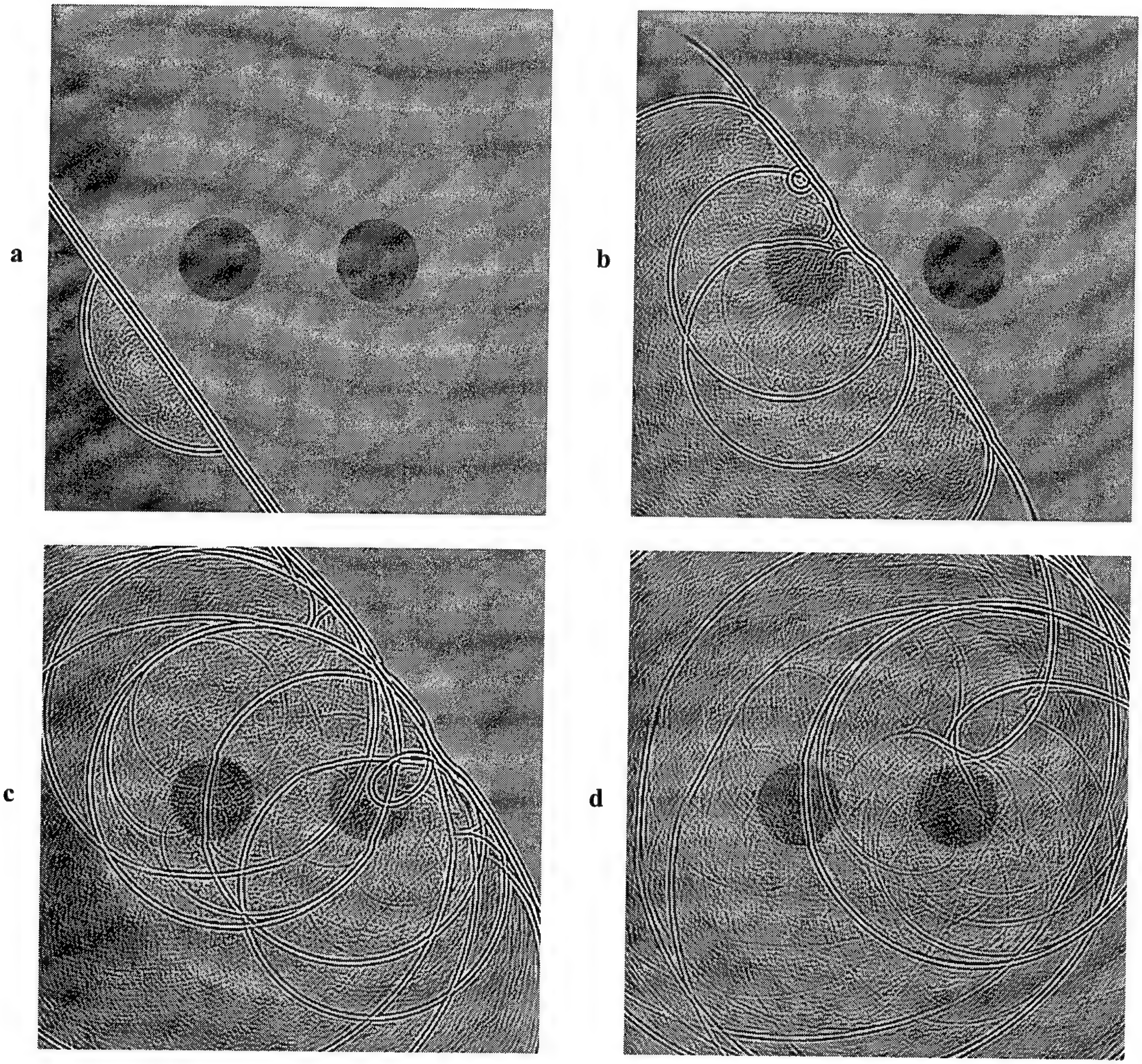

Figure 8: Computed pressure fields for a 48 mm diameter tissue-mimicking phantom. Panels (a)–(d) show the total acoustic pressure at intervals of 12 μs, superimposed on an image of the phantom. The area shown in each panel is 61 mm × 61 mm. Wavefields are plotted using a bipolar logarithmic scale with a dynamic range of 60 dB.

T. D. Mast: Acoustics Research Letters Online [PII S1529-7853(00)00102-X] Published Online 16 November 2000

Empirical relationships between acoustic parameters in human soft tissues

T. Douglas Mast

Applied Research Laboratory, The Pennsylvania State University,
University Park, Pennsylvania 16802
mast@sabine.acs.psu.edu

Abstract: Previously published summaries of sound speed, density, attenuation coefficient, and nonlinearity parameter, B/A, in human soft tissues are quantitatively analyzed. A highly significant empirical linear relationship is found to hold between sound speed and density for a wide range of soft tissues, including adipose, parenchymal, muscular, and connective tissues as well as body fluids. Even higher correlations occur between nondimensional parameters describing density variations and compressibility variations. Values for the nonlinearity parameter correlate significantly with sound speed and density, while the attenuation coefficient is found not to correlate significantly with any of the other parameters considered. Implications for tissue modeling and quantitative ultrasonic imaging are discussed.

© 2000 Acoustical Society of America

PACS numbers: 43.80.Cs, 43.80.Qf
Received: October 9, 2000 **Accepted**: November 6, 2000

Introduction

Understanding relationships between acoustic parameters of human soft tissues is important for several reasons, including scientific interest in tissue properties, accuracy in simulation of acoustic propagation in tissues, and effectiveness in design and interpretation of quantitative ultrasonic imaging methods.

Simulations of ultrasonic propagation in tissue require choices for acoustic properties such as sound speed, density, absorption, and nonlinear propagation characteristics. Previous research has resulted in simple empirical relationships between sound speed and density for compact calcified tissues [Lees et al., 1983] and a range of mammalian soft tissues [Aroyan, 1996]. These relationships are useful for tissue modeling; for example, the linear sound speed-density relationship observed by Lees et al. [1983] was used by Mast et al. [1999] to estimate the sound speed of calcified cartilage based on a density measurement. Aroyan [1996] used a similar piecewise-linear relationship to obtain three-dimensional maps of sound velocity in dolphin tissue, based on density maps estimated from computed tomography image data. To the extent possible, corresponding relationships between attenuation, nonlinearity parameter, and other acoustic parameters would also be useful for construction of tissue models.

Quantitative ultrasonic imaging methods such as diffraction tomography [Mast, 1999 and references therein] provide images of intrinsic tissue properties such as sound speed, density, compressibility, and absorption. The diagnostic efficacy and utility of such methods would be improved by a greater knowledge of the relationships between tissue parameters. For instance, if two parameters, such as sound speed and density, are highly correlated with one another for all tissue structures in the human body, measurement or imaging of both parameters will be of little diagnostic value. Analysis of correlation between tissue parameters would allow ultrasonic imaging methods to be designed for maximum diagnostic information content.

Tissue Properties

Reference sound speed, mass density, attenuation, and nonlinearity properties for a variety of human soft tissues were compiled from three secondary sources, each of which drew on many

Table 1: Sound speed, density, attenuation, and nonlinearity parameter values used for analysis. Sources: [1]Mast et al., 1997, [2]ICRU Report 61, 1998, [3]Duck, 1990.

Tissue Type	Speed (mm/μs)	Density (g/cm^3)	Atten. Coef. @ 1 MHz (dB/cm)	Nonlin. Param. (B/A)
Connective[1]	1.613	1.120	1.57	—
Muscle[1]	1.547	1.050	1.09	—
Fat[1]	1.478	0.950	0.48	—
Adipose[2]	1.450	0.950	0.29	10.0
Blood[2]	1.584	1.060	0.20	6.1
Brain[2]	1.560	1.040	0.60	7.1
Breast[2]	1.510	1.020	0.75	—
Eye: lens[2]	1.645	1.070	0.80	—
Eye: vitreous[2]	1.528	1.010	0.1	—
Kidney[2]	1.560	1.050	1.0	7.4
Liver[2]	1.595	1.060	0.50	6.6
Muscle, cardiac[2]	1.576	1.060	0.52	7.1
Muscle, skeletal[2]	1.580	1.050	0.74	6.6
Skin[2]	1.615	1.090	0.35	7.9
Fatty[2]	1.465	0.985	0.40	8.5
Non-fatty[2]	1.575	1.055	0.60	7.0
Blood cells[3]	1.627	1.093	0.28	—
Blood plasma[3]	1.543	1.027	0.069	—
Eye: cornea[3]	1.586	1.076	—	—
Spinal cord[3]	1.542	1.038	—	—
Spleen[3]	1.567	1.054	0.4	7.8
Testis[3]	1.595	1.044	0.17	—
Mean	1.561	1.043	0.54	7.5
St. Dev.	0.051	0.042	0.37	1.1

previously published measurements. Reference values for fat, muscle, and connective tissue were obtained from Mast et al. [1997], which summarized data from Goss et al. [1978; 1980b], and Woodard and White [1986]. Attenuation coefficients reported there were extrapolated to 1 MHz values assuming linear frequency dependence. Reference values for nine soft tissue types (adipose tissue, whole blood, brain, breast, liver, skeletal muscle, skin, "average" fatty soft tissue, and "average" non-fatty soft tissue), as well as for four specific tissues (kidney, cardiac muscle, eye—lens, and eye—vitreous), were taken from ICRU Report 61 [1998]. For the latter four tissues, values used here are means of the upper and lower limits presented in the report.

Parameters for five additional human soft tissues, not addressed in the above summaries, were compiled from values given by Duck [1990]. In all cases, only values measured on human tissues were employed. Sound speed values employed were only those measured at body temperature (37° C) or *in vivo*. When more than one listed sound speed measurement met those criteria, all available values for adult human tissue were averaged; when ranges were given, means of the upper and lower limits were taken. Density values were taken to be the mean of mass density ranges given by Duck. Attenuation coefficients, when necessary, were extrapolated to 1 MHz assuming a linear dependence of attenuation on ultrasonic frequency.

The compiled sound speed, density, attenuation, and nonlinearity parameter data are listed in Table I.

In addition to the four acoustic properties listed in Table I, two other parameters of particular interest are the compressibility variation γ_κ and the density variation γ_ρ, defined as

$$\gamma_\kappa \equiv \frac{\rho_0 c_0^2}{\rho c^2} - 1, \quad \gamma_\rho \equiv 1 - \frac{\rho_0}{\rho}, \tag{1}$$

where c and ρ are local values of sound speed and density, and c_0 and ρ_0 are reference values, taken here to be the mean sound speed and density values from Table I. These parameters are

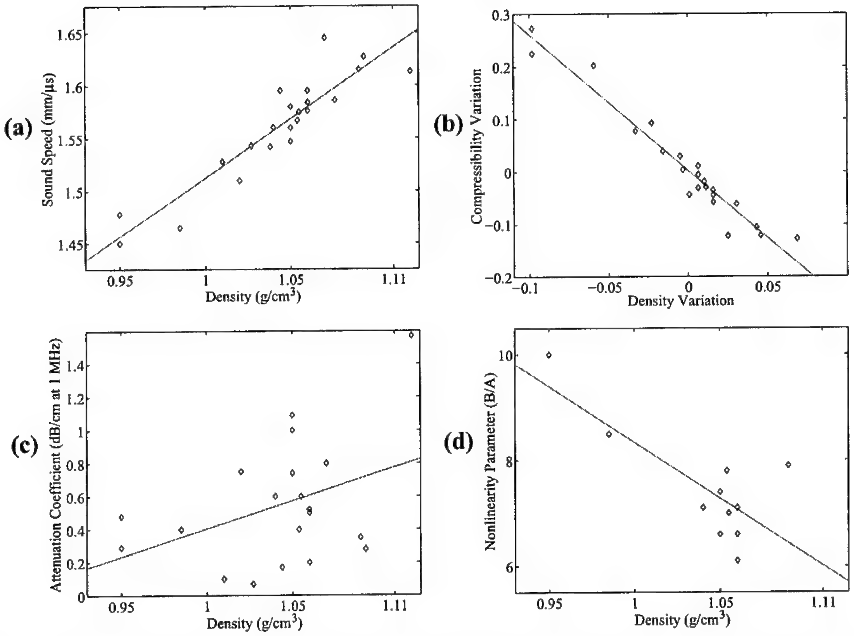

Figure 1: Pairs of acoustic properties for human soft tissues, plotted with corresponding lines of best fit.

convenient for scattering analyses. For example, the far-field pattern of fixed-frequency acoustic scattering from a fluid medium, under the Born approximation, is described by the equation [Morse and Ingard, 1968]

$$\Phi(\mathbf{I}-\mathbf{O}) = \frac{k^2}{4\pi}\int_V \left(\gamma_\kappa(\mathbf{r}_0) + \gamma_\rho(\mathbf{r}_0)\,\cos\vartheta\right) e^{i(\mathbf{I}-\mathbf{O})\cdot\mathbf{r}_0}\, dV_0, \tag{2}$$

where **I** and **O** are vectors with magnitudes equal to the wavenumber k and directions equal to the propagation direction of the incident wave and the measurement direction of the scattered wave, respectively, and ϑ is the angle between the vectors **I** and **O**. Many quantitative acoustic imaging methods have been devised to separately map γ_κ and γ_ρ or closely related quantities [*e.g.*, Devaney, 1985; Witten et al., 1988; Mensah and Lefebvre, 1997].

Empirical Relationships

In order to quantitatively analyze relationships between the four abovementioned parameters for human soft tissues, linear regression analysis was performed on all of the summary data listed in Table I. A regression between the nondimensional compressibility variation γ_κ and density variation γ_ρ was also performed. In each case, linear relationships of the form

$$y = (mx + b) \pm \sigma \tag{3}$$

were obtained, where m is the slope, b is the intercept, and the standard deviation σ is computed from the difference between the measured parameters and the line of least-squares fit. To assess the significance of each correlation, the Pearson correlation coefficient r (bounded between -1 and 1) and the corresponding p-values (*i.e.*, the probability of a correlation coefficient with magnitude equal to or greater than r occurring by chance [Bevington, 1969]) were also computed. A typical significance criterion is, for instance, $p < 0.05$.

Values from Table I are plotted in Fig 1 for four parameter pairs, together with the corresponding least-squares linear fit from Eq. (3). The correlation coefficients and p-values in Table I, as well as the corresponding plots in Fig. 1, provide clear indications of correlations

Table 2: Results of least-squares linear regressions between acoustic properties of human soft tissue.

Acoustic Properties	Slope m	Intercept b	Correlation Coefficient	St. Dev. σ	p-value
(c, ρ)	1.12	0.391	0.917	0.0203	2.03×10^{-9}
(α, ρ)	3.38	−2.98	0.393	0.341	0.0869
$(B/A, \rho)$	−21.18	29.52	−0.771	0.687	5.47×10^{-3}
(α, c)	1.50	−1.80	0.214	0.362	0.364
$(B/A, c)$	−16.58	33.28	−0.795	0.654	3.44×10^{-3}
$(\alpha, B/A)$	−0.0563	0.929	−0.271	0.216	0.421
$(\gamma_\kappa, \gamma_\rho)$	−2.58	0.00313	−0.972	0.0260	5.61×10^{-14}

between acoustic properties of human soft tissues. As seen in Fig. 1(a), sound speed and density are closely correlated for human soft tissues ($r = 0.9168$, $p = 2.03 \times 10^{-9}$). The corresponding nondimensional parameters γ_κ and γ_ρ are correlated even more closely ($r = 0.9715$, $p = 5.61 \times 10^{-14}$). The nonlinearity parameter B/A correlates significantly with the sound speed and density ($p = 3.44 \times 10^{-3}$ and 5.47×10^{-3}, respectively) but not with the attenuation coefficient ($p = 0.421$). The attenuation coefficient does not correlate highly with any of the other parameters considered, although its correlation with mass density might be considered marginally significant ($p = 0.0869$).

Discussion

An obvious question is the physical cause of the empirical linear relationships shown here to exist between acoustic parameters in human soft tissues. These relationships are not physically fundamental to propagation in fluid or solid media. The most likely causes of the nearly linear relationship between sound speed and density are the relative proportions of tissue constituents such as proteins, lipids, and water. Since the bulk acoustic properties of tissue are fairly well-characterized by mixture laws [Apfel, 1986; Sehgal et al., 1986; Hachiya and Ohtsuke, 1994], it seems reasonable to conclude that the present empirical linear relationships relate straightforwardly to tissue composition. Proteins such as collagen have a sound speed and density higher than water [Goss and Dunn, 1980], so that tissues with higher concentrations of collagen and other proteins have relatively higher density and sound speed [O'Brien, 1977; Goss et al., 1980a; Olerud et al., 1990]. Similarly, lipids have lower sound speeds and density than water, so that tissues with greater fat content have relatively lower sound speeds and densities.

For the limited data set available, the present study shows that the nonlinearity parameter B/A is significantly correlated with the sound speed and density of tissue. This relationship is consistent with previous results showing that the nonlinearity parameter can also be predicted using mixture laws [Apfel, 1986; Sehgal et al., 1986]. The weakly linear (marginally significant) relationship between attenuation coefficient and density found here is also consistent with a previous study, which showed that in canine skin and wound tissue the correlation between attenuation coefficient and collagen content was substantially smaller than the correlation between sound speed and collagen content [Olerud et al., 1990].

In modeling soft tissues, one may be concerned with point-to-point variations within tissues, as well as bulk properties of individual tissue types. The present study does not present direct evidence that the acoustic properties considered are linearly related except as bulk properties. However, any local variations in soft tissue properties are likely to be primarily caused by local variations in tissue composition, which should cause corresponding sound speed and density variations similar to those for bulk tissue. Likewise, acoustic parameters of other soft tissues, such as malignant tumors, may be expected to follow similar empirical relationships.

The results presented here should be useful for computational modeling of acoustic propagation in human soft tissues. For example, Borup et al. [1992] obtained model maps of tissue structure by processing two-dimensional x-ray computed tomography and magnetic resonance images of a human torsos, assigning values of a sound speed contrast function based on an assumed linear relationship to the image gray level. The empirical linear relationships between the parameters presented here in Table II could be employed to assign density variations, nonlinearity parameter variations, and absorption values consistent with those sound speed variations, thus resulting in a more realistic model.

In addition, sound speed can be difficult to measure accurately for certain small or fragile tissue structures, such as the thin septa that separate fat lobules within adipose tissue. However, density of any tissue structure can easily be determined *in vitro* using Archimedes' principle. The empirical relationships given here, like those presented by Lees et al. [1983] for calcified tissues, allow estimates of sound speed to be obtained from measurements of density.

Finally, the present results have implications for development of quantitative ultrasonic imaging methods. First, inversions yielding acoustic parameters such as the sound speed variation $c^2/c_0^2 - 1$ (which is nearly equal to $\gamma_\kappa + \gamma_\rho$) [*e.g.*, Borup et al., 1992; Mast, 1999] or the reflectivity function $\gamma_\kappa - \gamma_\rho$ [*e.g.*, Norton and Linzer, 1980; Mensah and Lefebvre, 1997] can be employed to obtain maps of more intuitive quantities such as the density and compressibility. Second, the results suggest that for human soft tissues little additional information may be gained by techniques that independently image density variations and compressibility variations. The high correlation coefficient found here between γ_κ and γ_ρ implies that separate images of compressibility and density variations in soft tissue should be expected to be highly correlated. Similarly, separate images of sound speed and density may provide little additional information compared to either individual image. This conclusion is consistent with experimental results in which sound speed and density images of excised breast cross sections have been found to be qualitatively similar and significantly correlated [Yang et al., 1991].

Additional information for quantitative images could come in several forms. One possibility is quantitative imaging of the nonlinear parameter *B*/*A* [*e.g.*, Cain, 1986; Burov et al., 1994]; however, the significant correlations found here between nonlinearity parameter, sound speed, and mass density suggest that images of the nonlinearity parameter may provide limited additional information relative to that obtained from sound speed or density mapping. Still, since the nonlinearity parameter was only available for eleven of the data points considered here, further study would be required to definitively assess correlations between *B*/*A* and other acoustic parameters of soft tissues.

The low correlation results between absorption and the other three parameters considered imply that multiple-parameter images including absorption maps [*e.g.*, Greenleaf and Bahn, 1981; Witten et al., 1988] may provide significant additional information beyond that obtained from maps of other parameters alone. However, because of the wide range of absorption values reported in the literature for most tissue types [Duck, 1990], the ultimate diagnostic value of quantitative absorption imaging cannot be assessed based on the data considered here. Still, the present results suggest that quantitative imaging techniques yielding maps of ultrasonic absorption as well as sound speed, density, or nonlinearity parameter are worthy of further study for medical diagnosis.

Acknowledgment

This research was funded by the Breast Cancer Research Program of the U.S. Army Medical Research and Materiel Command, under Grant No. DAMD17-98-1-8141.

References

Apfel, R. (1986). "Prediction of tissue composition from ultrasonic measurements and mixture rules," J. Acoust. Soc. Am. **79**, 148–152.

Aroyan, J. L. (1996). *Three-Dimensional Numerical Simulation of Biosonar Signal Emission and Reception in the Common Dolphin*, Ph.D. Thesis, University of California Santa Cruz.

Bevington, P. R., *Data Reduction and Error Analysis for the Physical Sciences* (McGraw-Hill, New York, 1969), pp. 310–311.

Borup, D. T., Johnson, S. A., Kim, W. W., and Berggren, M. J. (1992). "Nonperturbative diffraction tomography via Gauss-Newton iteration applied to the scattering integral equation," Ultrason. Imag. **14**, 69–85.

Burov, V. A., Gurinovich, I. E., Rudenko, O. V., and Tagunov, E. Y. (1994). "Reconstruction of the spatial distribution of the nonlinearity parameter and sound velocity in acoustic nonlinear tomography," Acoust. Phys. **40**, 922–929.

Cain, C. (1986). "Ultrasonic reflection mode imaging of the nonlinear parameter B/A: I. A theoretical basis," J. Acoust. Soc. Am. **80**, 28–32.

Devaney, A. J. (1985). "Variable density acoustics tomography," J. Acoust. Soc. Am. **78**, 120–130.

Duck, F. A. (1990). *Physical Properties of Tissue: a Comprehensive Reference Book* (Academic, London).

Goss, S. A., Johnston, R. L., and Dunn, F. (1978). "Comprehensive compilation of empirical ultrasonic properties of mammalian tissues," J. Acoust. Soc. Am. **64**, 423–457.

Goss, S. A., Frizzell, L. A., and Dunn, F. (1980a). "Dependence of the ultrasonic properties of biological tissue on constituent proteins," J. Acoust. Soc. Am. **67**, 1041–1044.

Goss, S. A., Johnston, R. L., and Dunn, F. (1980b). "Compilation of empirical ultrasonic properties of mammalian tissues II," J. Acoust. Soc. Am. **68**, 93–108.

Goss, S. A. and Dunn, F. (1980). "Ultrasonic propagation properties of collagen," Phys. Med. Biol. **25**, 827–837.

Greenleaf, J. F. and Bahn, R. C. (1981). "Clinical imaging with transmissive ultrasonic computerized tomography," IEEE Trans. Biomed. Eng. **28**, 177–185.

Hachiya, H. and Ohtsuki, S. (1994). "Relationship between speed of sound and density of normal and diseased rat livers," Jap. J. Appl. Phys. **33**, 3130–3133.

International Commission on Radiation Units and Measurements (1998). *ICRU Report 61: Tissue Substitutes, Phantoms and Computational Modelling in Medical Ultrasound* (ICRU Publications, Bethesda, Maryland).

Lees, S., Ahern, J. M., and Leonard, M. (1983). "Parameters influencing the sonic velocity in compact calcified tissues of various species," J. Acoust. Soc. Am. **74**, 28–33.

Mast, T. D., Hinkelman, L. M., Orr, M. J., Sparrow, V. W., and Waag, R. C. (1997). "Simulation of ultrasonic pulse propagation through the abdominal wall," J. Acoust. Soc. Am. **102**, 1177–1190. [Erratum: J. Acoust. Soc. Am. **102**, 1124–1125 (1998).]

Mast, T. D. (1999). "Wideband quantitative ultrasonic imaging by time-domain diffraction tomography," J. Acoust. Soc. Am. **106**, 3061–3071.

Mast, T. D., Hinkelman, L. M., Metlay, L. A., Orr, M. J., and Waag, R. C. (1999). "Simulation of ultrasonic pulse propagation, distortion, and attenuation in the human chest wall," J. Acoust. Soc. Am. **106**, 3665–3677.

Mensah, S. and Lefebvre, J. P. (1997). "Enhanced compressibility tomography," IEEE Trans. Ultrason. Ferroelect. Freq. Control **44**, 1245–1252.

Norton, S. J. and Linzer, M. (1980). "Ultrasonic reflectivity imaging in three dimensions: exact inverse scattering solutions for plane, cylindrical, and circular apertures," IEEE Trans. Biomed. Eng. **28**, 202–220.

O'Brien, W. D. (1977). "The role of collagen in determining ultrasonic propagation properties in tissue," in *Acoustical Holography*, Vol. 7, edited by L. W. Kessler (Plenum, New York), pp. 37–50.

Olerud, J. E., O'Brien, W. D., Riederer-Henderson, M. A., Steiger, D. L., Debel, J. R., and Odland, G. F. (1990). "Correlation of tissue constituents with the acoustic properties of skin and wound," Ultras. Med. Biol. **16**, 55–64.

Sehgal, C. M., Brown, B. M., Bhan, R. C., and Greenleaf, J. F. (1986). "Measurement and use of acoustic nonlinearity and sound speed to estimate composition of excised livers," Ultras. Med. Biol. **12**, 865–874.

Witten, A., Tuggle, J., and Waag, R. C. (1988). "A practical approach to ultrasonic imaging using diffraction tomography," J. Acoust. Soc. Am. **83**, 1645–1652.

Woodard, H. Q. and White, D. R. (1986). "The composition of body tissues," Br. J. Radiol. **59**, 1209–1219.

Yang, J. N., Murphy, A. D., Madsen, E. L., Zagzebski, J. A., Gilchrist, K. W., Frank, G. R., Macdonald, M. C., Millard, C. A., Faraggi, A., Jaramillo, C. A., and Gosset, F. R. (1991). "A method for in vitro mapping of ultrasonic speed and density in breast tissue," Ultras. Imag. **13**, 91–109.

(c)2000 Acoustical Society of America

Two- and three-dimensional simulations of ultrasonic propagation through human breast tissue

T. Douglas Mast
Applied Research Laboratory, The Pennsylvania State University,
University Park, Pennsylvania 16802
mast@sabine.acs.psu.edu

Abstract: Simulations of spherical-wave ultrasonic pulse propagation through human breast tissue are presented. Breast tissue models were created by processing of volumetric photographic data from the Visible Woman project. Tissue types were empirically mapped to hue, saturation, and value parameters of the photographic data; acoustic parameters of tissue were then mapped using empirical linear relationships between mass density, sound speed, and ultrasonic absorption. Computations of ultrasonic propagation were performed in two and three dimensions using a *k*-space method incorporating tissue-dependent absorption and reduced-reflection boundary conditions. The results show wavefront distortion effects similar to measurements on breast tissue. Wavefront distortion is significantly more severe for the three-dimensional simulations than for the two-dimensional simulations.

© 2000 Acoustical Society of America

PACS numbers: 43.80.Gx, 43.80.Qf, 43.20.Fn

Introduction

Direct simulation of ultrasound-tissue interaction is becoming a widespread tool for studies of ultrasonic imaging and therapy.[1–3] Continuous increases in computational power have made possible simulations of large-scale models incorporating realistic tissue structure and direct numerical solutions to the model equations. Ultrasonic propagation problems of interest typically employ transient pulses and domains that span tens to hundreds of wavelengths, so that large computational grids and fine temporal resolution are required. For these reasons, most previous investigations of ultrasonic propagation through tissue have employed two-dimensional tissue models, which present small computation and storage requirements compared to three-dimensional problems.[4]

This paper presents two- and three-dimensional simulations of propagation through breast tissue continuum models. The three-dimensional simulations are feasible in part because of an efficient implementation of the *k*-space method for computation of ultrasonic fields.[4] Realistic tissue models are obtained by an automated segmentation scheme applied to three-dimensional photographic data of the human female breast. Animations of three-dimensional propagation show the cumulative development of distortion effects. Wavefront distortion statistics for the three-dimensional simulations are computed and shown to be similar to experimental measurements. Analogous two-dimensional computations, performed using the same breast tissue models, produce significantly lower distortion.

Breast Tissue Model

To obtain realistic three-dimensional (3D) models of human breast tissue, volumetric image data was employed. The data set chosen was from the Visible Woman project, which includes 3D x-ray computed tomography (CT), magnetic resonance imaging (MRI), and photographic data for an entire female cadaver. This data set is publically available and has been extensively studied.[5] Although computed tomography data provides a firm basis for models of acoustic properties,[6] and similar modeling may be possible using MRI data, the CT and MRI data from the Visible Woman data set are of insufficient (about 1 mm) resolution for simulations of ultrasonic propagation. The volumetric photographic data, which was obtained by photographing the cadaver layer-by-layer, has a uniform voxel size of $(1/3\ \text{mm})^3$, which was judged adequate for the present simulations.

To map the photographic data to tissue properties, an empirical continuum model was developed. The basis for this model was manual sampling of hue, saturation, and value (HSV) parameters of the photographic data for regions containing fatty, connective, and parenchymal (glandular) tissue. Empirically estimated HSV values for each tissue type were incorporated into continuous mapping rules that provided smooth transitions between different tissue regions.

The rules employed are summarized as follows, in the order applied. First, to account for slice-to-slice variations in lighting and cut quality, the HSV maps of each slice were normalized so that their mean values matched the mean HSV values for the surrounding 17-slice (5.67 mm) region. The segmentation rules were then applied as follows, where H, S, and V are hue, saturation and value maps bounded by 0 and 1 and W, P, and C are local fractions of water, parenchymal tissue, and connective tissue. (Unmarked tissue is identified as fat.)

1. Mark exterior by hue and value: $W = 1 - [u(0.4 - H) + u(H - 0.8)] + u(0.1 - V)$.
2. Mark parenchyma based on value threshold: $P = (1 - W)\, u(0.67 - V)$.
3. Mark connective tissue based on saturation threshold: $C = (1 - W)\, u(S - 0.45) - P$. (Set to zero where $C < 0$.)
4. Compute sound-speed map: $c = c_F + (c_0 - c_F)W + (c_P - c_F)P + (c_C - c_F)C$.

In the above algorithm, u is a smoothed step function defined as

$$u(x) = \begin{cases} 0.5 - 0.5\cos[\pi(x+\epsilon)/(2\epsilon)], & -\epsilon < x < \epsilon \\ 0, & x < -\epsilon \\ 1, & x > \epsilon, \end{cases} \tag{1}$$

where the parameter ϵ employed here was 0.1. The sound speed values employed were, in mm/μs, $c_F = 1.478$ (fat), $c_0 = 1.524$ (water), $c_P = 1.547$ (parenchymal/glandular), and $c_C = 1.613$ (connective). Values of mass density and absorption were determined using empirical linear relations[6,7] based on fits to nominal tissue parameter values:[1]

$$\rho = 1.43\, c - 1.18, \quad \alpha = 0.71\, c - 1.01, \tag{2}$$

where the mass density ρ is in g/cm^3 and the absorption α corresponds to that defined in Ref. 8. The corresponding absorption in dB/mm is approximately $\alpha/(2c)\ 20\log_{10}(e)$.

Although the resulting volumetric maps are likely not to be as accurate as maps determined from CT data[6] or as manually segmented maps,[1,8] the tissue maps obtained using the rules described above were judged sufficiently realistic for the present simulations. As shown below, the maps produce distortion comparable to measurements on breast tissue specimens.

Computational Methods

Spherical-wave pulse propagation through the breast tissue models were computed using the k-space method.[4] This method directly solves the second-order linear acoustic wave equation for media with variable sound speed and density, and allows high accuracy to be obtained using relatively large temporal and spatial steps compared to other numerical methods.[4,9] Tissue-dependent absorption was incorporated using the Maxwell solid model described in Ref. 8, which results in frequency-independent absorption. Limited-reflecting boundary layers were incorporated using tapered absorption functions at each boundary:

$$\alpha(x/L) = \alpha_{\max}\,[0.375 - 0.5\cos(\pi x/L) + 0.125\cos(2\pi x/L)], \tag{3}$$

where x is the perpendicular distance within the absorbing layer of length L, taken here to be 20 pixels (2.22 mm), and $\alpha_{\max}$ is the maximum absorption coefficient within the layer, taken to be 16. Since the severity of absorption discontinuties is known to be directly related to the magnitude of spurious reflections,[10] the taper function of Eq. (3) was chosen so that both the first, second, and third spatial derivatives of the absorption are zero at the inner edge of each absorbing layer. Otherwise, the *k*-space method employed was as described in Ref. 4.

Fourteen cubic volumes of breast tissue were modeled from the Visible Woman data using the segmentation method described above. Each segmented volume was 60^3 voxels, or $(20\ \mathrm{mm})^3$. Fourier interpolation, performed simultaneously with a Gaussian low-pass filtering operation, was used to oversample the segmented volumes by a factor of three in each direction, so that the inhomogeneous region of the grid spanned 180^3 voxels. Computations were then performed on a 240 × 240 × 240 grid (240 × 240 for the 2D case) with a uniform voxel size of 0.111 mm. A spherical-wave source was simulated by adding the source distribution

$$q(\mathbf{r}, t) = e^{-|\mathbf{r}-\mathbf{r}_0|^2/(2\sigma_r^2)}\, e^{-(t-t_0)^2/(2\sigma_t^2)} \sin(2\pi f_0 t) \tag{4}$$

to the wavefield at each time step, where the source position $\mathbf{r}_0$ was centered at a position 0.7 mm below the lower boundary of the inhomogeneous region, the spatial Gaussian parameter σ_r was 0.1 mm, the temporal Gaussian parameter σ_t was 0.5 μs, and the center frequency f_0 was 2.5 MHz. A time step of 0.0364 μs, corresponding to a Courant-Friedrichs-Lewy number of 0.5, was employed in all cases. On an 650 MHz Athlon workstation with 768 MB of random-access memory, each three-dimensional computation took about 3.2 h.

Simulated wavefields were received by an 18 × 18 element aperture, with square elements at a pitch of 0.72 mm, centered 0.8 mm above the upper boundary of the inhomogeneous region. Waveforms for each simulated element were computed by integration of the received pressure with a step size of 0.18 mm. The pressure at each point was determined using a sinc-Kaiser interpolation method.[4]

The received waveforms were analyzed for wavefront distortion effects using previously established methods.[11] Before processing, wavefields were compensated for geometric delay and amplitude variations. Arrival time fluctuations were computed by cross-correlation of each waveform with a reference waveform obtained by summing all waveforms in the aperture after geometric compensation. The peak of each cross-correlation function was found from the zero crossing of the derivative of the cross-correlation envelope, computed using second-order accurate finite differences.

Waveforms were compensated for the computed arrival time fluctuations, centered in a window of length 5.8 μs, and Hanning windowed. Energy level fluctuations were then computed from the squared sum of each waveform in dB units. To account for any effects due to element directivity, distortion maps from an analogous computation in a homogeneous medium were subtracted from the computed maps. A waveform similarity factor[11] was also computed: this factor is a generalized cross-correlation coefficient that is equal to 1 when all waveforms in the aperture are identical.

To allow comparison of distortion effects for 2D and 3D propagation, 2D computations were carried out 18 times for each cubic inhomogeneity, corresponding to the 18 elevation positions of the receiving array from the 3D computations. All other processing was identical for the 2D cases, except that geometric corrections were based on the 2D geometry and that average arrival time and energy level fluctuations for each elevation were removed before statistical evaluation.

Results

Example breast tissue maps and propagation animations are shown in Fig. 1 for two representative model volumes. Each of the propagation animations shows the cumulative development of arrival time, energy level, and waveform distortion as wavefronts interact with inhomogeneities in the breast tissue. Volume 8 contains a mixture of fat, connective tissue, and parenchyma, and the propagation animations show large-scale arrival-time distortion as well as some waveform and energy-level distortion. Volume 10, which contains mainly fat and denser

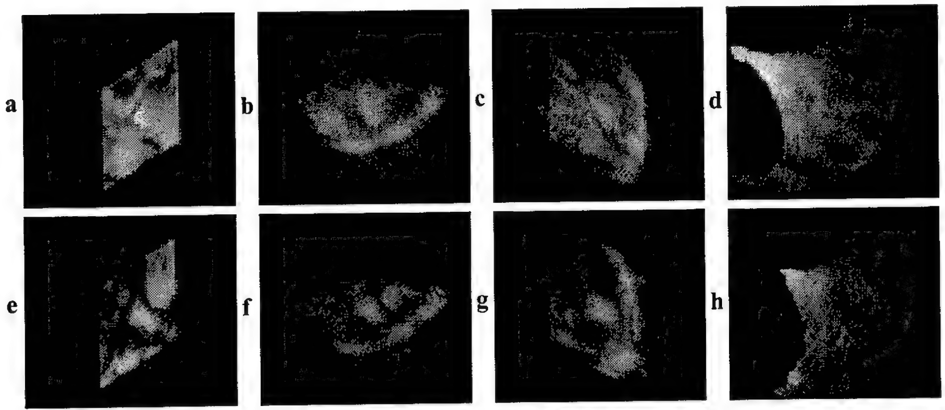

Figure 1: Visualizations of 3D breast models and propagation. Each panel contains a translucent image of the sound speed map for the entire model volume, with cyan representing fat, medium blue representing parenchymal tissue, and dark blue representing connective tissue. Mm. 1 (a) fly-through rendering of breast model volume 8 (587 kb) [fly8.mpg]. Mm. 2 (b) Horizontal slices of the 3D pressure field, shown on a bipolar logarithmic scale with a 65 dB dynamic range, and sound speed map for vol. 8 (226 kb) [hor8.mpg]. Mm. 3 (c) Vertical slices of pressure and sound speed for vol. 8 (244 kb) [ver8.mpg]. Mm. 4 (d) Isosurface renderings of the pressure field for vol. 8 (587 kb) [ver8.mpg]. Mm. 5 (e) fly-through, vol. 10 (582 kb) [fly10.mpg]. Mm. 6 (f) Horizontal slices, vol. 10 (227 kb) [hor10.mpg]. Mm. 7 (g) Vertical slices, vol. 10 (235 kb) [ver10.mpg]. Mm. 8 (h) Isosurface renderings, vol. 10 (231 kb) [iso10.mpg]. (http://www.placeholder.net/msxxx/)

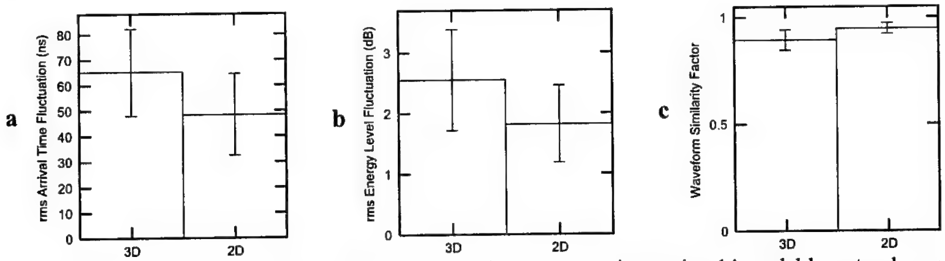

Figure 2: Summarized distortion statistics for 3D and 2D computations using 14 model breast volumes. The box heights represent the means of each statistic while the error bars span ±1 standard deviation. (a) rms arrival time fluctuations. (b) rms energy level fluctuations. (c) Waveform similarity factors.

connective tissue, produces more severe waveform and energy-level distortion due to interference between the main wavefront and waves scattered by connective tissue structures.

Computed 2D and 3D wavefront distortion statistics for the 14 model volumes are shown in Table I and summarized in Fig 2. These statistics indicate that, for a given medium model, 3D propagation produces significantly more wavefront distortion than 2D propagation. In almost all cases, each of the three statistics employed indicates greater distortion for the 3D computation. Also, for all three statistics investigated, the overall mean for 2D computation is about one standard deviation different from that for the 3D computation, in the direction indicating higher distortion. For an estimate of the significance of this result, one may note that, for a normally distributed variable with standard deviation σ and $N = 14$, a mean value $\mu \geq \sigma$ occurs with a probability of less than 10^{-4}.

The distortion seen for the 3D simulations qualitatively agrees with previous measurements of wavefront distortion caused by breast tissue *in vitro*. In Ref. 12, mean distortion statistics found for 9 breast specimens included a mean rms arrival time fluctuation of 66.8 ns, a mean rms energy level fluctuation of 5.03 dB, and a mean waveform similarity factor of 0.910. The statistics are not expected to be precisely comparable, however, since the experiments of Ref. 12

Table I: Wavefront distortion statistics for 3D and 2D simulations using 14 breast model volumes. Shown are the mean rms arrival time fluctuations (ATF), rms energy level fluctuations (ELF), and waveform similarity factors (WSF) for each volume, as well as overall means μ and standard deviations σ for each statistic. Volumes containing significant fractions of parenchymal tissue are denoted by asterisks.

Vol.	3D rms ATF (ns)	3D rms ELF (dB)	3D WSF	2D rms ATF (ns)	2D rms ELF (dB)	2D WSF
1	74.2	2.74	0.840	50.8	2.07	0.930
2*	56.8	1.85	0.946	45.7	1.48	0.962
3	64.0	2.55	0.920	35.6	1.44	0.969
4*	40.0	1.64	0.931	28.4	1.09	0.977
5	74.2	2.74	0.840	43.9	2.39	0.911
6*	46.8	1.95	0.943	31.1	1.29	0.971
7*	42.8	1.94	0.943	35.5	1.22	0.971
8*	85.2	3.59	0.881	42.4	1.82	0.945
9*	73.3	1.90	0.938	70.3	1.43	0.961
10	96.7	4.44	0.789	81.7	3.52	0.888
11*	65.0	2.38	0.920	42.6	1.46	0.966
12	58.5	2.31	0.872	42.9	2.10	0.939
13	84.6	3.75	0.876	58.7	2.09	0.950
14	50.2	2.01	0.893	69.6	2.13	0.938
$\mu \pm \sigma$	65.2 ± 17.1	2.56 ± 0.83	0.895 ± 0.048	48.5 ± 15.9	1.82 ± 0.64	0.949 ± 0.026

employed a higher-frequency, wider-band pulse (center frequency 3.75 MHz, −6 dB bandwidth 2.2 MHz) than the simulations reported here.

Discussion

The computations reported here show the feasibility of large-scale three-dimensional simulations of ultrasonic propagation through tissue. These simulations relied on an implementation of the k-space method that solves the second-order wave equation for the acoustic pressure. Formulations which solve coupled first-order propagation equations, including a recent adaptation of the k-space method,[13] require storage of more independent variables, but allow incorporation of desirable features including relaxation-process absorption and perfectly-matched-layer absorbing boundary conditions. Such methods may, given sufficient computing power, be preferable for three-dimensional simulations.

The continuum tissue model introduced here was based on three-dimensional photographic data. Although the 3D computations employing this model produce realistic propagation effects, comparable to measured wavefront distortion, the subjectivity required to establish the tissue-mapping rules is a disadvantage. Alternative imaging methods such as 3D x-ray computed tomography produce volumetric data quantitatively related to tissue properties. [6] Model development using 3D CT has proven useful in lower-frequency simulations of propagation through tissue,[6] and given sufficiently high spatial resolution would be ideal for models of ultrasonic propagation.

Substantially higher distortion was observed here for the three-dimensional computation than for the two-dimensional computations. This result suggests that three-dimensional propagation and scattering effects, such as spherical spreading of secondarily scattered wavefronts, are important aspects of ultrasonic wavefront distortion in tissue. Thus, simulations of ultrasonic imaging and therapy that employ two-dimensional tissue models are likely to underestimate the degrading effects of tissue on focus and image quality. As 3D computations become more feasible, direct simulations of ultrasonic wavefields should become correspondingly more realistic and more useful as a basic tool for medical ultrasound research.

Acknowledgments

This research was funded by the Breast Cancer Research Program of the U.S. Army Medical Research and Materiel Command, under Grant No. DAMD17-98-1-8141. Any opinions, findings, conclusions, or recommendations expressed in this publication are those of the author and do not necessarily reflect the views of the U.S. Army. Discussions with Laura Hinkelman, Leon Metlay, and Makoto Tabei are acknowledged with pleasure.

References

[1] T. D. Mast, L. M. Hinkelman, M. J. Orr, V. W. Sparrow, and R. C. Waag, "Simulation of ultrasonic pulse propagation through the abdominal wall," J. Acoust. Soc. Am. **102**, 1177–1190 (1997). [Erratum: J. Acoust. Soc. Am. **104**, 1124–1125 (1998).]

[2] G. Wojcik, B. Fornberg, R. Waag, L. Carcione, J. Mould, L. Nikodym, and T. Driscoll, "Pseudospectral methods for large-scale bioacoustic models," Proc. IEEE Ultrason. Symp. 1997, **2**, 1501–1506 (1997).

[3] I. M. Hallaj and R. O. Cleveland, "FDTD simulation of finite-amplitude pressure and temperature fields for biomedical ultrasound," J. Acoust. Soc. Am. **105**, L7–L12 (1998).

[4] T. D. Mast, L. P. Souriau, D.-L. Liu, M. Tabei, A. I. Nachman, and R. C. Waag, "A *k*-space method for large-scale models of wave propagation in tissue," IEEE Trans. Ultrason., Ferroelect., Freq. Contr. **48**, 341–354 (2001).

[5] M. J. Ackerman, "The Visible Human Project: a resource for anatomical visualization," Medinfo **9**, 1030–1032 (1998).

[6] J. L. Aroyan, "Three-dimensional modeling of hearing in the common dolphin," J. Acoust. Soc. Am., accepted (2001).

[7] T. D. Mast, "Empirical relationships between acoustic parameters in human soft tissues," Acoustics Research Letters Online **1**, 37–42 (2000).

[8] T. D. Mast, L. M. Hinkelman, L. A. Metlay, M. J. Orr, and R. C. Waag, "Simulation of ultrasonic pulse propagation, distortion, and attenuation in the human chest wall," J. Acoust. Soc. Am. **106**, 3665–3677 (1999).

[9] J. C. Mould, G. L. Wojcik, L. M. Carcione, M. Tabei, T. D. Mast, and R. C. Waag, "Validation of FFT-based algorithms for large-scale modeling of wave propagation in tissue," Proc. IEEE Ultrason. Symp. 1999, 1551–1556 (1999).

[10] R. Kosloff and D. Kosloff, "Absorbing boundaries for wave propagation problems," J. Comp. Phys. **63**, 363–376 (1986).

[11] D.-L. Liu and R. C. Waag, "Correction of ultrasonic wavefront distortion using backpropagation and a reference waveform method for time-shift compensation," J. Acoust. Soc. Am. **96**, 649–660 (1994).

[12] L. M. Hinkelman, D.-L. Liu, R. C. Waag, Q. Zhu, and B. D. Steinberg, "Measurement and correction of ultrasonic pulse distortion produced by the human breast," J. Acoust. Soc. Am. **97**, 1958–1969 (1995).

[13] M. Tabei, T. D. Mast, and R. C. Waag, "A *k*-space method for coupled first-order acoustic propagation equations," J. Acoust. Soc. Am, submitted.

Deconvolution of Scattered Acoustic Fields for Ultrasonic Imaging

James F. Kelly
Mathematics Honors Program
Applied Research Laboratory
The Pennsylvania State University

July 2, 2001

1 Introduction

1.1 Background

Ultrasound imaging of human tissue has found widespread clinical application. However, the diagnostic usefulness of such images is limited by poor spatial resolution, low contrast between different tissue structures, sensor noise, and image artifacts (such as blur and speckle introduced by emitted pulse). Physical limitations of the transducer employed (such as the effective bandwidth of the pulse) coupled with the dispersive and attenuating properties of human tissue lead to less than ideal data. Also, noise inherent in the system and incomplete data sets (due to the geometry of receive arrays) can further limit the usefulness of imaging systems. Therefore, image processing algorithms have recently been developed to restore the degraded ultrasound data prior to the application of the inversion algorithm used to image the tissue.

Imaging of human tissue can be performed by applying inverse scattering theory to the measured scattered pressure field [1]. A rough approximation of the "soft-obstacle" problem (*e.g.*, tumorous tissue buried in fatty tissue) models the received far-field data as a convolution of the interrogating pulse and the impulse response of the medium. The ideal imaging data would be produced by interrogating the medium with a Dirac-delta function; the quality of the measured data decreases as the effective bandwidth of the interrogating pulse decreases. The physical limitations of transducers limits the pass-band of the interrogating pulse and hence the effective bandwidth of the measured scattered field. Therefore, various deconvolution methods have been employed to extend the bandwidth beyond the passband of pulse emitted by the transducer. In particular, the use of deconvolution algorithms in the quantitative imaging of human tissue could lead to increased resolution in medical ultrasound imaging systems. By first applying one of many deconvolution methods to the measured scattering data, the effective spatial resolution of the reconstruction method (for instance, filtered backpropagation [2] or multiple-frequency time-domain methods [3] [4]) can be increased. Of particular interest is increasing the quality of reconstruction in the case of limited-angle data [5] [6] in synthetic aperture imaging.

Deconvolution methods have found wide application is such fields as speech analysis, seismic and geophysical applications, sonar, as well as biomedical imaging. In all these applications, the following signal model is employed: given some measured data $h[n]$ and possibly some "incident" signal $f[n]$ determine a signal $g[n]$ such that

$$h[n] = f[n] * g[n] + p[n] \tag{1}$$

where * denotes the operation of convolution and $p[n]$ denotes some additive noise signal. The case where $f[n]$ is unknown is termed *blind deconvolution* and is generally far more difficult than the case where $f[n]$ is known. Due to the attenuating and dispersive properties of human tissue, the interrogating pulse $f[n]$ is not equal to the pulse emitted by the transducer; therefore, pulse estimation [7][8] is often necessary for successful deconvolution of real data.

1.2 Ill-Posedness

As will be seen, the deconvolution problem is often *ill-posed* [9], meaning one of the following criteria fails:

1. The solution g[n] exists.
2. The solution g[n] is unique.
3. The solution g[n] is stable (*i.e.* $g[n]$ depends continuously upon the data $h[n]$).

In most cases, it is the instability of the deconvolution that prevents the application of a "simple-minded" deconvolution. To illustrate, let $f[n]$,$g[n] \in l^2$ (square-integrable sequences). We can apply the well-known convolution theorem [10] and Fourier transform (1) into the frequency domain, taking $p[n] \equiv 0$. Denoting $f[n] \leftrightarrow \hat{f}(\omega)$, $g[n] \leftrightarrow \hat{g}(\omega)$, and $h[n] \leftrightarrow \hat{h}(\omega)$ yields:

$$\hat{h}(\omega) = \hat{f}(\omega)\hat{g}(\omega) \tag{2}$$

Solving for $\hat{g}(\omega)$ and inverse transforming gives:

$$g[n] = \mathbf{F}^{-1}\left(\frac{\hat{h}(\omega)}{\hat{f}(\omega)}\right) \tag{3}$$

where $\mathbf{F}^{-1}$ denotes inverse Fourier transform.

The problem with (3) is that for most signals under consideration, the ratio $\frac{\hat{h}(\omega)}{\hat{f}(\omega)} \not\to 0$ as $|\omega| \to \infty$, yielding undesired singularities in the recovered $g[n]$. Our solution is hence unstable and the problem ill-posed. The addition of the noise term $p[n]$ complicates the problem further. To circumvent this problem, a number of deconvolution algorithms have been devised, which will be the focus of this paper. The following methods, as applied to ultrasound data, will be surveyed: regularized inverse filtering, homomorphic processing, and alternating projections onto convex sets (POCS). Each of these methods provides unique enhancements to the scattering data, along with its own problems (both theoretical and numerical). However, these methods do not exhaust known deconvolution methods; other methods such as wavelet analysis, maximum-likelihood deconvolution, and various adaptive blind deconvolution methods exist and have been successfully applied in a multitude of fields [11] [12] [13].

2 Regularized Inverse Filtering

2.1 Pulse Estimation Algorithm

Although the incident waveform $f(t)$ is known *a priori*, in general a more realistic estimate for the pulse is necessary that takes into account the attenuation and dispersion of the medium [14]. Since all data sets employed here had far-field measurements in multiple directions, the pulse could be estimated by averaging the magnitude spectrum over all received directions. That is, the pulse $f(t)$ was estimated in the frequency domain via $\hat{f}(\omega)$ by

$$\hat{f}(\omega) \approx \sqrt{\frac{1}{2\pi}\int_{-\pi}^{\pi} |\hat{p}_s(\theta,\omega)|^2 d\theta} \tag{4}$$

In the case of limited-aperture data, the integral is evaluated over the aperture interval. Note that our pulse estimate does not require any phase information, and therefore our estimate is unique only up to a phase factor. We therefore make the reasonable assumption that the pulse is minimum-phase, which holds for the class of pulses considered.

Equation (4) can be justified by the following reasoning: denote the pulse, as it propagates through the medium, by $u(t) \leftrightarrow \hat{u}(\omega)$, and let the (ideal) measured impulse response be denoted by $g(\theta,t) \leftrightarrow \hat{g}(\theta,\omega)$. Taking into account an additive Gaussian noise term $n(t) \leftrightarrow \hat{n}(\omega)$, the frequency response of the measured pressure can be expressed as:

$$\hat{p}_s(\theta,\omega) = \hat{u}(\omega)\hat{g}(\theta,\omega) + \hat{n}(\omega) \tag{5}$$

Inserting equation (5) into (4) with the assumptions that $n(t)$ is small with respect to $u(t)$, with a real spectrum yields:

$$\hat{f}(\omega) \approx \sqrt{\frac{1}{2\pi}\int_{-\pi}^{\pi} \left(|\hat{u}(\omega)\hat{g}(\theta,\omega)|^2 + 2\hat{n}(\omega)Re(\hat{u}(\omega)\hat{g}(\theta,\omega))\right) d\theta} \tag{6}$$

The frequency response $\hat{g}(\theta,\omega)$ fluctuates randomly in frequency; however, when averaged over many angular measurements, we can make the approximation $\frac{1}{2\pi}\int_{-\pi}^{\pi} |\hat{g}(\theta,\omega)| d\theta \approx 1$ (up to some multiplicative constant). That is, the averaged frequency response has an all-pass spectrum within the bandwidth considered. Although this approximation is crude and does not account for low-frequency attenuation, for sufficiently random medium with weak scattering characteristics, it should suffice. With these simplifications, we have

$$|\hat{f}(\omega)|^2 \approx |\hat{u}(\omega)|^2 + 2|\hat{n}(\omega)||\hat{u}(\omega)| \tag{7}$$

A simple binomial approximation yields

$$|\hat{f}(\omega)| \approx |\hat{u}(\omega)| \left(1 + \frac{|\hat{n}(\omega)|}{|\hat{u}(\omega)}\right) \tag{8}$$

so that, for a small noise spectrum, the averaged pulse $f(t)$ has approximately the same magnitude spectrum as the true pulse $u(t)$. Also, we can take into account certain *a priori* information about the pulse such as effective bandwidth, central frequency, and arrival times. Combined, equation (4) provides a good pulse estimation for the construction of a stable inverse filter. Moreover, it can be shown that the inverse filter constructed with the pulse estimate in (4) is equivalent to the regularized inverse filter of the true pulse $u(t)$.

2.2 The Inverse Filter

From the pulse estimate in equation (4), we can construct an inverse filter via

$$I(\omega) = \frac{1}{\hat{f}(\omega)} \tag{9}$$

If we assume the noise spectrum to be white, the approximation of the pulse in equation (8) shows that the inverse filter $I(\omega)$ is equivalent to a regularized inverse filter constructed from the true pulse $u(t)$. Thus, the filter in equation (9) can be used to execute a stable deconvolution on the data $p_s(\theta, t)$. A sample inverse filter created from a pulse estimate is shown in figure 2.

2.3 Construction of the Wiener Filter

The pulse estimate achieved by equation (4) can now be used to filter each recorded signal in the frequency domain; however, artifacts will build up outside the effective bandwidth of the pulse where noise predominates. To alleviate the problem, we can construct a Wiener filter that takes into account the corruption of noise. Denoting the noise-to-signal ratio by q, the Wiener filter $W(\omega)$ is given by:

$$W(\omega) = \frac{\hat{f}^*(\omega)}{|\hat{f}(\omega)|^2 + q^2} \tag{10}$$

From equation (8), we see that the noise-to-signal ratio $q \approx \frac{|\hat{n}(\omega)|}{|\hat{u}(\omega)|}$ is included in our pulse estimate (4). As stated earlier, the pulse estimation method destroys the phase information, so the Wiener filter implemented is simply:

$$W(\omega) = \frac{|\hat{f}(\omega)|}{|f(\omega)|^2 + q} \tag{11}$$

The filter $W(\omega)$ thus regularizes the ill-posed problem and gives a stable deconvolution. Figure 1 is shows a Wiener filter constructed from the same pulse estimate (using a noise to signal ratio of .01).

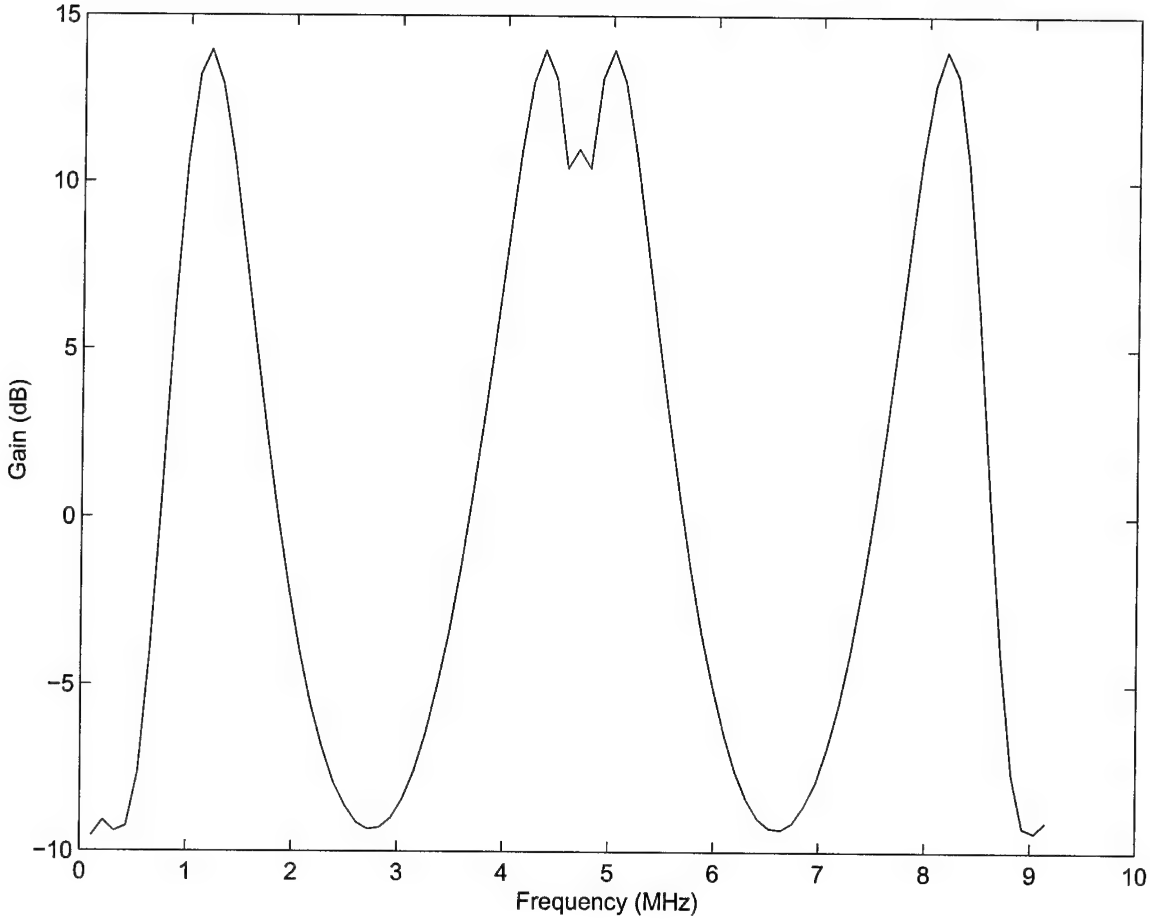

Figure 1: A Wiener filter constructed from a sample pulse estimate with q=.01. The filter amplifies frequencies in the lower and upper passband of the pulse (passband 1.5 MHz, centered at 2.5 MHz) while attenuating lower frequencies.

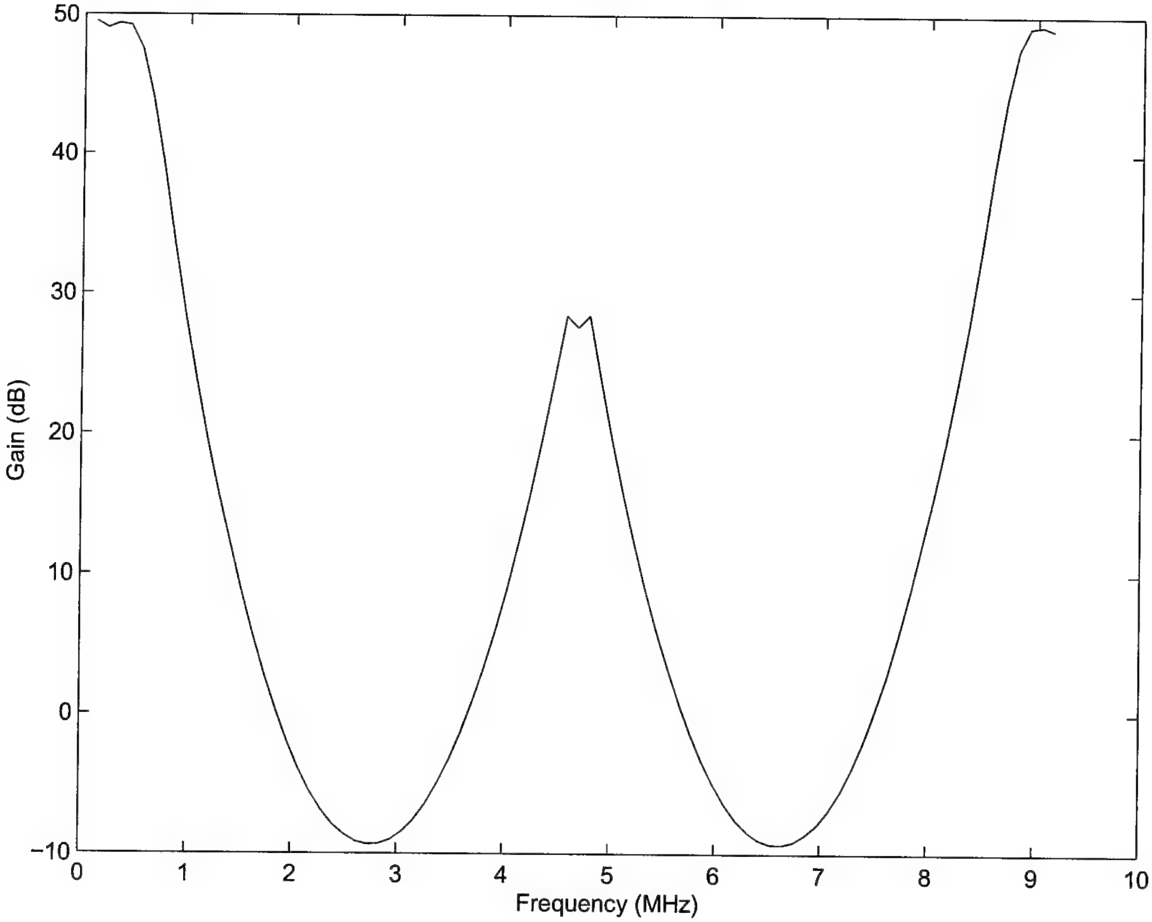

Figure 2: An inverse filter constructed from a sample pulse estimate. The filter dramatically amplifies frequencies below the passband of the pulse (passband 1.5 MHz, centered at 2.5 MHz) and those above the passband.

3 Cepstral Analysis and Homomorphic Filtering

3.1 Definitions and Formalism

A homomorphic system (K,*) satisfies a generalized superposition property; that is, there exists some function (a homomorphism) $\psi : K \to H$ such that $\psi(f * g) = \psi(f) + \psi(g)$ for all $f, g \in K$. The most commonly considered homomorphic system is the convolutional system; the homomorphism for this system is:

$$\psi(f) = \mathbf{F}^{-1}[\mathrm{Log}(\mathbf{F}[f])] \tag{12}$$

Usually, we denote $\hat{f} = \psi(f)$ as the complex cepstrum. The cepstrum was introduced by Bogert [15] for the problem of echo detection; the word "cepstrum" was chosen via interchanging the letters in"spectrum" to show that the cepstrum lay somewhere between the time-domain and the frequency-domain. By similar logic, Bogert termed the units in the cepstral domain "quefrency" by interchanging the letters in "frequency." Since most cepstrum calculations are done numerically, the forward and inverse Fourier transforms in (12) are replaced with forward and inverse z-transforms respectively [16]. Once the signal f is transformed into the cepstral domain, ideal low-pass or high-pass filtering can be applied to get an estimate for either the incident pulse or impulse response of the system.

3.2 Implementation Problems

Formally, we define the complex cepstrum of a data sequence f[n] as the inverse z-transform of the complex logarithm of the z-transform of the sequence (denoted by $F(z)$) via:

$$\hat{f}(n) = \frac{1}{2\pi i} \oint_C \mathrm{Log}(F(z)) z^{n-1} dz \tag{13}$$

where the contour of integration lies within a region where the integrand is analytic and single-valued [17]. Moreover, it can be shown that a finite, stable sequence possess a stable cepstrum if and only if both its z-transform is non-zero on the unit circle and its phase is continuous on the unit circle [18]. Obviously, this restriction raises problems for cepstrum computations with band-limited signals. To circumvent this difficulty, band-limited signals can be exponentially weighted via multiplication by the sequence β^n prior to the computation to the cepstrum.

Another difficulty with cepstrum calculations are phase-wrapping artifacts. If we denote the Fourier transform of $f[n]$ (i.e. the z-transform evaluated along the unit circle) in terms of its phase and magnitude:

$$F(e^{i\omega}) = |F(e^{i\omega})| e^{i\phi(\omega)} \tag{14}$$

where $\phi(\omega)$ denotes the wrapped phase. The log spectrum is thus given by:

$$\hat{F}(e^{i\omega}) = \mathrm{Log}|F(e^{i\omega})| + i\phi(\omega) \tag{15}$$

Since the z-transform must be analytic on the unit circle, it follows that the the function $\phi(\omega)$ must be continuous. However, digital phase computations are performed modulo 2π, so the computed phase function $\phi_w(\omega)$ must be unwrapped in order to get an accurate cepstrum calculation. The problem of phase unwrapping is non-trivial and, in the presence of noise, ill-posed [19]. The phase unwrapping problem has motivated several novel methods to calculate cepstra, such as the real cepstrum and complex cepstrum, which are discussed below.

3.3 Real Cepstrum and Generalized Cepstrum

3.3.1 Real Cepstrum

The real cepstrum of a sequence $f[n]$ is simply the inverse z-transform of the logarithm of the modulus of the z-transform:

$$\hat{f}(n) = \frac{1}{2\pi i} \oint_C \mathrm{Log}|F(z)| z^{n-1} dz \tag{16}$$

which drastically simplifies cepstral calculations by removing phase-unwrapping problems. However, all phase information of the signal is lost in a real cepstrum calculation, making the operation non-invertible in all cases where the signal is not minimum phase. Therefore, the real cepstrum is only applicable to a homomorphic filtering scheme in the case where the input is minimum phase (which, in the case of ultrasound data, cannot be guaranteed *a priori*).

3.3.2 Generalized Cepstrum

The generalized cepstrum [20] generalizes the complex cepstrum by using the mapping $s_\gamma(w)$ defined by

$$s_\gamma(w) = \frac{1}{\gamma}(w^\gamma - 1) \tag{17}$$

instead of the complex logarithm. Since $s_\gamma(w) \to \mathrm{Log}(w)$ as $\gamma \to 0$, the generalized cepstrum approaches the complex cepstrum for small γ. Similar to the inverse cepstrum, we can define an inverse mapping s_γ^{-1} via:

$$s_\gamma^{-1}(w) = (1 + \gamma w)^{\frac{1}{\gamma}} \tag{18}$$

The generalized cepstrum effectively "smoothes" the data in the cepstral domain by adding a convolved term. That is, the generalized cepstrum of a convolution becomes

$$\overline{f * g} = \bar{f} + \bar{g} + \gamma \bar{f} * \bar{g} \tag{19}$$

thus reducing artifacts caused by cepstral filtering.

3.4 An Analytic Calculation

3.4.1 Motivation and Definition

To give some insight into cepstral analysis, we present a simple "pencil and paper" deconvolution in the non-discrete case. While, in practice cepstral calculations are always performed digitally, we attempt here to define a cepstral operator for real and complex-valued functions (in general, for generalized functions or distributions). For clarity, we summarize here some basic definitions and facts from Fourier Analysis. For functions $f(t) \in S$ (good functions), more generally, $f(t) \in L^2$ (square-integrable functions) we can define the forward and inverse Fourier transforms as follows:

$$\hat{f}(\omega) = \mathbf{F}[f(t)] := \frac{1}{\sqrt{2\pi}} \int_{-\infty}^{+\infty} f(t) e^{-i\omega t} dt \qquad (20)$$

$$f(t) = \mathbf{F}^{-1}[\hat{f}(\omega)] := \frac{1}{\sqrt{2\pi}} \int_{-\infty}^{+\infty} \hat{f}(\omega) e^{i\omega t} d\omega \qquad (21)$$

In particular, it can be shown that the operators $F : S \to S$ and $F : L^2 \to L^2$ are bijective (along with their inverses) [21]. However, our calculations will often involve transforming functions which are not good (indeed, unbounded). Therefore, we need to generalize our space of functions to S', or the space of tempered distributions [10]. On the space S' we can define the generalized Fourier transform (and its associated inverse) $\mathbf{F}' : S' \to S'$ and $\mathbf{F}'^{-1} : S' \to S'$ defined as the adjoint of $f(t) \in S'$. That is, the generalized transform $\hat{f}(\omega)$ is defined by

$$< \hat{f}, \psi > = < f, \hat{\psi} > \qquad (22)$$

for any function $\psi \in S$. Of course, the generalized Fourier transform of a good function is given by the classical formulas (20) and (21). Using this machinery, we can define a cepstral operator $C : S' \to S'$ defined by

$$\bar{f}(t) = \mathbf{C}[f(t)] = \mathbf{F}'^{-1}[\text{Log}(\mathbf{F}'[f(t)])] \qquad (23)$$

where $\text{Log}(z)$ denotes the complex logarithm. Note that a necessary condition for the existence of $\bar{f}(t)$ is $\hat{f}(\omega) \neq 0$ for all ω. Likewise, we can define the inverse cepstral operator via

$$f(t) = \mathbf{C}^{-1}[\bar{f}(t)] = \mathbf{F}'^{-1}[\exp(\mathbf{F}'[\bar{f}(t)])] \qquad (24)$$

Now let $f(t)$ and $g(t)$ be of class S' such that $\bar{f}(t)$ and $\bar{g}(t)$ exist. If we let $h(t) := f(t) * g(t)$, then it follows (using the convolution theorem and the properties of the logarithm) that

$$\bar{h}(t) = \bar{f}(t) + \bar{g}(t) \qquad (25)$$

Thus, the cepstral operator transforms convolution in the time-domain into addition in the cepstral domain. The function $\text{Log}(z)$ in equation (23) homomorphically maps a product of Fourier transforms into a superposition of log spectra. We will use this generalized superposition of the cepstral operator to separate two signals convolved in the time-domain with an appropriate filter in the cepstral domain.

3.4.2 Sample Calculation

Consider an incident pulse modeled by the function

$$f(t) = e^{-t^2/(2\sigma^2)} \qquad (26)$$

and an impulse response of some medium given by an impulse train with $N+1$ terms

$$g(t) = \sum_{j=0}^{N} a_j \delta(t - t_j) \tag{27}$$

where we take $a_{j+1} < a_j \forall j$. Then the scattered field $h(t) = f(t) * g(t)$, or

$$h(t) := \int_{-\infty}^{+\infty} f(\tau) g(t-\tau) d\tau \tag{28}$$

is given by

$$h(t) = \sum_{j=0}^{N} a_i e^{-(t-t_j)^2/(2\sigma^2)} \tag{29}$$

Our task now is, given equation (29), find the incident pulse $f(t)$ and/or the impulse response $g(t)$. In many cases, we may have *a priori* knowledge of either $f(t)$ or $g(t)$. For instance, we may know $f(t)$ to have a Gaussian envelope (with known bandwidth parameter σ) or $g(t)$ to have compact support. In the ultrasound model, we can safely assume the interrogating pulse $f(t)$ to be smooth (n-times continuously differentiable) while $g(t)$ is random-like and hence non-differentiable. In this calculation, we take $f(t) \in S$ and $g(t)$ to have a sinusoidal spectrum.

This information allows us to choose an appropriate filter in the cepstral domain. Just as the Fourier transform indicates frequency content of a function, the support of the cepstrum of a function measures the smoothness of the function. In fact, for the subset of good functions which have a polynomial log spectrum, the cepstrum will have support only at the origin. This fact follows from the Fourier pair $\sum_{j=0}^{N} a_j x^j \leftrightarrow \sum_{i=0}^{N} a_j \delta^{(j)}$.

We can easily calculate the Fourier transform of (29), given by

$$\hat{h}(\omega) = \frac{\sigma}{\sqrt{2\pi}} e^{-\sigma^2\omega^2/2} \sum_{j=0}^{N} a_j e^{i\omega t_j} \tag{30}$$

which can also be obtained via transforming (26) and (27) and applying the convolution theorem. Note that $\hat{f}(\omega)$ is non-zero for all real ω, allowing the complex logarithm to be taken. After some manipulation, we find the complex cepstrum to be

$$\bar{h}(t) = (\log(\frac{\sigma}{\sqrt{2\pi}} + a_0))\delta(t) + \frac{\sigma^2\sqrt{2\pi}}{2}\delta''(t) + \phi(t) \tag{31}$$

where

$$\phi(t) = \bar{g}(t)/a_0 \tag{32}$$

Now $\phi(t)$ is a series of impulses, with no support at the origin. Taking into account that supp$\bar{f}(t) = \{0\}$, we can filter $\bar{h}(t)$ with the function

$$\begin{aligned} \bar{h_c}(t) &= h(t) \text{ if } t \neq 0 \\ &= 0 \text{ if } t = 0 \end{aligned}$$

giving

$$\bar{h}_c(t) = \phi(t) \tag{33}$$

Inversion of $\bar{h}_c(t)$ is straightforward via application of (24), yielding the final result

$$h_c(t) = \sum_{j=0}^{N} (a_j)/(a_0)\delta(t - t_j) \tag{34}$$

The above calculation can be specialized to an impulse response with only two spikes, providing insight into the cepstral filtering. The following calculations result (taking $t_0 = 0$ and $a_1 < a_0$):

$$\begin{aligned} h(t) &= a_0 e^{-t^2/(2\sigma^2)} + a_1 e^{-(t-t_1)^2/(2\sigma^2)} \\ \hat{h}(\omega) &= \frac{\sigma}{\sqrt{2\pi}} e^{-\sigma^2\omega^2/2}(a_0 + a_1 e^{i\omega t_1}) \\ \bar{h}(t) &= (\log(\frac{\sigma}{\sqrt{2\pi}} + a_0))\delta(t) + \frac{\sigma^2\sqrt{2\pi}}{2}\delta''(t) + \phi(t) \\ &\qquad \text{with} \\ \phi(t) &= \sum_{k=1}^{+\infty} \frac{(-1)^{k+1}}{k}(a_1/a_0)^k \delta(t - t_1 k) \end{aligned}$$

Application of the filter $\bar{h}_c(t)$ yields $\phi(t)$, which clearly has no support at the origin. This can be inverted back into the time domain to give

$$h_c(t) = \delta(t) + (a_1/a_0)\delta(t - t_1) \tag{35}$$

Note that the recovered impulse response $h_c(t)$ differs from the original by a multiplicative constant a_0; that is, we have lost the "DC-component" of the impulse response during the filtering process. Otherwise, this calculation completely separates the incident pulse from the response using the assumption that the pulse has limited support in the cepstral domain.

Some comments about this calculation include:

1. Can we find sufficient conditions for any $f \in S'$ to have a cepstrum $\bar{f} \in S'$? Can we extend the sufficient condition for finite l^2 sequences for function in S, or more generally, S'?

2. Since our data must be processed in a discrete fashion (and will invariably be contaminated by noise), the notion of "smoothness" becomes problematic. A more accurate model for the incident pulse defined by (26) would include a sinusoidal varying term; if the frequency of this term is high, the sampled version of f would lead to a non-smooth pulse and our deconvolution scheme would break down.

4 Projections onto Convex Sets

4.1 Background and the Fundamental Theorem

Projections onto Convex Sets provide a powerful framework for the construction of signal restoration and extrapolation algorithms. One of the first POCS algorithms was the Papoulis-Gerschberg algorithm [22] used to extrapolate a known-segment of a band-limited signal. Later, Youla and others [23] [24] [25] extended various isolated algorithms into a general mathematical theory. All POCS methods utilize various *a priori* information about the input and desired output, allowing a wide variety of implementations.

The general theory of vector space projections requires some basic knowledge of functional analysis; a good introduction to the basics can be found in [26] and [27]. For conciseness, we summarize some of the basic definitions and results.

We will work within the Hilbert space of square-integrable functions L^2, which physically denotes the space of finite-energy signals. The L^2 norm is defined by

$$\|f(x)\|_2 := \sqrt{\int_{-\infty}^{+\infty} |f(x)|^2 dx} \tag{36}$$

The L^2 norm defines a functional mapping a space of functions into a scalar field. Many POCS problems can be formulated by considering the minimization of a functional. In particular, the deconvolution problem modeled by (1) can be posed by minimization of the functional $J : L^2 \to \overline{\mathbf{R}_+}$ where

$$J := \|h[n] - u[n] * v[n]\|_2^2 \tag{37}$$

where $h[n]$ is some known data. Minimization of J entails finding the optimal pairs of functions $u[n]$ and $v[n]$. Obviously, as it stands, the problem as posed will have an infinite number of solutions. To restrict the solution set, we can define constraint sets C_f and C_g that u and v must satisfy. Associated with each constraint set, we can define an *orthogonal projector* that maps functions onto the constraint set. The following result tells us what types of constraint sets are admissible in a POCS algorithm.

Let H be a Hilbert space and let C_i with $1 \le i \le m$ be closed convex subsets of H and let $C_0 = \bigcap_{i=1}^{m} C_i$ denote the finite intersection of these sets. Now define $P_i : H \to C_i$ be the projector onto C_i. Define the composition projector $P = P_m P_{m-1} \cdots P_1$ Then the following holds:

Theorem 4.1 Fundamental Theorem of POCS *Let C_0 be non-empty. Then for all $x \in H$, the sequence $P^n x$ converges weakly to a point C_0.*

Thus theorem (4.1) assures the convergence of any POCS algorithm with well-defined constraint sets; however, unless C_0 is a singleton set, the algorithm will not automatically converge to a unique solution. Also, the rate of convergence may be exceedingly slow. To accelerate the POCS algorithm, several researchers [28] [29] have refined POCS with the introduction of relaxed projectors and other such improvements.

To devise a POCS algorithm for the ultrasound model, we incorporate both the convolutional model and certain *a priori* information about the pulse $f[n]$ and the impulse response $g[n]$, which we use to construct the constraint sets C_f and C_g. For acoustical data, more frequency-domain constraints are available, so the functional J in equation (37) can be Fourier transformed via Parseval's identity, yielding:

$$J = \frac{1}{2\pi} \|\hat{h}(\omega) - \hat{u}(\omega)\hat{v}(\omega)\|_2^2 \tag{38}$$

where $\hat{u}(\omega) \in C_f$ and $\hat{v}(\omega) \in C_g$. Once the constraint sets are found (and there associated projectors), a POCS algorithm can be implemented which minimizes J in equation (38).

4.2 Constraints and Implementation

In order to achieve a stable deconvolution, we need to know maximum *a priori* information about the data at hand. Far-field acoustic data can be especially problematic since it does not have the most commonly considered properties (*e.g.*, finite duration, strict band-limitation, non-negativity, etc.). Therefore, we propose several novel constraint sets that could be useful in a POCS algorithm.

4.2.1 Angle-Dependent Band-Limitation

Under the Born Approximation, the far-field frequency response of a 2D scatterer with a spatially-varying sound-speed contrast $\gamma(\mathbf{r})$ is given by [30]

$$\hat{p}_s(\boldsymbol{\alpha}, \boldsymbol{\theta}, \omega) = \frac{2\pi^2}{R} e^{ikR} k^2 \Gamma(k|\boldsymbol{\alpha} - \boldsymbol{\theta}|) \tag{39}$$

where R is the far-field measurement radius and $\Gamma(\mathbf{k})$ is the spatial Fourier transform of the contrast $\gamma(\mathbf{r})$. Since the object being imaged is of compact support (with radius a), the contrast function $\gamma(\mathbf{r})$ will have an analytic Fourier transform. However, we can use an uncertainty principle to estimate the effective "k-width" σ_k of $\Gamma(\mathbf{k})$. That is:

$$\sigma_k a \sim 1 \tag{40}$$

Therefore, $\Gamma(\mathbf{k})$ is effectively zero for spatial frequencies greater that σ_k. Equating this information with the argument in equation (39), we have

$$k_c|\boldsymbol{\alpha} - \boldsymbol{\theta}| \sim 1 \tag{41}$$

where k_c is the spatial frequency cutoff. From this, we can easily deduce an angle-dependent frequency cutoff given by

$$f_c \approx \frac{c}{\pi a} \csc\left(\frac{\theta - \alpha}{2}\right) \tag{42}$$

From this cutoff estimate, we see that the forward-scatter case gives a broadband response, while side and back scattering is band-limited. Equation (42) thus implicitly defines a band-limited set, which is known to be both closed and convex.

4.2.2 Low Bandwidth Envelope

Another possible frequency-domain constraint that could be applied is an upper bound on the spectrum. In general, the wideband response of a scatterer with contrast $\gamma(\mathbf{r})$ and support Ω is given by

$$\hat{p}_s(\boldsymbol{\alpha},\boldsymbol{\theta},\omega) = k^2\hat{f}(\omega)\int_\Omega G_0(R\boldsymbol{\theta}-\mathbf{r_0},\omega)\gamma(\mathbf{r_0})\hat{p}(\mathbf{r},\boldsymbol{\alpha},\omega)d\Omega_0 \tag{43}$$

where $G_0(\omega,\mathbf{r})$ is the frequency domain Green's function for the reduced wave equation (Helmholtz equation). By applying the Born approximation and the far-field approximation for a cylinder of radius a, equation (43) becomes:

$$\hat{p}_s(\theta,\alpha,\omega) = \frac{i}{4}k^2\hat{f}(\omega)\sqrt{\frac{2}{\pi kR}}\frac{e^{ikR\cos(\theta-\phi)}}{e^{-ikR}}\int_0^{2\pi}\int_0^a \gamma(r,\phi)e^{-ikr\cos(\theta-\phi)}r\,dr\,d\phi \tag{44}$$

Taking the modulus of both sides of (44) and approximating the integral with a n upper bound $\Gamma = \max\gamma(r,\phi)$ yields the inequality

$$|p_s(\omega)| \leq |\frac{1}{4}k^2\hat{f}(\omega)\sqrt{\frac{2}{\pi kR}}\pi a^2\Gamma| \tag{45}$$

which may be simplified to give

$$|p_s(\omega)| \leq K\omega^{3/2}|\hat{f}(\omega)| \tag{46}$$

where the constant K is given by

$$K = \frac{1}{4}\sqrt{\frac{2\pi}{Rc_0^3}}\Gamma a^2 \tag{47}$$

Equation (46) yields some *a priori* information about the scattered wave-field. Consider the ideal case where the incident pulse $f(t) = \delta(t)$; then $|\hat{f}(\omega)| = 1$, implying that the frequency response p_s is bounded by an envelope proportional to $\omega^{3/2}$. This bound allows us to enforce a frequency-domain constraint in the case of low-bandwidth extrapolation ($\omega \ll 2\pi f_0$), where f_0 is the central frequency of the incident pulse employed. Also, equation (46) coupled with Parseval's identity allows us to find a bound on the energy of the signal.

4.2.3 Other *A Priori* Constraints

Since the basic characteristics of the pulse (*e.g.*, effective bandwidth, central frequency, linear phase, *etc.*) are known *a priori*, constraint sets could be defined which reflect these parameters. For instance, a Gaussian envelope in the frequency domain could be used to bound the spectrum. Other possibilities include energy constraints (in either the time or the frequency domain) or angle-dependent amplitude limitation.

5 Computational Techniques and Numerical Results

5.1 Description of Data and Reconstruction Algorithm

We tested the deconvolution algorithms on two synthetic far-field time-domain scattering data sets computed via k-space method [31]. The first data set was generated from a cylinder with random internal structure with added white, Gaussian noise with an SNR value of 38.7 dB. The second data set was generated from a simulated breast model with sound speed contrast mimicking fat and tissue. No artificial noise was added to the breast data. The synthetic data was computed using N_α transmit angles and N_θ receive angles. The data sets are summarized in tables 1 and 2. Both data sets used the time-domain waveform

$$f(t) = \cos(2\pi f_0 t)e^{-t^2/(2\sigma^2)} \tag{48}$$

where f_0 is the central frequency and σ is the temporal Gaussian parameter.

After the deconvolution algorithm was applied, a the time-domain reconstruction algorithm outlined in [3] reconstructed the scatterers. The scattering configuration is shown in figure 3. The far-field data $p_s(\boldsymbol{\alpha}, \boldsymbol{\theta}, t)$ was used to reconstruct the sound-speed contrast function $\gamma(\mathbf{r})$ via the formula

$$\gamma_M(\mathbf{r}) = \frac{1}{N} \int \int \Phi(\boldsymbol{\alpha}, \boldsymbol{\theta}) \left(p_s(\boldsymbol{\alpha}, \boldsymbol{\theta}, \tau) + i\mathbf{H}^{-1}[p_s(\boldsymbol{\alpha}, \boldsymbol{\theta}, \tau)] \right) d\alpha \, d\omega \tag{49}$$

where the delay term τ is given by

$$\tau = \frac{R}{c_0} + \frac{(\boldsymbol{\alpha} - \boldsymbol{\theta}) \cdot \mathbf{r}}{c_0} \tag{50}$$

the coefficient N is determined by a frequency weight incorporating the bandwidth of the incident pulse $f(t)$, $\mathbf{H}^{-1}$ is the inverse Hilbert transform, and $\Phi(\boldsymbol{\alpha}, \theta)$ is a "filter" dependent upon the scattering geometry. In the case of 2D scattering, the filter is given by:

$$\Phi(\boldsymbol{\alpha}, \boldsymbol{\theta}) = |\sin(\theta - \alpha)| \tag{51}$$

The method embodied in equation (49) synthetically delays and sums all transmit angles $\boldsymbol{\alpha}$ and receive angles $\boldsymbol{\theta}$ to focus an image at position $\mathbf{r}$, using all available bandwidth of the incident pulse. Of special interest in deconvolving ultrasound data is its performance with limited-aperture data; that is, when only a limited number of transmit and receive angles are available. Therefore, we performed reconstructions at aperture width ϕ_{ap} where the integral in equation (49) was evaluated over

$$|\alpha| \leq \phi_{ap}/2 \text{ and } |\theta - \pi| \leq \phi_{ap}/2 \tag{52}$$

For brevity, we call aperture widths $\phi_{ap} = 2\pi$ full, $\phi_{ap} = \pi$ half, and $\phi_{ap} = \pi/2$ quarter in the descriptions of the reconstructions.

For reference, figures 5 and 6 show the raw far-field data reconstructed with no deconvolution, while figure 4 shows the actual (non-imaged) models.

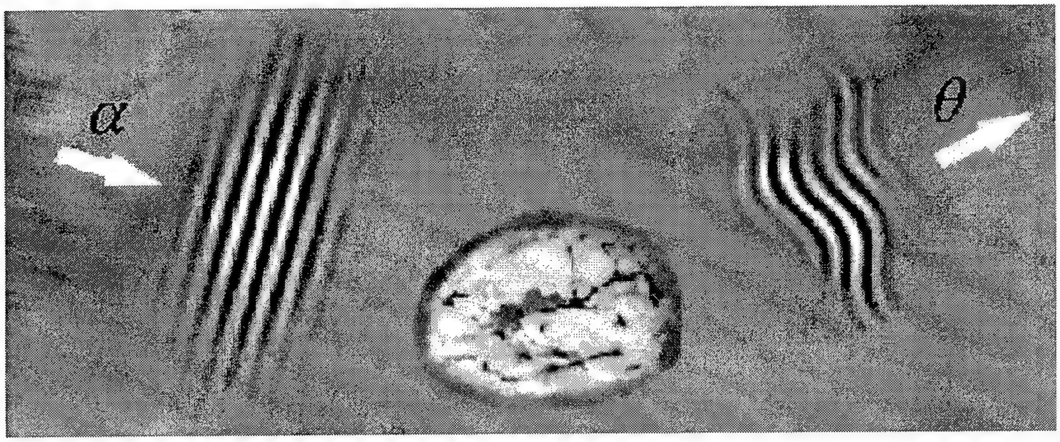

Figure 3: Illustration of the scattering configuration employed. An incident pulse $f(t-\boldsymbol{\alpha}\cdot\mathbf{r}/c)$ is scattered by some medium and the time-domain scattered pressure $p_s(\boldsymbol{\alpha}, \boldsymbol{\theta}, t)$ is measured in the far-field at radius R and angle θ.

Central Frequency f_0	2.5 MHz
Effective Bandwidth	1.5 MHz
Gaussian Parameter σ	.25 μs
Sampling Frequency	9.144 MHz
Number of Samples	84
Number of Receive Angles	256
Number of Send Angles	64
Radius of Cylinder	3.0 mm

Table 1: Summary for synthetic cylinder with random internal structure data.

Central Frequency	2.5 MHz
Effective Bandwidth	1.5 MHz
Gaussian Parameter σ	.25 μs
Sampling Frequency	9.153 MHz
Number of Samples	256
Number of Receive Angles	512
Number of Send Angles	128
Radius of Breast	8.5 mm

Table 2: Summary of simulated breast data.

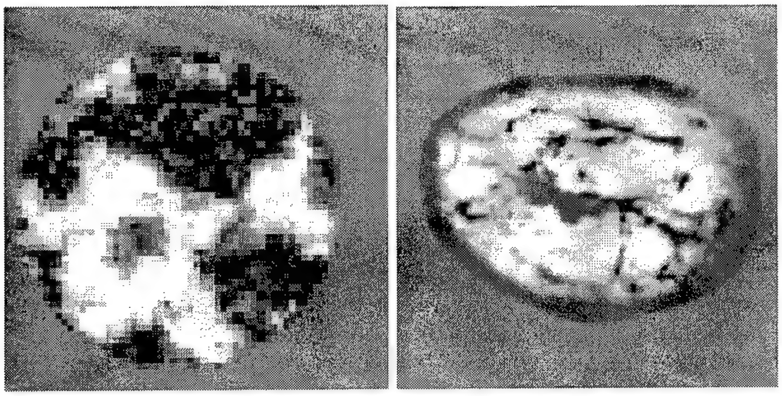

Figure 4: The actual models: cylinder with random internal structure and the simulated cross-section of a breast.

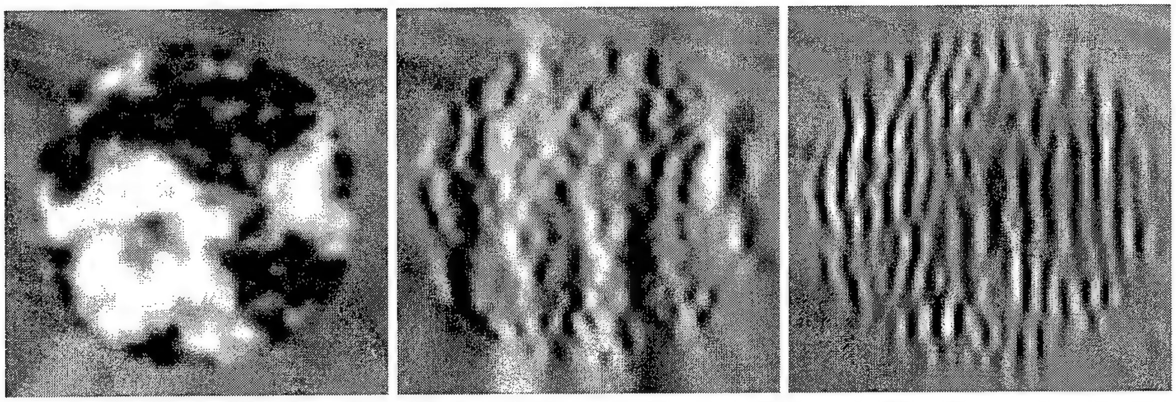

Figure 5: Full, half, and quarter aperture reconstructions of cylinder data.

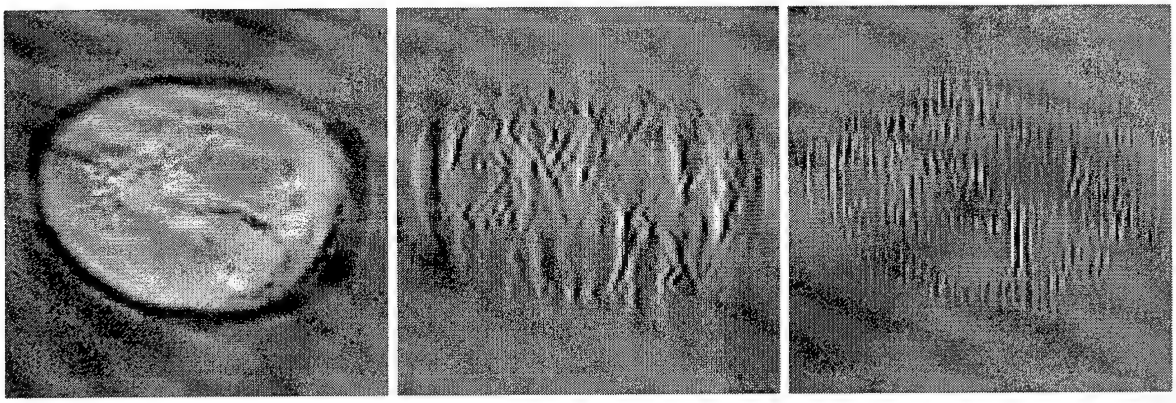

Figure 6: Full, half, and quarter aperture reconstructions of synthetic breast data.

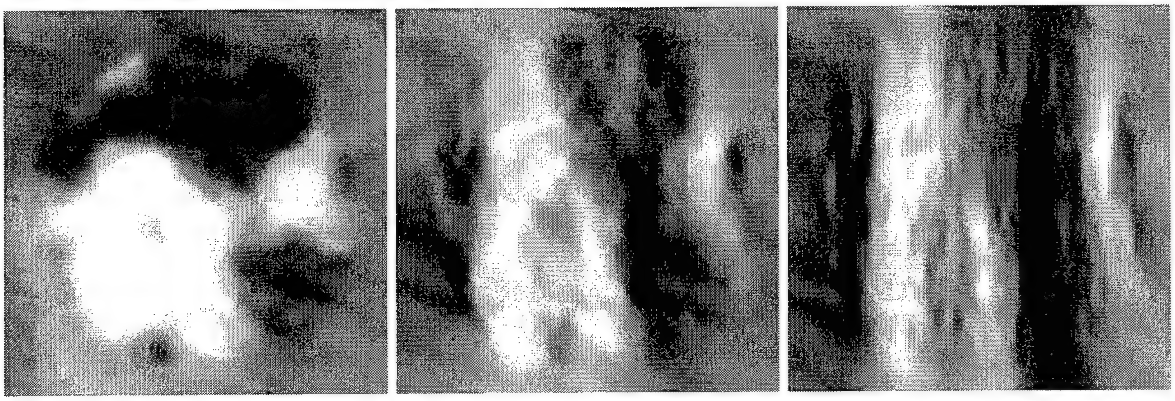

Figure 7: Full, half, and quarter aperture reconstructions of cylinder data deconvolved using an inverse filter from a pulse estimate.

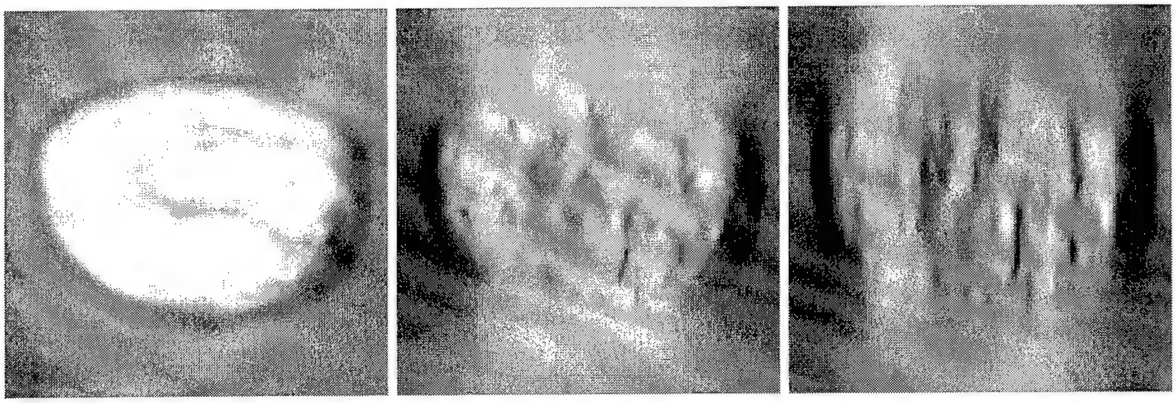

Figure 8: Full, half, and quarter aperture reconstructions of synthetic breast data deconvolved using an inverse filter from a pulse estimate.

5.2 Inverse Filtering Results

The inverse filtering algorithms are both the simplest to implement and the most widely used. We used both simple inverse filtering and a Wiener filter (*i.e.* regularized inverse filtering) constructed from a pulse estimation using equation (4). For the regularized algorithm, we use the parameter $q = .01$. Figures 7 and 8 show the inverse filtered cylinder and breast data (respectively) and figures 9 and 10 show Wiener filtered cylinder and breast data.

5.3 Homomorphic Filtering Results

As discussed above, homomorphic filtering is implemented in three steps:

1. The data (perhaps pre-processed via exponential weighing or the application of some window) is transformed into the cepstral domain via one of the algorithms discussed above.

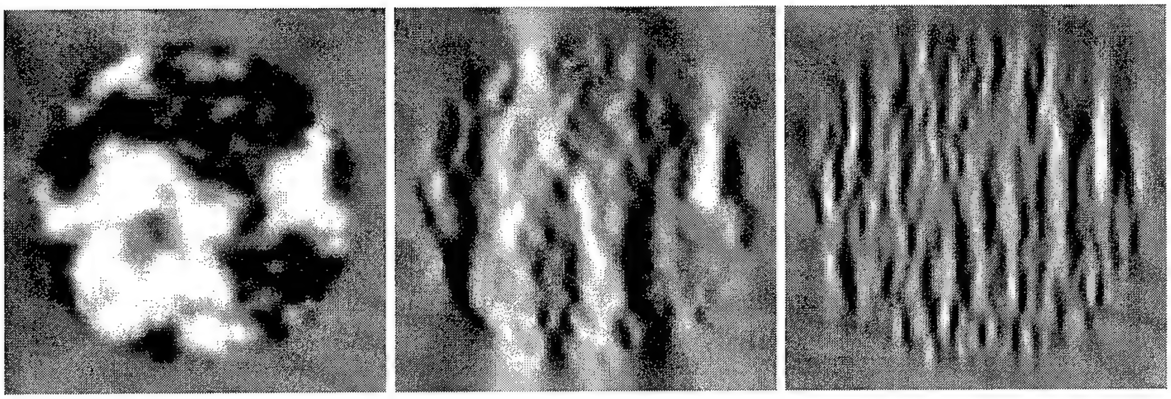

Figure 9: Full, half, and quarter aperture reconstructions of cylinder data deconvolved using a Wiener filter created from a pulse estimate.

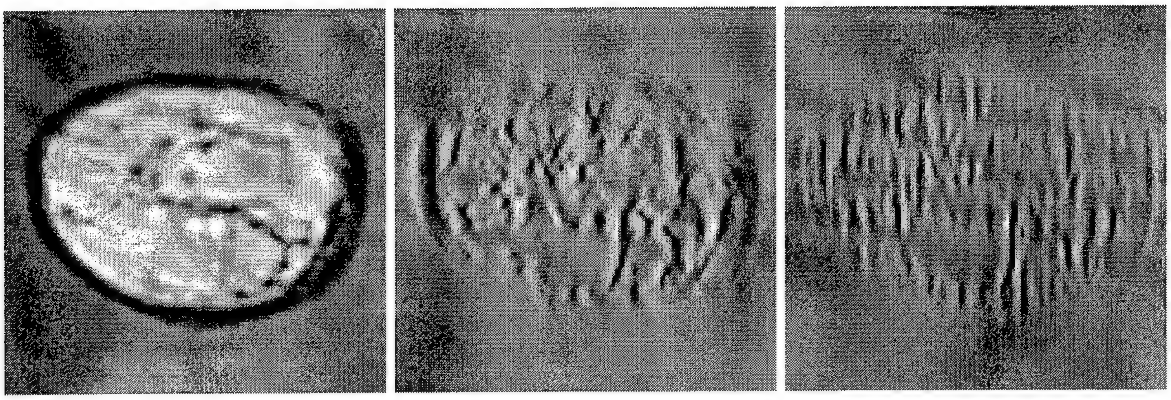

Figure 10: Full, half, and quarter aperture reconstructions of synthetic breast data deconvolved using a Wiener filter created from a pulse estimate.

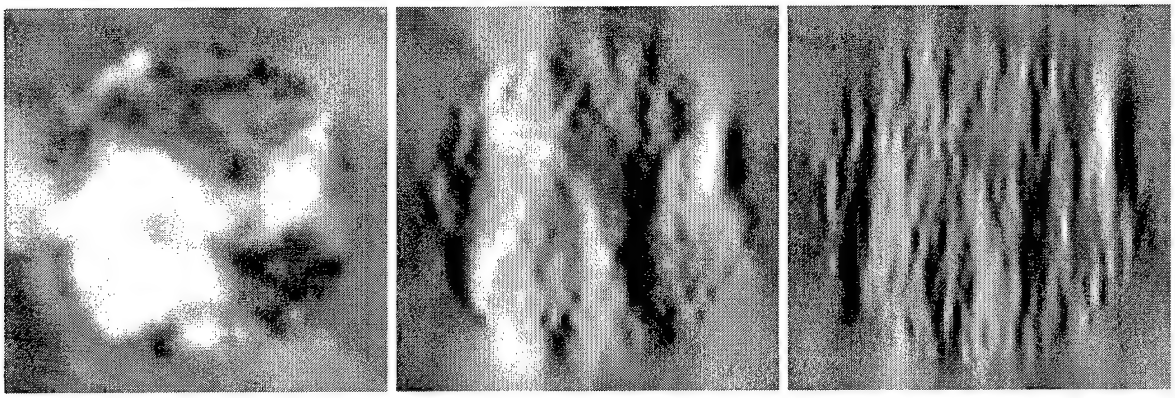

Figure 11: Full, half, and quarter aperture reconstructions of cylinder data using a one-stage cepstral deconvolution.

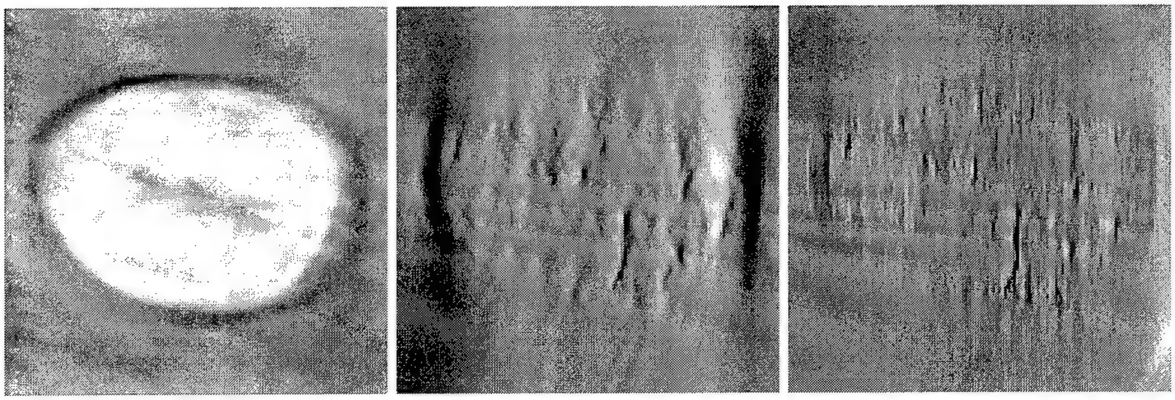

Figure 12: Full, half, and quarter aperture reconstructions of simulated breast data using a one-stage cepstral deconvolution.

2. The cepstrum is either low-pass filtered (in order to recover the pulse) or high-pass filtered (in order to recover the impulse response).
3. The filtered cepstrum is inverted back into the time domain.

Step 2 requires an estimate for a cepstral cutoff N_c; that is, we must identify the quefrency at which to apply the filter. To recover the pulse, for instance, we need an estimate of the quefrency band which its cepstrum occupies.

5.3.1 One-Stage Deconvolution

Here we present a simple 1-stage deconvolution scheme based on long-pass filtering of the complex and generalized cepstrum. The data was exponentially weighted by a factor $\beta = .975$ and high-pass filtered above $N_c = 7$ for the cylindrical speckle data and $N_c = 21$ for the breast data. Instead of a hard cut in the cepstral domain, a cosine taper of width 4 was applied. Figures 11 and 12 show the deconvolved reconstructions.

Cepstral Cutoff (speckle)	N_c	7
Cepstral Cutoff (breast)	N_c	21
Exp. Weighting Factor	β	.975
Noise-to-Signal Ratio	q	.001

Table 3: Parameters used in two-stage homomorphic deconvolution using the complex cepstrum.

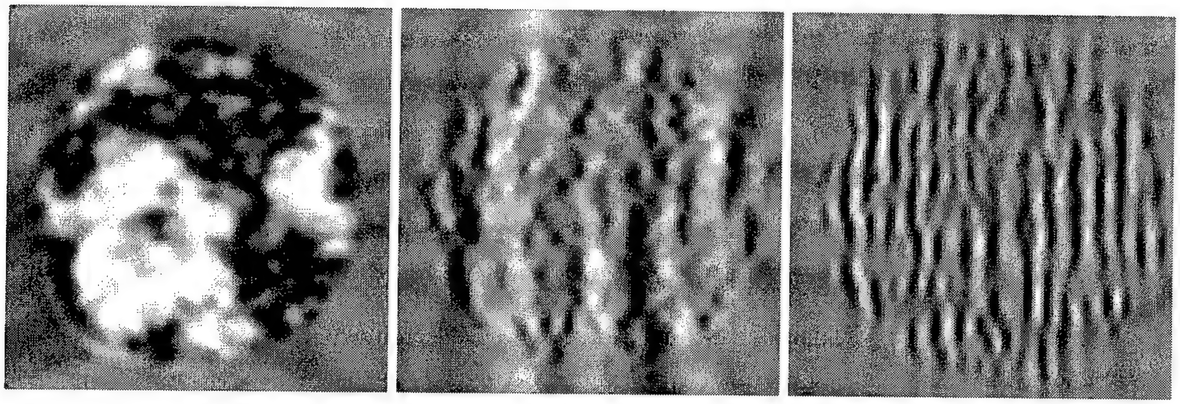

Figure 13: Full, half, and quarter aperture reconstructions of cylinder data deconvolved using a two-stage homomorphic deconvolution.

5.3.2 Two-Stage Deconvolution

Here we present a 2-stage deconvolution method based on the complex and generalized cepstrum. First the cepstrum of the data is calculated, then short-pass filtering is performed to recover a pulse estimate. The short-passed cepstrum is then averaged over all receive angles to get an improved pulse estimate. This final pulse estimate is used to construct a Wiener filter. In the calculation of the complex cepstrum, exponential weighting with parameter β was used to reduce phase wrapping. The exponential weighting changed the signal-to-noise ratio, so the parameter q in the Wiener filter had to be adjusted. This method was repeated using the generalized cepstrum. Tables 3 and 4 show the parameters chosen. The reconstructions using a complex cepstrum implementation are shown in figures 13 and 14 while those using the generalized cepstrum are shown in figures 15 and 16.

Cepstral Cutoff (speckle)	N_c	7
Cepstral Cutoff (breast)	N_c	21
Cepstrum Exponent	γ	.125
Noise-to-Signal Ratio	q	.001

Table 4: Parameters used in two-stage homomorphic deconvolution using the generalized cepstrum.

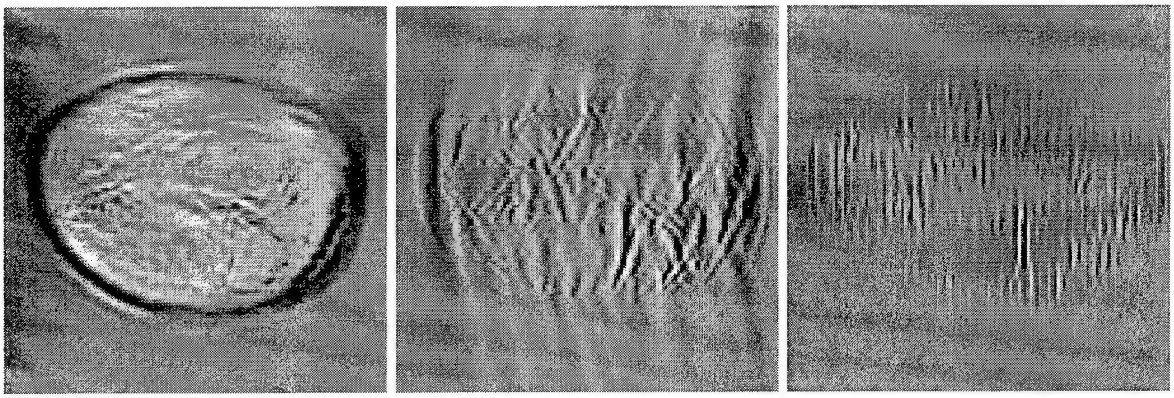

Figure 14: Full, half, and quarter aperture reconstructions of synthetic breast data deconvolved using a two-stage homomorphic deconvolution.

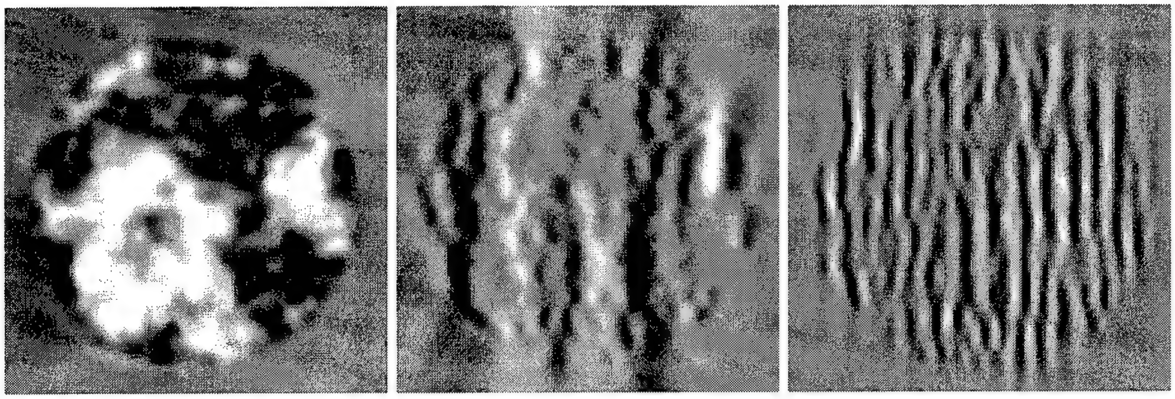

Figure 15: Full, half, and quarter aperture reconstructions of cylinder data deconvolved using a two-stage homomorphic deconvolution with the generalized cepstrum.

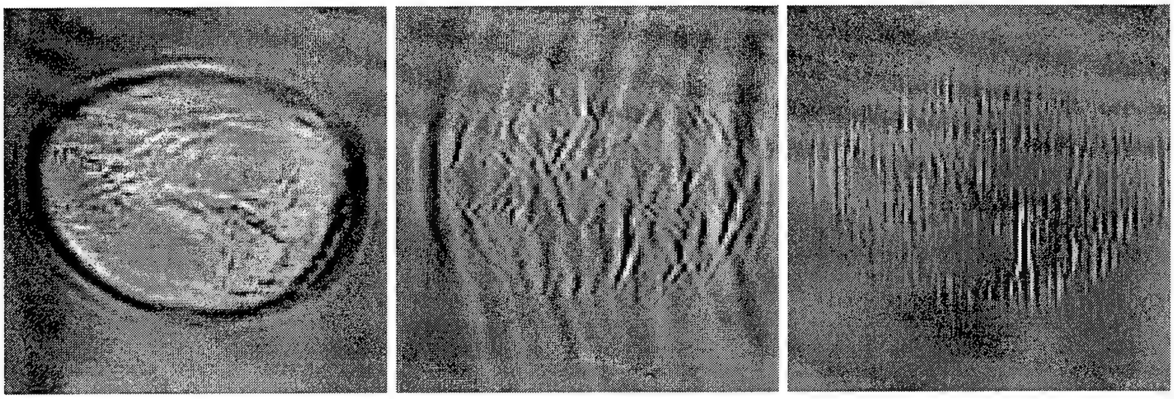

Figure 16: Full, half, and quarter aperture reconstructions of synthetic breast data deconvolved using a two-stage homomorphic deconvolution with the generalized cepstrum.

6 Conclusions and Remarks

6.1 Comparison of Methods

Inverse and Wiener filtering provided good results which can serve as a benchmark with which to compare other methods. For full aperture reconstruction, the Wiener filtered data (figures 9 and 10) provided a clean deconvolution, revealing small amounts of detail not present in the raw reconstruction. However, for half and quarter aperture sizes, the reconstructions became contaminated by lateral blurring and noisy artifacts. Although the unregularized inverse filtered data (figures 7 and 8) lost spatial resolution as the aperture size decreased, the artifact build-up was not as severe as in the case of Wiener filtering. Minimal internal features were still distinguishable even at quarter aperture. In fact, the inverse filtered reconstruction provided the best limited-aperture reconstruction, giving the most information about the imaged object. Perhaps the increased resolution at low aperture width can be attributed to the low frequency amplification provided by the inverse filter (figure 2), which is not present in the Wiener filter (figure 1).

The one-stage cepstral deconvolution (figures 11 and 12) attempted to separate the cepstrum of the impulse response from that of the pulse via high-pass filtering (liftering) in the cepstral domain. Most internal detail was lost at limited-aperture, although the boundaries remained distinct. From the results we achieved, high-pass filtering of the cepstrum failed as a viable deconvolution method.

From the numerical results presented above, the two-stage cepstral deconvolution (figures 13 and 14) does not give a degraded reconstruction at full aperture (unlike the other methods). It is similar in quality to the raw reconstruction. However, in the limited aperture reconstructions, broadband noise and severe lateral blurring builds up, making most internal features indistinguishable. As the aperture shrinks to $\pi/2$ radians, all internal features are lost with only the boundary remaining distinct. The effect of using both the complex and generalized cepstra in two-stage homomorphic filtering makes only a minimal difference in reconstruction quality. More detail can be found on competing cepstral realizations in [14].

The cepstral methods suffer from a need to estimate parameters such as minimum phase cutoff N_c and exponential weighting parameter β. It seems, however, that these parameters are dependent only upon the scattering configuration and the pulse waveform employed, thus independent of the medium being investigated.

Of the methods presented above, we must conclude that inverse filtering is the most viable deconvolution method. None of the methods provided significant improvement over no deconvolution at full aperture, yet inverse filtering preserved useful detail at half and quarter aperture, whereas all other methods failed. We attribute this to the pulse estimation algorithm, which incorporates both noise regularization and amplification at low frequencies. The Wiener filter apparently does not provide enough low frequency amplification to usable limited-aperture reconstructions. Likewise, the homomorphic filtering schemes do not give a strong enough deconvolution to provide a useful limited-aperture reconstruction.

6.2 Problems and Further Work

As we have seen, the acoustic deconvolution problem is highly non-trivial and there is much work to be done before any one algorithm can be used in a clinical installation. Inverse and Wiener filtering provide good results while having a low computational cost and simple implementation. The easiest way to improve an inverse filtering scheme is provide a better pulse and noise-to-signal estimate. The accuracy of the inverse filtering scheme at limited aperture provides evidence for the pulse estimation algorithm embodies in equation (4). Perhaps advances in inverse filtering could therefore start with a more precise estimation.

In the case of homomorphic deconvolution, the problem of phase unwrapping and the the computational realization of the cepstrum are persistent. Phase unwrapping is highly sensitive to noisy data and poses a severe problem to cepstrum calculations. Also, estimation of the parameters used in homomorphic filtering is largely *ad hoc*; although estimates from the rise-time of the log spectrum [7] and spatial extent of the pulse [14] have been proposed, there is presently no accurate way to estimate the cepstral cutoff N_c short of trial and error. Also, both the generalized and continuous-time cepstrum are not well-understood.

POCS algorithms have been widely applied in such fields as optics, spectral analysis, and digital communications, but their introduction into acoustic signal processing has been slow. Perhaps this is due to the lack of *a priori* information available to construct constraint sets; although the analytical work done on acoustic scattering is enormous, the mathematical complexities involved do not lend themselves easily to simple constraints. Other difficulties with POCS include the large number iterations often necessary for convergence, which could limit real-time implementation.

In summary, the deconvolution of ultrasound data is not fully understood and much work is needed for an algorithm that gives good results from limited data. From our research, it appears that work can be done in two directions: designing better inverse filters and finding a viable POCS implementation. Both directions hope to provide exciting areas of research.

7 Acknowledgements

This research was funded by the Applied Research Laboratory of the Pennsylvania State University under the ARL Mathematics Honors Program. I am very grateful for extensive discussion and direction provided by Dr. T. Douglas Mast, Applied Research Lab. I am also grateful for discussion with Dr. Jon T. Jacobsen, Dept. of Mathematics, Pennsylvania State University.

References

[1] D. Colton, J. Coyle and P. Monk, "Recent developments in inverse acoustic scattering theory" SIAM Review **42** 369-414 (2000).

[2] A. J. Devaney, "A filtered backpropagation algorithm for diffraction tomography," Ultrason. Imaging **4**. 336-350 (1982).

[3] T. Douglas Mast, "Wideband quantitative ultrasonic imaging by time-domain diffraction tomography," J. Acoustic. Soc. Am. **106** 3061-3071 (1999).

[4] Feng Lin, Adrian I. Nachman, Robert C. Waag, "Quantitative imaging using a time-domain eigenfunction method," J. Acoust. Soc. Am. **108** 899-912 (2000).

[5] A. J. Devaney, "The limited-view problem in diffraction tomography," Inverse Problems **5** 501-521 (1989).

[6] Barry P. Medoff, "Image Reconstruction from Limited Data: Theory and Applications in Computerized Tomography," *Image Recovery:Theory and Application* Ed. Henry Stark. (Academic Press, Orlando, 1987), pp.321-365.

[7] Jorgen Jensen and Sidney Leeman, "Nonparametric Estimation of Ultrasound Pulses," IEEE Transactions of Biomedical Engineering **41** 929-936 (1994).

[8] Jorgen Jensen et. al., "Deconvolution of *in-vivo* ultrasound B-mode images" Ultrasonic Imaging **15** 122-133 (1993)

[9] D. Colton and R. Kress, *Inverese Acoustic and Electromagnetic Scattering Theory* (Springer-Verlag, New York, 1998).

[10] C. Gasquet and P. Witomski, *Fourier Analysis and Application: Filtering, Numerical Computation, Wavelets* (Springer, New York, 1999).

[11] A. Ziolkowski, *Deconvolution* (Intl. Human Resources Development Corp., Boston, 1984)

[12] O. Husby, T. Lie, T. Lango, J. Hokland, H. Ruc, "Bayesian 2-D deconvolution: a model for diffuse ultrasound scattering" IEEE Transactions of Ultrasonics, Ferroelectrics, and Frequency Control **48** 121-130 (2001).

[13] J. M. Mendel *Maximum-Likelihood Deconvolution: A Journey into Model-Based Signal Processing* (Springer-Verlag, New York, 1990).

[14] T. Taxt, "Comparison of Cepstrum-based methods for radial blind deconvolution of ultrasound images" IEEE Transactions on Ultrasonics, Ferroelectrics, and Frequency Control **44** 666-675 (1997)

[15] B. P. Bogert, M.J. Healy, and J.W. Tukey, "The quefrency alanysis of time series for echoes: cepstrum, pseudo-autocovariance, corss-cepstrum, and saphe cracking" *Proc. Symposum Time Series Analysis* Ed. M. Rosenblatt (John Wiley and Sons, New York, 1963), pp. 209-243

[16] A. V. Oppenheim and R. W. Schafer, *Discrete-Time Signal Processing* (Prentice Hall, Englewood Cliffs, N. J., 1989).

[17] Donald G. Childers et. al., "The cepstrum: a guide to processing," Proceedings of the IEEE **65** 1428-1443 (1977).

[18] D. M. Goodman, "Some properties of the multidimensional complex cepstrum and their relationship to the stability of multidimensional systems" Circuits System Signal Process **6** 3-30 (1987).

[19] T. Taxt and G. V. Frolova, "Noise Robust One-Dimensional Blind Deconvolution of Medical Ultrasound Images" IEEE Transactions on Ultrasonics, Ferroelectrics, and Frequency Control **46** 291-299 (1999)

[20] T. Kobayashi and S. Imai, "Spectral analysis using generalized cepstrum" IEEE Transactions on Acoustics, Speech, and Signal Processing **5** 1087-1090 (1984)

[21] Ronald N. Bracewell, *The Fourier Transform and its applications* (Mc-Graw-Hill Book Company, New York, 1986)

[22] A. Papoulis, "A new algorithm in spectral analysis and band-limited extrapolation" IEEE Transactions on Circuits and Systems **9** 735-742 (1975)

[23] D.C. Youla and H. Webb, "Image restoration by the method of convex projections: Part 1-Theory," IEEE Transactions on Medical Imaging **2** 81-94 (1982)

[24] D.C. Youla, "Mathematical theory of image restoration by the method of convex projections" *Image Recovery:Theory and Application* Ed. Henry Stark. (Academic Press, Orlando, 1987), pp.29-77

[25] M. I. Sezan and H. Stark, "Image restoration by the method of convex projections: Part 2-Applications and numerical results," IEEE Transactions on Medical Imaging **2** 95-101 (1982)

[26] H. Stark and Y. Yang, *Vector Space Projections: A Numerical Approach to Signal and Image Processing, Neural Nets, and Optics* (John Wiley and Sons, New York, 1998).

[27] Robert J. Marks II, "Alternating Projections onto Convex Sets" *Deconvolution of Images and Spectra* Ed. Peter A. Jansson (Academic Press, San Diego, 1997), pp. 476-501

[28] Carmen Sanchez-Avila, "Behavior of nonlinear POCS higher-order algorithms in the deconvolution problem" Nonlinear Analysis, Theory, Methods and Applications **30** 4909-4914 (1997)

[29] Jorge L. C. Sanz and Thomas S. Huang, "Unified Hilbert space approach to iterative least-squares linear signal restoration" J. Opt. Soc. Am. **73** 1455-1465 (1983).

[30] P. M. Morse and K. U. Ingard *Theoretical Acoustics* (Princeton University Press, 1986)

[31] L. P. Souriau, T. D. Mast, D.-L. D. Liu, M. Tabei, A. I. Nachman, and R. C. Waag. "A k-space method for large-scale models of wave propagation in tissue," IEEE Trans. Ultrason. Ferrolectr. Freq. Control.**48** 341-354 (1999).

3:00–3:15 Break

Contributed Papers

3:15

4pBB4. Simulation of ultrasonic propagation, scattering, and attenuation in the human chest wall. T. Douglas Mast (Appl. Res. Lab., Penn State Univ., University Park, PA 16802, mast@sabine.acs.psu.edu), Laura M. Hinkelman (Penn State Univ., University Park, PA 16802), and Robert C. Waag (Univ. of Rochester, Rochester, NY 14627)

A finite-difference time-domain model for ultrasonic pulse propagation through soft tissue [Mast *et al.*, J. Acoust. Soc. Am. **102**, 1177–1190 (1997)] has been extended to incorporate absorption effects as well as longitudinal-wave propagation in cartilage and bone. This extended method has been used to simulate ultrasonic propagation through anatomically detailed chest wall models. The inhomogeneous chest wall structure is represented by two-dimensional tissue maps determined by staining chest wall cross sections to identify connective tissue, muscle, fat, cartilage, and bone, scanning the stained cross sections at 300 dpi, and processing the scanned images to assign a tissue type to each pixel. Each pixel of the tissue map is then assigned a sound speed, density, and absorption value determined from published measurements to be representative of the local tissue type. Computational results for wavefront distortion including amplitude fluctuations, arrival time fluctuations, and waveform distortion show qualitative agreement with measurements performed on the same specimens [Hinkelman *et al.*, J. Acoust. Soc. Am. **101**, 2365–2373 (1997)]. Visualization of simulated tissue-ultrasound interactions in the chest wall shows possible mechanisms for image aberration in echocardiography, including effects due to reflection and diffraction from rib structures.

3:30

4pBB5. Coupled thermal-acoustic simulation results with temperature-dependent tissue parameters for therapeutic ultrasound. Ibrahim M. Hallaj (Appl. Phys. Lab., Univ. of Washington), Robin O. Cleveland, Ronald A. Roy, and R. Glynn Holt (Boston Univ., Boston, MA)

Recently the authors used direct simulations of the transient acoustic pressure field to calculate heat energy deposition and, thus, temperature fields in two-dimensional tissue like media [J. Acoust. Soc. Am. **102**, 3172(A) (1997)]. It is known that acoustic-induced temperature rises will alter the properties of the medium in hyperthermia situations. In this presentation the simulations are extended to simultaneously solve the wave propagation and tissue heating problems so that the effect of temperature-dependent tissue parameters can be accounted for directly. In other words, there is a continuous feedback of temperature on the sound propagation parameters, which in turn affects the thermal energy deposition. The simulations are second order accurate in time, fourth order in space full wave calculations using the finite-difference time-domain technique, and allow for finite-amplitude wave propagation in an inhomogeneous, thermoviscous fluid. The model allows for spatially and temporally varying sound speed, density, attenuation coefficient, and nonlinearity parameter, as well as variable thermal properties and perfusion. Acoustic pressure, thermal dose, and tissue temperature are calculated, and conclusions are made regarding qualitative and quantitative aspects of focusing behavior contrasted to the case where the propagation and thermal parameters are kept constant. [Work sponsored by ONR and DARPA.]

3:45

4pBB6. Bubble-mediated hyperthermia in an instrumented tissue phantom. Patrick Edson, R. Glynn Holt, and Ronald A. Roy (Dept. of Aerosp. and Mech. Eng., Boston Univ., Boston, MA 02215)

The coagulation of blood by ultrasound, a procedure termed acoustic hemostasis by us, involves the contributions of several physical and biophysical effects. To investigate these effects, experiments have been undertaken involving rapid hyperthermia in an instrumented tissue phantom. Previously, the authors have reported a sharp increase in the rate of heating with increasing peak negative insonation pressure [J. Acoust. Soc. Am. **103**(A) (1998)]. This increase occurs at a well-defined pressure, a threshold effect not unlike that observed at the onset of inertial acoustic cavitation. It was postulated that this effect may be the result of such cavitation activity leading to bubble-enhanced heating. The results of experiments in which the temperature rise and cavitation activity are monitored simultaneously are reported. The results will be interpreted in the light of the aforementioned cavitation effect, as well as competing explanations such as the excess absorption associated with the formation of nonlinearity in the pressure profile. [Work supported by DARPA.]

4:00

4pBB7. Ultrasonic periodontal probe. Mark Hinders, Alan Guan, and John Companion (Appl. Sci. Dept., College of William and Mary, Williamsburg, VA 23187)

This talk discusses proof of concept *in vitro* testing of an ultrasonic probe for imaging periodontal structures. This technique allows accurate measurements of disease activity for patient risk assessment and treatment outcome evaluation without the need for ionizing radiography or manual periodontal probing. This technique promises reduced variability and improved ease of use, in comparison to conventional manual periodontal probing. The work discussed here is the first step to establish the ultrasound periodontal probe as a clinically valuable tool for patient assessment and the first noninvasive measure of periodontal disease activity. Data from cadaver samples using a prototype intraoral ultrasound instrument is compared to conventional manual probing subsequently performed on the annotated cadaver samples. The results discussed here are being used to refine the technique, improve the analysis of scan signals, and develop the framework of the software that will be used during a subsequent *in vitro* testing program.

4:15

4pBB8. An estimation technique of the vector component of blood flow from Doppler information on a plane. Shigeo Ohtsuki (Precision and Intelligence Lab., Tokyo Inst. of Technol., Midori-ku Nagatsuta 4259, Yokohama, 226-8503 Japan)

The information of the ultrasonic Doppler effect is the velocity component of ultrasonic scatters in the direction of the ultrasonic beam in fluid. Scanning the ultrasonic beam, a colored Doppler image can be obtained on a plane. Using this data, the velocity component perpendicular to the ultrasonic beam is estimated. In this case, the observation plane is in three-dimensional flow. Considering sources of fluid in the plane, the flow function method [S. Ohtsuki and M. Tanaka, J. Visual. Soc. Jpn. **1869**, 40–44 (1998)] is applied. This flow function method was developed for streamlines on a medical ultrasonic colored Doppler image of blood flow in the heart. The flow function without sources is expressed as a single-valued function. The flow function of sources is a multi-valued function named a laminar function. The flow function on an observation plane is the combination of these two functions. The gradient of the flow function on the plane is a flow vector component. The estimation technique introduced here is an application of the flow function method.

8:40

2aPAb3. Atomic force acoustic microscopy: Acoustical imaging on the nm scale. Ute Rabe and Sigrun Hirsekorn (Fraunhofer Inst. for Nondestructive Testing, Bldg. 37, Univ., D-66123 Saarbruecken, Germany, rabe@izfp.fhg.de)

High-resolution imaging techniques are important tools in materials evaluation and nondestructive testing. Conventional acoustical imaging techniques allow the determination of elastic properties and defect detection with a spatial resolution dependent on the wavelength of the imaging ultrasound. Research work over the last years has shown that this limit can be overcome by combining atomic force microscopy (AFM) with acoustic microscopy. Inducing ultrasonic vibrations in the contact formed by the sample surface with the sensor tip of an AFM opens its high lateral resolution to ultrasonic imaging. Different measurement techniques in which linear and nonlinear effects play a role are possible and have been demonstrated experimentally. An overview of the imaging techniques will be given. Theoretical models which allow the explanation of the image contrast and the derivation of quantitative surface qualities will be discussed.

9:00

2aPAb4. Material characterization using micro-machined air transducers. Butrus T. Khuri-Yakub, F. Levent Degertekin, Sean T. Hansen, and Neville R. Irani (Stanford Univ., E. L. Ginzton Lab., Stanford, CA 94305, khuri-ya@ee.stanford.edu)

This paper presents the application of micro-machined ultrasonic air transducers (MUT) to material characterization. The transducers are made of thin membrane capacitors with very thin vacuum gaps. A system analysis that details the design of the transducers and the transmitter and receiver electronics to deliver over a 100-dB dynamic range while operating in the 1–5-MHz range is presented. The transducers and electronics system are used both in pulse–echo and pitch–catch modes to evaluate materials. In transmission and reflection, the system is used to image defects in carbon epoxy composites. Transducers are designed, using Lamb wave theoretical calculations, to excite selected Lamb wave modes in composite and other materials. The transducers are then used to characterize the composites with respect to defect detection (via Lamb wave velocity changes) and material characterization (via slowness curve inversion).

9:20

2aPAb5. Imaging with a 16 000-element 2-D array. Ken Erikson and Tim White (Lockheed Martin, 2 Forbes Rd., Lexington, MA 02421)

Imaging with acoustical lenses in the low MHz frequency range using fully populated 2-D arrays offers the potential for high-resolution, real-time, 3D volume imaging, together with low power and low cost. A 2-D composite-piezoelectric receiver array bonded directly to a large custom-integrated circuit is the enabling technology for a new implementation of the original acoustical imaging paradigm. This 128×128 (16 384 total) element transducer hybrid array (THA) uses massively parallel, on-chip signal processing and is intended for medical and underwater imaging applications. The system under development, which is the acoustical analog of a video camera, will be discussed in this paper.

9:40–10:00 Break

Contributed Papers

10:00

2aPAb6. Time-domain ultrasound diffraction tomography. T. Douglas Mast (Appl. Res. Lab., Penn State Univ., University Park, PA 16802, mast@sabine.acs.psu.edu)

A quantitative ultrasonic imaging method employing time-domain scattering data is presented. This method provides tomographic images of inhomogeneous media using scattering measurements made on a surface surrounding the medium of interest, e.g., on a circle for two-dimensional problems or on a sphere for three-dimensional problems. These scattering data are used to construct a time-domain analog of the far-field scattering operator. Images of compressibility variations are then reconstructed using a coherent combination of the far-field scattered waveforms, delayed and summed in a manner that numerically focuses on the unknown medium. This approach is closely related to synthetic aperture imaging; however, unlike conventional synthetic-aperture methods, the present method provides quantitative reconstructions of compressibility variations, analogous to frequency-compunded filtered backpropagation images weighted by the spectrum of the incident wave. Example reconstructions, obtained using synthetic data for two-dimensional scattering of wideband pulses, show that the time-domain reconstruction method can provide image quality superior to single-frequency reconstructions for objects of size and contrast relevant to medical imaging problems such as ultrasonic mammography. Reconstructions also illustrate the dependence of image quality on the number of incident-wave insonifications and on the range of scattering angles available for measurements.

10:20

2aPAb7. Transient elastography in biological tissues. Laurent Sandrin, Stefan Catheline, and Mathias Fink (ESPCI—LOA, 10 rue Vauquelin, 75005 Paris, France, laurent.sandrin@espci.fr)

Elastography is used in different ways to characterize soft tissues. Ophir uses static elastography to estimate strains in the tissue after a quasi-static compression. Strains can also be measured by sonoelasticity using mechanically forced low-frequency vibrations and the ultrasonic pulsed Doppler method (Parker and Sato). These techniques are subjected to bias due to unknown boundary conditions. In this article a technique called transient elastography is presented which is not sensible to boundary conditions. It uses a low-frequency pulsed vibration (~100 Hz) and a cross-correlation technique to measure displacements on the order of 1 μm. This technique was first developed for one-dimensional measurements on the axis of the ultrasonic transducer. It is now used with an array of 64 transducers to get time-dependent two-dimensional displacements at a rate of 2000 frames per second. Movies of the shear wave propagation of large acoustic lenses provides zoom and focal plane control for magnified imaging with enhanced resolution and depth. Both systems have undergone preliminary investigation in large groups of patients with known abnormalities to assess their suitability for detection and characterization of breast disease and to provide accurate guidance for biopsy or tumor ablation. Results of laboratory and clinical findings will be presented.

9:20

2aBB3. Recent progress on nonuniform fast Fourier transform algorithms and their applications. Q. H. Liu, B. Tian, X. Xu, and Z. Q. Zhang (Dept. of Elec. Eng., Duke Univ., Durham, NC 27708-0291)

Recently, nonuniform fast Fourier transform (NUFFT) algorithms have received significant attention [Dutt and Rokhlin, SIAM J. Sci. Stat. Comput. **14**, 1368–1393 (1993)]. Unlike the regular fast Fourier transform (FFT) algorithms, the NUFFT algorithms allow the data to be sampled nonuniformly. The leading order of the number of arithmetic operations for these NUFFT algorithms is $O(N \log_2 N)$. Here, we review the recent progress of the NUFFT algorithms using the regular Fourier matrices and conjugate-gradient method for the forward and inverse NUFFT algorithms [Liu and Nguyen, IEEE Microwave Guid. Wave Lett. **8**, 18–20 (1998); Liu and Tang, Electron. Lett. **34**, 1913–1914 (1998)]. Because of their least-square errors, these NUFFT algorithms are about one order of magnitude more accurate than the previous algorithms. These NUFFT algorithms have been applied to develop the nonuniform fast Hankel transform (NUFHT) and nonuniform fast cosine transform (NUFCT) algorithms. Both NUFFT and NUFHT algorithms have been used to solve integral equations in computational electromagnetics and acoustics; The NUFCT has been used to solve time-dependent wave equations. Numerical examples will demonstrate the efficiency of the fast transform algorithms, and the applications in computational electromagnetics and computational acoustics.

9:45

2aBB4. Noncontact ultrasonic imaging for the evaluation of thermal injury. Joie P. Jones (Dept. of Radiological Sci., Univ. of California—Irvine, Irvine, CA 92697-5000)

Although conventional wisdom suggests that ultrasonic imaging of the body cannot be accomplished without direct contact (or at least via water coupling), we have shown that noncontact imaging through air is possible, certainly for superficial body regions, provided judicious choices of piezoelectric materials and matching layers are made. In preliminary experiments and clinical studies reported here, noncontact imaging is demonstrated for the evaluation of thermal injury (including the quantitative measurement of burn-depth), for the assessment of wound healing, and for the examination of assorted skin lesions. Specifically, in the case of thermal injury, reflections from the dermal/fat interface in human skin is clearly seen using a noncontact 5-MHz transducer. Such measurements are sufficient to determine burn-depth which, in turn, are sufficient to provide, for the first time, a quantitative and noninvasive method for burn evaluation and treatment specification. Evaluating over 500 burn sites in some 100 patients, noncontact ultrasound showed a much greater accuracy and sensitivity than standard clinical assessment. Our method is applicable to a conventional clinical environment as well as a battlefield situation and should prove particularly effective for large-scale medical triage.

10:10–10:20 Break

Contributed Papers

10:20

2aBB5. Focus-directed processing of acoustic holography images. Ruming Yin, Shira L. Broschat (School of Elec. Eng. and Computer Sci., Washington State Univ., P.O. Box 642752, Pullman, WA 99164-2752), and Patrick J. Flynn (The Ohio State Univ., Columbus, OH 43210-1272)

Acoustic holography is a transmission mode imaging technique which was first proposed in the 1970s. As with optical holography, an image is obtained using coherent interference of the transmitted acoustic signal with a reference signal. The interference pattern is illuminated with a laser, and the resulting image is digitized. However, since image reconstruction is performed optically, acoustic holography introduces a focusing problem characteristic of optical systems. Ideally, an image is focused on tissues at a given depth along the optical axis—that is, in one planar slice of the object. In practice, the image is focused over a range of depths so that objects at different depths are blurred but still visible. In this paper, we consider several postprocessing algorithms developed to improve images obtained using an acoustic holography system. First, a focus measure technique is used to determine when the object of interest is best focused. Second, a technique called depth from focus is used to determine the depth of an object. Third, a technique is developed to increase the "in focus" interval, or focusing range. These techniques will be discussed and imaging results will be presented. [Work supported by the National Science Foundation and the Carl M. Hansen Foundation.]

10:35

2aBB6. A new k-space method for simulation of ultrasonic propagation in tissue. T. Douglas Mast (Appl. Res. Lab., Penn State Univ., University Park, PA 16802, mast@sabine.acs.psu.edu), D.-L. Donald Liu (Siemens Medical Systems, Issaquah, WA 98027), Laurent P. Souriau, Adrian I. Nachman, and Robert C. Waag (Univ. of Rochester, Rochester, NY 14642)

A new k-space method for large-scale computations of ultrasonic propagation is presented. In the new method, spatial derivatives from the second-order acoustic wave equation for inhomogeneous media are evaluated by Fourier transformation. Solutions are advanced in time using a $k-t$ space Green's function. Computational results indicate that the new method shares advantages of both past k-space and pseudospectral methods. For scatterers with properties similar to soft tissue, the k-space method provides much higher accuracy and lower computational cost than a 2–4 finite-difference time domain method. The k-space method also allows high accuracy to be obtained for time steps much larger than those required by a leapfrog pseudospectral method. The low dispersion inherent to the k-space method is illustrated by large-scale quasi-one-dimensional computations, in which pulse waveforms incur negligible shape change for propagation distances as large as 1000 wavelengths. Example applications of the k-space method are demonstrated, including simulation of propagation through a large-scale tissue cross-sectional model and incorporation of a k-space solver into a nonlinear inverse scattering method employing eigenfunctions of the far-field scattering operator.

TIME-DOMAIN INVERSE SCATTERING FOR QUANTITATIVE ULTRASONIC MAMMOGRAPHY

T. Douglas Mast

Applied Research Laboratory
The Pennsylvania State University

mast@sabine.acs.psu.edu

A new method for ultrasonic mammography is presented. This method provides quantitative tomographic images of inhomogeneous tissue using time-domain scattering measurements made on a surrounding surface (for example, on a circle for images of a two-dimensional breast cross section). High-resolution, quantitative images of tissue are reconstructed using coherent combination of far-field scattered ultrasound waveforms, delayed and summed to focus at each image point. The focused image is a reconstruction of the spatially-dependent sound speed variation, and is equivalent to a wideband filtered backpropagation reconstruction weighted by the spectrum of the incident wave. The resulting images are higher in quality than frequency-domain quantitative reconstructions and contain more diagnostic information than conventional B-scans.

Rigorous testing of the new imaging method is carried out using simulated ultrasonic propagation through breast tissue. Breast tissue models are obtained both from segmentation of stained cross sections and from analysis of high-resolution three-dimensional data from the Visible Woman project. Computations of ultrasonic propagation are performed using a new *k*-space method, in which the spatial differential equations are solved by Fourier transformation and temporal iteration is performed using a *k-t* space propagator. Numerical results indicate that this method is highly accurate for large-scale soft-tissue computations, with much greater efficiency than that of competing methods. Thus, the *k*-space method is particularly appropriate for large-scale two-dimensional and three-dimensional computations of propagation through breast tissue.

Quantitative images, obtained using synthetic data for two-dimensional and three-dimensional scattering of wideband pulses as well as measured scattering data from a 2048-element ring transducer, confirm that the time-domain reconstruction method provides superior image quality for objects of size and contrast relevant to ultrasonic mammography. The new method can also be extended to incorporate available image-enhancement techniques, such as time-gain compensation to correct for medium absorption and aberration correction methods to reduce error associated with weak scattering approximations.

The US Army Medical Research and Materiel Command under DAMD17-98-1-8141

supported this work.

TIME-DOMAIN INVERSE SCATTERING FOR QUANTITATIVE ULTRASONIC MAMMOGRAPHY

T. Douglas Mast

Applied Research Laboratory
The Pennsylvania State University

New methods for breast cancer detection and characterization are the focus of this project, supported by the US Army Medical Research and Materiel Command. Major goals are to establish a new high-resolution, quantitative ultrasonic imaging method and to test this method using simulated propagation of ultrasonic pulses through accurately detailed breast tissue models.

Detailed breast tissue models have been obtained both from stained breast cross sections and from analysis of high-resolution three-dimensional data from the Visible Woman project. To accurately compute ultrasonic propagation through these tissue models, a new *k*-space method for ultrasound simulation has been developed. The *k*-space method is more accurate, more efficient, and requires less storage than alternative methods, and is thus ideal for computation of large-scale 2D and 3D ultrasonic propagation in breast tissue.

A new time-domain ultrasonic mammography method provides quantitative images of inhomogeneous media including breast tissue. High-resolution maps of the tissue sound speed are obtained from processing of measured ultrasonic scattering. Unlike previous frequency-domain inverse scattering methods, the entire signal bandwidth is used, so that reconstructed images have higher point resolution (ability to detect small structures such as microcalcifications) and contrast resolution (ability to distinguish subtle differences between tissue structures). The new method employs a straightforward time-domain reconstruction algorithm, similar to synthetic-aperture methods used by current clinical scanners, but provides much more diagnostic information than current B-scan devices. The high efficiency of the reconstruction algorithm makes the new method particularly well-suited for three-dimensional quantitative ultrasonic mammography.

Quantitative images, obtained both from synthetic and measured ultrasound data, confirm that the new imaging method provides superior image quality and accurate quantitative information. After further development and clinical implementation, the new ultrasonic mammography method is expected to become competitive with magnetic resonance imaging and x-ray computed tomography as a tool for breast cancer detection and characterization, while maintaining inherent advantages of ultrasound such as lower cost, ability to characterize cystic and solid lesions, and safe, nonionizing radiation.

10:30

3aBB7. Aberration-corrected time-domain ultrasound diffraction tomography. T. Douglas Mast (Appl. Res. Lab., Penn State Univ., University Park, PA 16802)

The inverse scattering problem of reconstructing a spatially dependent sound speed variation from far-field time-domain acoustic scattering measurements is considered. Such reconstructions are quantitative images with applications including ultrasonic mammography. Although the linearized time-domain inverse scattering problem is shown to have no general solution for finite signal bandwidth, an approximate solution to the linearized problem is constructed using a simple delay-and-sum method analogous to "gold standard" ultrasonic beamforming. The form of this solution suggests that the full nonlinear inverse scattering problem can be approximated by applying appropriate angle- and space-dependent time shifts to the time-domain scattering data; this analogy leads to a general approach to aberration correction. Two related methods for aberration correction are presented: one in which delays are computed from estimates of the medium using an efficient straight-ray approximation, and one in which delays are applied directly to a time-dependent linearized reconstruction. Numerical results indicate that these correction methods achieve substantial quality improvments for imaging of large scatterers. [Work supported by the Breast Cancer Research Program of the U.S. Army Medical Research and Materiel Command.]

10:45

3aBB8. Theoretical considerations for the use of microbubbles as point targets for phase aberration correction. Dimitris Psychoudakis (Elec. Eng. and Computer Sci., Univ. of Michigan, Ann Arbor, MI 48109-2122), J. Brian Fowlkes, John L. Volakis, Oliver D. Kripfgans, and Paul L. Carson (Univ. of Michigan, Ann Arbor, MI 48109-0553)

Bubbles can be produced by vaporization of perfluorocarbon droplets of a few μm diameter. These bubbles can reach up to 100 μm in diameter and their backscatter is calculated to be more than 10 dB above that of several organ tissues. At these sizes and for diagnostic frequencies (2–8 MHz), bubbles can be approximated by the nonrigid sphere scattering solution employed here. This presentation concerns the bubble size and its implications on the backscatter amplitude and the phase error introduced in diagnostic ultrasound when assuming that the bubble acts as a point target for phase aberration correction. The phase error is the difference between the phase at each location along the receiving aperture relative to that at the aperture center, compared with the same relative phase for a perfect point target. Evaluations were made of the phase error with respect to a range of transducer f-numbers (0.5–2.0) for a specific bubble size (30 μm radius) and at certain frequencies (2–8 MHz). For example, at 5 MHz the phase error introduced by the point target assumption is maximally 5 deg, while the phase error of breast tissue scattering is around 160 deg. [Work supported by PHS Grant No. R01HL54201 from the National Heart, Lung, and Blood Institute.]

11:00

3aBB9. Comparison between time reversal and spatio-temporal inverse filter application to focusing through a human skull. Mickael Tanter, Jean-Francois Aubry, Jean-Louis Thomas, and Mathias Fink (Laboratoire Ondes et Acoustique, ESPCI, Paris VII Univ., Paris, France)

Ultrasonic imaging systems capabilities are strongly dependent on the focusing quality of the ultrasonic beam. In the case of brain imaging, the skull strongly degrades the ultrasonic focusing pattern by introducing strong phase and amplitude aberrations of the wave-front. In previous work, this degradation of the beam focus had been partially corrected by coupling the time reversal focusing process to an amplitude compensation of the emission signals. In that case, the optimal focus was reproduced down to -20 dB, but the sidelobe level remained at about -25 dB. This elegant technique will be compared to another focusing technique recently developed in our laboratory, called spatio-temporal inverse filtering. Thanks to this method, based on the inversion of the propagation operator at each frequency within the bandwidth of our transducers, experimental focusing through the skull is now comparable to optimal focusing in a homogeneous medium. Those two methods not only differ theoretically, but also suffer differently from all the experimental defects, such as the limited bandwidth of the transducers or the limited aperture of the arrays. A comparson of the results obtained with both techniques in water and through a human skull clearly highlights the advantages and the drawbacks of each method.

11:15

3aBB10. Integrated matrix arrays. Ken Erikson, Jason Stockwell, and Robert McPhie (BAE Systems, P.O. Box 868, Nashua, NH 03061-0868)

Improved image quality requires the use of matrix ($n \times m$) arrays with a thousand or more elements. As element numbers increase and their dimensions grow smaller, limitations to present fabrication technologies arise. Cost, ergonomics, produceability, and reliability are important issues. Signal loss due to the capacitance of interconnecting coax cables becomes a fundamental problem. Connecting an integrated circuit directly to the array elements alleviates all these problems. Each unit cell of such a custom transmitter/receiver integrated circuit (TRIC) may have high voltage switches for transmitting; a preamplifier which minimizes signal loss due to capacitance in coax cables and a multiplexer to send the array signals over fewer wires. Additional signal processing and beam forming may also be included. Issues with currently available arrays are reviewed. The new technology for direct connection of arrays to IC's is described. The paper concludes with speculation about future possibilities of this approach.

11:30

3aBB11. Measurements of the spatial coherence of the fundamental and second-harmonic beams for a clinical imaging system. Russell J. Fedewa, Kirk D. Wallace, Mark R. Holland (Lab. for Ultrason., Dept. of Phys., Washington Univ. of St. Louis, One Brookings Dr., St. Louis, MO 63130), James R. Jago, Gary C. Ng, Matthew R. Rielly, Brent S. Robinson (ATL Ultrasound, Bothell, WA 98041-3003), and James G. Miller (Lab. for Ultrason., Washington Univ. of St. Louis, St. Louis, MO 63130)

Spatial coherence of backscattered signals underlies correlation-based phase aberration corrections. The van Cittert–Zernike theorem relates frequency-independent spatial coherence to the autocorrelation of the transmit apodization. Previous studies suggest that the mainlobe of the nonlinearly generated harmonic beam is wider and exhibits lower sidelobes than a beam linearly generated at the harmonic frequency. The objective of this study was to measure the spatial coherence associated with fundamental and nonlinearly generated harmonic beams. Using data experimentally acquired from a clinical scanner (ATL HDI5000), two independent methods were employed to measure the spatial coherence. One approach measured the spatial coherence of backscatter from a tissue-mimicking phantom using rf signals from individual elements of a linear array. In the second approach, the effective apodization was determined by a linear angular spectrum backpropagation of hydrophone-sampled data from a transverse plane in the focal zone. The results show that the effective apodization of the nonlinearly generated harmonic beam is more aggressive than the actual transmit apodization. The spatial coherence associated with the second-harmonic beam differs from the spatial coherence of the fundamental beam, but is predicted by the effective apodization. [Supported in part by NIHHL40302 & ATL.]

11:45

3aBB12. Efficient computation of field of 2-D array with limited diffraction array beams. Jian-yu Lu and Jiqi Cheng (Ultrasound Lab, Dept. of Bioengineering, The Univ. of Toledo, Toledo, OH 43606, jilu@eng.utoledo.edu)

Two-dimensional (2-D) arrays are useful for improving quality of three-dimensional (3-D) medical imaging in ultrasound. Beams produced with a 2-D array are usually simulated with the Rayleigh–Sommerfeld diffraction formula (RSDF). In general, the RSDF requires a 2-D integra-

APPENDIX L

T. Douglas Mast

Senior Biomedical Engineer, Ethicon Endo-Surgery,
4545 Creek Rd. ML 40, Cincinnati, OH 45242
(513) 337-3144 (tel.), (513) 337-4144 (fax), dmast@eesus.jnj.com

Technical Expertise

Ultrasonic imaging, wave propagation and scattering in inhomogeneous media, physical acoustics, inverse scattering, numerical methods, flow/sound interaction, bioacoustics, nondestructive evaluation.

Education

Ph.D. in Acoustics, The Pennsylvania State University, 1993. Thesis: *Physical Theory of Narrow-Band Sounds Associated with Aneurysms.* Advisor: Allan D. Pierce. GPA: 3.93/4.0.

Certificate (comparable to B.A.) in Music, The Naropa Institute, 1988.

B.A. in Physics and Mathematics, Goshen College, 1987. GPA: 3.89/4.0.

Present and Recent Employment

Senior Biomedical Engineer, Ethicon Endo-Surgery (a Johnson and Johnson Company), 2001–present.

Research Associate and Assistant Professor of Acoustics, Applied Research Laboratory, The Pennsylvania State University, 1999–2001.

Research Associate, Applied Research Laboratory, The Pennsylvania State University, 1997–1999.

Postdoctoral Scholar, Applied Research Laboratory, The Pennsylvania State University, 1996–1997.

Postdoctoral Fellow, Ultrasound Research Laboratory, University of Rochester, 1993–1996.

Research Asst., Graduate Program in Acoustics, Pennsylvania State University, 1988–1993.

Research Asst., Turner Laboratory of Precision X-Ray Measurements, Goshen College, 1986–1987.

Teaching Asst., Department of Physics, Goshen College, 1985–1987.

Honors, Awards and Society Affiliations

President, Central Pennsylvania Chapter of the Acoustical Society of America, 1999–2000.

Vice President, Central Pennsylvania Chapter of the Acoustical Society of America, 1998-1999.

Listed in *Who's Who in Science and Engineering.*

Kenneth E. Simowitz Memorial Award, The Pennsylvania State University, 1996.

F. V. Hunt Fellowship, Acoustical Society of America, 1994–1995.

Kenneth E. Simowitz Memorial Citation, The Pennsylvania State University, 1992.

General Electric Teaching Incentive Loan, 1990.

Turner Laboratory Fellowship, Goshen College, 1986.

Member of Acoustical Society of America.

Member of American Institute of Ultrasound in Medicine.

Member of Institute of Electrical and Electronics Engineers (Ultrasonics, Ferroelectrics, and Frequency Control Society).

Courses Taught

Acoustic Scattering (ACS 597C), Penn State Graduate Program in Acoustics, Spring 2000.

Scattering in Inhomogeneous Media (ACS 598E), Penn State Summer Program in Acoustics, to be taught Summer 2001.

Other Professional Activities

Organized and chaired special sessions for Acoustical Society of America meetings: "Models for tissue-ultrasound interaction" (Fall 1998), "Beamforming and adaptive aberration correction" (Spring 2001).

Served on Diagnostic Imaging Study Section for National Institutes of Health, 1999–2000.

Reviewed many papers for archival journals including *IEEE Trans. Ultrason., Ferroelect., Freq. Contr.*, *J. Acoust. Soc. Am.*, *J. Biomech*, *IEEE Trans. Biomed. Eng.*, *Ultrasonics*, and *J. Opt. Soc. Am.*.

Scientific Publications

Tabei, M., Mast, T. D., and Waag, R. C., "A new *k*-space method for coupled first-order acoustic propagation equations," submitted to *J. Acoust. Soc. Am.* (2001).

Jansson, T., Jurkonis, R., Mast, T. D., Persson, H. W., and Lindström, K., "Frequency dependence of speckle in continuous-wave ultrasound: implications for blood perfusion measurements," submitted to *IEEE Trans. Ultrason., Ferroelect., Freq. Contr.* (2001).

Mast, T. D., Swanson, D. C., Mahon, M. P. and Norris, D. E., "Resolution of multipath outdoor sound propagation using spread spectrum signals," submitted to *J. Acoust. Soc. Am.* (2001).

Mast, T. D. and Gordon, G. A., "Quantitative flaw reconstruction from ultrasonic surface wavefields measured by electronic speckle pattern interferometry," *IEEE Trans. Ultrason., Ferroelect., Freq. Contr.* **48**, 432–444 (2001).

Mast, T. D., Souriau, L. P., Liu, D.-L., Tabei, M., Nachman, A. I., and Waag, R. C., "A *k*-space method for large-scale models of wave propagation in tissue," *IEEE Trans. Ultrason., Ferroelect., Freq. Contr.* **48**, 341–354 (2001).

Mast, T. D., "Empirical relationships between acoustic parameters in human soft tissues," *Acoustics Research Letters Online* **1**, 37–42 (2000).

Mast, T. D., Lin, F., and Waag, R. C., "Time-domain ultrasound diffraction tomography," *1999 IEEE Ultrasonics Symposium Proceedings*, Vol. 2, pp. 1617-1620.

Mould, J. C. Wojcik, G. L., Carcione, L. M., Tabei, M., Mast, T. D., and Waag, R. C., "Validation of FFT-based algorithms for large-scale modeling of wave propagation in tissue," *1999 IEEE Ultrasonics Symposium Proceedings*, Vol. 2, pp. 1551-1556.

Mast, T. D., "Wideband quantitative ultrasonic imaging by time-domain diffraction tomography," *J. Acoust. Soc. Am.* **106**, 3061–3071 (1999).

Mast, T. D., Hinkelman, L. M., Metlay, L. A., Orr, M. J., and Waag, R. C., "Simulation of ultrasonic pulse propagation, distortion, and attenuation in the human chest wall," *J. Acoust. Soc. Am.* **106**, 3665–3677 (1999).

Gordon, G. A. and Mast, T. D., "Wide-area imaging of ultrasonic Lamb wave fields by electronic speckle pattern interferometry," *Proc. SPIE* **3586**, 297–309 (1999).

Myers, L. F, Lovette, M., Kilgus, C. C., Giannini, J. A., Swanson, D. C., Reichard, K. M., Mahon, M. P., and Mast, T. D., "Java-based information system for wayside sensing and control," *Proceedings of the IEEE/ASME Joint Railroad Conference*, 135–147 (1998).

Hinkelman, L. M., Mast, T. D., Metlay, L. A., and Waag, R. C., "The effect of abdominal wall morphology on ultrasonic pulse distortion. Part I: Measurements," *J. Acoust. Soc. Am.* **104**, 3635–3649 (1998).

Mast, T. D., Hinkelman, L. M., Orr, M. J., and Waag, R. C., "The effect of abdominal wall morphology on ultrasonic pulse distortion. Part II: Simulations," *J. Acoust. Soc. Am.* **104**, 3650–3664 (1998).

Mast, T. D., Hinkelman, L. M., Orr, M. J., Sparrow, V. W., and Waag, R. C., Erratum: "Simulation of ultrasonic pulse propagation through the abdominal wall," [*J. Acoust. Soc. Am.* **102**, 1177–1190 (1997)], *J. Acoust. Soc. Am.* **104**, 1124–1125 (1998).

Jansson, T. T., Mast T. D., and Waag, R. C., "Measurements of differential scattering cross-section using a ring transducer," *J. Acoust. Soc. Am.* **103**, 3169–3179 (1998).

Mast, T. D., Nachman, A. I., Liu, D.-L., and Waag, R. C., "Quantitative imaging with eigenfunctions of the scattering operator," *1997 IEEE Ultrasonics Symposium Proceedings*, Vol. 2, pp. 1507–1510.

Hinkelman, L. M., Mast, T. D., Orr, M. J., and Waag, R. C., "Effects of abdominal wall morphology on ultrasonic pulses," *1997 IEEE Ultrasonics Symposium Proceedings*, Vol. 2, pp. 1493–1496.

Mast, T. D., Nachman, A. I., and Waag, R. C., "Focusing and imaging using eigenfunctions of the scattering operator," *J. Acoust. Soc. Am.* **102**, 715–725 (1997).

Mast, T. D., Hinkelman, L. M., Orr, M. J., Sparrow, V. W., and Waag, R. C., "Simulation of ultrasonic pulse propagation through the abdominal wall," *J. Acoust. Soc. Am.* **102**, 1177–1190 (1997).

Mast, T. D. and Waag, R. C., "Wave space resolution in ultrasonic scattering measurements," *J. Acoust. Soc. Am.* **98**, 3050–3058 (1995).

Mast, T. D. and Pierce, A. D., "A theory of aneurysm sounds," *J. Biomech.* **28**, 1045–1053 (1995).

Mast, T. D. and Pierce, A. D., "Describing-function theory for flow excitation of resonators," *J. Acoust. Soc. Am.* **97**, 163–172 (1995).

Mast, T. D., "Limit cycles of flow-excited resonators: a describing-function analysis," in *Structural Acoustics, Scattering, and Propagation: Theoretical and Computational Acoustics—Volume I*, Edited by J. E. Ffowcs Williams, D. Lee, and A. D. Pierce, (River Edge, New Jersey: World Scientific, 1994), pp. 389-403.

Mast, T. D. and Pierce, A. D., "Flow-induced sounds associated with aneurysms," in *Flow Noise Modeling, Measurement, and Control*, edited by T. M. Farabee, W. L. Keith, and R. M. Lueptow (New York: American Society of Mechanical Engineers, 1991), pp. 129–134.

Other Activities and Interests

Volunteer DJ for Penn State NPR radio station, WPSU.

Volunteer and Board Member for Acoustic Brew folk concert series.

Musician: tenor banjo, mandola, and tenor guitar player in string band Steele Hollow.

Research in genealogy (Amish/Mennonite origins).

Recreational computer programming.